DISCRETE ELEMENT MODELLING OF CEMENTED SAND AND PARTICLE CRUSHING AT HIGH PRESSURES

JOHN PATRICK DE BONO, BEng.

Thesis submitted to the University of Nottingham

for the degree of Doctor of Philosophy

DECEMBER 2013

ABSTRACT

This project aims to provide an insight into the behaviour of cemented sand under high pressures, and to further the understanding of the role of particle crushing. The discrete element method is used to investigate the micro mechanics of sand and cemented sand in high-pressure triaxial tests and one-dimensional normal compression.

Using the software PFC3D, a new triaxial model has been developed, which features an effective flexible membrane that allows free deformation of the specimen and the natural failure mode to develop. The model is capable of exerting and sustaining high confining pressures. Cementation has been modelled using inter-particle bonds, and a full investigation of the bond properties is presented, highlighting their influence on the macroscopic behaviour (e.g. failure mode and volumetric response).

A simple particle breakage mechanism is used to model the one-dimensional normal compression of sand. By considering the stresses induced in a particle due to multiple contacts, and allowing particles to fracture without the use of agglomerates, this work aims to explain the mechanics of normal compression. The influence of the mechanics of fracture on the slope of the normal compression line is investigated, and the normal compression is linked to the evolution of a fractal particle size distribution. A new equation for the one-dimensional normal compression line is proposed, which includes the size-effect on average particle strength, and demonstrates agreement with experimental results. It is shown that this new equation holds for a wide range of simulations. The time dependence of particle strength is incorporated in to this model to simulate one-dimensional creep tests, leading to a new creep law.

The normal compression of cemented sand is investigated, and the results show that bonding reduces particle crushing, and that it is both the

magnitude and distribution of bond strengths that influence the compression curve of the structured material. Simulations are also presented that show that it is possible to capture the effects of particle crushing in high-pressure triaxial tests on both sand and cemented sand. Particle crushing is shown to be essential for capturing realistic volumetric behaviour, and the intrusive capabilities of the discrete element method are used to gain insight into the effects that cementation has on the degree of crushing.

ACKNOWLEDGEMENTS

The author would like to express his sincere gratitude to the following:

- Professor Glenn McDowell, for his expert guidance, supervision, selfless patience and encouragement, and friendship;
- Dr Dariusz Wanatowski, for his support and skilled advice;
- Mr Robin Dollery, for his invaluable assistance;
- The EPSRC, for their financial support;

without whom, this thesis would not have been possible. Finally, he would like to express his eternal appreciation and thanks to: his parents, Susan and Joe; his brother Matt, and his family; his sister Caroline, and her family; and his girlfriend Evgenia; for their constant love, confidence and understanding.

LIST OF CONTENTS

LIST OF FIGURES

LIST OF TABLES

NOTATION

b	size effect on strength for a material
C	creep coefficient
C_c	compressibility index
C_u	coefficient of uniformity
d	particle size (diameter)
d_0	initial particle size
d_{bond}	parallel bond size (diameter)
d_i	particle size corresponding to hierarchical rank i
d_{mem}	diameter of the triaxial membrane
d_s	smallest particle size
D	dilatancy
D_{fr}	fractal dimension
e	voids ratio
e_0	initial voids ratio
e_c	voids ratio at an applied stress of σ_c
e_y	voids ratio corresponding to the yield stress σ_y in normal compression
F	force
G	shear modulus
K_0	coefficient of lateral earth pressure at rest
k_n	particle normal stiffness
k_s	particle shear stiffness
L	size
M	frictional constant determining the slope of the critical state line in q-p' space
m	Weibull modulus
N	number of objects
n	slow crack growth exponent
p	mean stress
q	deviatoric/octahedral shear stress
q_0	value of octahedral shear stress such that 37% of a given size of particles are stronger
q_m	mean octahedral shear strength
S	structure index

t	time
t(test)	time taken for tensile test
t_0	time from which creep strains are measured
v	specific volume
V	volume
V_0	initial/reference volume
β	destructuring index
Γ	gamma function
ε_a	axial strain
ε_1	major principal strain
ε_2	intermediate principal strain
ε_3	minor principal strain
ε_r	radial strain
ε_v	volumetric strain
ε_q	deviatoric strain
η	stress ratio
λ	gradient of the normal compression line in e–ln(stress) space
μ	friction coefficient
ν	Poisson's Ratio
σ	stress
σ_0	value of stress at which 37% of the tested items of a given size survive
$\sigma_{0,d}$	value of σ_0 for particles of size d
σ_1	major principal stress
σ_2	intermediate principal stress
σ_3	minor principal stress
σ_c	current stress on the normal compression line
σ_f	stress at failure
σ_h	horizontal stress
σ_s	strength of smallest particles
$\sigma_{s,0}$	strength of smallest particles at time t
$\sigma_{s,y}$	vertical stress at which yield of structured soil occurs in normal compression
σ_t	tensile stress

σ_{TS}	strength measured from tensile test
σ_y	vertical yield stress in normal compression
σ_v	vertical stress
φ	friction angle

CSL	critical state line
DEM	discrete element method
PFC3D	Particle Flow Code in Three Dimensions (software)
NCL	normal compression line

CHAPTER 1
INTRODUCTION

1.1 BACKGROUND

The understanding of the mechanical behaviour of granular soils has long been an area of interest in the civil engineering community. A knowledge of the strength and stiffness of soil is essential for the safe design of any construction project.

Cemented granular materials in general have been of particular interest, due to their unique behaviour and natural abundance. Both naturally and artificially cemented soils have been subjected to extensive laboratory testing throughout the years (e.g. Coop and Atkinson, 1993). Among the various tests, the triaxial is the most commonly used for analysing the stress and strain characteristics of granular soils, due to the ability to control drainage and measure deformations. The significant majority of triaxial testing has been at conventional pressures; typically less than 1 MPa. More recently, cemented sands have also been subjected to high-pressure laboratory testing (e.g. Marri, 2010), and it is under such pressures that particle crushing in sand becomes prominent and has a large influence on the macro-scale behaviour (Yamamuro and Lade, 1996). However, during typical laboratory tests, it is not possible to observe internal particle mechanisms, nor is it possible to discover the true properties and behaviour of the inter-particle bonding that results from cementation. In general, little is known about the soil response at the grain level; this is particularly true at high pressures.

Particle crushing is also highly significant in the normal compression of granular soils; the yield point and slope of the ensuing normal compression line have long been attributed to crushing. In comparison to cohesive soils such as clay, there have been comparatively few experimental studies on the one-dimensional or isotropic compression of sands, in particular silica sands

due to the high pressures required. Nonetheless, there have been studies investigating the influence that factors such as initial voids ratio, and particle shape, strength and size have on crushing during compression (e.g. Hagerty et al., 1993; Nakata et al., 2001a; Nakata et al., 2001b). The compression of sand has also been associated with the evolution of fractal particle size distributions (e.g. Turcotte, 1986), with authors such as McDowell and Bolton (1998) and Russell (2011) linking the linear slope of the normal compression line to the theory of fractal crushing, using energy equations. So although the role of particle crushing in granular soils has been acknowledged, the micro mechanics have not been truly investigated—for example, it is not possible to observe and investigate fracture mechanisms and properties such as the distribution of strengths and size-hardening laws, and their influence on the macroscopic behaviour.

The discrete element method (DEM) is a branch of numerical methods for calculating the behaviour of an assembly of particles, an effective technique for modelling granular mechanics. DEM, which was originally developed by Cundall and Strack (1979), is commonly used to model discontinuous materials, and is an effective alternative to continuum methods. The fundamental purpose of DEM is to recreate the microscopic mechanics of the independent particles to allow understanding of the macroscopic behaviour, and most significantly, to enable the investigation of the micro mechanics of materials that would otherwise be difficult or impossible to study in physical tests. Hence, it provides a useful numerical tool for studying soil mechanics, and is used herein to investigate micro mechanics of sand and cemented sand under high pressures.

1.2 AIMS AND OBJECTIVES

The principal aims of this research are to improve understanding of cemented sand and to gain insight to the micro mechanics of particle crushing at high pressures, ultimately allowing *better predictions* of the behaviour of soil to be

made. Using the discrete element method software PFC3D, the objectives can be summarised as follows:

- To create a realistic triaxial model, capable of simulating high-pressure triaxial shear tests, and featuring a flexible membrane that allows the specimen to deform realistically.
- To develop a practical method of modelling cementation, allowing cemented sand to be modelled, and the micro properties to be fully investigated.
- To implement an effective particle breakage mechanism, enabling the soil model to exhibit realistic particle crushing at high pressures and allowing the mechanics of fracture to be investigated.
- To study the behaviour of sand and cemented sand in high-pressure triaxial shearing and normal compression, and gain an insight into the role of particle crushing, and its influence on the macroscopic behaviour.

1.3 SCOPE

This thesis presents a numerical-based investigation into the mechanical behaviour of granular soil. The soils studied are sand and cemented sand, with a focus on the drained behaviour of these soils in triaxial shear and one-dimensional normal compression, at high pressures.

The study includes discussion on how cementation influences the behaviour of sand in such tests; particular attention is also given to the role of particle crushing, which is of considerable importance at high pressures.

There were some limitations, however, which should be mentioned regarding the use of the discrete element method:

- The DEM software used, PFC3D (v3.1), uses two entities: walls and balls. Therefore all soil particles were modelled simply by using

spheres, which failed to reflect the irregular shape of real sand particles. Incorporating realistic shape would change the mechanical behaviour of the virtual soil, which is discussed where relevant. However, the work presented is a necessary, fundamental step required before implementing realistic shape using 'clumps' of balls.

- Cementation was modelled by using virtual bonds, which appeared to capture the effects of cementation successfully. However, these bonds failed to reproduce the change in grading that the addition of cement fines causes in laboratory tests. After breaking, the virtual bonds had no affect on the behaviour of the soil, whereas the presence of broken cement in reality would be expected to still have an influence after breaking.
- Time and computational constraints meant that only a relatively small number of particles were used in simulations throughout the thesis. This was primarily due to the fact that the time taken for calculations, and to update the system after a single 'timestep' is proportional to the total number of particles; hence it was not possible to use a realistic quantity.
- Similarly, these constraints also limited the extent of the simulations; several of the simulations in Chapters 4 and 5 were terminated when the 'size' of the timestep became too small. The size of the timesteps were most greatly influenced by the *range* of particle sizes in the system. Simulations with wide ranges of particle sizes had *very* small timesteps, therefore requiring a much larger *number* of timesteps to progress. Hence the simulations with extensive crushing were ended when they became too onerous. The desktop computer used had an *Intel® Core™ 2 Quad 3.00 GHz CPU*; with *3.00 GB of RAM*. The simulations presented in Chapter 3 all took approximately between 1–3 weeks to complete. In Chapter 4, the shortest simulation was completed in 2 weeks; while the key simulation of silica sand ran for approximately 10 weeks before it was terminated. In Chapter 5, the

longest triaxial simulation (at the highest confining pressure) ran for approximately 10 weeks before it was terminated.

1.4 THESIS OUTLINE

This thesis consists of six chapters; the following five are organised as follows:

Chapter 2 provides a literature review, which covers both experimental and numerical research. A general background on cemented sand is given, accompanied by an analysis of the behaviour of such granular soils in both triaxial shearing and normal compression. This is followed by a review of particle crushing and relevant applications of the discrete element method in modelling soil.

Chapter 3 describes the triaxial model developed to simulate high-pressure shear tests. Details are provided of the flexible membrane, which allows correct failure modes to develop, and a study of bond parameters used in modelling cemented sand is given.

Chapter 4 gives details of the basic particle breakage mechanism and fracture criterion developed to model particle crushing. The one-dimensional normal compression of sand is modelled using an oedometer; various mechanisms and strength parameters are investigated, and the compression is linked to the evolution of a fractal particle size distribution.

Chapter 5 presents three applications of the particle crushing mechanism. Creep is modelled and investigated by incorporating a time-dependency on particle strengths, a study of the one-dimensional compression of cemented sand is then presented, and finally the high-pressure triaxial behaviour of crushable cemented and uncemented sand is analysed.

Chapter 6 contains the conclusions from this work and the recommendations for future research.

CHAPTER 2

LITERATURE REVIEW

2.1 INTRODUCTION

The literature review focuses on the behaviour of cemented sand at high pressures, and the role of particle crushing.

An introduction to the behaviour of uncemented sand is given, as well as a background on cemented sand, after which a thorough review of literature on the mechanical behaviour of cemented sand in conventional and high pressure triaxial shearing is given, highlighting the influence of cementation and confining pressure. A review of the normal compression of cemented sand is provided.

A review of particle crushing is also included, along with related phenomena such as the occurrence of fractal distributions. Finally, a background on the discrete element method (DEM) is presented, followed by a review of contemporary literature that uses DEM to model such behaviour.

2.2 BACKGROUND ON CEMENTED SAND

Cemented soils can be divided into two groups: those occurring naturally and those that are artificially cemented. Natural soil cementation can occur from a number of complex causes—such as the deposition of either silica, carbonates, hydroxides or organic matter at particle contacts, the re-crystallization of minerals during weathering, or cold welding under high pressures at particle contacts (Leroueil and Vaughan, 1990). These processes 'bind' the soil grains together, and can take millions of years; generally occurring below the water table. Soils are artificially cemented primarily to improve their performance. Cemented soil is stronger than most naturally occurring uncemented soil and is therefore commonly used in slope protection, pipe bedding, and in intermediary subbase layers protecting the subgrade in road construction.

The strength and stiffness associated with bonding or cementation were previously only really considered in rock mechanics, but are now commonly accepted in many materials recognised as soils. Schnaid et al. (2001) aptly describe cemented soils as an intermediate class of geomechanics, placed in between rock mechanics and classical soil mechanics.

Important research into cemented soils has been conducted in the last few decades. Clough et al. (1981) contributed significantly to this area by carrying out laboratory tests on both naturally and artificially cemented samples. The samples tested varied from very weak to very strong naturally cemented sands, as well as a range of artificially cemented sands to determine the effects of the amount of cementing agent and sand density on soil response.

Further studies were triggered by the widely reported difficulties encountered during the construction of the North Rankin platform off North West Australia, in 1982. Piles were driven into large amounts of cemented calcarenites (soils containing high proportions of calcium carbonate). There were concerns over the pile shaft friction capacity, and this led to much research and testing of extracted soil samples (King and Lodge, 1988, Jewell and Andrews, 1988, Jewell and Khorshid, 1988), as noted by Coop and Atkinson (1993).

A key feature of naturally cemented samples is their high variability; the carbonate soils extracted from North Rankin varied greatly in both grading and degree of cementation, ranging from loose uncemented sediments to very strongly cemented calcarenites. Some of this variation is generally attributed to the different causes of natural cementation, as these depend directly on the chemistry of the local environment, and as such there is significant scatter. In addition, there are difficulties when extracting soil while avoiding sample disturbance (e.g. loss of particle contacts and damage to cement bonds), which causes a decrease in stiffness and strength (Leroueil and Vaughan, 1990) so an alternative approach is often pursued: the testing of artificially cemented samples.

This raises the question as to whether artificial samples accurately simulate the behaviour of naturally cemented samples. Leroueil and Vaughan (1990) showed that 'structured soils', i.e. cemented soils, clays and weak rocks, all follow a general pattern—stiff behaviour followed by yield. They determined that it is the physical properties of the cemented soil that govern its behaviour, rather than the individual cause of cementation. This justifies the study of artificially cemented samples instead, avoiding the aforementioned difficulties in studying natural samples. This was demonstrated further by Airey (1993).

2.3 TRIAXIAL BEHAVIOUR

2.3.1 Uncemented Sand

The triaxial behaviour of sand (both cemented and uncemented) has long been an area of interest, as triaxial tests are one of the most commonly used methods of measuring the strength of soil. This is due both to the ability to control drainage conditions and that pore water pressure or volume change can be measured easily. However, much of the available research on the triaxial behaviour of soils is at conventional pressures (typically under 1 MPa). Before reviewing literature on drained triaxial shearing of cemented sand, a brief discussion of the behaviour of uncemented sand will be given.

The general understanding of the behaviour of soil under triaxial shearing has been covered extensively, and can be idealized according to the critical state concept first developed by Roscoe et al. (1958). It is widely accepted that at a given low confining pressure, loose sands will undergo strain hardening and contraction until they reach a steady (critical) state; dense sands at the same confining pressure will demonstrate a peak stress state and strain softening, localised failure in the forms of shear bands, and undergo volumetric dilation (Figure 2.1). Peak stresses are caused by the density of the sample and are directly related to the dilatancy, with the peak stress and maximum rate of dilation coinciding (Bolton, 1979). Increasing the confining pressure

decreases the density at the critical state, thereby suppressing the dilation and peak states of the sand.

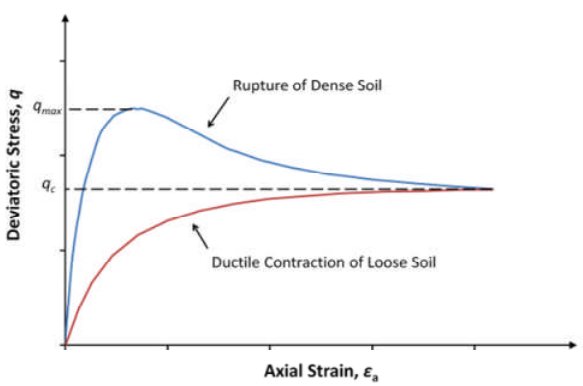

(a)

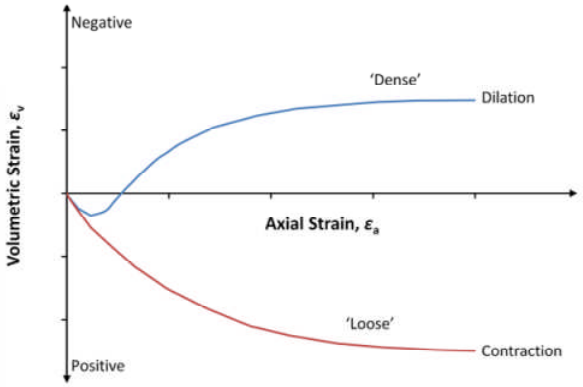

(b)

Figure 2.1 Drained Triaxial Behaviour of 'loose' and 'dense' samples of the same soil at the same confining pressure (Bolton, 1979)

Critical states are defined by a state of continuous shearing with no changes in volume. All the critical states for a given soil form a critical state line (CSL), defined in its simplest form as either:

$$q = Mp' \qquad [2.1]$$

where q is deviatoric stress, M is a frictional constant determining the magnitude of deviatoric stress needed to keep the soil flowing continuously and p' is the mean effective stress, or:

$$v = \Gamma_0 - \lambda \ln p' \qquad [2.2]$$

where v is the specific volume, and Γ_0 and λ are soil constants, where λ describes the rate the volume of soil decreases as the logarithm of mean effective stress increases (Figure 2.2). A simplified explanation of the behaviour of sand during triaxial shearing utilizing critical state soil mechanics can be found in Bolton (1979).

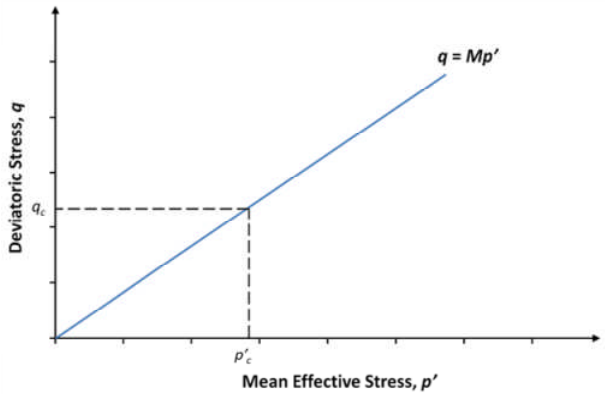

(a)

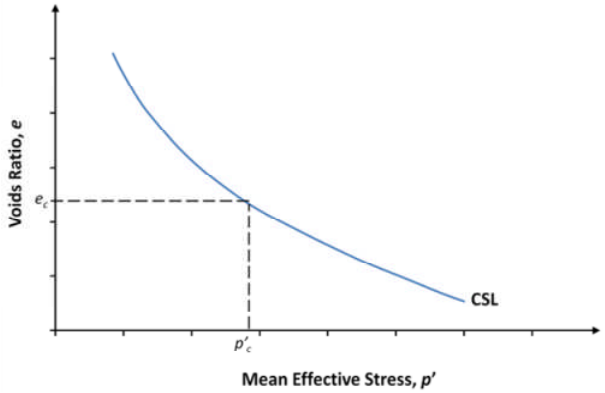

(b)

Figure 2.2 Critical state lines in q-p' and e-p' space (Bolton, 1979)

Typical triaxial results, highlighting the effects of confining pressure and initial density are given in Figure 2.3 from Wanatowski and Chu (2007), which shows the drained triaxial behaviour of silica sand at conventional pressures. Figure 2.3(a) shows the behaviour of samples in a very loose state (voids ratios of approximately 0.90) tested under confining pressures between 35–225 kPa. All results demonstrated strain hardening and volumetric contraction. Both the deviatoric stress and the volumetric strain increased gradually before reaching steady values. Similar tests on the same material with denser initial states (voids ratio approximately 0.66) are shown in Figure 2.3(b)—these

demonstrated volumetric dilation and mild peak stress states. The ultimate (and failure) states of the loose samples formed a critical state line, shown in Figure 2.4.

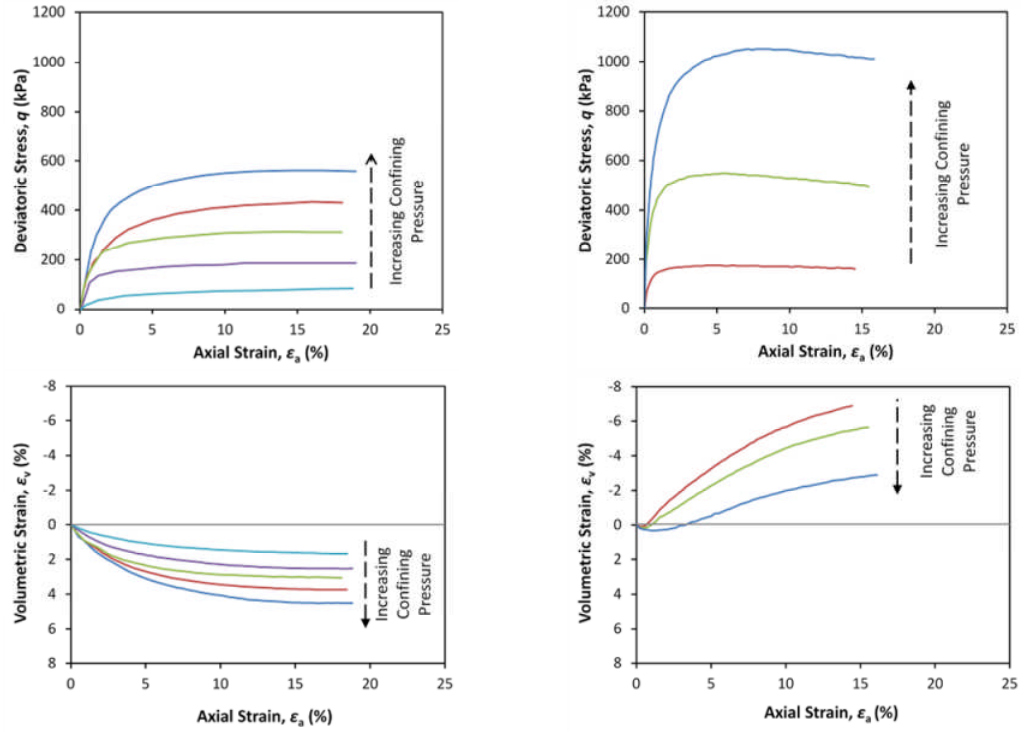

Figure 2.3 Drained Triaxial Behaviour of loose (a) and dense (b) sand across a range of confining pressures (Wanatowski and Chu, 2007)

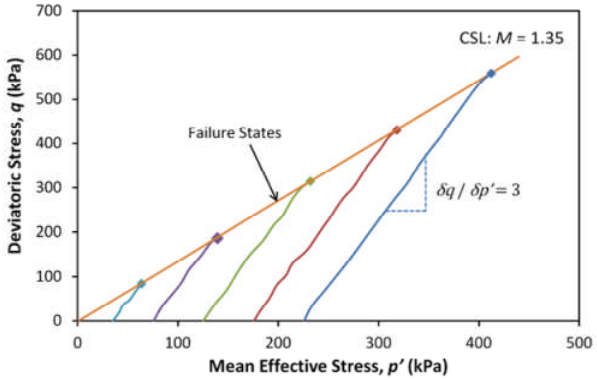

Figure 2.4 Drained triaxial stress paths for a loose sand sheared under a range of confining pressures (Wanatowski and Chu, 2007)

Coop (1990) performed a series of drained triaxial tests on uncemented carbonate sands at both conventional and high pressures. This work is of note, as carbonate soils are often cemented—although not exclusively. Carbonate soils are those in which carbonate minerals form a large

constituent, and are found in many of the continental shelves and cover most of the underwater abyssal plains. Carbonate sands themselves are highly compressible due to the weak nature of the individual grains and low densities—however, Coop (1990) showed they exhibit the same qualitative behaviour as conventional sands, such as the silica sand shown above. Triaxial results from Coop (1990) demonstrated that critical states could be reached (i.e. a state of continuous shearing with no changes in volume) for carbonate sands, thus the behaviour is consistent with the principles of critical state soil mechanics, which at first was uncertain due to the weak particles of such soils.

At high pressures, Yamamuro and Lade (1996) and Marri (2010) presented drained triaxial tests on sand to pressures in excess of 50 MPa. At such stress levels, the sands invariably exhibited strain hardening, volumetric contraction and particle breakage, even when in a dense initial state.

2.3.2 Cementation

Carbonate sands, as mentioned earlier are very widely distributed, and these sands often develop bonds between the particles due to carbonate precipitation and carbonate crystal growth on the grains, resulting in cemented soil with highly irregular variation. These form the majority of naturally encountered cemented sands. Airey (1993) conducted drained triaxial shear tests on a range of natural calcarenites, and the inherent variation in density and cement content of their natural specimens was evident from the significant scatter seen in the drained triaxial responses, given in Figure 2.5(a). However, they were able to observe that cementation had two main effects on soil during shearing: it increased both the shear modulus and the size of the yield locus. From conducting many further tests, they were able to observe that most samples approached a constant stress ratio (q/p') which indicated a critical state, and when these points were plotted in specific volume–mean effective stress space, a critical state line was estimated, as shown in Figure 2.5(b).

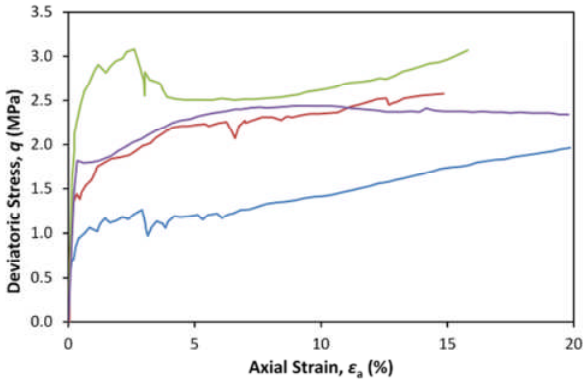

(a)

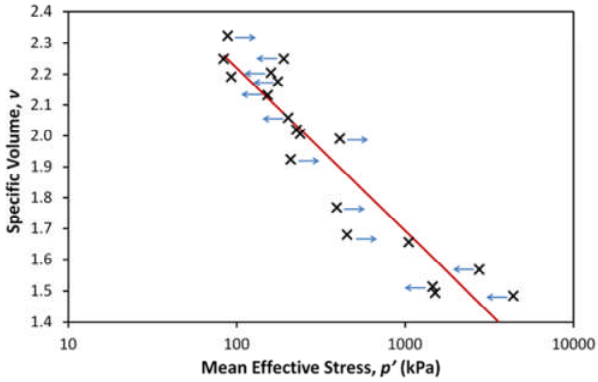

(b)

Figure 2.5 Natural calcarenite: typical drained triaxial behaviour (a), and estimated critical state line (b), where arrows indicate the direction the tests were heading at termination (Airey, 1993)

Artificially cemented sands on the other hand, are typically formed by mixing various quantities of gypsum, Portland cement, calcite or lime with a base sand. The cementing agent chosen can depend on a number of reasons, but primarily to either simulate natural cementation or to achieve desired soil improvement factors such as an increase in strength or density. In the literature there have been key studies on naturally and artificially cemented sands with various cementing agents, including *carbonates*: Airey (1993), Coop and Atkinson (1993), Cuccovillo and Coop (1997, 1999), Lagioia and Nova (1995); *Portland cement*: Abdulla and Kiousis (1997), Consoli et al. (2007), Haeri et al. (2005a), Lo et al. (2003), Marri et al. (2012), Schnaid et al. (2001); Gypsum: Haeri et al. (2005b), Huang and Airey (1998); *Lime* or *Calcite*: Asghari et al. (2003), Ismail et al. (2002a). There are also studies in which various cementing agents are compared, such as by Ismail et al. (2002b) and Haeri et al. (2006).

In addition to various cementing agents, a variety of sands have been used in the available literature, often rendering a direct comparison difficult. Nonetheless, Leroueil and Vaughan (1990) showed that 'structured soils', i.e. cemented sands, over-consolidated clays and weak rocks all follow the same principal behaviour, and can be considered within the same framework. They stated that despite different origins, cementation within sand causes an increase in strength and increases the domain in which the soil exhibits stiff behaviour. In addition to cemented sands, they analysed the behaviour of clays and weak rocks, and reported that all these exhibited similar behaviour under drained triaxial shearing.

It is generally accepted that the shear strength of cemented soils can be represented by linear Mohr-Coulomb style failure envelopes, defined by a friction angle and cohesion intercept, and that under shear deformation, cemented soils exhibit stiff behaviour up until yield, which is largely controlled by the cementation followed by a progressive loss of structure.

In a series of drained triaxial tests carried out on artificially cemented sands, Coop and Atkinson (1993) established that the addition of cementitious material into sand introduced well defined yield points into the stress-strain response during shearing, which is related to the breakage of cement bonds. Both cemented and uncemented specimens reached a critical state after large strains during shearing, and appeared to have the same critical state line. They also defined three modes of shearing behaviour of sands (Figure 2.6). The first mode is when the sample is sheared at relatively low confining pressures, causing a peak stress state to occur. The third mode of behaviour is when the sample reaches its yield point during confinement (i.e. isotropic compression before shearing commences), and the shearing produces behaviour similar to that of an uncemented soil, with no clear yield point. The second mode occurs at intermediate confining pressures, and although the cement bonds are initially intact, they yield during shearing and any peak state is governed by frictional behaviour.

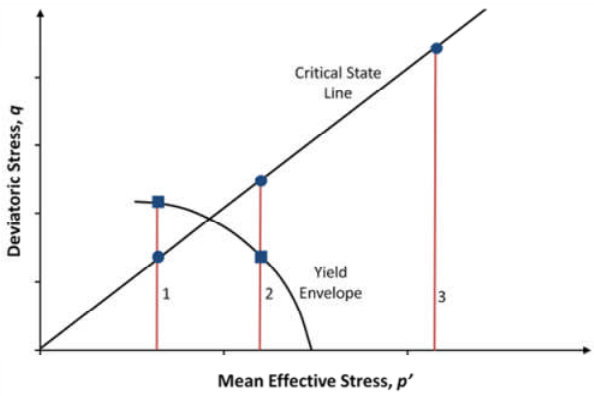

(a)

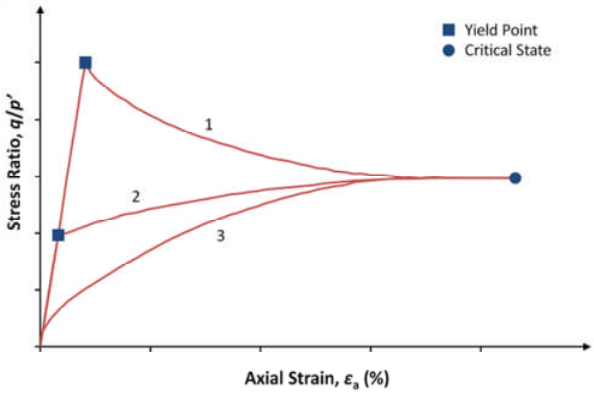

(b)

Figure 2.6 Schematic diagram showing modes of shearing behaviour for cemented sands (Coop and Atkinson, 1993)

Lagioia and Nova (1995) also performed tests on specimens of calcarenites, and provided a useful theoretical analysis of the behaviour during triaxial shearing. Their analysis focused on what they described as a 'destructuration phase', in which marked the transition from rock-like behaviour to soil-like behaviour. In their tests they categorised three phases: an initial elastic, reversible phase; an easily recognisable destructuration phase; and a hardening or softening phase which leads to an ultimate state. At low confining pressures, the destructuration phase was associated with a peak, while at higher confining pressures this phase was marked by approximately constant stress, both of which are shown in Figure 2.7.

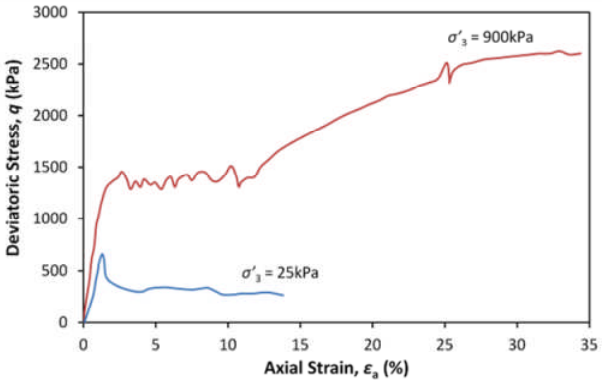

Figure 2.7 Triaxial response of naturally cemented sand at two confining pressures, showing the 'destructuration' phase (Lagioia and Nova, 1995)

Huang and Airey (1998) stated that for drained triaxial tests in which the confining pressure was less than the apparent preconsolidation stress, i.e. yield stress, cementation caused an increase in stiffness, peak strength, maximum dilation rate and the specimens became more brittle and these effects increased with increasing cement content. For confining pressures greater than the yield stress, the cementation appeared broken down and normalised stress-strain responses for various cement contents were almost identical. These results could essentially be described as mode one and mode three according to the categories of triaxial behaviour of a cemented sand proposed earlier by Coop and Atkinson (1993).

Schnaid et al. (2001) performed a number of drained tests on sand bonded with Portland Cement up to 5% dry weight. From comparing their results of cement contents ranging from 0% (uncemented) to 5%, it can be clearly seen in Figure 2.8 that soil behaviour is largely dependent on the cement content. As one would expect, the cemented samples display initially stiff, apparently linear behaviour up to a well defined yield point after which the soil undergoes plastic deformation until failure. Increasing the cement content appears to cause an increase in peak strength and initial stiffness. Schnaid et al. (2001) observed that cemented sands undergo an initial volumetric contraction followed immediately by a strong dilation, with the maximum rate of dilation occurring *after* the peak strength, as opposed to coinciding as observed for uncemented samples. This was attributed to the peak strength

being controlled by cement bonds rather than density, an observation also made by Coop and Atkinson (1993). The peak stresses decreased until critical states were reached. At failure, visible shear planes were reported. Their results were in agreement with those of Coop and Atkinson (1993) as they all showed the specimens to reach a similar ultimate stress, regardless of the cement content. Although it should be noted that Schnaid et al. (2001) contested using the percentage of dry weight to describe the degree of cementation.

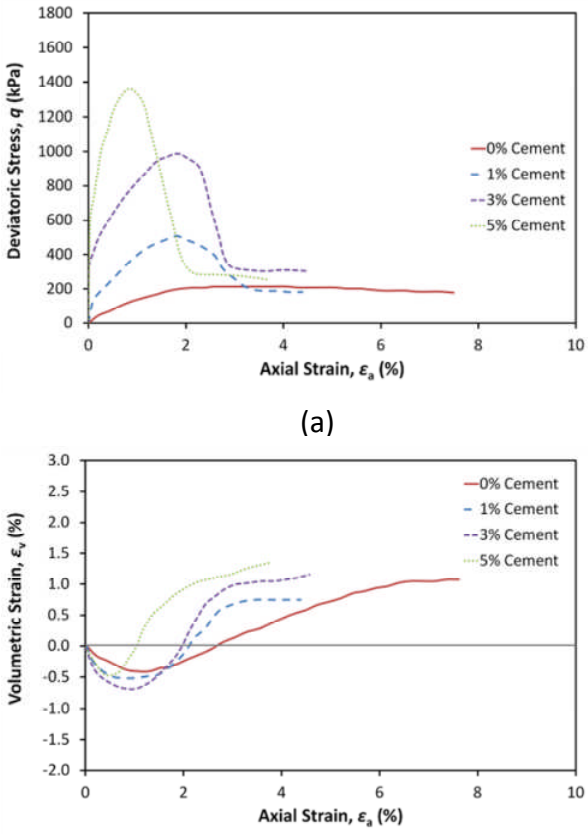

Figure 2.8 Triaxial response for artificially cemented sand with various cement contents, shearing under a confining pressure of 60 kPa (Schnaid et al., 2001)

Asghari et al. (2003) and Haeri et al. (2005a) also observed similar behaviour as discussed, and proposed a general pattern of failure modes: barrelling for uncemented samples, and shearing for most cemented samples (Figure 2.9), although confining pressure heavily influenced the failure behaviour. All cemented samples sheared at relatively low confining pressures demonstrated brittle failure with shear zones (Figure 2.9), with brittleness

increasing with cementation. Asghari et al. (2003) suggested that the thickness of the shear zone was dependant on the amount of cementation, while Haeri et al. (2005a) observed that the inclination of the shear bands increased with degree of cementation. They both stated that the strain associated with peak strength decreased with an increase in cementation, and that the post-yield behaviour is highly dependent on degree of cementation. The failure envelopes from Asghari et al. (2003) were linear for uncemented and destructured soils, but were curved for the cemented specimens (Figure 2.10).

(a)

(b)

Figure 2.9 Failure modes of cemented sand: barrelling in uncemented samples (a) and shear zones in cemented samples (b) (Asghari et al., 2003)

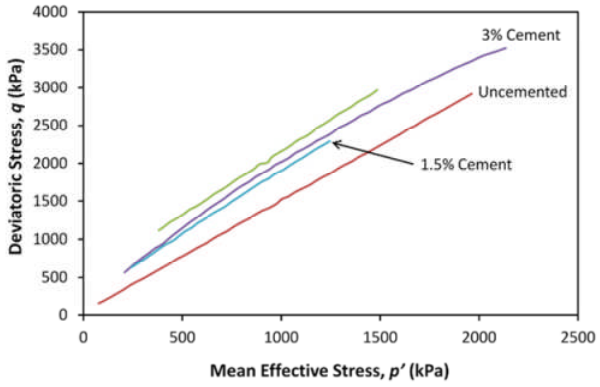

Figure 2.10 Failure envelopes for cemented sand with various degrees of cementation (Asghari et al., 2003)

Cuccovillo and Coop (1997) studied two naturally structured sands: a calcarenite consisting of a medium carbonate sand bonded by calcium carbonate, and a silica sand bonded by iron oxide. They attempted to distinguish between the effects of inter-particle bonding and 'fabric' (i.e. the arrangement and distribution of the soil particles comprising the soil). They analysed the shear behaviour under very small strains, and reported that yielding is noticeable by a rapid decrease in stiffness, degradation of bonding and the development of plastic strains. They claimed that for the bonded silica sand, the structure predominantly arises from the interlocking soil fabric, whereas for the carbonate sand the structure arises solely from bonding. For the bonded carbonate sand, they observed a progressive transformation of the bonded soil into a frictional material, with the shear stiffness becoming more controlled by state, rather than structure. For the silica sand, they observed that despite bond degradation, the influence of structure still persisted, giving higher values of shear stiffness at comparable strains. They concluded that the loss of bonding must precede any disruption to the fabric, i.e. particle arrangement.

Cuccovillo and Coop (1999) went on to further analyse the triaxial behaviour of the two soils across large strains. Although the two soils shared behaviour typical of structured soils, they once again highlighted the influence of fabric. They claimed that the bonded silica sand, which was considered to have significant fabric, could not be adequately described by the bonding alone,

and that the behaviour of 'fabric-dominated' sands is considerably frictional, and the deformation is dominated by dilation. During the triaxial tests, the yielding of the calcarenite was coincident with the peak stress and was followed by rapid loss of strength and contraction. However the yielding of the silica sandstone was accompanied by dilation and plastic strains which developed after the soil had yielded, suggesting the peak strength was in fact frictional, as opposed to the calcarenite which had a cohesive peak strength. The failure envelopes showed that the peak states were much higher for the cemented soils when compared with the reconstituted soil, and the peak envelope appeared to converge to the CSL at high confining pressures. Finally, they summarised that interlocking fabric could not be described adequately by conventional framework, in particular the mechanisms described by Coop and Atkinson and shown in Figure 2.6. They identified a new schematic, depicted in Figure 2.11. They proposed that for much of the range of confining pressures considered, the stress-strain behaviour would be non-linear (mode 2b), and any linearity seen would be limited to the initial part of shearing (mode 2a).

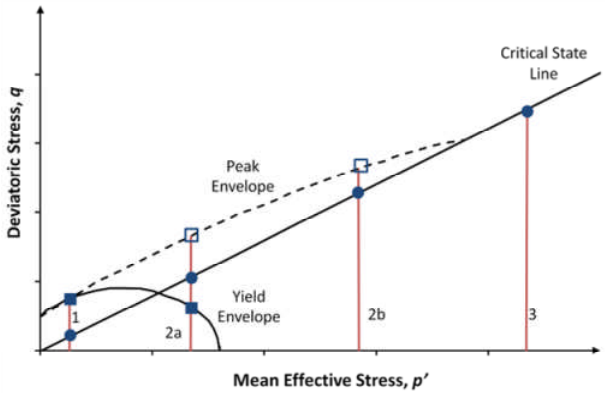

(a)

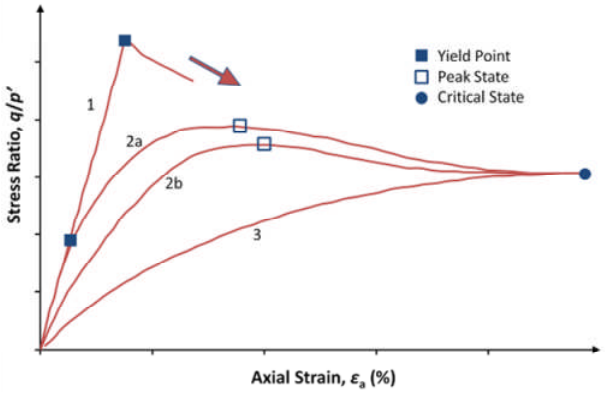

(b)

Figure 2.11 Schematic diagram showing modes of shearing behaviour for a cemented sand (Cuccovillo and Coop, 1999)

Lo et al. (2003) provided a similarly useful insight into the mechanics of cemented sands. They carried out drained triaxial testing on two artificially cemented soils: a quartz sand, and a natural silt; bonded with a Portland cement fly ash mixture. Principally, they confirmed Leroueil and Vaughan's (1990) hypothesis that all structured soils behave within the same framework. Lo et al. (2003) thoroughly investigated the direct contribution of a bonding agent to the behaviour of soil, and, like Cuccovillo and Coop (1999) they observed that some soils may already possess structure, and the addition of a cementing agent simply increases the structure, and gives the soil a larger yield surface. They investigated the gradual degradation of bonding by monitoring the irreversible decrease in stiffness and peak strength during virgin loading, as can be seen in Figure 2.12.

Haeri et al. (2006) provided one of the few comprehensive studies of the effects of cement type on the triaxial behaviour of a cemented sand.

Although several authors have shown that all structured soils, and therefore all cemented sands can be considered within the same framework, Haeri et al. (2006) compared the behaviour of a gravelly sand cemented with Gypsum, Portland cement and lime. Tests results for samples with low cement contents (1.5%) indicated that in general, cementation by Gypsum gave the highest shear strength, however at higher cement contents (e.g. 4.5%), the samples with Portland Cement consistently provided the highest shear strength (Figure 2.13). They concluded that Gypsum appeared the most brittle cementing agent, and Portland cement seemed the most ductile. The gypsum samples consistently developed shear planes, and at relatively low cement contents underwent the largest dilation. The behaviour of the samples bonded with Portland cement was largely dependent on the actual cement content: only at relatively high contents (e.g. 4.5%) did they exhibit significant dilation and shear planes.

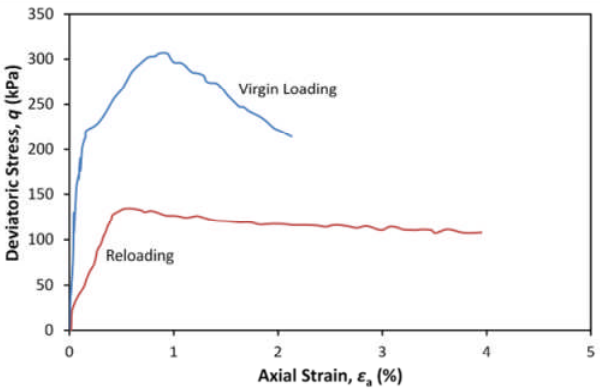

Figure 2.12 Virgin loading and reloading stress-strain curves for a cemented quartz sand, with a confining pressure of 20 kPa (Lo et al., 2003)

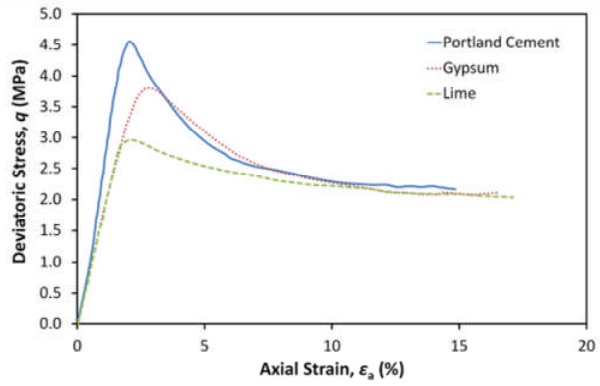

(a)

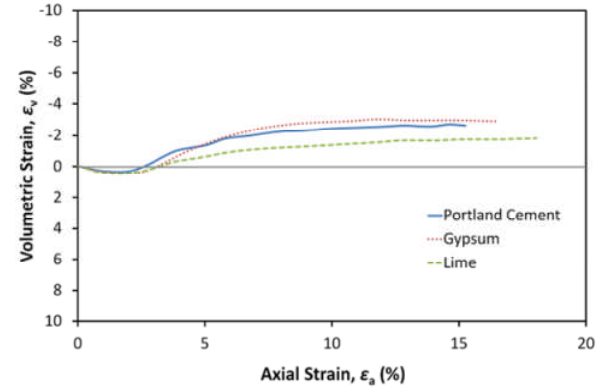

(b)

Figure 2.13 Triaxial behaviour of a gravelly sand with 4.5% cement content of various cementing agents (Haeri et al., 2006)

2.3.3 Confining Pressure

Confining pressure plays an equally as important role as cement content on the behaviour of cemented soil in triaxial shearing. Much of the literature already mentioned included tests across a range of confining pressures, with the common observation that increasing the confining pressure suppresses the effects of cementation, and renders the behaviour more ductile/less brittle.

As described earlier, Leroueil and Vaughan (1990) and Coop and Atkinson (1993) described three modes of behaviour for cemented sand. Coop and Atkinson (1993) concluded that for triaxial tests on cemented soils at low confining pressures, shearing may result in yield at strengths higher than the frictional failure envelope of the equivalent uncemented soil, leading to strain softening (mode 1). At higher confining pressures yield often occurs during

compression, in which case the strength is frictional and leads to strain hardening (mode 3), shown in Figure 2.6.

At relatively low confining pressures, a moderate cement content causes sands to demonstrate brittle behaviour with shear planes upon failure. An increase in confinement generally causes a transition to ductile failure, resulting in barrelling (e.g. Clough et al., 1981; Schnaid et al., 2001; Asghari et al., 2003). Haeri et al. (2005a) observed that the inclination of any shear bands caused by the addition of cement decreased with increasing confining pressure.

It is accepted that although the addition of a cementitious material increases the brittleness of a soil, with this effect increasing with cement content, the effect decreases with an increase in confining pressure. Typical results, such as those from Asghari et al. (2003) in Figure 2.14 show the effects of increasing confining pressure on the drained triaxial response of sand bonded with Portland cement: an increase in both peak and ultimate deviatoric stress, an increase in the axial strain associated with peak deviatoric stress, less dilation (more contraction) and in general the effects of cementation are suppressed and the behaviour tends towards that of the uncemented sand. There is also an increase in the initial stiffness, in agreement with observations also made by Huang and Airey (1998).

Abdulla and Kiousis (1997) and Asghari et al. (2003) showed that increasing the confining pressures caused uncemented samples to demonstrate more contraction during shear, while cemented samples still exhibited dilation. At low confining pressures by comparison, all samples exhibited dilation regardless of cement content. Asghari et al. (2003) demonstrated that the *relative* peak strength—the peak strength of the cemented sample normalised by that of the uncemented material—of cemented samples decreases with confinement, as shown in Figure 2.15.

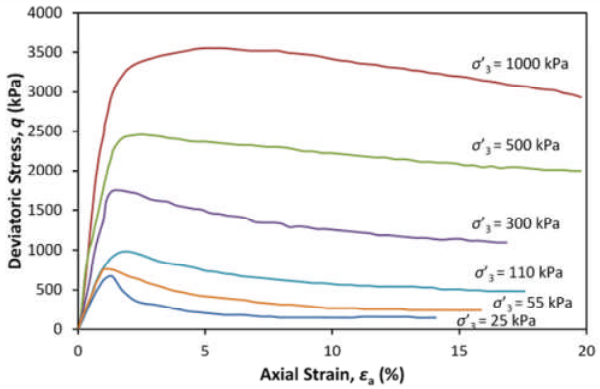

(a)

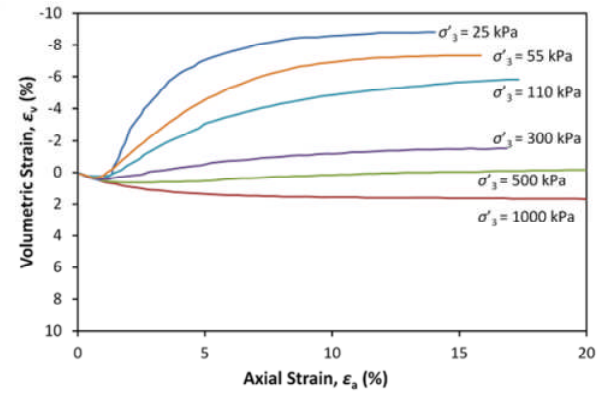

(b)

Figure 2.14 Triaxial behaviour of a sand cemented with 3% Portland cement across a range of confining pressures (Asghari et al., 2003)

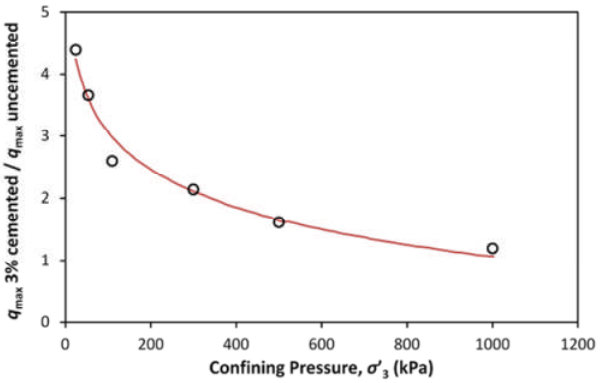

Figure 2.15 Influence of confining pressure on the increase in strength due to cementation (Asghari et al., 2003)

Cuccovillo and Coop (1999) and Lo et al. (2003) both gave the failure envelopes of cemented sand, obtained from performing triaxial tests with a range of confining pressures. The failure envelopes showed that failure stress increased with confining pressure. They also appeared to converge with the critical/ultimate state line at higher pressures, which highlighted the reducing

influence of cementation, as the increasing confining pressure breaks the inter-particle bonds and destructures the soil (Figure 2.16).

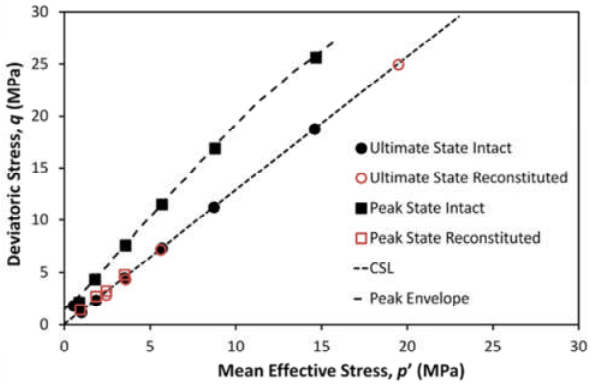

Figure 2.16 Peak and failure states and envelopes for silica sandstone (Cuccovillo and Coop, 1999)

Although the literature offers a respectable amount of research on the drained triaxial behaviour of cemented soils under triaxial conditions, there is comparatively little to date using high confining pressures (generally exceeding 1 MPa). Marri (2010) performed an extensive set of experiments under such pressures on Portaway sand with a range of Portland cement contents (0–15% dry weight). Broadly speaking, the same observations can be made at these high pressures; the addition of cement causes an increase in peak deviatoric stress, a reduction in the strain associated with this stress, and an increase in dilation. As with lower confining pressures, an increase in cement content causes the behaviour to become more brittle.

Marri (2010) showed that uncemented specimens sheared under high pressures (1–12 MPa) exhibit strain hardening with no peak deviatoric stress, and undergo contraction during shearing, i.e. they demonstrate completely ductile behaviour. The addition of cement causes a peak stress to occur, with the peak increasing and becoming more distinguished with higher cement content. This is consistent with the discussed literature at low pressures (e.g. Abdulla and Kiousis, 1997).

Marri (2010) showed that by increasing the cement content, the axial strain associated with the peak reduces, the initial modulus of deformation

becomes higher, and increases both the amount and the rate of dilation. For a given high confining pressure, both uncemented and cemented deviatoric stress responses appeared to converge, or were approaching convergence after large strains, due to the cemented specimens becoming destructured, i.e. the behaviour tended towards uncemented (Figure 2.17). However, even at high pressures they did not always converge, especially at high cement contents such as 10 or 15% dry weight, due to a significant portion of bonds remaining intact, which resulted in groups of particles behaving as larger particles, effectively changing the macroscopic grading.

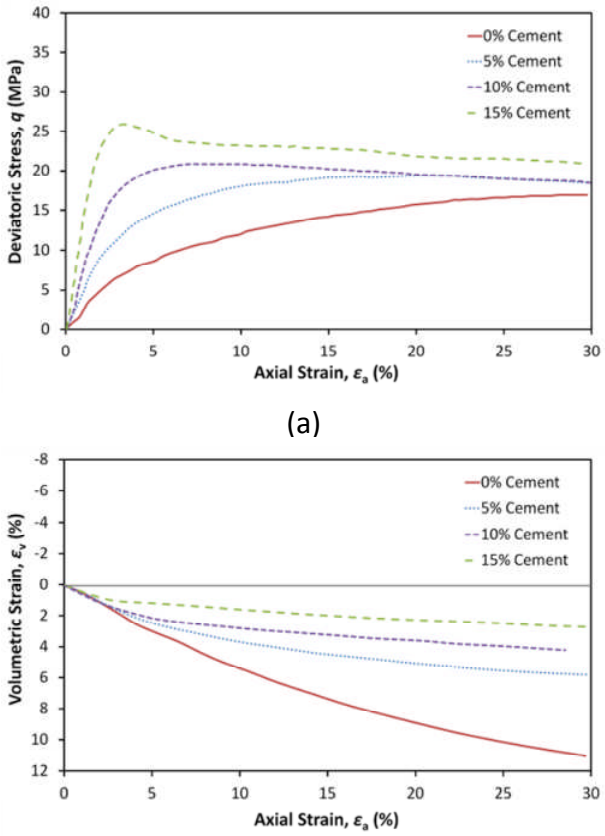

Figure 2.17 Triaxial responses of sand with various cement contents, sheared under a confining pressure of 8 MPa (Marri, 2010)

At high pressures, an increase in pressure still has a large influence on the soil behaviour, suppressing the effects of cementation and rendering the behaviour from ductile to brittle. Marri (2010) demonstrated that increasing

the confining pressure (e.g. from 1 to 12 MPa) resulted in a higher maximum deviatoric stress and reduced dilation (increased contraction). At the highest pressures no clear peak stress was apparent, and all specimens displayed ductile behaviour with gradual strain hardening. These specimens all underwent contraction, in contrast to the heavily cemented samples sheared at relatively lower pressures. However, the effects of cementation were still very evident at high confining pressures demonstrated in Figure 2.18 which shows the response of sand with 10% cement content sheared under various high pressures.

Finally, Marri (2010) showed the failure envelopes for various cement contents up to high confining pressures. As shown at conventional pressures, the cementation caused the failure envelope to move upwards in *q*-*p*' space, and the envelopes exhibited curvature towards the ultimate state line of the uncemented sand (Figure 2.19). In addition, Marri plotted the failure stress ratio against confining pressure, which also showed the suppression of cementation with increasing confining pressure; the difference in peak and failure stress reduced greatly as pressure was increased (Figure 2.20).

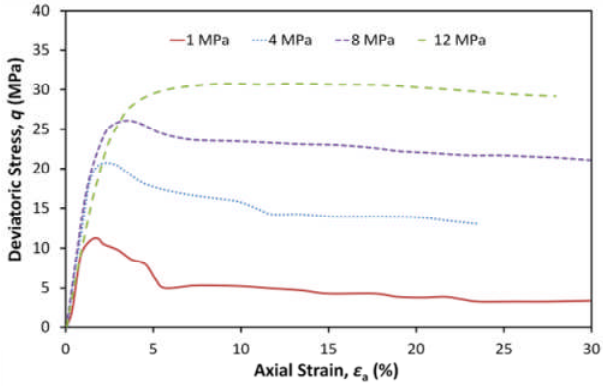

(a)

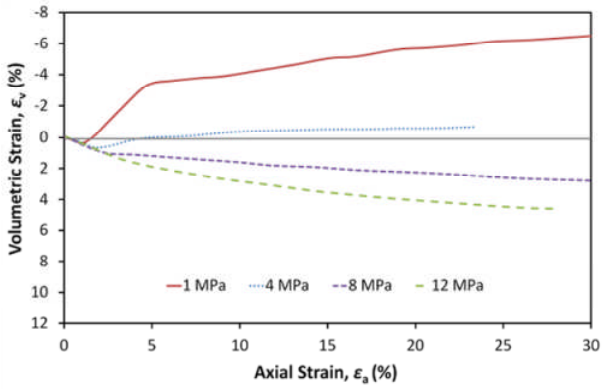

(b)

Figure 2.18 Triaxial responses of sand with 10% Portland cement, sheared under a range of confining pressures (Marri, 2010)

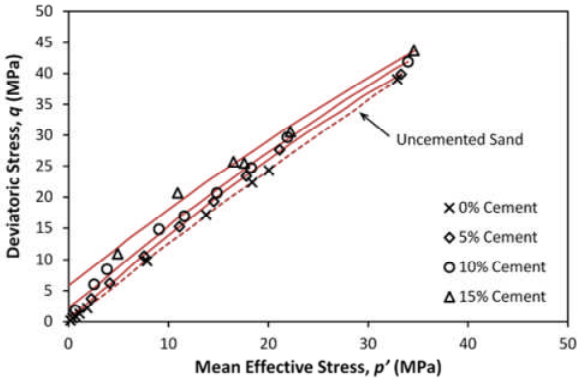

Figure 2.19 Drained triaxial failure envelopes of sand with various cement contents (Marri, 2010)

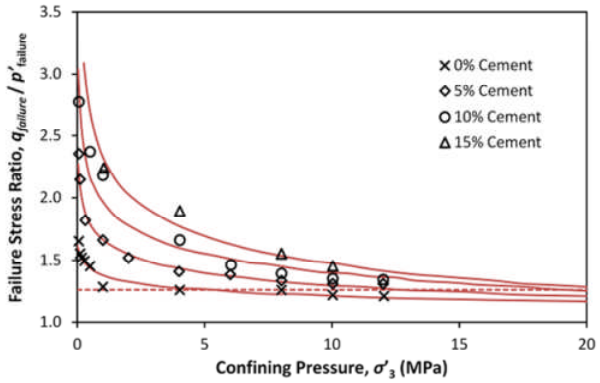

Figure 2.20 Effect of confining pressure on the stress ratio at failure for a range of cement contents (Marri, 2010)

2.3.4 Stress-Dilatancy

Cement content and confining pressure have both been shown to influence the volumetric strain of sand subjected to triaxial shearing. The actual tendency of dense granular materials to dilate, i.e. to increase in volume when sheared is termed as the dilatancy, and plays an important role in understanding the shear strength. According to the critical state concept, both the effective stress state and initial soil density affect the dilation of soil, and as shown in the previous sections cement content also has a dramatic influence. The general stress-dilatancy relation is usually expressed in the form $R = KD$, where R is the stress ratio (σ'_1 / σ'_3), K is a constant and D is the dilatancy ($1 - \delta\varepsilon_v / \delta\varepsilon_1$). Rowe (1962) is generally credited with introducing the 'stress-dilatancy theory', which was deduced from the minimum energy considerations for particle sliding, and was described as follows:

$$\frac{\sigma'_1}{\sigma'_3} \times \frac{1}{1 - \frac{\delta\varepsilon_v}{\delta\varepsilon_1}} = \tan^2\left(\frac{\pi}{4} + \frac{\phi'_f}{2}\right) + \frac{2c}{\sigma'_3}\tan\left(\frac{\pi}{4} + \frac{\phi'_f}{2}\right) \qquad [2.3]$$

where σ'_1 and σ'_3 are the major and minor principal effective stresses, $\delta\varepsilon_v$ and $\delta\varepsilon_1$ are the increments of volumetric and major principal strains respectively, c is the interparticle cohesion and φ'_f is the friction angle. Rearranging, the above equation can be written as:

$$1 - \frac{\delta\varepsilon_v}{\delta\varepsilon_1} = \frac{\frac{\sigma'_1}{\sigma'_3}}{\tan^2\left(\frac{\pi}{4} + \frac{\phi'_f}{2}\right) + \frac{2c}{\sigma'_3}\tan\left(\frac{\pi}{4} + \frac{\phi'_f}{2}\right)} \quad [2.4]$$

which shows that the dilatancy of a soil is influenced by the stress state, inter-particle friction and the cohesion. It is clear from equation [2.4] that the dilatancy of a soil is inhibited by the presence of cohesion, or cementation between the particles, which is in accordance with experimental data (e.g. Coop and Atkinson, 1993; Cuccovillo and Coop, 1999; Lo et al., 2003). Moreover, in the previous section it was shown that increasing the confining pressure changes the behaviour of cemented sand from brittle to ductile, and because cementation is brittle, this suggests that at higher confining stresses the behaviour is primarily frictional rather than cohesive. This is somewhat represented in equation [2.4], where the inter particle bonding represented by *c* is normalized by the triaxial confining pressure, σ'_3.

Cuccovillo and Coop (1999) analysed the dilatancy of cemented soils during triaxial shearing, and reported significantly higher dilatancy for intact specimens when compared to reconstituted specimens, in which much of the structure and bonding was already degraded. However, despite this difference between intact and 'destructured' samples, the peak dilatancies (D_{max}) for a given soil all followed the expression $R = KD_{max}$. Prior to the peak, two interesting observations were made: intact samples at a given stress ratio exhibited *less* dilatancy than the reconstituted samples, confirming that *c* inhibits dilatancy; and that the *rate* of dilation for intact samples decreased with reducing confining pressure (Figure 2.21). However these delays were compensated for by much faster dilation which culminated at the peak dilatancy. They postulated that if work is spent on degrading the bonding, the rate of dilation *has* to decrease; up to yielding, the bonding prevents the intact soil from dilating. After yielding, the gradual degradation initially inhibited dilation, but this was recovered by a rapid increase until a maximum dilatancy was reached.

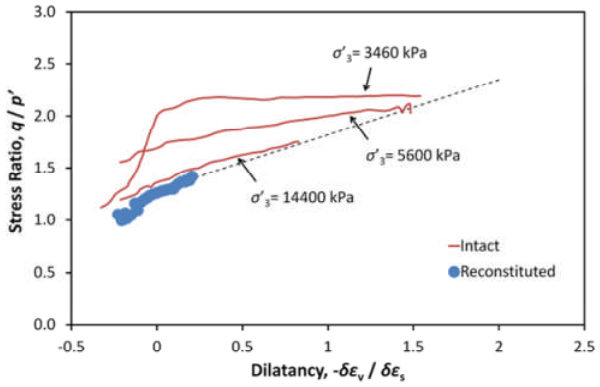

Figure 2.21 Stress-dilatancy relationships of intact and reconstituted silica sandstone over a range of confining pressures (Cuccovillo and Coop, 1999)

Similarly, Lo et al. (2003) showed that at low strains, cemented soil displayed lower dilatancy than the equivalent parent soil, which they attributed to the presence of bonds which suppressed dilation. However, at large strains, the breakage of bonds resulted in a soil fabric that was more dilatant than the parent soil, leading to significantly higher dilatancy. This increase in dilatancy was attributed to the change in grading caused by the broken bonds, and this dilatancy in turn resulted in higher shear strength.

Yu et al. (2007) also analysed the stress-dilatancy of cemented sand, and developed a modified constitutive model for bonded granular materials. By manipulating Rowe's equation, and ensuring compatibility with critical state soil mechanics, the dilatancy could be expressed:

$$\frac{\delta\varepsilon_{\mathrm{v}}}{\delta\varepsilon_{\mathrm{q}}} = \frac{9(M-\eta) + 6\frac{c}{p'}\sqrt{(3+2M)3 - M(3-M)}}{9 + 3M - 2M\eta + 4\frac{c}{p'}\sqrt{(3+2M)(3-M)}} \qquad [2.5]$$

where $\delta\varepsilon_v$ and $\delta\varepsilon_q$ are the increments of volumetric and deviatoric stain respectively, M is the critical state parameter defining the slope of the critical state line in q-p' space, η is the stress ratio (q / p'), and c is the inter-particle cohesion. Yu et al. (2007) plotted idealised dilatancy curves (Figure 2.22) using equation [2.5] which demonstrated that when sheared under the same confining pressure, the effect of increasing c was to shift the dilatancy curve to the left, reducing or preventing dilatancy at a given stress. Increasing the

cohesion was also seen to linearise the dilatancy curve. Increasing the mean effective stress (larger confining pressure) shifted the plot to right, increasing the dilatancy. Their plot suggested that the presence of bonding would cause a material to reach the critical state, i.e. intercept the y-axis at a higher stress than the equivalent unbonded material. However, they emphasised that the bonding, i.e. *c*, is *not* constant during shear, and implemented a cohesion degradation rate which allowed realistic stress-dilatancy plots to be modelled. The inclusion of bond degradation caused the maximum rate of dilatancy to occur *after* the peak strength, with the dilatancy line changing direction to approach the purely frictional (i.e. c / p' = 0) dilatancy line. Yu et al. (2007) also presented dilatancy plots for artificially cemented sands from the triaxial tests performed at low pressures by Schnaid et al. (2001), shown in Figure 2.23 and the correct patterns of behaviour were observed: increasing the cement content shifted the plot to the left; while increasing the confining pressure shifted the plot to the right, confirming the relationship expressed in equation [2.5].

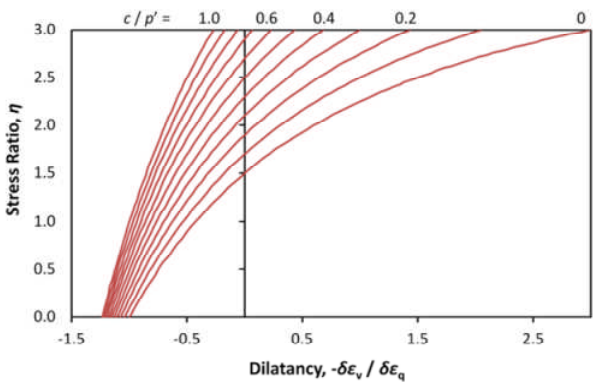

Figure 2.22 Idealised stress-dilatancy curves showing the effect of the cohesion intercept (Yu et al., 2007)

Marri et al. (2012) presented stress-dilatancy plots in a similar manner as Yu et al. (2007) for samples of Portaway sand bonded with Portland cement sheared at high confining pressures. For a given confining pressure, increasing the cement content from 5 to 10 and 15% shifted the dilatancy curve upwards in stress ratio–dilatancy space, shown in Figure 2.24(a). This resulted in larger stress ratios at the peak and ultimate states. For a given

stress, increasing the cement content was seen to increase the bonding between particles. However, the differences in dilatancy curves for various cement contents were far less pronounced than those reported by Yu et al. (2007), showing how the effects of cementation diminish at high confining pressures. For a given cement content, increasing the confining pressure was seen to reduce dilatancy at a given stress, shown in Figure 2.24(b).

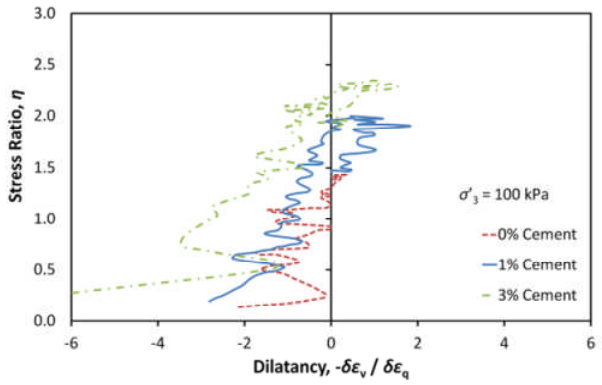

(a)

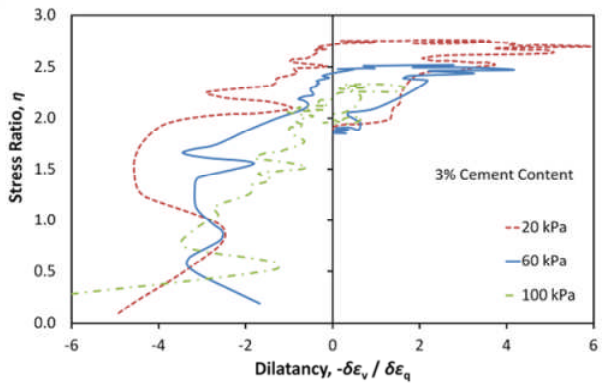

(b)

Figure 2.23 Stress-dilatancy responses for artificially cemented sands: showing the effect of cement content (a) and confining pressure (b) (Yu et al., 2007)

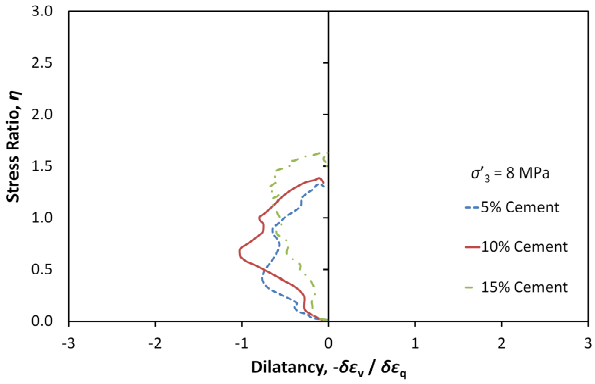

(a)

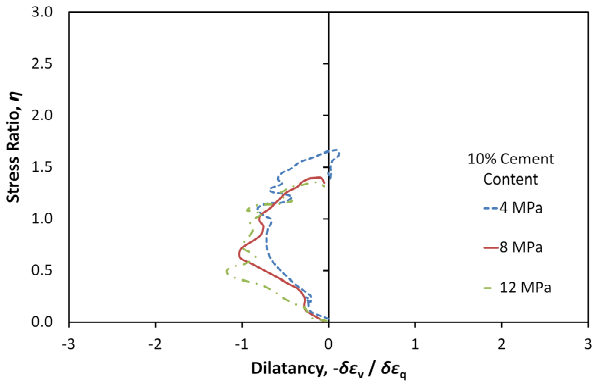

(b)

Figure 2.24 Stress-dilatancy responses for artificially cemented sands sheared under high confining pressures: showing the effect of cement content (a) and confining pressure (b) (Marri, 2010)

2.3.5 Other Factors influencing Behaviour

A number of other factors influence the behaviour of cemented sands during shear, most notably the soil particle properties and the density of the specimen. Particle properties include the size and grading, intrinsic particle strength and shape (e.g. angularity). There is a moderate amount of literature highlighting the effects of varying the specimen density of cemented soils, although the same cannot be said for particle properties.

Abdulla and Kiousis (1997) questioned previously published research on the behaviour of cemented soils, scrutinising the variation in specimen size, shape, and preparation methods used by various authors. They found that for triaxial testing, the diameter of samples ranged from 38 mm to 83 mm, with 50 mm the most common. They suggested 38 mm to be too small to

provide reliable results, as smaller samples demonstrate stiffer and stronger behaviour when compared to larger samples tested under the same conditions. They also analysed the shape of samples used in the literature, i.e. the aspect ratio (height ÷ diameter), however almost all research available on triaxial testing of cemented materials use samples with an aspect ratio of 2, albeit with some variation in size.

Some of the research already discussed included triaxial tests on a given material with a range of different initial densities. For example, Huang and Airey (1998) took into account the influence density had on the effect of cementation, and as such recommended against using the proportion by weight as a measure of cement content. They claimed that any measure based on proportion by dry weight (as is the usual procedure) would be unable to describe the changing influence of cementation with density, and furthermore, such a measure would be difficult to determine in natural soils. They suggested instead using the strength of the bonded soil in proportion to the strength of the unbonded soil as a gauge of the degree of cementation. Huang and Airey (1998) observed that for a given cement content (e.g. 20%), a increasing the density increased both the shear modulus and strength. However, they suggested the *relative* effects of cementation decrease with increasing density. The addition of cement resulted in a relatively larger increase in strength and modulus for the looser specimens. Figure 2.25 shows that for a given overconsolidation ratio (estimated from the apparent preconsolidation pressure of the cemented samples), the addition of cement increased the stiffness, and had a greater influence on the specimens with smaller dry unit weight. They stated that for the addition of a given amount of cement, the effectiveness reduced with increasing density, and suggested this be the case for all cemented soils, which echoed previous work by Airey (1993). They suggested at high densities, particle friction and interlocking are more important than at lower densities, where the contribution of cement is more influential. They acknowledged that the addition of cement fines has an effect even on uncemented samples, due to the inherent changes in density

and grading that this causes, and appreciated the difficulties in completely isolating these factors. Marri (2010) investigated the influence of density on the behaviour of cemented sands at moderately high pressures, in particular influence on dilation. He found that increasing the initial relative density resulted in a higher rate of dilatancy, and an increased level of dilation, similar to the effects described and widely known for uncemented sands, as highlighted in Figure 2.26.

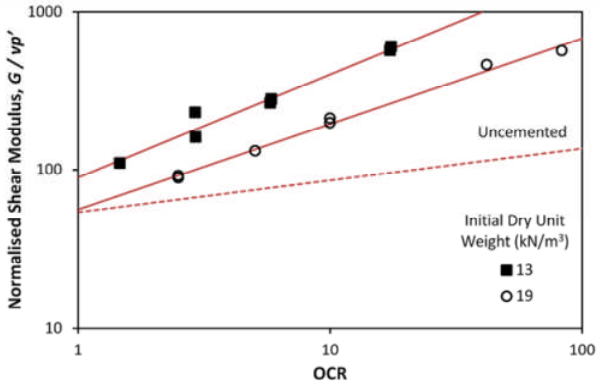

Figure 2.25 Influence of dry unit weight on the normalised shear modulus for artificially cemented sand with 20% gypsum (Huang and Airey, 1998)

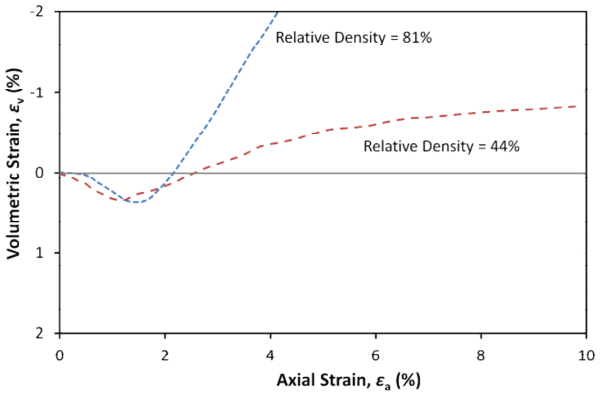

Figure 2.26 Effect of relative density on the dilation of cemented sand sheared under a confining pressure of 1 MPa (Marri, 2010)

Ismail et al. (2002a) investigated the influence of various particle characteristics, and found that for a soil bonded with calcite the strength increases with: strength of the individual grains, density, decreasing particle size and roundness of the grains. Using various base soils, and with the aid of microscopy images they concluded that geometry of particles determines the shape and distribution of the contact surfaces between grains, and that spherical particles form the most efficient mechanism to transfer load when

bonded together. In addition, they postulated that spherical particles will in general be exposed to more points of contact with other particles. In comparison, irregularly shaped particles will have fewer contacts, less efficient bonding mechanisms and will lead to a concentration of stresses; however it was unclear if they considered density in making this observation. With regard to particle size, Ismail et al. (2002a) showed that for a given initial density, grading and cement content, reducing the particle size results in a higher strength after cementation. This was mainly due to the increase in contact points (and therefore number of inter-particle bonds).

2.3.6 Summary

Data obtained from naturally cemented sediments are often highly scattered, therefore artificially cemented sands have been tested to develop a general framework for the behaviour. The key points that have been discussed are the influence of cementation, degree of cementation, and confining pressure on the stress-strain response, volumetric behaviour, dilatancy, and failure modes.

The introduction of cement induces clear peak stresses into the deviatoric stress curve (increasing the failure stress), increases the initial stiffness of the material, the maximum rate of dilation, overall dilation, and renders the material more brittle. Increasing the cement content amplifies these effects while reducing the axial strain at the peak stress and maximum rate of dilation. Confining pressure on the other hand suppresses these effects and renders the materials more ductile, as the cementation is more readily broken down. Brittle failure is associated with shear planes, while ductile failure is associated with no strain localisation and barrelling. Cement content has been shown to have no major influence on the CSL in q-p' space.

Although much of the available studies are at conventional pressures, the essential influence of cementation is still evident at high pressures. The same trend in behaviour is observed, but dilation is greatly suppressed, with

cemented sand specimens almost exclusively demonstrating volumetric contraction.

2.4 COMPRESSION BEHAVIOUR

2.4.1 Uncemented Sand

The behaviour of soil in compression has always been a topic of interest in geotechnical engineering, and as such there is a wealth of literature on the subject. The normal compression of a soil generally describes the change in volume of an element of soil when subjected to a normal stress. It is most often expressed in terms of specific volume, v or voids ratio, e against either mean effective stress p' (for isotropic normal compression), or vertical effective stress σ_v' (for one-dimensional normal compression). For a soil being compressed for the first time (virgin compression), it is widely accepted that the relationship between volume and the natural logarithm of applied effective stress following yield is approximately linear, where yield is defined as the transition between elastic and plastic deformation. This line—the normal compression line (NCL) comprises equilibrium states for the soil in virgin compression after yield, and can be described by the equation:

$$e = e_0 - \lambda \ln p' \qquad [2.6]$$

for isotropic normal compression, and:

$$e = e_0 - \lambda \ln \sigma'_v \qquad [2.7]$$

for one-dimensional normal compression, where λ is the gradient of the normal compression line, and e_0 is the voids ratio at a stress of 1 kPa, represented in Figure 2.27. Although one-dimensional and isotropic normal compression have slightly different measurements, the equation describing the change in volume with stress takes the same form for each; soils exhibit the same phenomena and similar behaviour under both types of compression. It is generally accepted soils have the same compression slope in one-dimensional and isotropic compression, and for convenience will be

considered analogous herein. Jaky (1948) proposed that the coefficient of lateral earth pressure at rest, K_0, which describes the ratio between horizontal and vertical effective stress in soil subject to zero lateral strains:

$$\sigma'_{\mathrm{h}} = K_0 \sigma'_{\mathrm{v}} \qquad [2.8]$$

could be related to the effective angle of friction, φ':

$$K_0 = 1 - \sin \varphi' \qquad [2.9]$$

and so is a soil property, therefore leading to the assumption that p' is linearly proportional to σ'_{v} (e.g. Wroth, 1984; Coop, 1990).

For unloading and reloading the behaviour is much stiffer and is considered elastic, and idealised as a straight line in voids ratio–ln stress space with a gradient κ:

$$e = e_k - \kappa \ln \sigma'_v \qquad [2.10]$$

where e_κ is the voids ratio at a stress of 1 kPa, also shown in Figure 2.27.

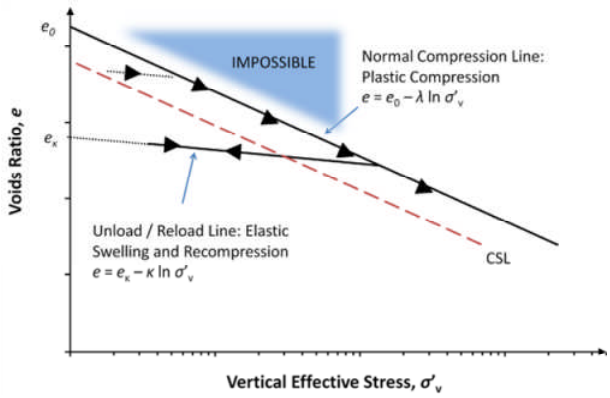

Figure 2.27 Schematic showing the definition of a normal compression line

If common logarithms are used, then the compressibility index, C_{c} and recompression index, C_{r} are used in place of λ and κ respectively:

$$e = e_0 - C_{\mathrm{c}} \log \sigma'_{\mathrm{v}} \qquad [2.11]$$

$$e = e_0 - C_r \log \sigma'_v \quad [2.12]$$

Typical one-dimensional compressions plots for uncemented silica sand are given in Figure 2.28 from McDowell (2002). The sands demonstrated classic stiff elastic behaviour followed by linear plastic compression, with a distinct yield point. The normal compression lines shown have the same slope, as the compressibility index C_c is a material constant.

Yielding is considered to signify the onset of particle crushing (e.g. Coop, 1990; Hagerty et al., 1993; McDowell and Bolton, 1998; Nakata et al., 2001a), and as such, the yield stress is related to the individual particle strengths. Samples that consist of the same material, compressed at the same initial density but with dissimilar initial particle sizes will have different yield stresses, although they will have the same compressibility index. A sample comprising fine particles will exhibit a larger yield stress than an equivalent sample made up of larger particles, due to the size effect on particle strength, i.e. smaller particles are statistically stronger. Nakata et al. (2001b) demonstrated this by conducting compression tests on samples with identical initial voids ratios but with various initial particle sizes, shown in Figure 2.29(a). Furthermore, a looser assembly of a given material will exhibit a lower yield stress than a denser sample with the same particle size distribution, demonstrated by further compression tests performed by Nakata et al. (2001b) shown in Figure 2.29(b). This behaviour is due to the looser assembly having fewer particle contacts, thus having larger inter-particle stresses for a given applied macroscopic stress (Hagerty et al., 1993).

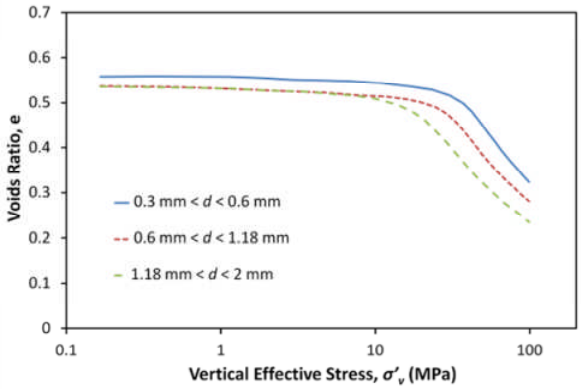

Figure 2.28 Compression plots for various uniform initial gradings of silica sand (McDowell, 2002)

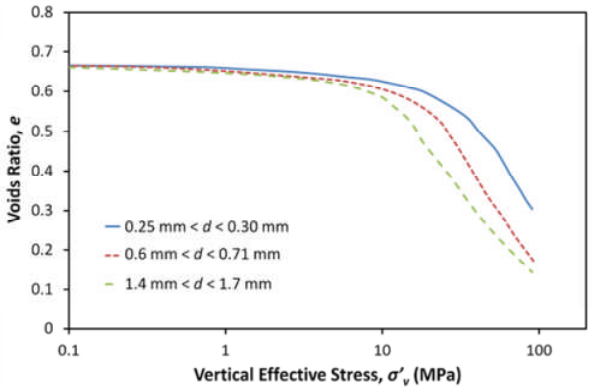

(a)

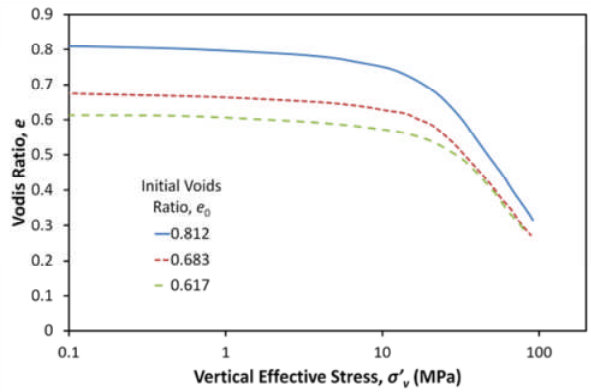

(b)

Figure 2.29 Compression plots showing the effects of particle size (a) and initial voids ratio (b) (Nakata, et al. 2001b)

One-dimensional and isotropic compression lines for sands usually have compressibility indices in the region 0.4–0.5 (Pestana and Whittle, 1995), and there exist a number of theoretical explanations for these values (e.g. McDowell, 2005; Russell, 2011), all of which associate the reduction in volume with particle crushing. Pestana and Whittle (1995) proposed a new

framework to describe the compression of cohesionless soils, featuring a 'limiting compression curve' (LCC) which is linear in a *double* logarithmic plot of voids ratio versus effective stress, highlighted in Figure 2.30. Their LCC compression model essentially consisted of three parameters: a reference stress, the slope of the LCC curve in log-log space, and one parameter characterizing the plastic transition (yielding).

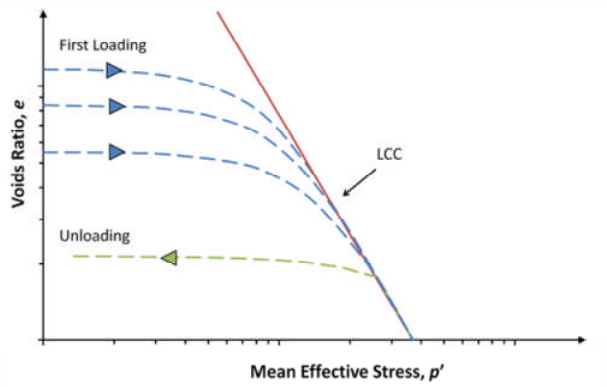

Figure 2.30 Conceptual model of compression behaviour, showing the linear relationship on double logarithmic axes (Pestana and Whittle, 1995)

Their suggestion of plotting the compression in double logarithmic space has gained attention in recent years, and was justified kinematically by McDowell (2005) using fractal crushing theory. McDowell (2005) suggested that normal compression lines should be linear when plotted on such graphs, and, assuming a constant fractal dimension emerges for compressible granular materials, was able to relate the slope of the NCL to the strengths and size-hardening law of the particles. Russell (2011) on the other hand, suggested that the slope of the NCL for a crushable soil was solely a function of the fractal dimension of the particle size distribution, although this would suggest most soils would in fact have the same slope, as experiments have shown fractal distributions with a dimension of 2.5 to consistently emerge for granular materials under pure crushing (e.g. McDowell, 2005).

2.4.2 Cementation

The effects of cementation on the compression behaviour of any soil is best illustrated when compared with the behaviour of the equivalent uncemented soil, i.e. the same material including cement fines but in an unbonded state.

This is generally achieved through either destructuring naturally cemented soil samples or artificial preparation.

On the whole, the behaviour of cemented soils can be considered similar to uncemented soils during compression: they both exhibit an initially stiff elastic response followed by yielding. Leroueil and Vaughan (1990) stated that yielding in cemented soils appears similar in manner to the yielding of uncemented sands in compression, but emphasised that it is in fact a different mechanism, and different terminology should be used. In general, cemented sands display a higher yield stress under compression compared to the equivalent uncemented sands and can reach states outside of the uncemented NCL (e.g. Leroueil and Vaughan, 1990; Coop and Atkinson, 1993; Cuccovillo and Coop, 1999), meaning cemented soil can exist in states impossible for the uncemented soil. These states lie within 'structure-permitted space' on the voids ratio–stress plot, bounded by the compression line of the uncemented soil in its loosest state and that of the densest, most cemented soil (Figure 2.31).

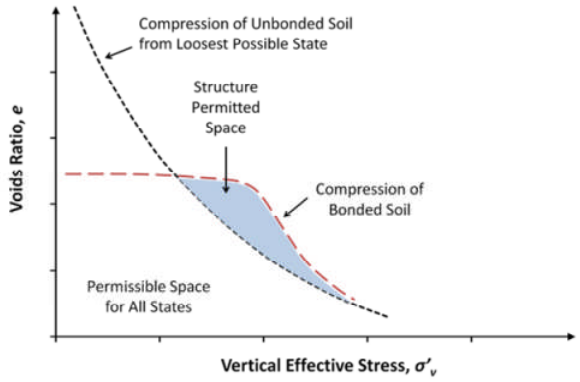

Figure 2.31 Comparison of structured and unstructured soils in compression (Leroueil and Vaughan, 1990)

Coop and Atkinson (1993) highlighted that cementation causes a sand to have a more distinct yield point, and that the onset of bond breakage often coincides with the onset of particle crushing. Typical compression responses of cemented sand are given in Figure 2.32, from Airey (1993), which show the compressive response of naturally cemented calcarenites along with an estimated normal compression line.

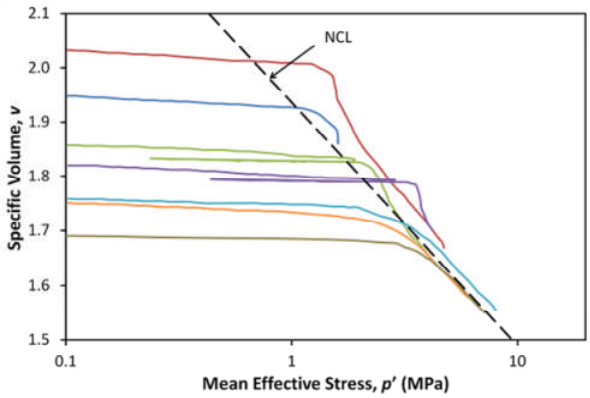

Figure 2.32 Typical compression responses of natural calcarenites (Airey, 1993)

Later, Huang and Airey (1998) performed series of isotropic compression tests on a sand cemented with various gypsum cement contents (0–20%). They found that all the cemented soils demonstrated a stiff elastic response up to a well-defined yield stress, upon which the soils underwent large plastic strains following a normal compression line. They proposed that the slopes of the NCLs were independent of the cement content, and as the cement content increases, the NCL simply shifts to the right in a voids ratio–log stress plot. This shift was attributed to the change in grading caused by the addition of cement fines, and resulted in an increase in yield stress with cement content, which appeared to be a linear relationship.

Although they tested a highly organic soil, Bobet et al. (2011) presented experimental data that suggested that increasing the quantity of Portland cement shifts the compression curves to the right in e–log σ_v space (Figure 2.33). The plots show that the greater the cement content, the greater the yield stress, and the greater the vertical stress that could be sustained at a given voids ratio.

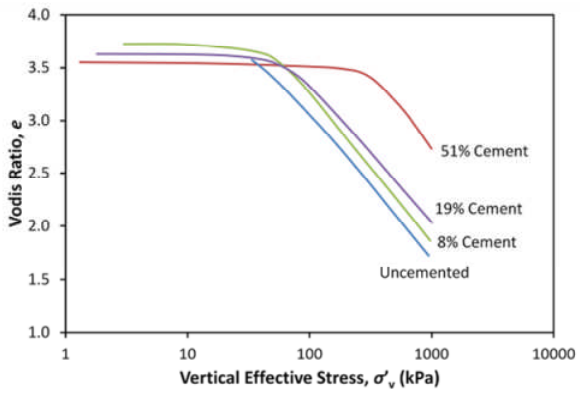

Figure 2.33 Compression plots showing the behaviour of increasing content of Portland cement, for a highly organic soil (Bobet et al., 2011)

Cuccovillo and Coop (1999) however, suggested that samples of a given soil all converge to a single NCL, regardless of cement content. They observed that soils with any initial voids ratio will follow a compression path unique for a given degree of cementation, with strongly cemented materials reaching states far outside the normal compression line of the uncemented soil, before converging to the behaviour of the unbonded material, outlined in the schematic in Figure 2.34(a). They commented that the 'post-yield compression line', unique for a given cement content, defined the boundary for possible states attainable in compression. The position of the post yield compression line (which was related to the yield stress) and its inclination (i.e. the rate at which it approached and converged with the uncemented NCL) were controlled by the degree of cementation, shown in Figure 2.34(b) and (c). An increasing cement content caused the post yield compression line to shift to the right and increased its inclination, resulting in a larger 'structure-permitted space' as described by Leroueil and Vaughan (1990).

Rotta et al. (2003) tested cemented specimens cured under stress and reported much the same findings, however they described a yield locus, located between the post yield compression line and intrinsic normal compression line of the uncemented material, demonstrated in Figure 2.35. However, Rotta et al. (2003) remarked that actual convergence between the cemented and uncemented soils was not always observed, conceding that much higher stresses would need to be applied to confirm if convergence

occurs for moderate degrees of cementation. In addition to the above effects, an increasing degree of cementation has been observed to increase the bulk modulus of sands subjected to compression (Huang and Airey, 1998), however the unloading appears unaffected by the cement content.

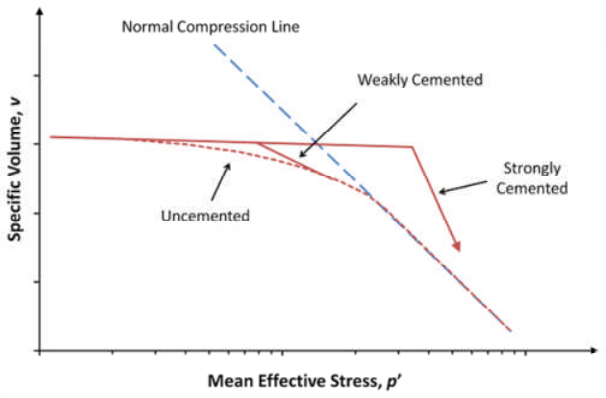

(a)

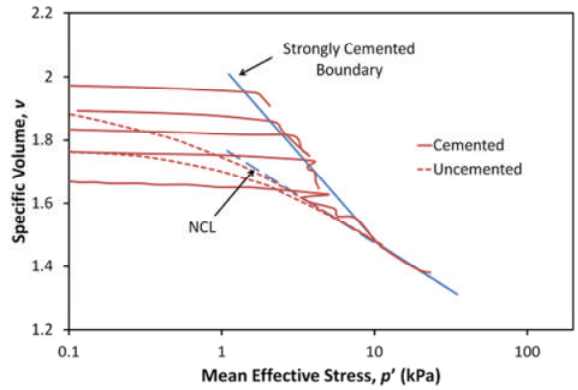

(b)

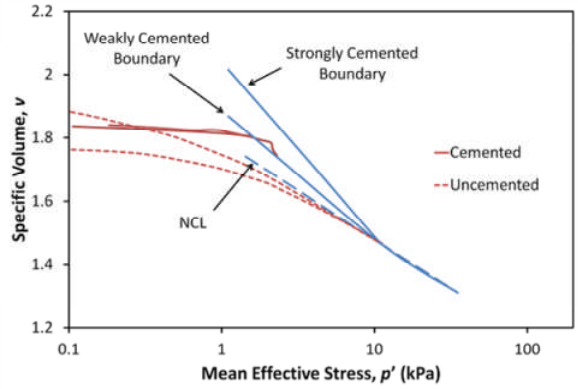

(c)

Figure 2.34 Schematic diagram showing behaviour of cemented sand in isotropic compression (a), and the isotropic compression responses of strongly cemented (b) and weakly cemented sand (c) (Cuccovillo and Coop, 1999)

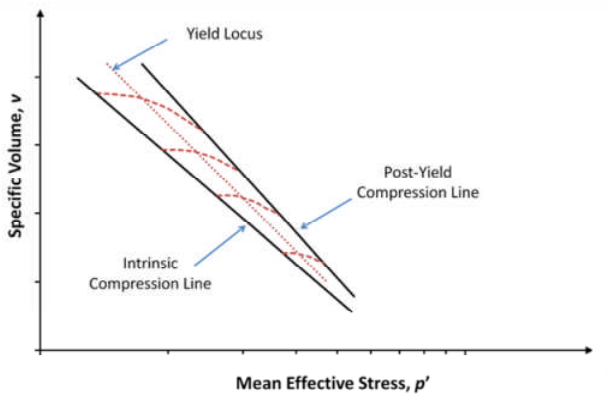

Figure 2.35 Behaviour observed during isotropic compression of cemented materials, showing the post-yield compression line, yield locus and intrinsic normal compression line of the unbonded material (Rotta et al., 2003)

Dos Santos et al. (2009) and Marri et al. (2012) also investigated the influence of cement content on the isotropic compression of cemented silica sand. They both used Portland cement, and observed that the degree of cementation reduced the compressibility of the sand, although whether the assorted compression curves were convergent or independent from one another was unclear. Marri et al. (2012) concluded that cement suppressed particle breakage, because it is particle breakage that facilitates the large plastic reduction in volume during compression.

Liu and Carter (1999) studied the virgin compression of structured soils, and proposed a new equation for describing both isotropic and one-dimensional normal compression. As shown in the literature, for a given applied stress the voids ratio for an intact structured soil is higher than that of the reconstituted soil of the same mineralogy. During compression, the intact soil becomes destructured and the voids ratio sustained by the structure decreases, and the compression curve of the structured soil usually tends towards that of the reconstituted (unbonded) soil, idealised in Figure 2.36(a). Liu and Carter (1999) idealised this behaviour, and said the post-yield behaviour in one-dimensional compression could be described by:

$$e = e_0 + \Delta e - \lambda \ln \sigma'_{\mathrm{v}} \qquad [2.13]$$

where Δe is the additional part of the voids ratio sustained by the soil structure. If the soil has no structure, then Δe = 0, and equation [2.13] reduces to the familiar expression for one-dimensional compression in equation [2.7]. Their model proposed that the additional component of voids ratio, Δe is inversely proportional to the applied effective vertical stress (or mean effective stress in the case of isotropic compression), expressed as:

$$\Delta e = S\left(\frac{\sigma'_{\mathrm{s,y}}}{\sigma'_{\mathrm{v}}}\right)\ln \sigma'_{\mathrm{s,y}} \qquad [2.14]$$

where S is a soil parameter termed the 'structure index', $\sigma'_{\mathrm{s,y}}$ is the vertical stress at which yielding of the structured soil occurs, and σ'_{v} is the current vertical effective stress. In their work, values of S were calculated from test data. Although most of the data they used was from the compression of clay, and few from cemented sands, both soils exhibit structure, and as mentioned earlier, Leroueil and Vaughan (1990) illustrated that structured soils should be considered within the same framework. Although equations [2.13] and [2.14] fitted their data (mostly clays) reasonably well, they imply that all structured soils become destructured and approach the behaviour of the equivalent unbonded at the same rate. They rectified this and accounted for varying rates of destructuring later (Liu and Carter, 2000) by introducing a 'destructuring index', β into a modified equation for Δe:

$$\Delta e = S\left(\frac{\sigma'_{\mathrm{v,y}}}{\sigma'_{\mathrm{v}}}\right)^{\beta}\ln \sigma'_{\mathrm{v,y}} \qquad [2.15]$$

The parameter β quantified the rate of destructuring, with a value of 0 indicating that the additional voids ratio sustained by structure remains unchanged during compression, therefore no destructuring takes place; a value of infinity indicates that the soil structure collapses immediately after the yield stress is reached. The effects of β are illustrated in Figure 2.36(b). This new equation was able to accurately match data on the compression of various structured soils including clays and artificially cemented sand.

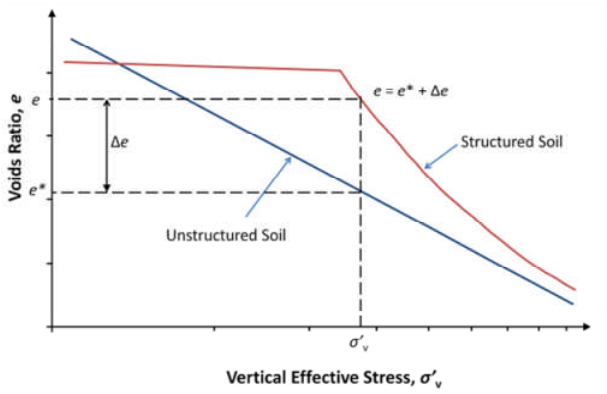

(a)

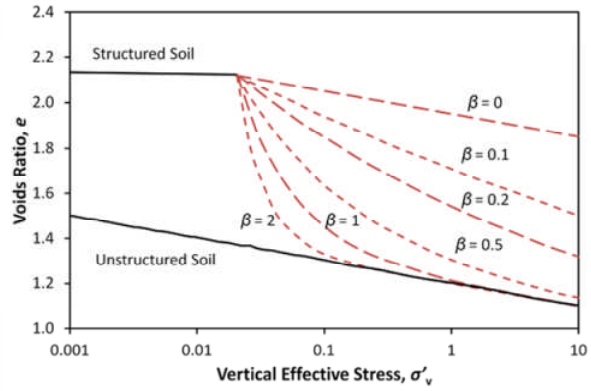

(b)

Figure 2.36 Idealisation of structured soils in compression (a) and the effects of the destructuring index, β on this behaviour (b) (Liu and Carter, 1999, 2000)

2.4.3 Other Factors influencing Behaviour

It has been shown across the literature, that for a given uncemented soil, the initial packing has a significant influence on the behaviour during compression. However, there are relatively few studies looking solely at factors such as particle size and shape on the compression of cemented sand. Leroueil and Vaughan (1990) studied the effects of the density of cemented sands under compression, and from reviewing the work of Maccarini (1987), they commented that yielding in isotropic compression is much more clearly defined at larger initial voids ratios.

Although cementation enables soils to exist at higher voids ratios under a given pressure than the equivalent uncemented soil (e.g. Leroueil and Vaughan, 1990), Huang and Airey (1998) noted that the *addition* of cement is associated with increases in density and a change in gradation, hence the reported changes in the position of the NCL. They reported that increasing

the density alone leads to an increase in the number of particle contacts, therefore increasing the resistance to further compression and the yield stress. The effects of increasing density were observed to be more substantial with coarser grained materials, although this was somewhat dependent on particle angularity and mineralogy. Huang and Airey (1998) also suggested that increasing the density of a cemented sand has a greater effect than increasing the cement content, which can be seen from Figure 2.37 where the yield stress is plotted as a function of cement content for various initial dry unit weights. Like with increasing the cement content, density had no effect on the unloading line. Essentially, their study showed that the *relative* effects of cementation diminishes with increasing density, as the contribution of inter particle friction and interlocking become more significant. Similar results were observed by both Cuccovillo and Coop (1999) and Rotta et al. (2003).

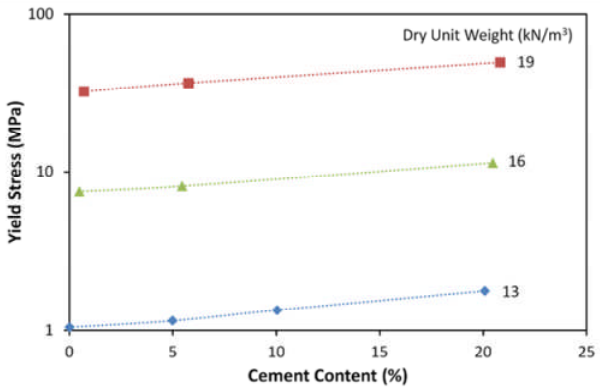

Figure 2.37 Variation of yield stress with dry unit weight and cement content (Huang and Airey, 1998)

2.4.4 Summary

In the literature, the normal compression of sand has unequivocally been linked to the onset of particle crushing. The behaviour of uncemented and cemented sand has been reviewed in this section, with an emphasis on the influence of cementation.

Both cemented and uncemented sand exhibit stiff elastic initial behaviour before yielding. Cementation has been shown to increase the yield stress, with bond breakage coinciding or preceding particle breakage. Cementation

also increases the zone in e–ln σ_v space that the material can exist in, with these effects increasing with degree of cementation. The NCLs of cemented materials are speculated to converge with the intrinsic NCL of the equivalent unbonded material at high stresses, with increasing degree of cementation increasing the disparity of these lines.

2.5 PARTICLE FRACTURE

2.5.1 Introduction

The global behaviour of a soil, in particular the strength and strain is largely affected by the degree of particle crushing, or fragmentation. The degree of crushing itself is controlled by the particle size distribution, particle shape, the mineralogy and strength of the grains, density, the water condition of the soil, the stress path, and arguably most importantly the effective stress state. As such, the influence of particle crushing is greatest at high pressures (i.e. stress states causing particles to exceed their strength). Particle crushing is responsible for the irreversible reduction in volume in one-dimensional and isotropic compression, and causes a significant reduction in dilation during triaxial shearing at high enough confining pressures (Hardin, 1985).

2.5.2 Single Particle Breakage

McDowell and Amon (2000) demonstrated that Weibull (1951) statistics can successfully be applied to the fracture of soil grains. It is widely accepted that the failure of a spherical particle under pure compression is tensile, and also that fractures initiate from existing flaws and the associated stress concentrations. Jaeger (1967) proposed that the tensile strength of grains could be measured by diametral compression between flat platens as:

$$\sigma_f = \frac{F}{d^2} \qquad [2.16]$$

where σ_f is the tensile stress at failure, F is the diametral force measured from the platens and d is the diameter of the grain at failure. Using this equation, McDowell and Bolton (1998) reported that the tensile strengths obtained

from single particles of various sizes crushed between flat platens could be related to size by:

$$\sigma_{\mathrm{f}} \propto d^{b} \qquad [2.17]$$

where *b* describes the size-hardening effect (after Billam, 1972; Lee, 1992).

A Weibull distribution in itself is described by two parameters: one defining the shape of the probability distribution, usually termed the Weibull modulus, *m*; and the other defining the magnitude/scale, usually a characteristic value of the distribution such that 37% of random variables are greater. For a given magnitude, increasing the modulus decreases the variability of the random variable. The effect of increasing the Weibull modulus for a random variable *X* is shown in the cumulative distributions given in Figure 2.38.

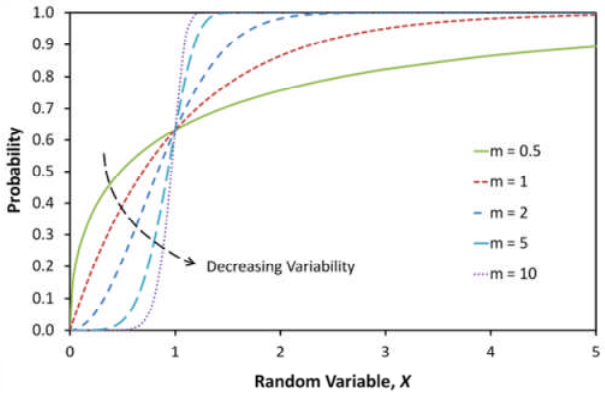

Figure 2.38 Cumulative distribution functions for various Weibull distributions, with a characteristic value $X_0 = 1$, showing the influence of the Weibull modulus

Weibull (1951) studied the tensile strength of brittle ceramics and stated that for a tested block to survive, all of its constituent parts must remain intact. He proposed that for a block of material of volume *V* under a uniform tensile stress σ, the probability of survival of the block $P_{\mathrm{s}}(V)$ could be given by:

$$P_{\mathrm{s}}(V) = \left[\exp\left[-\left(\frac{\sigma}{\sigma_0}\right)^{m}\right]\right]^{\mathrm{V/V_0}} \qquad [2.18]$$

which rearranges to:

$$P_s(V) = \exp\left[-\frac{V}{V_0}\left(\frac{\sigma}{\sigma_0}\right)^m\right] \quad [2.19]$$

where V_0 is a reference volume of material, such that

$$P_s(V_0) = \exp\left[-\left(\frac{\sigma}{\sigma_0}\right)^m\right] \quad [2.20]$$

and σ_0 is the value of tensile stress at which 37% (i.e. exp[-1]) of the total number of tested blocks (of volume V_0) survive, and m is the Weibull modulus. The Weibull modulus increases with decreasing variability in tensile strength. McDowell and Bolton (1998) showed that for a block of material of volume V_1 under tension, equation [2.19] gives the 37% strength σ_1 as:

$$\sigma_1 = \sigma_0\left(\frac{V_0}{V_1}\right)^{1/m} \quad [2.21]$$

Using equation [2.19] and assuming that sand particles are geometrically similar, McDowell and Bolton then gave the survival probability of a particle of size d under diametral compression as:

$$P_s(d) = \exp\left[-\left(\frac{d}{d_0}\right)^3\left(\frac{\sigma}{\sigma_0}\right)^m\right] \quad [2.22]$$

where σ was the tensile stress induced in the particle given by equation [2.16], and σ_0 was the value of induced tensile stress at which 37% of the tested particles of size d_0 survive. Equations [2.21] and [2.22] both show that the value of stress for a block of material such that 37% of tested specimens survive is a function of size. From equation [2.22], this characteristic value of stress, $\sigma_{0,d}$, for particles of size d can be shown to be:

$$\sigma_{0,d} = \left(\sigma_0 d_0^{3/m}\right) d^{-3/m}$$

$$\sigma_{0,d} \propto d^{-3/m} \qquad [2.23]$$

which is of the same form as equation [2.17]. McDowell and Amon (2000) confirmed this could be applied to sand particles by single particle crushing tests. Grains of a range of sizes were crushed, and for each particle size category, the survival probability was determined for each induced tensile stress at failure. The Weibull modulus was determined from plotting ln (ln (1/P_s))) against ln σ_c, as well as the 37% strength, $\sigma_{0,d}$. All grain sizes for a particular sand revealed very similar values for the Weibull modulus, m, and plotting the 37% strength as a function of particle size at failure on a double logarithmic graph confirmed the relationship given in equation [2.23].

McDowell (2001, 2002) further investigated the distribution of strengths for a given size of particle, and emphasized the importance of correctly measuring the variance as well as the average strength for a given size of soil particle. The strength as a function of size for silica sand is illustrated in Figure 2.39, where the measured strengths are plotted along with a trend line corresponding to equation [2.23]. This work assumed that bulk fracture dominates during the breakage of particles. In later work Lim and McDowell (2004) considered surface facture as the dominant mode of breakage, which implies particles break once a critical value of surface stress is reached. Using the same working as introduced by McDowell and Amon (2000) and summarised above, this lead to an alternative expression for the size effect on characteristic strength:

$$\sigma_{0,d} \propto d^{-2/m} \qquad [2.24]$$

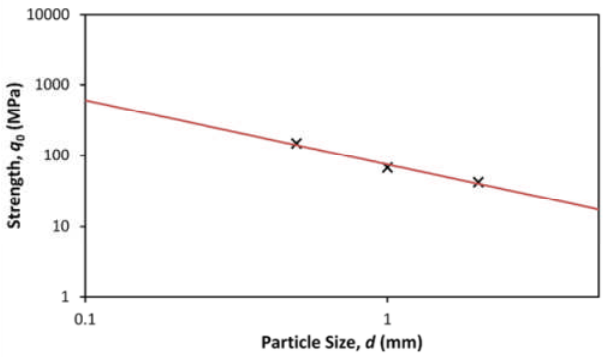

Figure 2.39 Strength as a function of particle size for silica sand, with the trend line corresponding to equation [2.23] (McDowell, 2002)

2.5.3 Particle Crushing during Shear

Yamamuro and Lade (1996) performed a series of drained triaxial tests with confining pressures up to 52 MPa on dense sand to investigate the role of particle crushing. As they stated, relatively few high pressure triaxial studies have been performed, with high pressure behaviour only extensively investigated during compression. Figure 2.40 shows the triaxial behaviour with confining pressures up to 52 MPa. Figure 2.40(a) shows the principal stress ratio versus axial strain and Figure 2.40(b) displays the volumetric strain as a function of axial strain. The former shows that as the confining pressure is increased, the inclination of the initial part of the deviatoric stress–axial strain curves tend to decrease, and the maximum principal effective stress ratio tends to decrease in magnitude. This was associated with in an increase in the amount of volumetric compression, and an increase in the axial strain at failure. Focusing on the tests at the highest pressures (20–52 MPa), all stress-strain plots in Figure 2.40(a) appear very similar, with three apparent 'sections': an initial steep linear portion, a prominent middle linear section between approximately 2–20% axial strain, and a final horizontal section at the failure stress ratio. The middle section, i.e. the part of the curve indicated by a steady gradient before reaching the ultimate state, was reported to be indicative of continual particle breakage; samples with a highly pronounced 'middle section' of the normalised stress-strain curve had greatly decreased slopes of volumetric strain upon failure, suggesting that the majority of crushing had already taken place. Most revealing in the work of Yamamuro

and Lade (1996) was the observation that for confining pressures in excess of 17.2 MPa, volumetric contraction appears to stop increasing, and actually begins to decrease, visible in Figure 2.40(b). This was suggested as being due to large amount of volumetric contraction that occurred during the isotropic consolidation phase prior to shearing, although alternatively it could be related to the stress paths taken to reach the CSL in *v*-*p*' space. With very high confining pressures, the samples are sheared at initially lower voids ratios, resulting in stiffer samples.

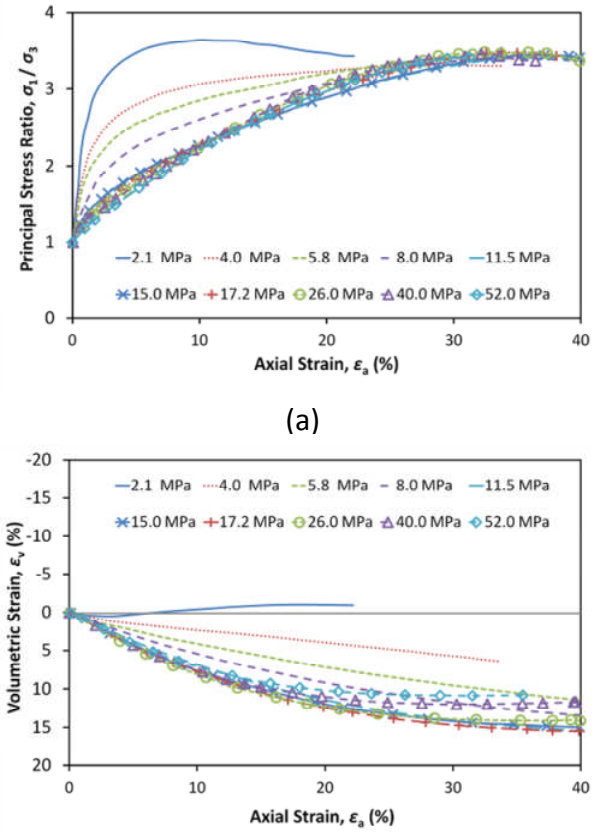

Figure 2.40 Triaxial behaviour of dense sand: principal stress ratio (a) and volumetric strain (b) versus axial strain with confining pressures up to 52 MPa (Yamamuro and Lade, 1996)

Yamamuro and Lade (1996) attempted to quantify the amount of particle breakage by using Hardin's (1985) relative breakage parameter, B_r. This parameter is a measure of the difference in grading curves before and after shearing, with a higher value indicating more particle breakage. As one would expect, their tests showed that this parameter increases with increasing mean effective stress at failure, demonstrated in Figure 2.41 and was seen to

increase rapidly for mean effective failure stresses above 4 MPa. This matched with observations of strain at failure—both volumetric strain at failure and axial strain at failure were also seen to increase rapidly with mean effective stress at failure above 4 MPa. This indicated that the sharp rise in strains at high pressures is caused by a marked increase in particle crushing. As the volumetric strain stopped increasing, and actually started to decrease at very high confining pressures, the relative breakage appeared to have stabilised, with no further increase in breakage observed. Later, Lade et al. (1996) went on to define their own quantification of breakage, which was related to total input energy, which could be applied to a variety of tests other than triaxial shearing.

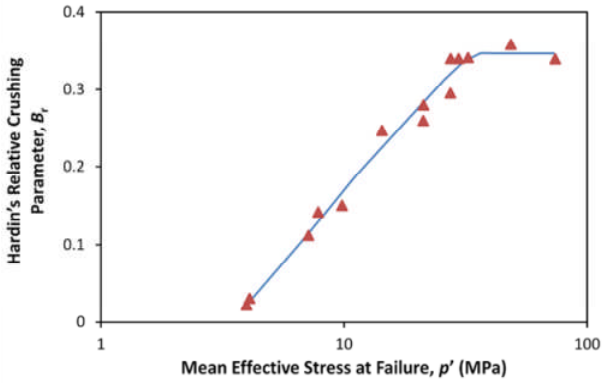

Figure 2.41 The influence of increasing stress on particle breakage during drained triaxial shearing (Yamamuro and Lade 1996)

Marri (2010) analysed particle breakage resulting from high pressure triaxial tests on cemented and uncemented sand. Marri provided photographic images of samples after shearing to approximately 30% axial strain, covering a range of confining pressures and cement content, given in Figure 2.42. The images compare an uncemented sample of sand (a) and a sample with 15% content of Portland cement (b), both sheared under a confining pressure of 20 MPa. Marri (2010) suggested that the amount of particle crushing appeared less in the cemented soil—although both images reveal what appear to be broken particles. However, the images are non-intrusive, and in the case of the cemented sand, the cementation obscures the particles somewhat, so the images may be considered inconclusive. The image of

highly cemented sand (15% dry unit weight) sheared under a confining pressure of 1 MPa (c), appears to reveal less breakage, indicating that increasing the confining pressure resulted in increased particle crushing. Marri (2010) reported that the cemented soil sheared at 1 MPa mainly showed only broken cement bonds (along the shear plane), while the soil sheared at 20 MPa displayed both bond *and* particle breakage.

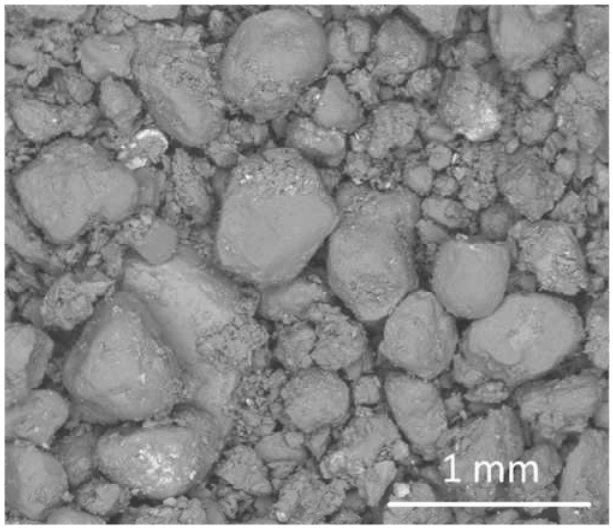

(a)

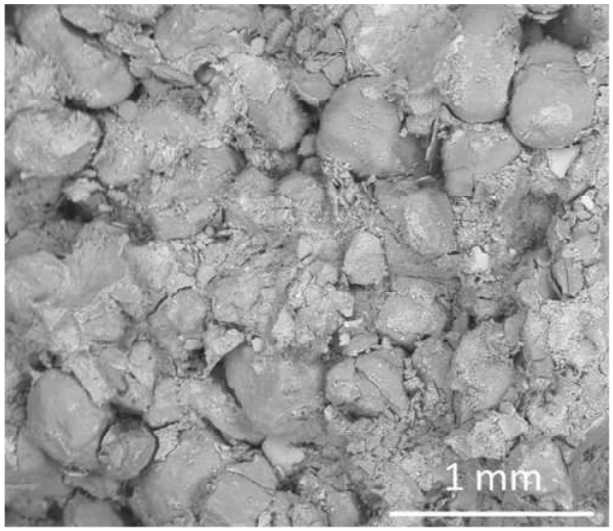

(b)

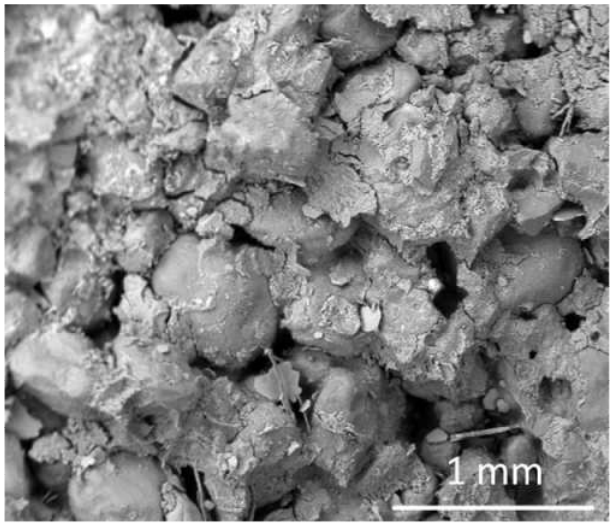

(c)

Figure 2.42 Photographs showing close ups of specimens after drained triaxial shearing: uncemented sand under 20 MPa confining pressure(a); sand with 15% cement content under 20 MPa (b); sand with 15% cement content under 1 MPa (c) (Marri, 2010)

2.5.4 Particle Crushing during Compression

Hagerty et al. (1993) performed extensive one-dimensional compression tests on a range of granular materials, with a focus on the fundamental role of particle crushing, and the phenomena associated with it, rather than on the macroscopic behaviour of the compressed material. It has been widely accepted in the literature (see earlier) that the slope of the normal compression line for a material is determined by particle crushing, allowing a decrease in volume; Hagerty et al. investigated how crushing itself was influenced by initial voids ratio, particle size, particle angularity, and material composition by performing tests up to 689 MPa. The yield stress in compression, which Hagerty et al. (1993) termed the 'break point stress', indicated the onset of crushing, and like in previous literature was shown to increase with decreasing initial voids ratio, regardless of the material being compressed. The location of the yield stress was also seen to be affected by the angularity of the particles, which was revealed by compression tests on spherical versus angular glass beads. The larger particles showed an earlier, lower yield stress, and the final grading analysis (Figure 2.43) revealed the larger particles had undergone a greater degree of crushing, the larger initial median grain size meaning fewer inter-particle contacts and therefore larger stresses. Angular glass beads also revealed a greater degree of crushing, again due to fewer contacts.

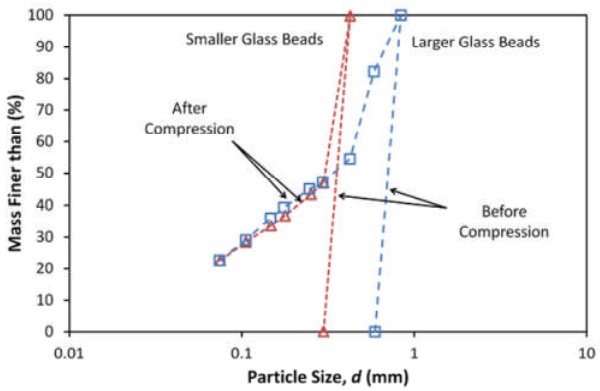

Figure 2.43 The particle size distributions before and after compression for large and small glass beads (Hagerty et al., 1993)

McDowell et al. (1996) and McDowell and Bolton (1998) provided both a numerical and experimental study of the irrecoverable compression of aggregates, and related the continuous splitting of grains to the progressive evolution of a particle size distribution. Firstly, they declared that the conventional relationship for one-dimensional compression given in equation [2.7] is dimensionally inconsistent, and that the vertical stress ought to be normalized by some material parameter. They suggested that it is the continuous fracture of the *smallest* particles that results in a linear NCL in voids ratio–log stress space: these particles continue to crush under increasing stress, filling the voids and facilitating the decrease in volume. As such, they proposed that the current applied macroscopic stress during compression, σ_c should be proportional to the average strength of the smallest particles, σ_s:

$$\sigma_c = k\sigma_s \qquad [2.25]$$

where *k* is a constant, independent of particle size due to self-similarity across different orders of particle size. If the yield stress in compression is proportional to the average tensile strength of the grains, which they proposed, then they suggested the vertical effective stress could be normalized by a reference stress, if the voids ratio at that stress is known, thus the equation for a linear normal compression line can be expressed:

$$e = e_c - \lambda \ln\left(\sigma/\sigma_c\right) \qquad [2.26]$$

where σ is the vertical stress, σ_c is simply a stress on the normal compression line, proportional to the strength of the smallest particles at that stress, and e_c is the voids ratio at that applied stress.

Nakata et al. (2001a) performed a series of one-dimensional compression tests on silica sand and related the macroscopic behaviour to fundamental crushing mechanics. They related the curvature of the compression line at yield to the initial grading of the material: uniformly graded sand had a much

more marked, distinct yielding; well-graded sand had a less distinct, less rapid yielding. They reported a direct relationship between the initial coefficient of uniformity and the curvature of the yield point of the NCL. They observed that the compressibility index, C_c increased with vertical effective stress until reaching a steady value at approximately 20–30 MPa, regardless of initial grading. From marking individual particles and tracking their progress, it was found that the majority of particle fragmentation occurred in the period between the yield stress and the point at which C_c reached a steady value. It was seen that of the tracked particles, approximately 60% had suffered 'major' grain splitting at the end of the test. From tracking particles in the graded sample, it was observed that larger grains were more likely to undergo 'surface grinding', or breakage of asperities, while smaller particles were more likely to under 'major' splitting. Finally, they suggested that the grain size distribution curves for the smaller size particles evolved towards a common line, alluding towards a critical grain size distribution for one-dimensional compression.

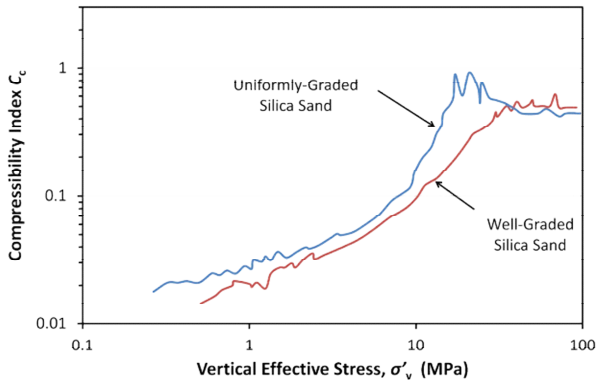

Figure 2.44 Compressibility index as function of increasing vertical effective stress (Nakata et al., 2001a)

Nakata et al. (2001b) later related the macroscopic compression behaviour, in particular the one-dimensional yield stress, to single particle crushing strength. They performed one-dimensional compression tests on materials consisting of single sized particles, coupled with single particle crushing tests to establish individual strength characteristics. Results showed that the yield stress reduced with increasing median particle size, which was due to the

observed size-strength relation observed from crushing tests. Furthermore, their results indicated that for a mixture of soil consisting of grains of two different materials, it is the stronger material which dominates the crushing behaviour, e.g. the yield stress.

McDowell and Humphreys (2002) confirmed the observation that one-dimensional yield stress is proportional to the average strength of the grains by performing single particle crushing tests as well as one-dimensional compression tests on a range of uniformly graded materials, including pasta and cereals as well as sand. The compression curves of these materials, plotted against stress normalised by the strength of the constituent grains, shown in Figure 2.45 share similar normalised yield stresses. The negative voids ratios were a result of using the *estimated* density of rice krispies and corn flakes to calculate the voids ratio.

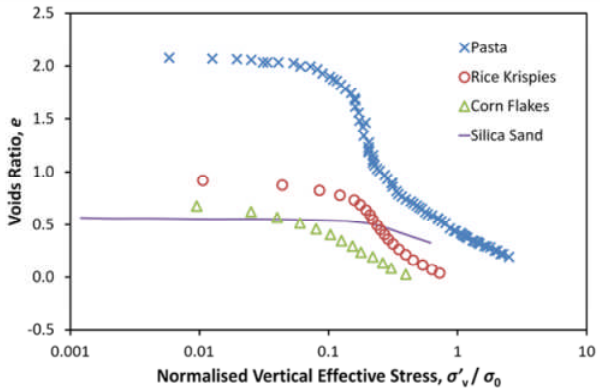

Figure 2.45 Voids ratio plotted against vertical stress normalised by particle strength for a range of materials (McDowell and Humphreys, 2002)

2.5.5 Creep

Granular materials, and soils in particular have long been observed to undergo creep, i.e. to deform plastically under a constant stress. Sand is known to exhibit creep under constant effective stress (Murayama et al., 1984; Leung et al., 1996; Lade and Liu, 1998), such that creep strain is usually reported to be proportional to the logarithm of time:

$$\varepsilon = C \log\left({}^{t}/_{t_0}\right) \qquad [2.27]$$

where C is the creep coefficient, and t_0 is the time from which creep strains are measured; stereotypical linear behaviour is shown in Figure 2.46.

In one-dimensional conditions, creep has often been related to the continuing fracture of grains (e.g. Leung et al., 1996; Pestana and Whittle, 1998), with the rate of strain dependent on the stress state, time and material properties. Bowman and Soga (2003) related the creep of dense sands in triaxial conditions not only to breakage, but also to particle rearrangement, when subjected to high stress ratios.

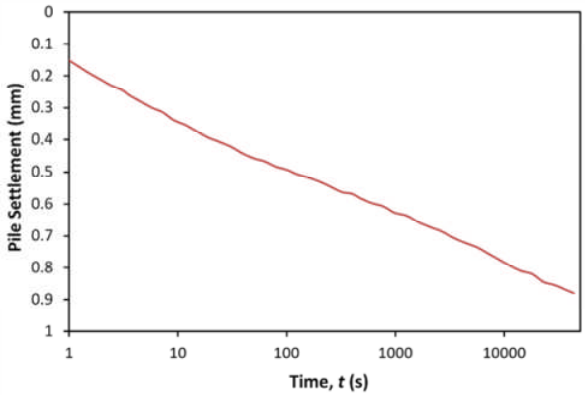

Figure 2.46 Variation of vertical strain (pile settlement) with the logarithm of time (Leung et al., 1996)

McDowell (2003) proposed a theoretical explanation for observed creep behaviour, relating creep to the time dependence of particle strength, and showed that equation [2.27] was consistent with equation [2.26] for a granular material subjected to creep at constant stress under one-dimensional conditions. According to equation [2.26] ($e = e_c - \lambda \ln(\sigma/\sigma_c)$) an assembly of soil particles will be in equilibrium with a voids ratio e_c under an applied stress σ_c. Recalling that the current macroscopic stress, σ_c should be proportional to the average strength of the smallest particles σ_s, McDowell substituted equation [2.25] into equation [2.26] to give:

$$e = e_c - \lambda \ln\left(\sigma/k\sigma_s\right) \qquad [2.28]$$

McDowell (2003) then applied the well-established law for the time dependence of strength of ceramics (Davidge, 1979; Ashby and Jones, 1986)

to soil particles. For a tensile test on a ceramic specimen, if the standard test used to measure the tensile strength, σ_{TS}, takes a time t(test), then the stress σ_t that the sample will safely support for a time t is given by:

$$\left(\frac{\sigma_t}{\sigma_{TS}}\right)^n = \frac{t(\text{test})}{t} \qquad [2.29]$$

where n is the slow-crack growth exponent. Data for n is limited, but is usually between 10–20 for oxides at room temperature (Ashby and Jones, 1986). If $\sigma_{s,0}$ is the average particle strength measured at time $t = t_0$ then the average strength σ_s after time t, would according to equation [2.29] be:

$$\sigma_s = \sigma_{s,0}\left(t_0/t\right)^{1/n} \qquad [2.30]$$

McDowell then substituted equation [2.30] into equation [2.28] to give:

$$e = e_c - \lambda \ln\left(\sigma/k\sigma_s\right) - \frac{\lambda}{n}\ln\left(t/t_0\right) \qquad [2.31]$$

Hence the reduction in voids ratio Δe as a function of time after time t_0 is:

$$\Delta e = \frac{\lambda}{n}\ln\left(t/t_0\right) \qquad [2.32]$$

McDowell and Khan (2003) went on to demonstrate the validity of this theory by conducting one-dimensional compression tests and creep tests on pasta: linear normal compression lines emerged and creep strain appeared to be proportional to the logarithm of time. They also observed that a higher rate of creep was linked to a higher degree of particle crushing.

2.5.6 Fractal Distributions

Turcotte (1986) investigated the phenomenon of fractal size distributions resulting from fragmentation, and defined a 'fractal' by the relationship

between number and size: if the number N of objects with a characteristic *linear* dimension r is given by:

$$N \propto r^{-D_{\mathrm{fr}}} \qquad [2.33]$$

then a fractal is defined with a fractal dimension of D_{fr}. Considering a granular material, a fractal size distribution is one such that the number of particles N of size L greater than d, $N(L > d)$, is given by:

$$N(L > d) \propto d^{-D_{\mathrm{fr}}} \qquad [2.34]$$

The nature of this equation means that a fractal particle size distribution would appear linear on a distribution plot with two logarithmic axes, with the fractal dimension emerging as the slope. Most granular materials (not only soils but materials such as coal, fault gouge, ice) under pure crushing evolve towards a distribution with a fractal dimension between 2.0 and 3.0, remarkably usually about 2.5 (Turcotte, 1986; Sammis et al. 1987; Palmer and Sanderson, 1991; Steacy and Sammis, 1991, McDowell and Daniell, 2001), and demonstrated in Figure 2.47.

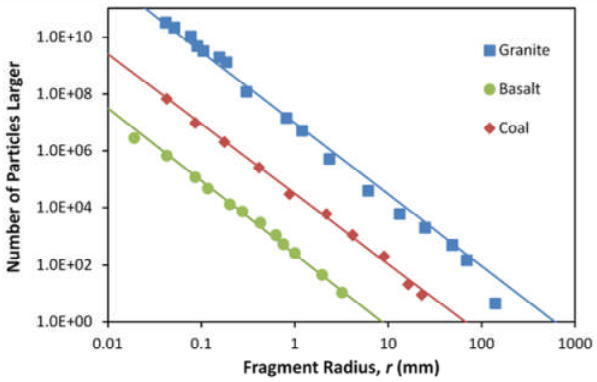

Figure 2.47 Particle size distributions for various crushed materials, showing consistent fractal dimensions of 2.5 (Turcotte, 1986)

McDowell et al. (1996) presented a numerical study investigating the irrecoverable compression of aggregates, and related the splitting of grains to the evolution of fractal particle size distributions. At a given applied macroscopic stress, the likelihood of a particle fracturing decreases with

reducing particle size but increases with reducing coordination number. The study showed that if coordination number is the most dominant factor influencing the probability of fracture, then a fractal distribution emerges with a realistic fractal dimension. If the opposite is considered: if size was the dominant factor influencing probability of fracture, then because smaller particles are stronger than large particles, the largest particles would be always the most likely to fracture, leading to a uniform matrix of fine particles, behaviour which is not evident in the literature. McDowell et al. (1996) stated that although the smallest particles are the strongest, they also have the fewest contacts, which increases the induced tensile stress (Jaeger, 1967). So there are two opposing effects on particle 'survival', and evidence suggests coordination number is the most important. They proposed that it is indeed the smallest particles which continue to fracture as stress is increased, and these particles become statistically stronger and fill the voids. From one-dimensional compression tests on a carbonate sand, and using digital photography, Cheng et al. (2001) showed that once the 'fractal' NCL has been reached, many particles had undergone a large number of successive fractures. McDowell and Bolton (1998) applied the McDowell et al. (1996) model to experimental data, and used a work equation which considered the energy dissipated by the fracture of particles and the assumption of a Weibull distribution of particle strengths, justified a linear normal compression line plotted on a voids ratio–log stress graph.

McDowell and Daniell (2001) investigated why a fractal dimension of 2.5 consistently emerges for soils and other granular materials. They analysed simulations from Steacy and Sammis (1991) which featured arrays of uniform blocks with various fragmentation mechanisms, and who proposed that fragmentation occurs to eliminate same-sized neighbours. Using a deterministic mechanism such that no neighbouring blocks could exist at the same size, two-dimensional simulations produced the fractal pattern shown in Figure 2.48. Simulations using three-dimensional blocks resulted in a fractal dimension of 2.6. The criteria for what defined two blocks to be

considered ‘neighbouring’ were investigated by Steacy and Sammis (1991), as well as giving blocks a probability of failure dependent on the number of same-sized neighbours. Also investigated was the effect of a ‘stress bias’, which rendered particles more vulnerable to breakage if they were near a previous breakage. These different permutations resulted in fractal dimensions between 2.0 and 2.9. McDowell and Daniell (2001) drew attention to the fact that a value of 2.5 emerged when neighbouring blocks were defined as blocks having finite contact area, and a ‘stress bias’ influenced the probability of fracture, although it should be recognised that this was using cubes, not irregular particles.

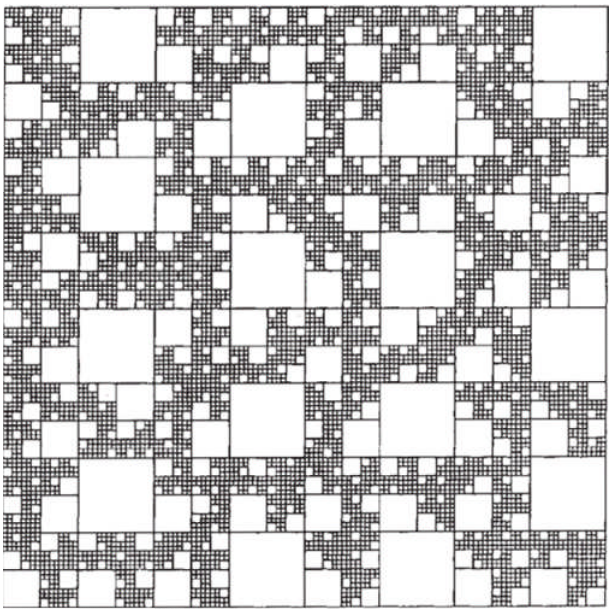

Figure 2.48 Typical fractal pattern produced from 2D simulations, in which no neighbouring particles can have the same size (Steacy and Sammis, 1991)

McDowell (2005) later used fractal crushing theory to justify use of a double logarithmic compression plot, and suggested that in fact normal compression lines should be linear when plotted on a log voids ratio–log stress graph in accordance with earlier suggestions by Pestana and Whittle (1995). Assuming a fractal of 2.5 emerges, as is the case for many granular materials under pure crushing, and using equation [2.34], McDowell gave the number of particles $N(L \geq d_s)$ greater than or equal to a size d_s as:

$$N(L \geq d_s) \propto {d_s}^{-2.5} \qquad [2.35]$$

the number of particles $N(L \geq d_{s-1})$ greater than or equal to a size d_{s-1} as:

$$N(L \geq d_{s-1}) \propto {d_{s-1}}^{-2.5} \quad [2.36]$$

and then that the number of the smallest $N(L = d_s)$ particles satisfied:

$$N(L = d_s) \propto {d_s}^{-2.5} \quad [2.37]$$

Given that the volume of a smallest particle is proportional to d_s^3, the total volume of all of the smallest particles was given as:

$$V(L = d_s) = N(L = d_s) \cdot d_s^3 \propto {d_s}^{1/2} \quad [2.38]$$

As mentioned earlier, McDowell and Bolton (1998) proposed that the smallest particle size is a function of stress level. For the silica sand in Figure 2.28, McDowell (2002) found the Weibull modulus m to be approximately 3 and therefore the size effect on the average strength σ_0 to be:

$$\sigma_0 \propto d^{-3/m} \propto d^{-1} \quad [2.39]$$

And, assuming that the current stress level was proportional to the average strength of the smallest grains according to equation [2.25], substituting equation [2.39] into equation [2.38] implied:

$$V(L = d_s) \propto \sigma^{-1/2} \quad [2.40]$$

Finally, McDowell (2005) proposed that the void space is proportional to the total volume of all the smallest particles once a fractal distribution has emerged, therefore:

$$e \propto \sigma^{-1/2} \quad [2.41]$$

Which evidently gives the slope of the compression curve in log e–log σ_v as 0.5, which matches the slope of the experimental curve when plotted on double logarithmic axes, as shown in Figure 2.49.

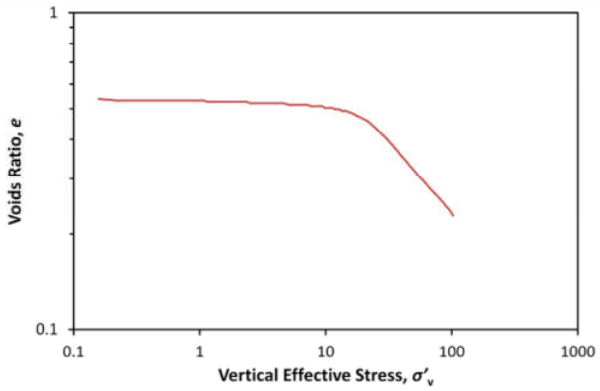

Figure 2.49 Compression behaviour for silica sand plotted on log e–log σ_v axes (McDowell, 2005)

2.5.7 Summary

The crushing of particles is controlled by many factors, as briefly summarised in this section. The failure of a particle is generally tensile, and the literature on single particle breakage shows that the tensile strengths of soil grains can be fitted to distributions and related to particle size.

The phenomena of crushing during laboratory tests have been discussed, with the quantity of crushing directly linked to particle strength and macroscopic stress. In triaxial testing, particle breakage accommodates the large volumetric contraction during shear.

In isotropic and one-dimensional normal compression, particle crushing allows the decrease in volume with increasing applied stress, and has also been shown to be responsible for observed creep. The evolution of particle size distributions have also been discussed, with fractal distributions shown to consistently emerge as a result of crushing.

2.6 DISCRETE ELEMENT METHOD

2.6.1 Introduction

The discrete element method (DEM) is a branch of numerical methods for calculating the behaviour of an assembly of particles. DEM can be defined as

a numerical technique for modelling granular mechanics, which emphasises inter-particle contacts. Although originally designed primarily or modelling the behaviour of granular materials, DEM is now an effective alternative to continuum methods such as the finite element method. It has grown in popularity in recent years, and is widely used to model discontinuous materials. The increase in use is mainly due to modern advances in computing, as DEM is inherently computationally expensive.

Granular materials are defined as consisting of small-scale discrete particles, which behave individually and only interact at contacts. The fundamental purpose of DEM is to recreate the microscopic mechanics of the independent particles to allow understanding of the macroscopic behaviour. The properties of the discrete particles determine the complex behavioural response of the whole assembly, analogous to the behaviour of real soils as outlined earlier.

Discrete element method has a range of applications, and has been used to model materials such as grains, cereals, sugars, avalanches, proteins, and chemicals (e.g. Tijskens et al., 2003; Banton et al., 2009; Fu et al., 2006) as well as soils, but this document will focus on its applications to geotechnical engineering and soils, in particular the modelling of triaxial tests, cemented sand and particle crushing. A major advantage of using DEM to model such scenarios is the ability to provide information difficult to obtain from physical models, such as the micro-scale inter-particle behaviour and contact force distributions, and the repeatability of simulations.

The general principle of DEM was developed by Cundall and Strack (1979) who initially applied it in the field of rock mechanics. They later developed this and pioneered a method directly applicable to soil mechanics, referred to as the *distinct* element method, based on the finite difference formulation of the equation of motion. They also validated the use of DEM as a research tool by comparing numerical results with photoelasticity. There have been numerous other discrete element methods developed over the years, such as

the discontinuous deformation analysis (Shi, 1998), the lattice type model (Budhu et al. 1997) and modal methods (Williams and Mustoe, 1997)—as noted by O'Sullivan (2002), who gave a fairly comprehensive summary of the many discrete element methods.

Until the last few years, much of the modelling using DEM was in two dimensions, however the increase in availability of high-performance computers has enabled many situations to be modelled in three-dimensions. The behaviour of an assembly can be determined by tracing the movements and forces of individual particles. The fundamental basis of this method involves breaking down the behaviour using time increments, then for a given increment, the initial positions and velocities of the particles are known. The algorithm proposed by Cundall and Strack (1979), which is most commonly used for geotechnical problems, then applies Newton's Second Law to the particles and a force-displacement law to the contacts to determine the forces acting at the contacts, and the resulting accelerations, and obtains the particle positions and information at the end of the time increment.

2.6.2 Particle Flow Code in Three Dimensions

The software used in this research is Itasca's Particle Flow Code in 3 Dimensions 3.1, referred to herein as PFC3D. A detailed description of the underlying theory behind the code can be found in the manual (Itasca, 2005). PFC3D is currently the most commonly used DEM software, and uses two entities: a ball and a wall to model interactions and Newton's 2nd Law together with a contact law to establish accelerations, velocities and displacements of particles via a time-stepping scheme. Key assumptions include treating the particles as spherical, rigid bodies, and the behaviour at the contacts use a soft-contact approach where the rigid particles are allowed to overlap one another. The magnitude of this contact is related to the contact force via the force-displacement law, and all overlaps are small in relation to particle sizes. Two principal contact laws are used: linear springs, and Hertzian, which will be detailed later, as well as the various bonds which can exist at contacts.

The behaviour of a model in PFC3D is represented numerically by a time-driven algorithm, in which the velocities and accelerations are assumed to be constant within each timestep. At all times, the forces on each particle are resolved by determining the interaction with other particles/walls in contact. The speed at which a disturbance can propagate is a function of the physical properties of the discrete system, so the timestep is chosen to satisfy this constraint. The calculations alternate between applying Newton's 2nd Law to the particles and a force-displacement law at the contacts. Newton's 2nd Law is not applied to walls, since the wall velocity is always defined by the user, so only the force-displacement law is used at ball-wall contacts.

The actual calculation cycle is a timestepping algorithm, and requires repeatedly applying the law-of-motion to each particle, the force-displacement law to each contact, and constantly updating the wall positions. At the beginning of each timestep, the set of contacts (either ball-ball or ball-wall) is updated from the known positions of all entities. The force-displacement law is then applied to all contacts, obtaining new contact forces. Using Newton's second law of motion, the acceleration of each particle is determined from the resultant forces and moments arising from contacts and body forces. The acceleration of each particle is integrated to obtain its updated velocity and then again to determine displacement and its position, while the wall positions are simply updated from their specified velocities. The calculations in the boxes in Figure 2.50 can effectively be done in parallel.

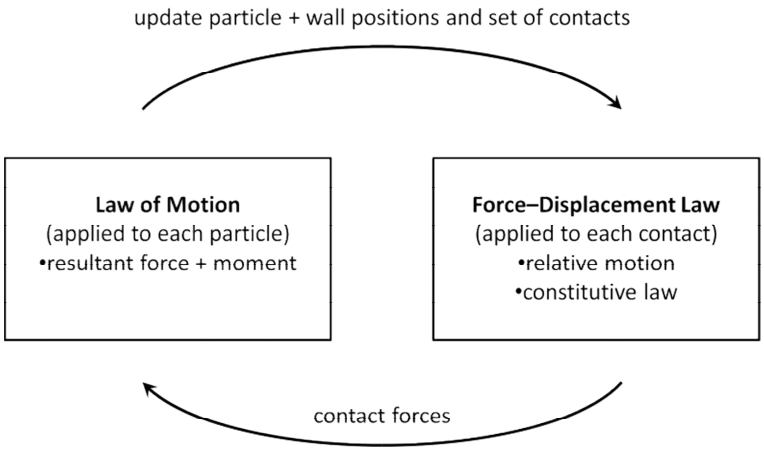

Figure 2.50 Calculation cycle used in PFC3D (Itasca, 2005)

The force displacement law relates the relative displacement between two entities at a contact to the contact force acting on them. All contacts are considered to occur at a single point. For contacts between balls, a distributed stress and moment can act if there is a parallel bond present. The contact point between two balls occurs on a contact plane described by a unit normal vector, which is directed along the line between ball centres. For contacts between a ball and wall, the normal vector is directed along the line defining the shortest distance between the ball centre and the wall. The contact force for any contact is broken down into a normal component and shear component, acting in the direction of the normal vector and the contact plane respectively. The components of force are related to the corresponding components of displacement by the force-displacement law using the normal and shear stiffnesses at the contact. The normal contact force vector is calculated by:

$$F_i^{\mathrm{n}} = K^{\mathrm{n}} U^{\mathrm{n}} n_i \qquad [2.42]$$

Where K^{n} is the normal secant stiffness, relating *total* displacement and force, U^{n} is the overlap of the two entities, and n_{i} is the unit normal defining the contact plane. The shear force is calculated in an incremental fashion; when the contact is formed, the total shear contact force is initialized to zero. Subsequent increments of shear displacement result in an increment of shear force that is added to the current value, this vector is calculated by:

$$\Delta F_i^s = -k^{\mathrm{s}} \Delta U_i^s \qquad [2.43]$$

Where k^{s} is the tangent shear stiffness at the contact, and ΔU_i^{s} is the shear component of the contact displacement increment vector. Note that uppercase, *K* denotes secant stiffness; lowercase, *k* denotes tangent stiffness. The new shear contact force is then calculated by summing the shear force vector at the start of the timestep with the increment shear force vector:

$$F_i^s = \langle F_i^s \rangle_{\mathrm{old}} + \Delta F_i^s \qquad [2.44]$$

The Law of Motion dictates that the motion of a particle is determined by the resultant force and moment vectors acting upon it. The translational motion of a particle is described in terms of its position, velocity and acceleration, while the rotational motion is described in terms of its angular velocity and angular acceleration. These two equations of motion are integrated using a centred finite-difference procedure involving a timestep, Δ*t*. PFC3D determines a critical timestep, below which the system remains stable. The software is based upon the idea that the timestep chosen may be so small that, during a single timestep, disturbances cannot propagate further from any particle than its immediate neighbours—since the speed at which a disturbance can propagate is a function of the physical properties of the discrete system, the timestep can be chosen to satisfy the above constraint. PFC uses a relatively simple procedure to determine this value, which can be summarised as:

$$t_{\text{crit}} = \sqrt{m^{\text{p}}/k^{\text{tran}}} \quad \text{for translational motion} \qquad [2.45]$$

$$t_{\text{crit}} = \sqrt{I/k^{\text{rot}}} \quad \text{for rotational motion} \qquad [2.46]$$

Where m^{p} is the mass, I is the moment of inertia, k^{tran} is the translational stiffness and k^{rot} is the rotational stiffness for an individual particle.

PFC3D applies the above to each degree of freedom to each particle; the final critical timestep is taken to be a fraction of the minimum of all critical timesteps calculated. The manual can be consulted for a thorough demonstration of the procedure for determining the critical timestep for a system (Itasca, 2005).

In PFC3D, in general the loading of an assembly is applied by application of gravity or wall movement. For walls, the user is able to specify velocities, but not forces directly—this requires a user-created servo-function. Additionally,

it is possible for the user to apply forces, moments and velocities to each ball in the assembly.

The constitutive model at an individual contact consists of three parts: a stiffness model; a slip model; and a bonding model. The stiffness model gives an elastic relation between the contact force and the relative displacement via the force-displacement laws in equations [2.42] and [2.43]. The stiffnesses used in these equations are assigned different values depending on whether the linear model or Hertz-Mindlin model is employed. The linear contact model is a simple, linear formulation that is defined by the normal and shear stiffnesses, k_n and k_s respectively, of the two contacting entities. This model is commonly used in DEM due to the ease of implementation, and the fact that it is one of the least computationally demanding contact models—and is used in the initial simulations presented in Chapter 3. However, it fails to capture the nonlinearity one would expect from two interacting elastic spheres, and in the case of particles of various sizes, needs to be scaled accordingly to reflect the material elastic modulus. The linear contact stiffnesses, K^n and k^s, are computed assuming that the stiffnesses of the entities act in series:

$$K^{\mathrm{n}} = \frac{{k_{\mathrm{n}}}^{[\mathrm{A}]}{k_{\mathrm{n}}}^{[\mathrm{B}]}}{{k_{\mathrm{n}}}^{[\mathrm{A}]} + {k_{\mathrm{n}}}^{[\mathrm{B}]}} \qquad [2.47]$$

$$k^{\mathrm{s}} = \frac{{k_{\mathrm{s}}}^{[\mathrm{A}]}{k_{\mathrm{s}}}^{[\mathrm{B}]}}{{k_{\mathrm{s}}}^{[\mathrm{A}]} + {k_{\mathrm{s}}}^{[\mathrm{B}]}} \qquad [2.48]$$

note that the for linear model, the normal tangent stiffness k^n is equal to the normal secant stiffness, K^n.

The Hertz-Mindlin contact model is a nonlinear formulation based on the theory of Mindlin and Deresiewicz (1953) as described by Itasca (2005). The theory is only applicable to spheres in contact, although it does not reproduce the continuous nonlinearity in shear. This model is more computationally

demanding than the linear springs model, but is considered more realistic, and is used from Chapter 4 onwards. In addition to capturing the non-linear stiffness of two interacting spheres, it also automatically accounts for the variation of contact stiffness with particle size. The Hertz-Mindlin model is defined by the shear modulus, *G* and Poisson's ratio, *v* of the two contacting balls. The contact normal secant stiffness is given by:

$$K^{\mathrm{n}} = \left(\frac{2\langle G\rangle\sqrt{2\tilde{R}}}{3(1-\langle \nu\rangle)}\right)\sqrt{U^{\mathrm{n}}} \qquad [2.49]$$

and the contact shear tangent stiffness by

$$k^{\mathrm{s}} = \left(\frac{2\left(\langle G\rangle^2 3(1-\langle \nu\rangle)\tilde{R}\right)^{1/3}}{2-\langle \nu\rangle}\right)|F_i^{\mathrm{n}}|^{1/3} \qquad [2.50]$$

where U^{n} is the sphere overlap, and $|F_{\mathrm{i}}^{\mathrm{n}}|$ is the magnitude of the normal contact force. The multipliers are a function of the geometric and material properties of the two entities in contact, and are given by:

$$\tilde{R} = \frac{2R^{[\mathrm{A}]}R^{[\mathrm{B}]}}{R^{[\mathrm{A}]}+R^{[\mathrm{B}]}} \qquad [2.51]$$

$$\langle G\rangle = \frac{1}{2}\left(G^{[\mathrm{A}]}+G^{[\mathrm{B}]}\right) \qquad [2.52]$$

$$\langle \nu\rangle = \frac{1}{2}\left(\nu^{[\mathrm{A}]}+\nu^{[\mathrm{B}]}\right) \qquad [2.53]$$

for ball-to-ball contacts, and the following for ball-to-wall contacts:

$$\tilde{R} = R^{[\mathrm{ball}]} \qquad [2.54]$$

$$\langle G\rangle = G^{[\mathrm{ball}]} \qquad [2.55]$$

$$\langle v \rangle = v^{[\mathrm{ball}]} \qquad [2.56]$$

where G is the elastic shear modulus, v is the Poisson's ratio, R is the sphere radius, and [A] and [B] denote the two spheres in contact. Note that the normal tangent stiffness (k^n) and the normal secant stiffness (K^n) are related by:

$$k^{\mathrm{n}} = \frac{3}{2} K^{\mathrm{n}} \qquad [2.57]$$

The slip model provides a relation between the shear and normal contact forces so that the two contacting balls may slip relative to one another. This model is defined by the friction coefficient at the contact, μ, which is taken to be the minimum friction coefficient of the two contacting entities. If the overlap is greater than zero, then maximum allowable shear contact force is calculated:

$$F_{\mathrm{max}}^{\mathrm{s}} = \mu |F_i^{\mathrm{n}}| \qquad [2.58]$$

If $|F_i^s| > F_{max}^s$, then slip occurs during the following calculation cycle by setting the magnitude of F_i^s equal to F_{max}^s.

The bonding model acts to limit the total normal and shear forces that the contact can bear by enforcing bond-strength limits. Two models are provided in the software, the contact bond model and the parallel bond model. Once a bond is created, it continues to exist until it is broken.

The contact bond can be envisioned as a pair of elastic springs with constant normal stiffnesses acting at the contact point, with specified shear and tensile normal strengths. The contact bond precludes the possibility of slip, and the normal and shear constitutive behaviour is shown in Figure 2.51.

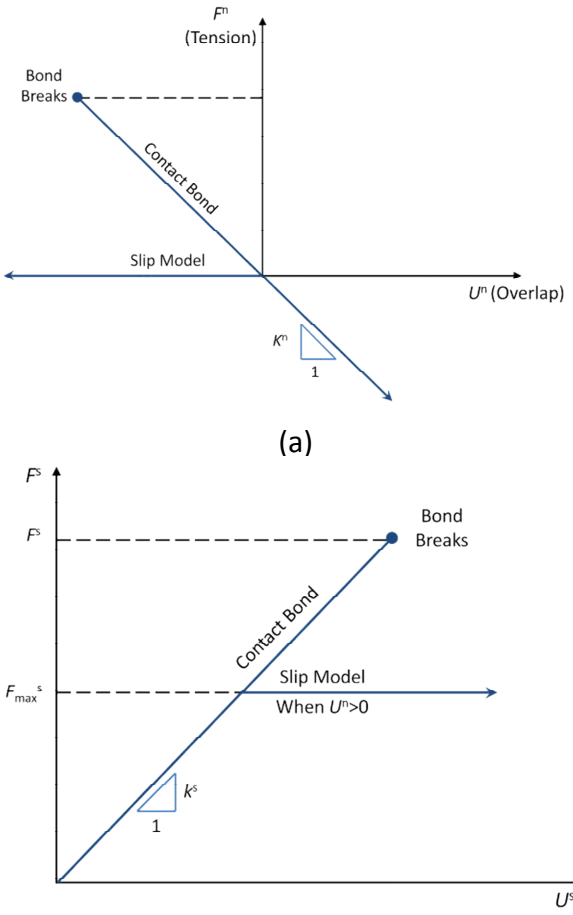

Figure 2.51 Constitutive behaviour relating the normal (a) and shear (b) components of contact force and relative displacement for particle contact (Itasca, 2005)

The parallel bond model can be envisaged as a piece of cementitious material deposited between two particles, or as a set of elastic springs with constant normal and shear stiffnesses uniformly distributed over a circular disk on the contact plane. This additional elastic interaction acts in parallel with the slip model, and can transmit both forces and moments between particles. Total force vectors are resolved into normal and shear components $\overline{F}_i^{\mathrm{n}}$ and $\overline{F}_i^{\mathrm{s}}$ respectively, as is the total moment vector, to $\overline{M}_i^{\mathrm{n}}$ and $\overline{M}_i^{\mathrm{s}}$. These vectors are illustrated in Figure 2.52.

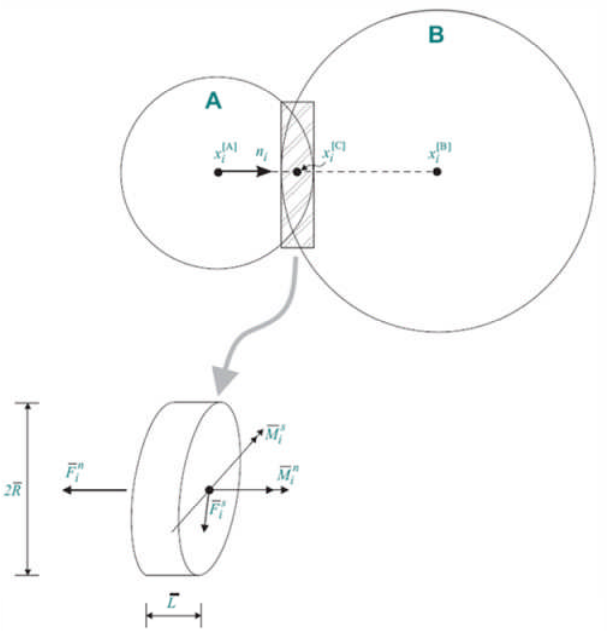

Figure 2.52 Schematic of parallel bond, depicted as a cylinder of cementitious material (Itasca, 2005)

The maximum tensile and shear stresses acting on the bond periphery are calculated by:

$$\sigma_{\max} = \frac{-\overline{F}^{\mathrm{n}}}{A} + \frac{\overline{M}_i^{\mathrm{s}}}{I}\overline{R} \qquad [2.59]$$

$$\tau_{\max} = \frac{\left|\overline{F}^{\mathrm{s}}\right|}{A} + \frac{\left|\overline{M}_i^{\mathrm{n}}\right|}{J}\overline{R} \qquad [2.60]$$

Where *A* is the area of the bond disc, *J* is the polar moment of intertia of the disc cross-section, *I* is the moment of inertia of the disc about an axis through the contact point, and $\overline{R}$ is the radius of the bond disc.

2.6.3 Triaxial Tests

Much of the available literature involving modelling triaxial tests using DEM is limited to two-dimensions, for example Utili and Nova (2008). However, the widespread availability of commercial DEM codes and recent advances in computing have enabled triaxial tests to begin to be modelled in three-dimensions. Many researchers have simulated true triaxial tests, i.e. a cubical

sample with flat rigid boundaries (e.g. Sitharam et al., 2002; Ng, 2004; Belheine et al., 2009; Salot et al., 2009).

For the purpose of simulating accurate laboratory conditions, it is essential that any membrane allows the correct confining pressure to be applied while allowing free deformation. In laboratory testing, although membrane effects have been acknowledged (Henkel and Gilbert, 1952) real membranes still allow free deformation of the specimen, and the natural failure mode to develop. The importance of flexible membranes in numerical models has been highlighted in recent years. In two-dimensions, biaxial tests with flexible membranes have been modelled by researchers such as Iwashita and Oda (1998), Wang and Leung (2008), and Jiang et al. (2011), etc. who used membranes consisting of smaller particles bonded together, demonstrated in Figure 2.53.

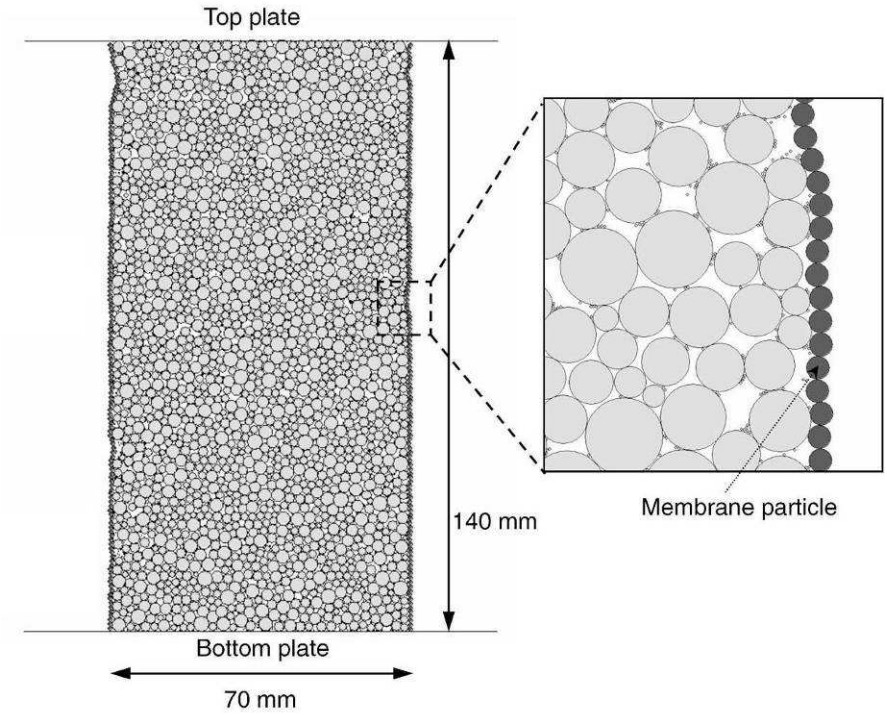

Figure 2.53 Diagram showing flexible membrane consisting of bonded particles, in 2D (Wang and Leung, 2008)

In three-dimensions, authors such as Cheung and O'Sullivan (2008) and O'Sullivan and Cui (2009) simulated the effects of confining pressure by applying forces directly to the sample and allowing it to deform freely. This

resembles real laboratory conditions more closely than rigid walls, however it is unclear how accurately they account for the change in surface area of the sample during shearing. They projected the coordinates of the outer particles in the specimen to a rectangular plane, then used Voronoi cells (displayed in Figure 2.54) to obtain the corresponding area of each outer particle. Although somewhat effective, this method assumed the sample and 'membrane' remains cylindrical, which is not true for a triaxial test with flexible boundaries. Furthermore, the virtual confining forces applied by Cheung and O'Sullivan (2008) were always directed to the centre of the specimen, as shown in Figure 2.55, rather than normal to the specimen surface which does not quite recreate true confining pressure, and finally their method did not give consideration to the vertical component of confining pressure, considering only the *x* and *y* components, as visible from the figure.

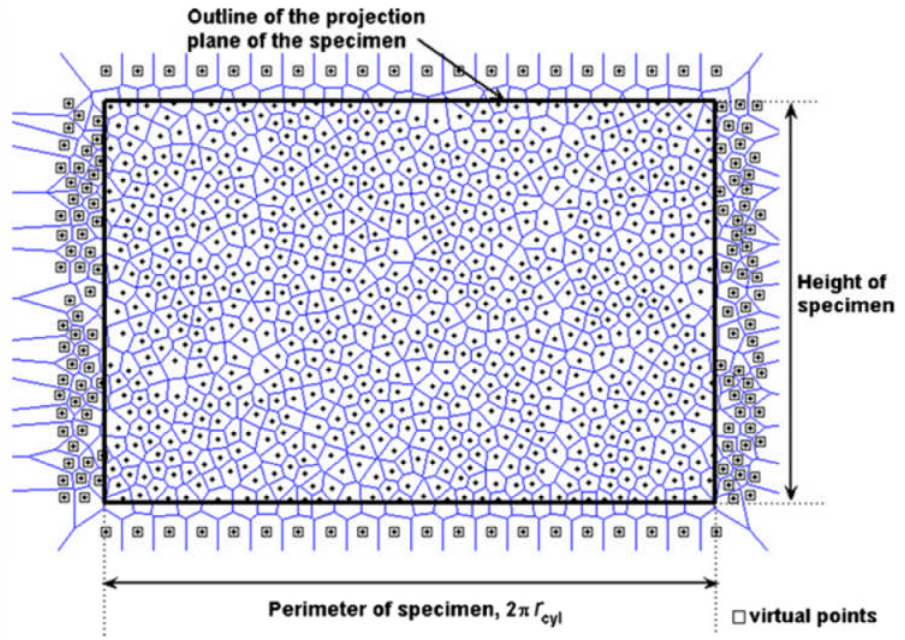

Figure 2.54 Voronoi diagram derived from the projected coordinates of outer particles (Cheung and O'Sullivan, 2008)

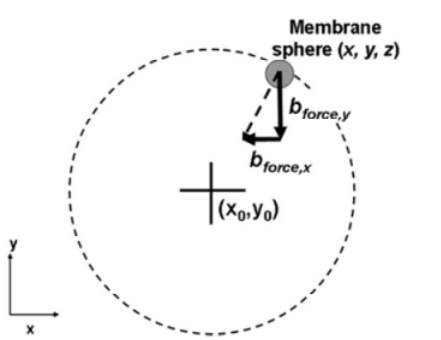

Figure 2.55 Direction of the calculated components of confining pressure, applied to membrane spheres (Cheung and O'Sullivan, 2008)

Cheung and O'Sullivan (2008) did however show the significant advantages of flexible membrane in allowing the correct deformation and avoiding significant non-uniformities in stress along the boundary. The deformation was observed by plotting the cumulative particle rotations, given in Figure 2.56 which revealed strain contrasting strain localisation. The simulation with the flexible membrane displayed concentrated particle rotations around the centre, accompanied by bulging, akin to barrelling failure (a) while the rotations from the rigid-walled specimen displayed shear planes (b), as irregular deformation of the membrane was not permitted.

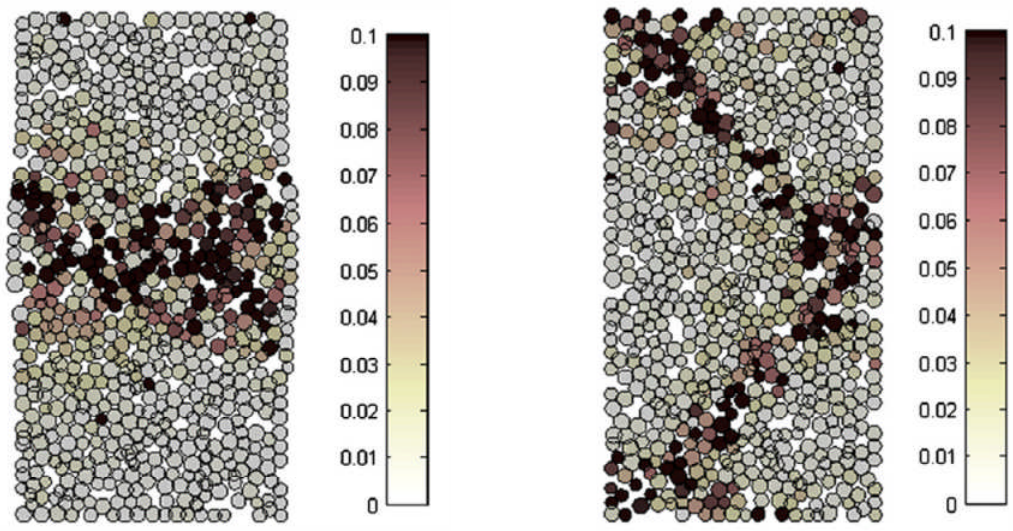

(a) (b)

Figure 2.56 Particle rotations (scale in radians) on a central plane through 3D specimens, for simulation with flexible membrane (a) and rigid wall membrane (b) (Cheung and O'Sullivan, 2008)

The flexible boundary also indicated a reduction in non-uniformities in the stresses along the boundaries. Figure 2.57 shows the applied forces on the

outer particles of the simulations with a flexible membrane, alongside the contact forces between the outer particles and the cylindrical wall from the simulation with rigid boundaries, on a projected plane. It shows that the rigid wall, by not allowing irregular deformation, produces stress concentrations. In comparison, the flexible membrane results in a much more uniform distribution of stress.

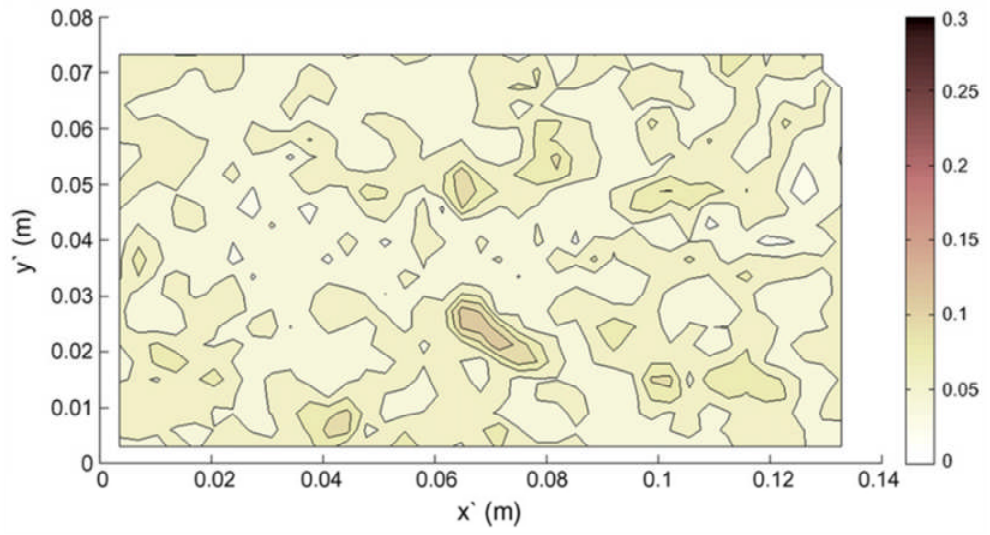

(a)

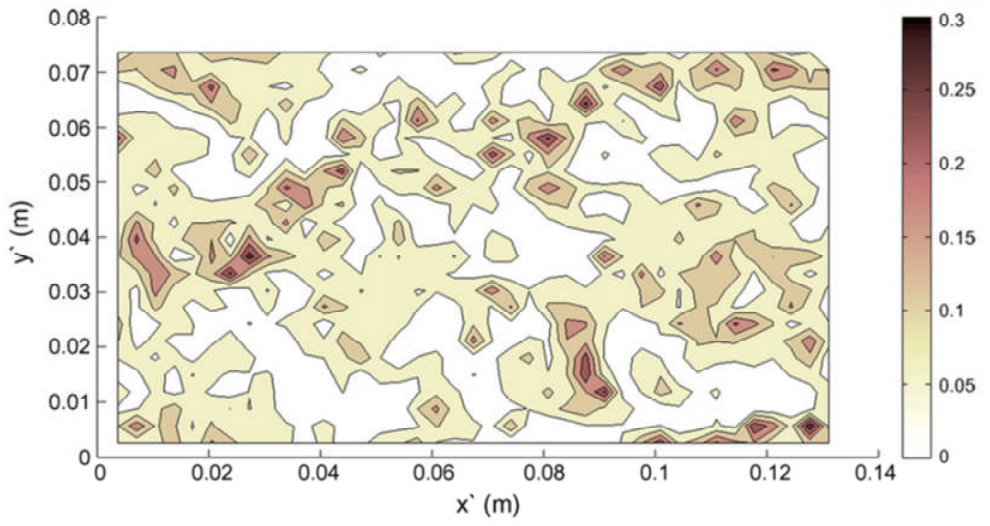

(b)

Figure 2.57 Contours indicating the distribution of outer particle forces on a projection plane for flexible boundary (a) and rigid boundary (b) (Cheung and O'Sullivan, 2008)

Cheung and O'Sullivan (2008) reported a slight difference in stress strain response for the two boundary conditions (the rigid-walled simulation displays a slightly higher peak stress), as did Wang and Tonon (2009), who

simulated the effects of confining pressure in a similar approach. Another disadvantage of solely modelling the effects of confining pressure and not the actual membrane is that it does not leave scope for investigating the role the membrane plays, and how its properties influence the macroscopic behaviour of the material being tested. Nonetheless, these works highlight the important role of flexible boundaries, and demonstrate how rigid boundaries inhibit correct strain localization, and cause significant non-uniformities in the stresses along the boundary.

2.6.4 Cemented/Bonded Granular Materials

In the literature, there exist a number of attempts at modelling in DEM the effects of bonding using various techniques. For example Jiang et al. (2005, 2006) outlined an approach to capture the bonding effect in structured sands using a bond contact model which included a rigid bond element at the contact and developed their own code, NS2D. They showed that it is possible to effectively capture the effect of cementing material between particles by implementing bonds into a two-dimensional sample which was subjected to isotropic compression. The normal compression lines from their simulations were able to exist in part of the voids ratio–log stress space that is not accessible to unbonded materials, and post yield, the compression lines converged (Figure 2.58). However, no particle breakage was considered, somewhat invalidating the post yield parts of the NCLs, and as mentioned, their simulations were limited to two-dimensions.

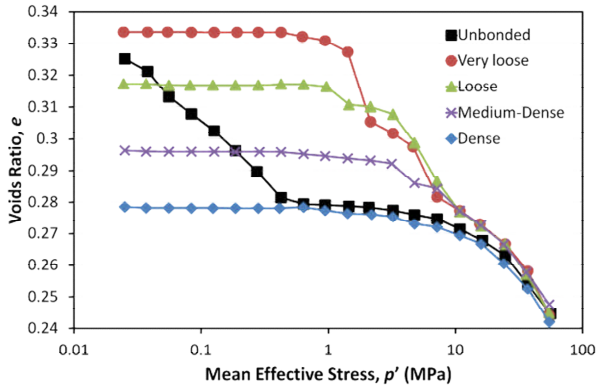

Figure 2.58 Isotropic compression simulations on a bonded granular material with various initial densities, with bond strength 10 N (Jiang et al., 2006)

Wang and Leung (2008) published simulations on triaxial testing of cemented sands in two-dimensions. Their work included a flexible membrane and they bonded the sand particles by introducing fine cement particles and using parallel bonds, illustrated in Figure 2.59. The introduction of cementation was seen to produce a more stable and uniform force-chain network, with longer force-chains and less irregular stress concentrations. The cemented samples demonstrated strain softening (Figure 2.60) and exhibited shear bands during shearing, and within these shear bands it was possible to observe intense bond breakage, particle movement and rotations, and concentrated force-chains. Although two-dimensional, their work provided a useful insight into the micromechanics of cemented sand. They observed that the presence of bonds initially resisted volumetric dilation and caused the stress ratio to increase rapidly. At the peak stress state the strength was influenced by two competing but related processes: the breakage of bonds decreased the strength, but also triggered dilation which increases shear strength. As such, the peak strength and dilatancy were found to be directly linked to cement content, as expected, and as witnessed in experimental results, the maximum rate of dilation and peak strength did not coincide. At ultimate state, there still existed intact bonds, which helped to maintain the overall volumetric dilation.

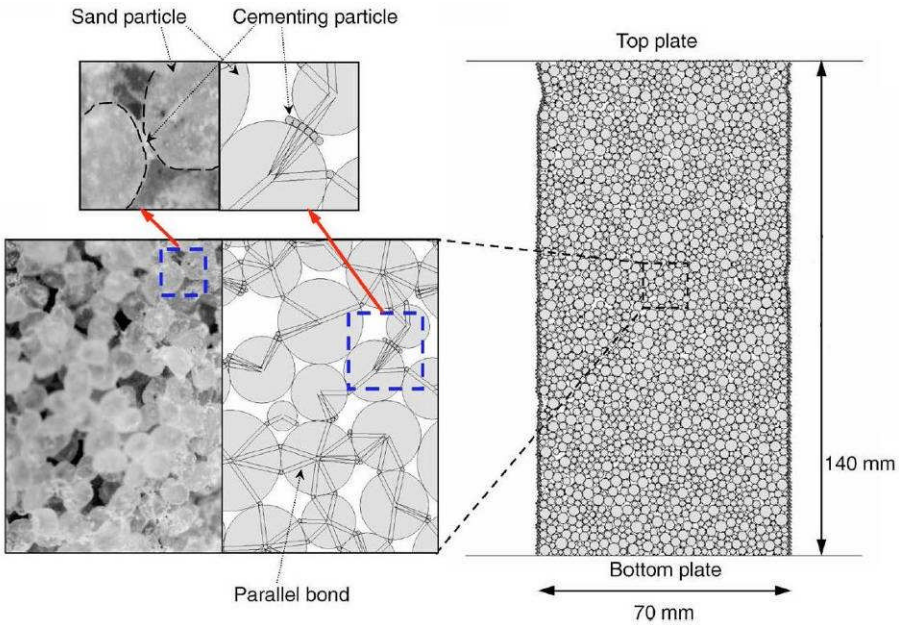

Figure 2.59 Diagram showing cementation consisting of smaller particles bonded with parallel bonds (Wang and Leung, 2008)

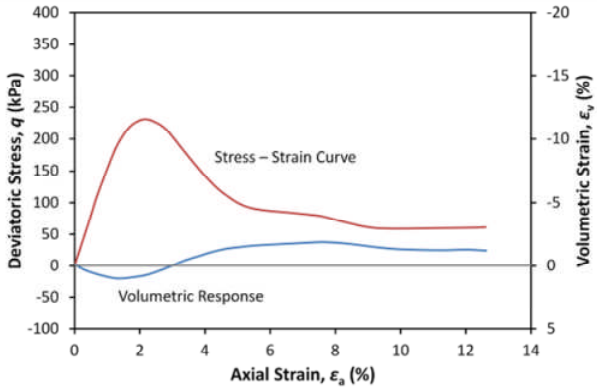

Figure 2.60 Triaxial behaviour showing strain softening and dilation for 2D simulations of cemented sand (Wang and Leung, 2008)

Although Cheung and O'Sullivan (2008) used their triaxial model to simulate tests on cemented sand, the use of a bonded material was solely to demonstrate the capabilities of the flexible boundaries, and as such the mechanics of cemented sand were not studied thoroughly.

Camusso and Barla (2009) presented simulations of loose uncemented and cemented sand also in two-dimensions, with a rigorous calibration of micro-properties. Although their model didn't feature flexible boundaries, they included irregular particle shape by use of clumps, and their results demonstrated good qualitative agreement with observed behaviour, and most notably they commented that a combination of weak and strong inter-

particle bonds was needed for realistic strength characteristics, failure, and force chains. Different failure modes for these bond combinations are shown in Figure 2.61.

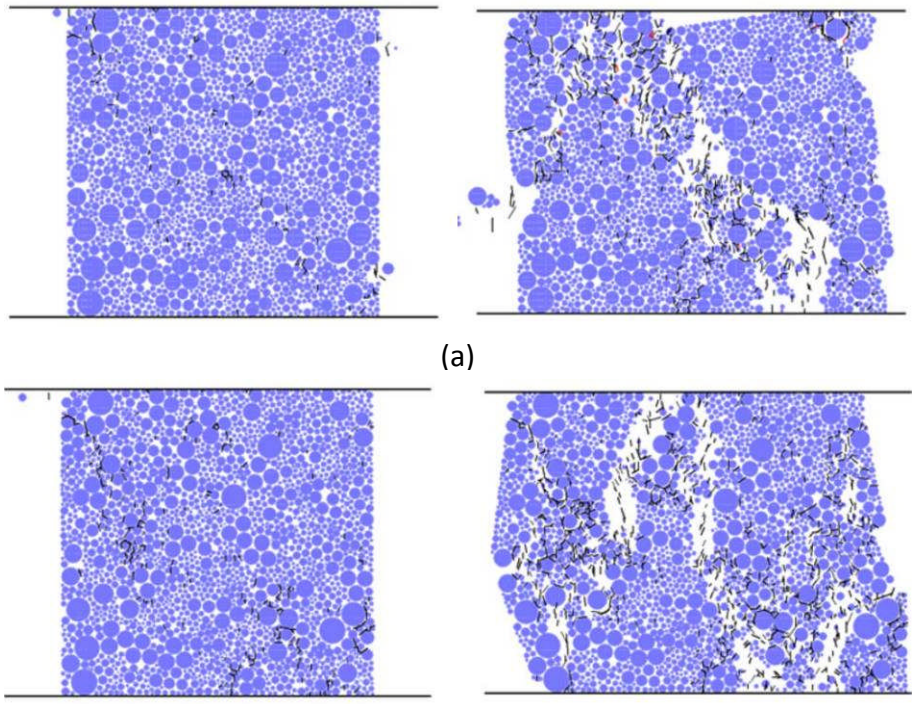

(a)

(b)

Figure 2.61 Numerical specimens at failure (left) and after testing to 3% axial strain (right), for samples with single bond strengths (a) and a combination of weak and strong bond strengths (b) (Camusso and Barla, 2009)

Jiang et al. (2011) went on to further investigate the mechanisms of bondage, comparing their previous bonding model with the contact bond model available in PFC3D. This time they simulated two-dimensional biaxial behaviour, featuring a flexible membrane consisting of bonded particles. The two alternative bonding mechanisms yielded similar results, they both induced strain softening behaviour and shear dilatancy, compared to strain hardening and shear contraction associated with the unbonded simulation. Analysis of the shear plane (given in Figure 2.62), showed that as the sample was sheared, thick columnar force chains developed, which became almost perpendicular to the plane. The shear plane also displayed concentrated particle rotation and bond breakage.

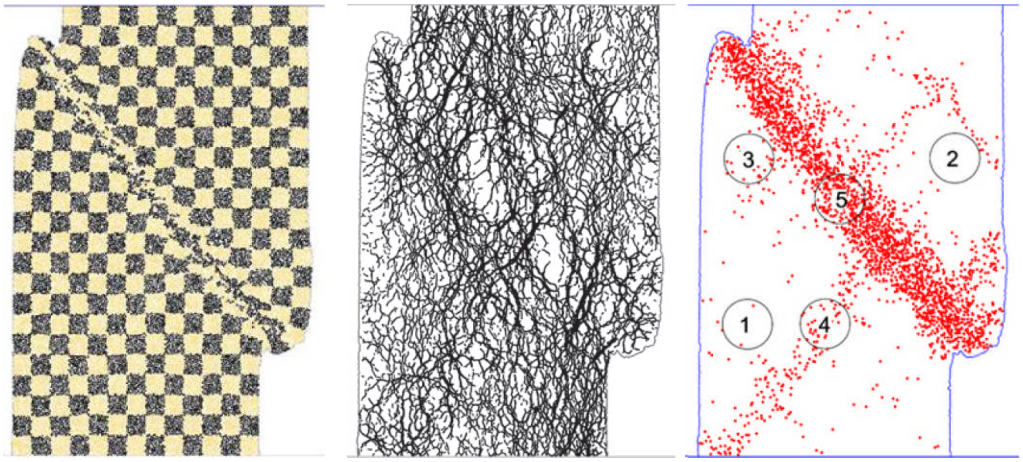

(a) (b) (c)

Figure 2.62 Images showing numerical specimen (a), contact force distribution (b) and bond breakages (c) after biaxial test (Jiang et al., 2011)

Several authors have used DEM to simulate the behaviour of rock, which is similar in essence to cemented sand. Potyondy and Cundall (2004) for example used PFC3D to investigate the mechanical behaviour of rock by bonding a dense packing of spheres. Notably, they thoroughly calibrated the micro-properties of the model to real values, and were able to recreate some realistic behaviour, however most of their work was two-dimensional and focused on comparisons with continuum models and applications such as excavations. Utili and Nova (2008) simulated a two-dimensional analysis of a simplified cliff failure, and demonstrated the ability of DEM to reproduce well-established theoretical behaviour, and as a useful tool as an alternative to continuum methods. Wang and Tonon (2009) modelled three-dimensional triaxial tests on rock, also consisting of bonded spheres. Their model featured a flexible membrane, and they were able to reproduce the classic peak strengths and strain softening associated with such materials, however, the main focus of their work was to showcase the advantage of flexible boundaries and not the micro-mechanics of bonded soil. Ergenzinger et al. (2011) used DEM to model the failure of rock in uniaxial compression in a similar manner to Potyondy and Cundall (2004), however of particular interest was their investigation of various particle size distributions, bond strength distributions and their implementation of a progressive failure mechanism. This consisted of reducing the strengths of bonds locally to

resemble the effects of stress concentrations near crack tips which do not arise in particle models.

2.6.5 Particle Breakage

Using DEM, crushing has generally been modelled in the literature via two alternative methods: replacing 'breaking' grains with new, smaller fragments; or by using agglomerates—groups of bonded particles with finite bond strengths. Åström and Herrmann (1998) were amongst the first to show that it was possible to model the fragmentation of grains in two-dimensions using DEM, by subjecting a 2D array of particles to pressure by decreasing the size of the enclosing 'box', and replacing breaking grains with new smaller particles. They investigated two principal variables: fracture criterion and fracture mode. Two fracture criteria were studied: the first was a threshold value of pressure on a grain, i.e. the total compressive force on a particle; the second was a threshold value for the largest compressive force at a single contact, although no significant differences were observed between the two, and it was unclear if they used a size-strength law.

Åström and Herrmann (1998) investigated the fracture mechanism with three aims in mind: to keep the number of new fragments at each breakage low; to pack the new fragments in such a way to reduce local pressure; and to mimic the real event as closely as possible. Again, they used two different mechanisms: the first simply replaced the breaking grain with two new equal fragments; the second involved replacing a grain with twelve new fragments, of three different sizes both inside and outside the area of the original particle. The resulting arrays of particles are shown in Figure 2.63. The latter mechanism, shown in Figure 2.63(b) caused the radii to decrease much faster, meaning small fragments quickly surrounded large, unbroken grains. This resulted in more unbroken grains remaining, contrasting with the first fracture mechanism (replacing grains with two new fragments) in which no grains remained unbroken. However, the fragment size distributions that

resulted from crushing over many repeated simulations appeared very similar for the two cases.

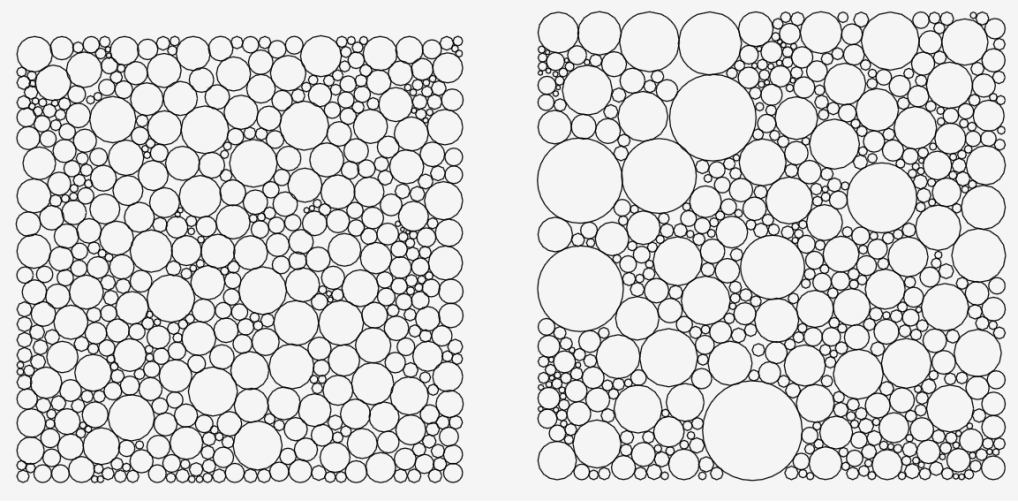

(a) (b)

Figure 2.63 Resulting assortments of particles for two alternative breakage mechanisms: replacing breaking particles with 2 new spheres (a), and 12 new spheres (b) (Åström and Herrmann, 1998)

Tsoungui et al. (1999) used the second fracture mechanism described by Åström and Herrmann (1998) to simulate oedometric compression in two-dimensions (illustrated schematically in Figure 2.64). Their simulations, coupled with experiments using plaster disks revealed that initially, fragmentation increased rapidly with compression, characterised by grains close to the boundaries and then in the centre of the specimen fracturing, evident from images in Figure 2.65. Then as the grains become surrounded by many smaller particles, the effect of hydrostatic pressure slows down the rate of fragmentation, with particle breakage becoming more difficult.

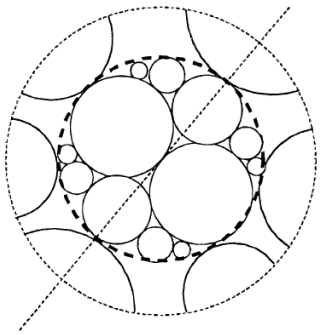

Figure 2.64 Disk breakage configuration for 2D simulations (Tsoungui et al., 1999)

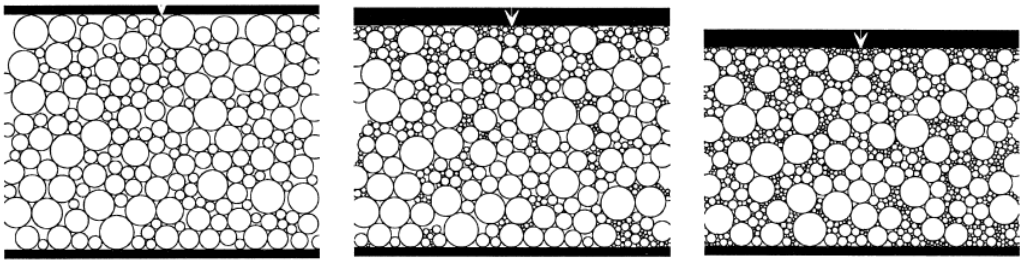

Figure 2.65 Successive stages of 2D simulations, showing progressive particle breakage (Tsoungui et al., 1999)

In a similar fashion, Lobo-Guerrero et al. (2006) modelled particle crushing in two-dimensions by replacing broken grains with smaller grains but did not obey conservation of mass. For the fracture criterion, they considered only grains with 3 or less contacts, then assumed 'Brazilian test' conditions, i.e. diametral compression to estimate the induced tensile stress. They described a size-hardening law thereby giving smaller particles higher strengths than larger particles. They also analysed the evolution of a grain size distribution, and suggested the final emerged distribution was fractal in nature, although conservation of mass was not observed.

Ben-Nun and Einav (2010) developed their own fracture criteria and mechanisms in two-dimensions. They described two criteria, the first of which used a measure of shear stress obtained from the stress tensor for a particle, and the second of which allowed particles to break under hydrostatic stress, similar in essence to the two fracture criteria investigated by Åström and Herrmann (1998). Ben-Nun and Einav (2010) developed a fracture mechanism which involved replacing broken grains with new smaller particles, initially of smaller size to avoid any overlap, then gradually expanding them to maintain conservation of mass while minimizing any artificial pressure spikes. The particles had strengths fitting a Weibull distribution, with a size-hardening effect. The new particles were randomly orientated, and various numbers of new particles were investigated (3, 5 and 6), also illustrated in Figure 2.66. From subjecting the array of particles to uniaxial compression, they consistently observed an ultimate grain size distribution with a fractal dimension of about 1.1–1.4, which did not appear

to be affected by initial porosity, initial grading, or fracture mechanism (Figure 2.67). The fractal nature of the final distribution was also evident in the topology of the sample after crushing, with random self-similarity observed (Figure 2.68).

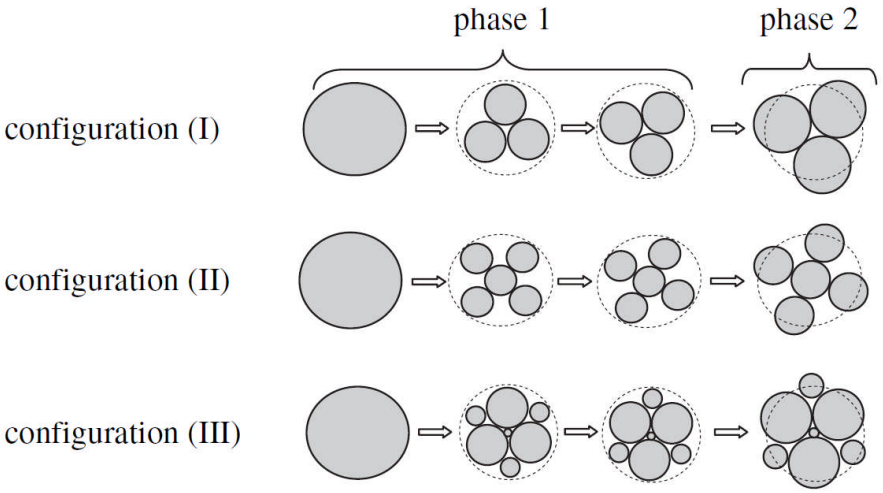

Figure 2.66 Three alternative breakage configurations, showing the random rotation followed by expansion of the new particles(Ben-Nun and Einav, 2010)

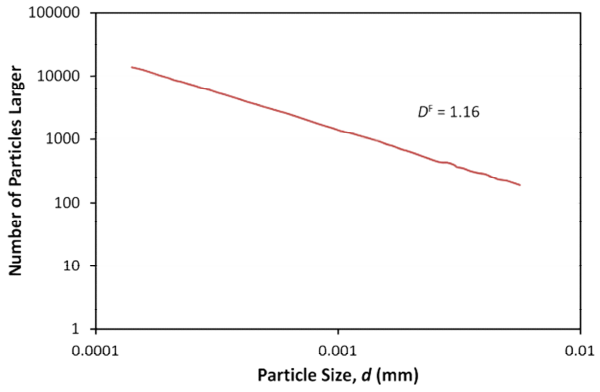

Figure 2.67 Final particle size distribution for typical 2D simulation, with the slope giving a fractal dimension of 1.16 (Ben-Nun and Einav, 2010)

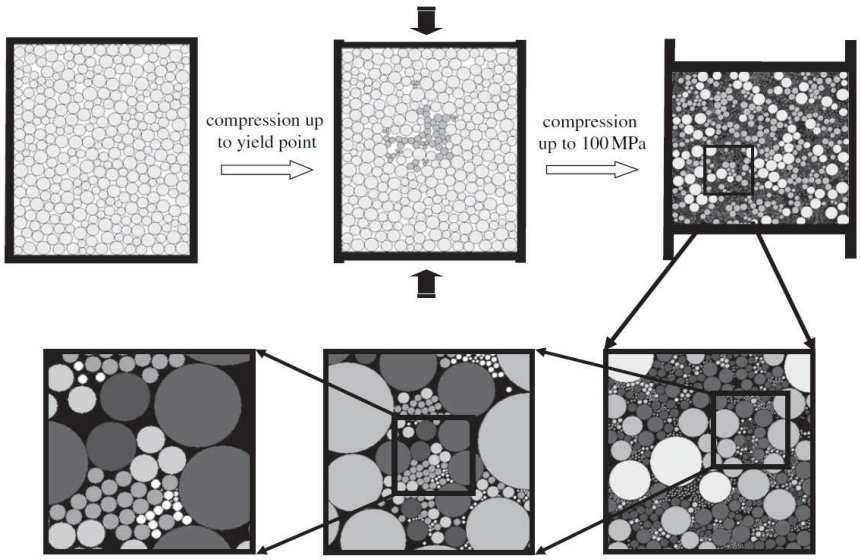

Figure 2.68 Final topology of crushed 2D sample, showing self-similarity across scales (Ben-Nun and Einav, 2010)

In the literature, crushing has also been modelled by use of agglomerates, for example McDowell and Harireche (2002a), who represented individual soil grains by bonding a number of discrete particles. Typically, a 0.5 mm soil particle was modelled with an agglomerate consisting of approximately 140 bonded balls (Figure 2.69), with the bond strengths proportional to the grain fracture stress. The desired distribution of strengths and Weibull modulus for a given size of soil particle was obtained by removing a random number of balls from within the agglomerate. It was observed that the correct size effect on strength was only achieved by correctly introducing enough random flaws within an agglomerate. McDowell and Harireche (2002b) later used their agglomerates to model the yielding and normal compression of sand, and confirmed numerically that yield during compression is the onset of particle breakage, and that yield stress is proportional to the average strength of the grains. They used a basic oedometer to simulate normal compression on aggregates of different sized agglomerates, and approximately linear normal compression lines emerged after yielding (Figure 2.70). Subsequently, they investigated cyclic loading (McDowell and Harireche, 2003) and showed again that volumetric strain is almost exclusively related to particle crushing. Lim and McDowell (2005) used the same methodology but with larger

agglomerates to model the degradation of railway ballast, including oedometer tests.

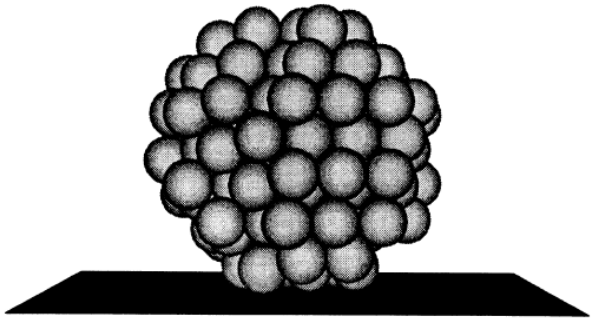

Figure 2.69 Typical 0.5 mm agglomerate, with randomly removed balls (McDowell and Harireche, 2002a)

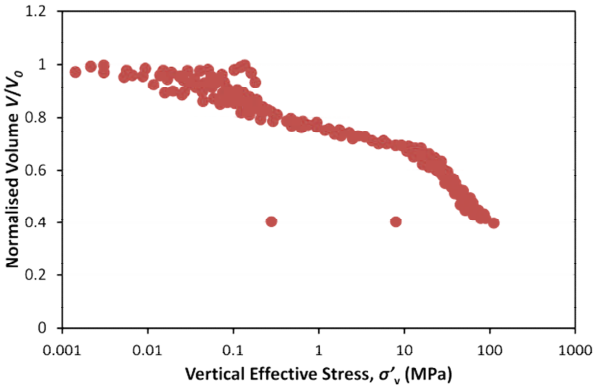

Figure 2.70 Compression behaviour of an array of agglomerates (McDowell and Harireche, 2002b)

Cheng et al. (2003) also used bonded agglomerates to simulate crushable soil, simulating both compression and triaxial shearing (using a rigid, cubical cell, Figure 2.71). Using crushable agglomerates of the same nature as McDowell and Harireche (2002a), Cheng et al. (2003) subjected the aggregate to isotropic compression then investigated various stress paths attempting to establish a critical state line in voids ratio–mean stress space. The ability of the grains to crush during drained triaxial shearing allowed significant contraction to occur, broadly consistent with reality, although not conforming completely to stress-dilatancy theory, as volume continued to decrease after the deviatoric stress reached a stable value. Cheng et al. (2004) later thoroughly explored the critical state behaviour of soil using the same agglomerates and investigating a more extensive range of stress paths. They also highlighted the importance of allowing grains to break during shearing by

comparing behaviour of crushable and uncrushable simulations. They quantified crushing by monitoring the percentage of bonds broken, and plotted yield surfaces at various levels of bond breakage. Bolton et al. (2008) then used the same model to further investigate the fundamental role of crushing in triaxial shearing, and showed that allowing breakage enabled realistic volumetric contraction to be achieved (Figure 2.72). They analysed the various types of particle breakage—i.e. asperity breakage, internal shear cracking and internal tensile cracking. Although the triaxial simulations were using a rigid, cubical cell, the use of agglomerates allowed realistic particle shape effects to be captured, enabling insightful plots showing how the average coordination number for the agglomerates and the deviatoric 'fabric' changed with strain.

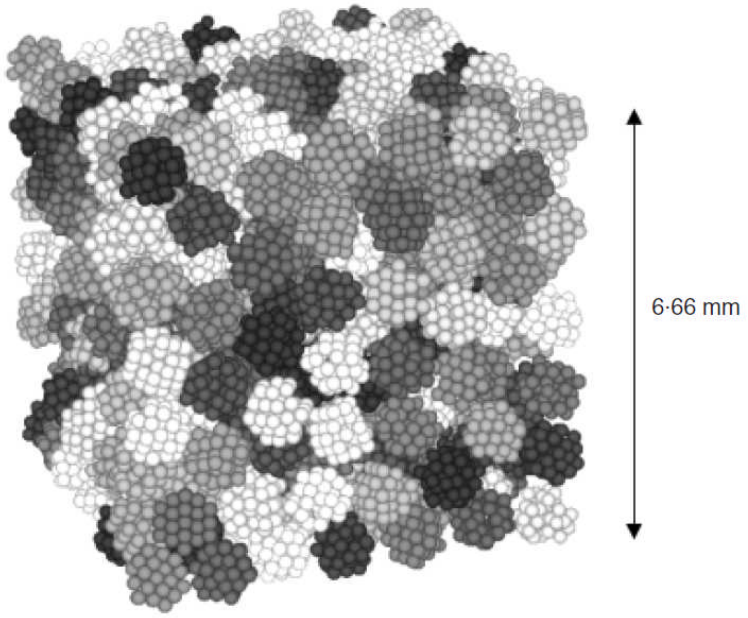

Figure 2.71 3D sample consisting of an array of agglomerates (Cheng et al., 2003)

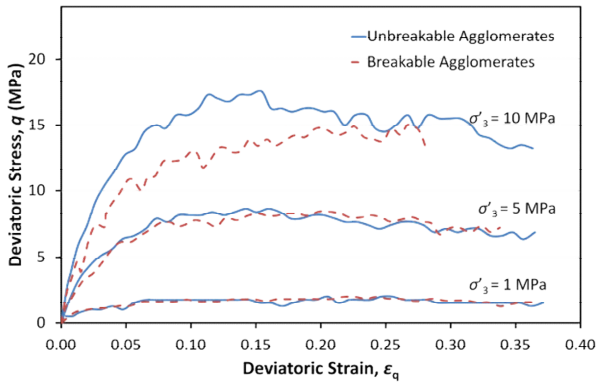

(a)

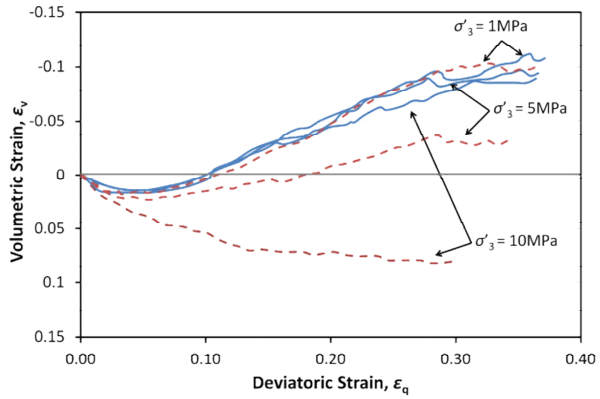

(b)

Figure 2.72 Triaxial behaviour of breakable and unbreakable agglomerates, subjected to a range of confining pressures, using a rigid cubical cell (Bolton et al., 2008)

2.6.6 Summary

The basic concepts and background of the discrete element method have been discussed, and the general workings of the software PFC3D briefly described.

As a relatively new tool, which is highly reliant on computing power, it is only quite recently that DEM simulations using moderate numbers of particles or in three-dimensions have been completed. A brief review of the available relevant literature was given, focusing first on triaxial models, which have demonstrated the necessity of flexible membranes. Modelling of bonded granular materials was then discussed, including the various methods for simulating cementation. Finally the modelling of particle breakage was reviewed, comparing the agglomerate method with directly replacing broken grains.

CHAPTER 3

DISCRETE ELEMENT MODELLING OF HIGH-PRESSURE TRIAXIAL TESTS ON CEMENTED SAND

3.1 INTRODUCTION

The high pressure triaxial apparatus has the capacity of applying confining pressures as high as 64 MPa. The apparatus features the use of flexible membranes, which often vary in thickness according to the confining pressure. Although membrane effects have been acknowledged (Henkel and Gilbert, 1952) they still allow free deformation of the specimen, and the natural failure mode to develop.

For the purpose of simulating accurate laboratory conditions, it is essential that any membrane allows the correct confining pressure to be applied while allowing free deformation. The importance of such boundaries has already been shown using DEM, as discussed in the literature review, by authors such as Cheung and O'Sullivan (2008) and Wang and Tonon (2009). However, the numerical membranes proposed were numerically complex in the case of using Voronoi diagrams, and had numerous limitations. A new triaxial model, which features an effective flexible membrane which satisfies the above two criteria, and is capable of exerting and sustaining high confining pressures is presented.

Using the software PFC3D (Itasca, 2005), this chapter aims to show that it is possible to simulate high-pressure triaxial tests on cemented sand, with cementation modelled using bonding between particles. The bond properties are explored, with their influence on the macroscopic behaviour (in particular the failure mode and volumetric dilation) presented and discussed.

3.2 TRIAXIAL MODEL

3.2.1 Specimen

The numerical specimens used in simulating triaxial tests are based on the standard size cylindrical triaxial samples, with a height of 100 mm and a diameter of 50 mm. Sand grains are represented by spherical particles, generated using the radii expansion method. This involves creating a predetermined number of particles at a size much smaller than desired, before gradually expanding them.

The sample developed in this model requires the user to specify 3 parameters: initial voids ratio e_0, coefficient of uniformity ($C_u = d_{60} / d_{10}$) and the minimum sample particle diameter (d_{min}). The sample is continuously graded, with a simplified grading curve derived from the coefficient of uniformity (C_u), similar to the method described by Potyondy and Cundall (2004). The coefficient of uniformity C_u, can also be interpreted as the gradient of the particle size distribution between these values, and for simplicity this gradient is assumed to be applicable to the full grading curve, illustrated in Figure 3.1.

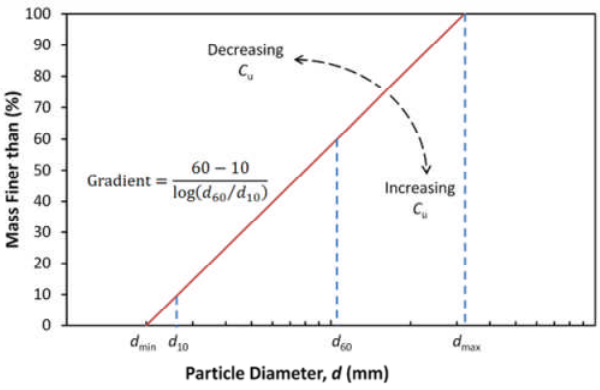

Figure 3.1 Schematic of simplified grading curve for triaxial samples

From these three parameters, the total number of required particles is calculated, and the particles are then created at random locations within the bounding cylinder, a factor of 0.2 times the required size, before being expanded over 100 increments to satisfy the desired grading. Thus for a given voids ratio and packing, the specified minimum diameter, d_{min} directly

determines how many particles are generated. The size of the smallest particle controls the numerical timestep as well as the total number of particles which in turn influences the calculation time. Varying d_{min} does not necessarily change the packing geometry; it shifts the position of the grading curve. For the following simulations, the purpose of which is to model a triaxial apparatus capable of applying high confining pressures, the continuously graded sample has a minimum particle diameter, d_{min} of 2 mm, a coefficient of uniformity, C_u of 2.0 (resembling that of Portaway sand used by Marri, 2010) and a voids ratio of 0.55. This gives a sample consisting of 6759 particles, shown in Figure 3.2.

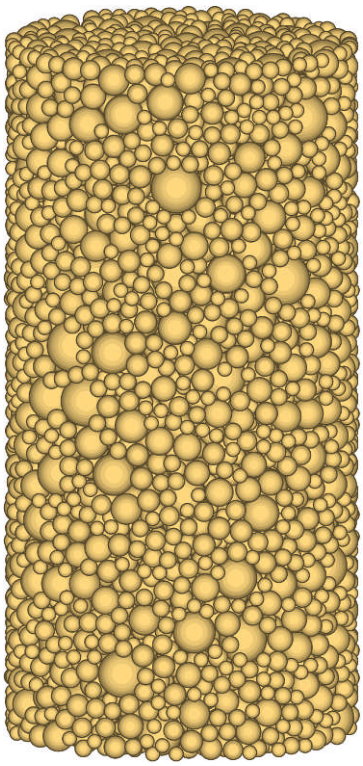

Figure 3.2 Numerical specimen, consisting of approximately 7000 particles

The linear spring contact model is used for efficiency and simplicity. Wang and Leung (2008) suggested using a normal particle stiffness of the order 10×10^6 N/m for quartz sand, and also that the same value can be used for both normal and shear stiffness. In these simulations, the sand particles were given a normal stiffness of 10×10^6 N/m, and to reduce the number of input parameters particle shear stiffness was also assigned this value. Density was set at 2650 kg/m^3, reflecting the density of the sand used in the

aforementioned laboratory experiments (Marri, 2010), and a particle friction value of 0.5 was attributed. The properties are summarized in Table 3.1.

Table 3.1 Summary of DEM properties of the triaxial sample

Triaxial Sample Properties	
Size: height x diameter (mm)	100 x 50
No. of particles	6759
Particle friction coefficient	0.5
Contact model	Linear springs
Normal stiffness, k_n (MN/m)	10
Shear stiffness, k_s (MN/m)	10
Density (kg/m^3)	2650
Coefficient of uniformity, C_u	2.0
Minimum particle diameter, d_{min} (mm)	2.00
Median particle diameter, d_{50} (mm)	4.00
Voids ratio, e_0	0.55
Wall friction coefficient	0

The numerical triaxial samples in this chapter are invariably created in relatively very dense states (e = 0.55). For the given particle size distribution, this was found to be the densest state possible using the radii expansion method while avoiding any locked-in stresses. Samples are created in such a way to avoid excessive compaction during the application of the (isotropic) confining pressure. At the pressures considered (σ_3 > 1 MPa), loose unbonded samples compact to a dense state during isotropic compression, resulting in volumetric dilation during shearing, similar to the initially dense simulations. This inability to maintain volume and resist compaction arises from the lack of irregular shape offered by the spherical particles. Loose *bonded* samples on the other hand will undergo less compaction during consolidation, with the parallel bonds maintaining the looser soil skeleton, and will demonstrate volumetric contraction upon shearing. This is in disagreement with experimental literature, in which the introduction of cement usually increases dilation. However, this phenomenon in the simulations is similar in essence to the observations made by Yamamuro and Lade (1996)—who saw the volumetric contraction begin to decrease at very high pressures. This was attributed to the excessive decrease of volume in

isotropic consolidation prior to shearing. To avoid this incongruity, samples are created as dense as possible to minimise the reduction in volume prior to shearing.

3.2.2 Flexible Membrane

The membrane developed in this study consists of a cylindrical array of bonded particles encasing the lateral boundary of the specimen, with discrete forces applied to each particle to give the effect of confining pressure. The membrane particles are hexagonally arranged; the identity of each membrane particle is known, allowing their properties to be retrieved and manipulated easily. It is important that the membrane particles are small enough to prevent penetration of the specimen particles through the membrane; however their size impacts on the calculation time, so with this in mind, the membrane particles are generated a factor of $^2/_3$ times the smallest sample particle, d_{min}.

The membrane particles are bonded using contact bonds (Itasca, 2005), the details of which were given in section 2.6.2, which transmit no moments, ensuring membrane flexibility. The bonds are defined by shear and normal tensile strengths, set arbitrarily high enough (1×10^9 N) that the membrane does not split. Contact bonds are not attributed values of stiffness; for tensile displacement, the particle stiffness is used, which is discussed in section 3.2.4.

Considering the membrane as a series of individual rows means the vertical surface area can be calculated. Each row consists of a series of particles connected in a loop. The vertical position of a given row is obtained by averaging the z-coordinates of the component particles, and the row thickness is approximated by interpolation between the position of that row and the adjacent rows (Figure 3.3), although all rows have equal thickness initially. The length of each row is obtained from summing the distance between each neighbouring row particle, obtained from their coordinates. By multiplying this length by the thickness, the vertical surface area of the row can be determined: summing for all rows gives the total vertical membrane

surface area. Repeating this process, but considering the planar area enclosed by the row (the area of the polygon created by the membrane particles) instead of the length, gives the volume (Figure 3.4).

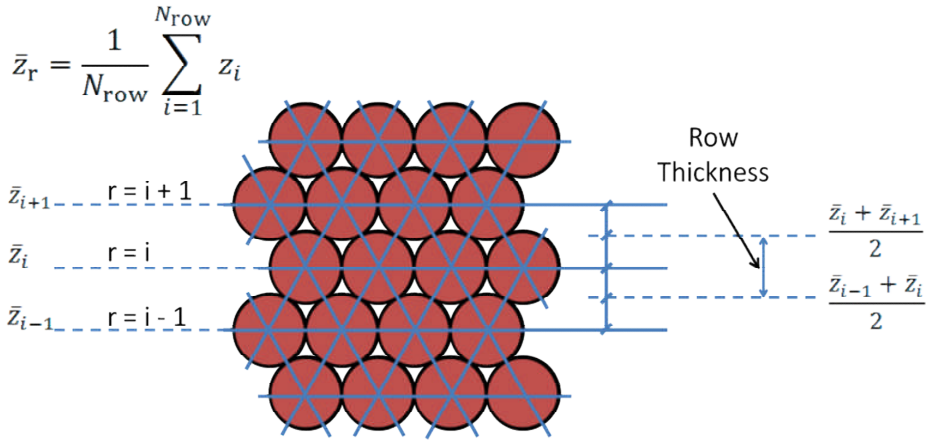

Figure 3.3 Detail showing the thickness of row *i* (consisting of N_{row} number of particles)

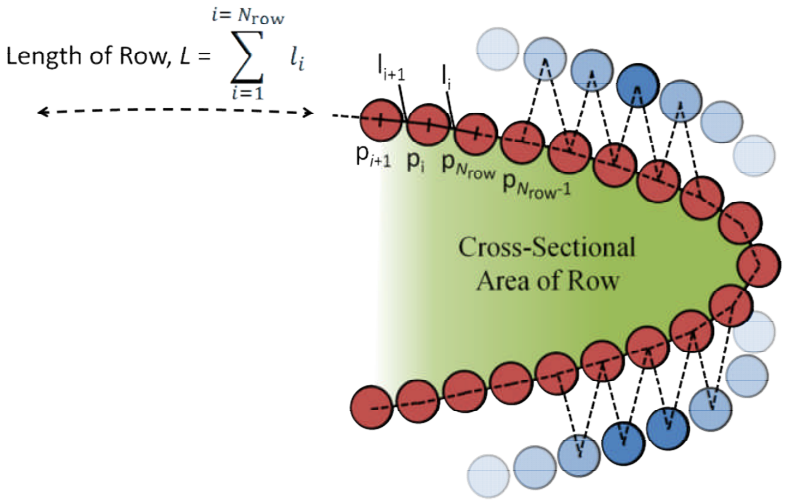

Figure 3.4 Schematic diagram illustrating the length and cross sectional area of a given row of membrane particles

For a row of membrane particles, the total horizontal force is the product of the confining pressure and vertical surface area; this force distributed equally to the particles in the row. This ensures the confining pressure is applied evenly to the specimen regardless of significant changes in shape and avoids complex calculations used by authors such as Cheung and O'Sullivan (2008). Each discrete horizontal particle force is applied in a direction normal to the

membrane surface, i.e. bisecting the line joining the two adjacent spheres, illustrated in Figure 3.5.

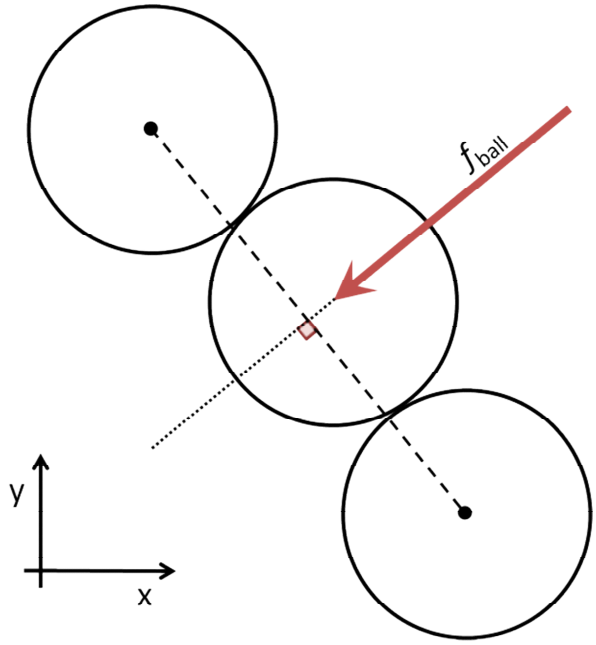

Figure 3.5 Diagram showing the direction of the horizontal component of confining pressure applied to a membrane particle

The vertical component of force necessary to give the true confining pressure has little effect on the results until large strains, however it is calculated and applied in a similar manner. If the cross-sectional area enclosed by a row of membrane particles is considered, as well as that for the row above and the row below, this gives a measurement of the local shape of the membrane, and the vertical component of confining pressure can then easily be inferred. For example, initially, the horizontal area enclosed by every row of membrane particles will be approximately 0.002 m^2 - the cross-sectional area of the sample before deformation. Because each row has the same horizontal area, this implies no vertical component of confining pressure. After deformation, considering the cross-sectional area of a given row, if the corresponding area of the row above is larger and the row below has a smaller area, this implies an upwards component of force which can be estimated from the disparity in area. The membrane extends beyond the platens by 20%, and the top and bottom loops of particles are fixed to simulate the effects of o-rings (Figure 3.6). Platen friction is set to zero. After generation of the sample and

membrane, the confining pressure is applied after which the top platen is accelerated over 100000 timesteps to a velocity of 0.05 m/s, which was deemed to be the highest value while avoiding dynamic effects.

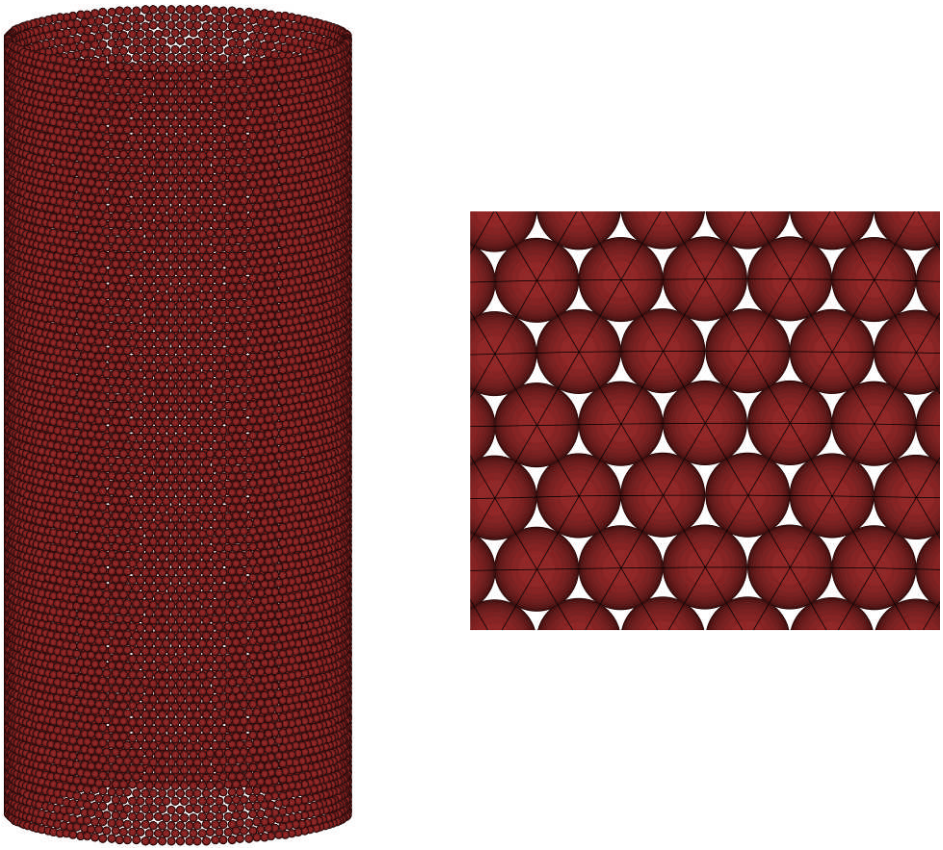

Figure 3.6 Numerical membrane consisting of bonded particles

3.2.3 Measurements

The primary variables monitored and recorded during the simulations are the deviatoric stress q, the major principal (axial) strain, ε_1 and volumetric strain, ε_v. The deviatoric stress is the difference between the major (σ_1) and minor (σ_3) principal stresses (where the major principal stress is obtained from the average stress acting on the top and bottom platens):

$$q = \left(\frac{\sigma_{\text{top}} + \sigma_{\text{bottom}}}{2}\right) - \sigma_3 \qquad [3.1]$$

although the platen velocity is kept low enough to ensure there is no significant difference between the top and bottom platen stress until significant deformation has taken place. The minor principal stress, σ_3 (which

is equal to the confining pressure in triaxial conditions), is retrieved by measuring the radial stress acting on the membrane particles or via measurement spheres (see section 3.2.4). The mean effective stress is calculated and recorded as follows:

$$p' = \left(\frac{\sigma_1 + 2\sigma_3}{3}\right) \quad [3.2]$$

The axial strain (i.e. the major principal strain in a triaxial test) is simply obtained from the vertical displacement of the top platen after confinement, Δl, divided by the original height of the specimen, l_0:

$$\varepsilon_{\mathrm{a}}(\%) = \varepsilon_1 = \frac{\Delta l}{l_0} x\ 100 \quad [3.3]$$

The volumetric strain, ε_{v} (i.e. the sum of the principal strains) is calculated from the change in volume divided by the original volume of the specimen:

$$\varepsilon_v(\%) = \varepsilon_1 + \varepsilon_2 + \varepsilon_3 = \frac{\Delta V}{V_0} x\ 100 \quad [3.4]$$

where the volume at any time is calculated using the locations of the enclosing membrane particles, as briefly detailed above (section 3.2.2). The voids ratio:

$$e = \frac{V_{\mathrm{v}}}{V_{\mathrm{s}}} \quad [3.5]$$

which is also recorded during the simulations can either be deduced from the current sample volume (V) and the volume of the particles (V_{balls}), or estimated from the voids ratios returned from measurement spheres. However, the first method doesn't account for overlaps between particles, and second method is not accurate in the case of there being individual overlaps between three or more particles. Furthermore measurement spheres only return local measurements, i.e. the voids ratio within the

measurement sphere. For this reason, the voids ratio is calculated manually by discretising the three-dimensional model space into finite-sized cells, and summing the vacant cells and those occupied by particles. The discrete cells are cubical, with linear dimensions equal to $^1/_{12}$ of the diameter of the smallest particle, d_{min}; a simplified diagram of this scheme is provided in Figure 3.7. Each cell is scanned, and if the centroid is within the radius of any sample particle, then the cell is marked as solid; cells that are not occupied by any particle are marked as being voids. The volume of the cells marked as voids are summed to give the volume of voids, V_v; likewise the cells marked as solid are summed to give the total volume of solids, V_s. The model space outside of the membrane is ignored, and the volume of voids and solids are totalled to confirm the calculation of volume outlined in section 3.2.2.

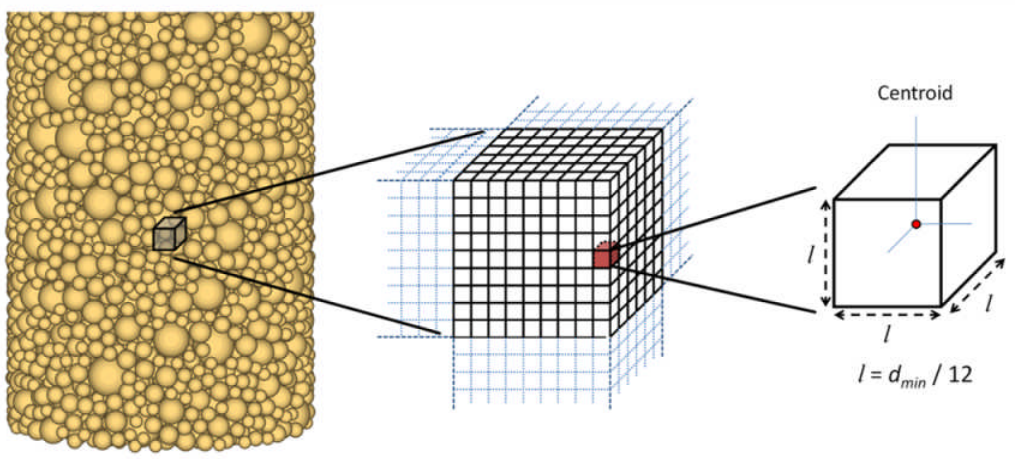

Figure 3.7 Diagram showing how the three-dimensional model space is discretised (not to scale)

The radial strain ε_r (which is equivalent to the minor principal strains) is calculated from the change in diameter of the specimen:

$$\varepsilon_r(\%) = \varepsilon_2 = \varepsilon_3 = \frac{\Delta d_{mem}}{d_{mem,0}} x\ 100 \qquad [3.6]$$

Where $d_{mem,0}$ is the original membrane diameter, and the current diameter, d_{mem} is estimated from the volume and height of the sample using:

$$d_{\mathrm{mem}} = \sqrt{\frac{4 \times V}{\pi \times l}} \qquad [3.7]$$

These enable the deviatoric/shear strain, ε_q to be calculated from:

$$\varepsilon_q = \frac{2}{3}(\varepsilon_a - \varepsilon_r) \qquad [3.8]$$

And finally, the dilatancy, *D* is recorded from:

$$D = {-\delta\varepsilon_v}\Big/{\delta\varepsilon_q} \qquad [3.9]$$

3.2.4 Properties for High Confining Pressures

Due to the standard contact model considering stiffnesses to act in series between two interacting objects, as in equation [2.47], it is not possible to calibrate the numerical membrane with laboratory conditions. If the membrane particle normal stiffness (used in tension as well as compression when bonds are used) is adjusted so that the membrane has a realistic 'elastic extension modulus' (Henkel and Gilbert, 1952), excessive overlap occurs between the membrane and the sample when subjected to high confining pressures. The membrane particles completely enter the specimen, disappearing and causing sand particles to escape, as shown in Figure 3.8. Using an artificially high stiffness to prevent this leads to unwanted hoop tension being induced when the specimen expands.

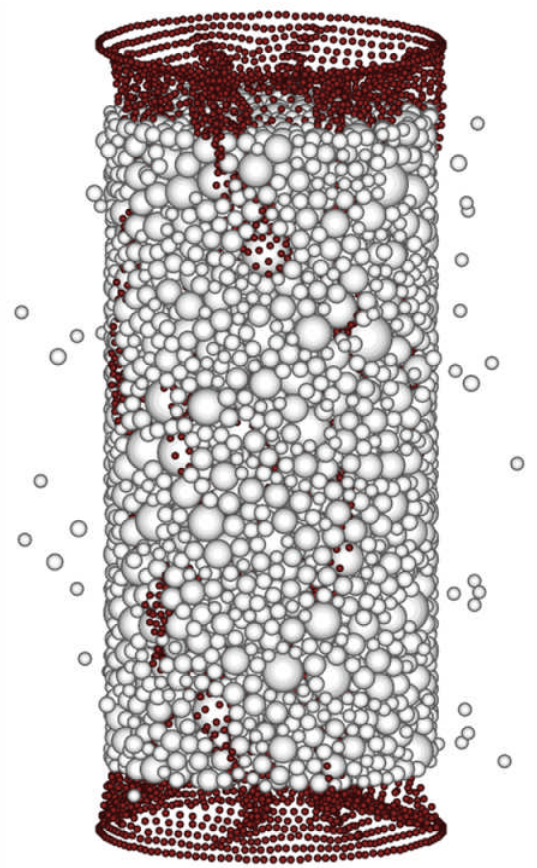

Figure 3.8 Failure of the membrane due to low particle stiffness causing excessive overlap

Additionally, the contact normal stiffness is important for particle interaction within the membrane; if the bonded membrane particles are given a high compressive stiffness and low tensile stiffness (user-defined contact model), the particles don't stay aligned. Because of the high pressures, the discrete forces applied to the membrane particles are large enough to render the resistance to tensile displacement between bonded particles negligible; the membrane particles slide apart and behave as if unbonded, demonstrated in Figure 3.9.

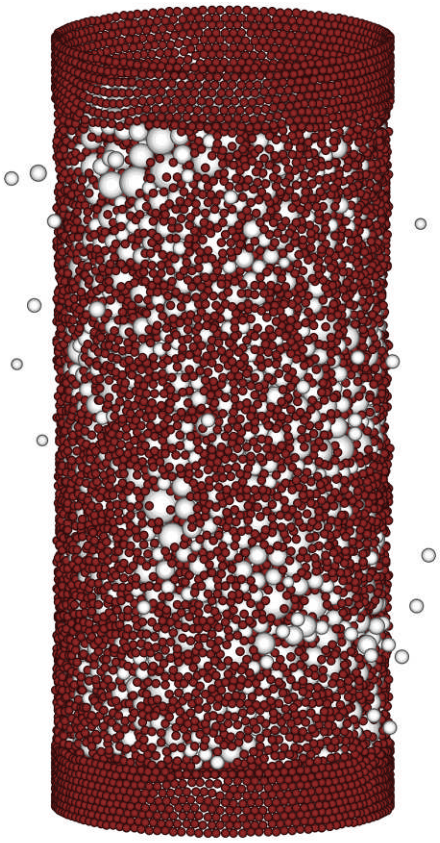

Figure 3.9 Failure of the membrane due to particles not staying correctly aligned

To avoid a complex user-defined contact model, the membrane particles are given artificially high stiffnesses (for the duration of the simulations), with a system in place to adjust the radii of certain membrane particles relieving the unwanted hoop tension. As the specimen begins to deform the material typically expands; as the membrane stretches, rows of membrane particles will cover an increased length, accommodated by tensile displacement between the bonded membrane particles. For each row, the mean displacement between neighbouring particles is monitored, and if this exceeds 1% of the particle radius, then all the particles in the row are expanded, alleviating the associated forces and avoiding unwanted pressure. The value of 1% means the radii are only expanded by 0.5% at a time, ensuring a gradual process with no sudden overlaps.

Any value of stiffness above a threshold proportional to confining pressure can be attributed to membrane particles to prevent them entering the sample. This value is determined by trial and error; for the membrane

described earlier and a confining pressure of 12 MPa, the minimum required value of stiffness is 0.6 MN/m, which is sufficient to prevent membrane particles sliding apart from one another. Lower values cause the membrane to fail at high strains, while higher values have no effect on the results. The details of the membrane parameters are given in Table 3.2.

Table 3.2 Summary of DEM parameters for the triaxial membrane

Triaxial Membrane Properties	
No. of particles	11979
Friction coefficient	0
Contact model	Linear springs
Normal stiffness, K_n (MN/m): e.g. for σ_3 = 12 MPa	0.6
Shear stiffness, k_s (MN/m): e.g. for σ_3 = 12 MPa	0.6
Density (kg/m^3)	1000
Particle diameter, d_0 (mm)	0.67

The minor principal stresses are checked using 'measurement spheres' (a function of the software) to ensure the confining pressure is being applied correctly. Measurement spheres are able to return the stress tensors for specified spherical volumes. Several are used, throughout the height of the specimen, as large as possible without protruding outside the sample. Using the sample depicted in Figure 3.2 (described by the properties in Table 3.1), the membrane's ability to maintain a constant pressure can be demonstrated. The results of two simulations sheared under confining pressure of 1 MPa are shown in Figure 3.10. Both have the same membrane (Figure 3.6, Table 3.2); one alleviates hoop tension by the method described, the other allowing hoop tension to be induced. The simulation which alleviates hoop tension by expanding particles ensures a constant minor principal stress; the alternative simulation displays an increasing value, with the rate of increase determined by the membrane particle stiffness. This effect is also visible in the higher value of deviatoric stress. The minor principal stresses are checked for all simulations, and in any case never deviate more than 5% from the applied pressure in the simulations with no hoop tension.

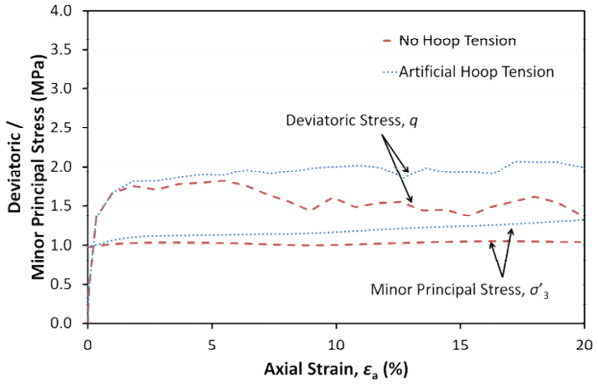

Figure 3.10 Minor Principal stress and deviatoric stress versus axial strain for unbonded samples sheared at 1 MPa confining pressure

For the simulation with constant confining pressure (i.e. alleviating additional hoop tension), increasing the membrane particle stiffness further has a negligible effect on the results. Increasing the membrane particle size reduces the number of contacts between the membrane and the specimen, and if large enough can lead to specimen particles penetrating the membrane. Giving the membrane particles friction leads to a slight increase in peak stress, although further work is needed to fully clarify the role membrane friction plays in laboratory tests.

3.2.5 Failure Behaviour

As a prelude to modelling cemented sand, but primarily to demonstrate brittle deformation and the ability of the flexible boundary to accommodate various potential failure modes, a series of simulations featuring a bonded granular material have been conducted across a range of confining pressures.

As shown extensively in the literature review, there has been much experimental work on cemented sand; in which there have been categorised failure modes: brittle failure/shear planes for cemented samples, and barrelling failure for equivalent uncemented samples. An increase in confining pressure suppresses the effects of cementation and causes a transition from brittle to ductile behaviour.

The sample particles are bonded using parallel bonds (details provided in section 2.6.2), which have been used in previous studies such as Potyondy

and Cundall (2004), and Wang and Leung (2008). These consist of a finite-sized cylindrical piece of material between the two particles, which acts in parallel with the standard force-displacement contact model. The bonds are defined by normal and shear stiffness (stress/displacement), normal and shear strength (stress) and size.

A detailed exploration of the parallel bond input parameters is given later in the section on modelling cemented sand (3.3). For the purpose of these simulations however, the parallel bond size, d_{bond} is set equal to the minimum sample particle size, i.e. $d_{bond} = d_{min}$. Parallel bond stiffnesses have been defined to give values equal to the particle stiffnesses (in terms of force/displacement) in pure tension and shear. The bond strengths have been defined as 15.92 N/mm^2 so as to give strengths of 50 N also in pure tension or shear. The same numerical sample is used, and parallel bonds are installed at existing contacts between particles before the sample is subjected to confinement, resulting in approximately 17000 bonds.

The use of bonds causes a peak deviatoric stress to appear and increases the maximum stress; varying the magnitude of the bond strength changes the maximum stress and prominence of the peak. Figure 3.11 shows the triaxial results for the same bonded material sheared at 1, 4, 8 and 12 MPa confining pressures. Increasing the confining pressure leads to a higher maximum deviatoric stress, comparable to experimental data in Figure 2.18 (Marri, 2010). The strain associated with the maximum stress increases with confining pressure. The peak is much more prominent at lower pressures, becoming less distinguished at 12 MPa. There is a transition from brittle to ductile behaviour, with the effects of the bonds being suppressed by increasing confinement. The dilation also decreases with increasing confining pressure.

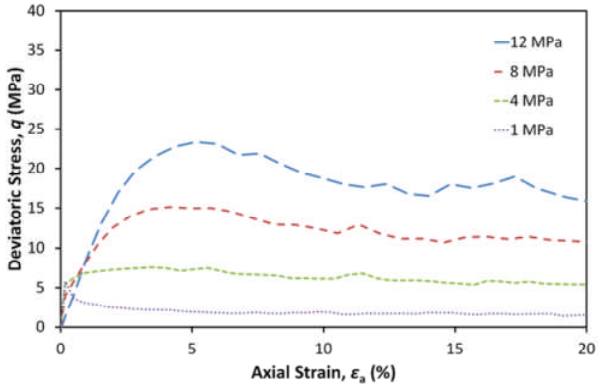

(a)

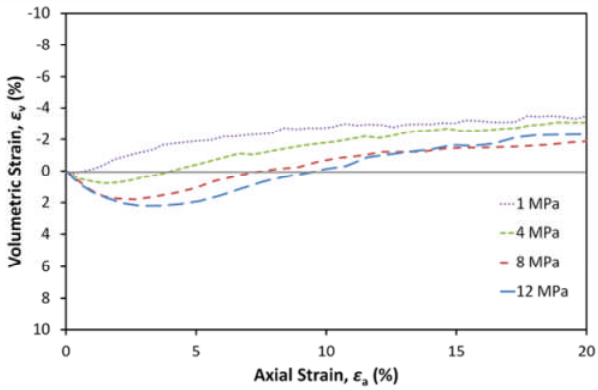

(b)

Figure 3.11 Triaxial response of bonded material sheared across a range of confining pressures

The flexibility of the membrane is demonstrated by observing the failure modes after deformation. Cemented specimens sheared at relatively low confining pressures have been shown to exhibit shear planes (e.g. Figure 2.9), while uncemented specimens, or cemented specimens sheared at high confining pressures demonstrate barrelling (Marri, 2010). This contrast in behaviour in the numerical samples is best observed by plotting particle rotations. Figure 3.12 shows the particle rotations on a vertical plane at 1 and 12 MPa confining pressures, at the point of maximum rate of dilation (1.0% and 7.5% axial strain respectively). No clear shear plane is visible at 12 MPa, whilst there is a prominent shear plane visible at 1 MPa. The samples sheared at higher pressures display the correct barrelling failure and in between these pressures there is transitional behaviour. Without a flexible membrane, the formation of these failure modes would be inhibited, as shown by Cheung and O'Sullivan (2008).

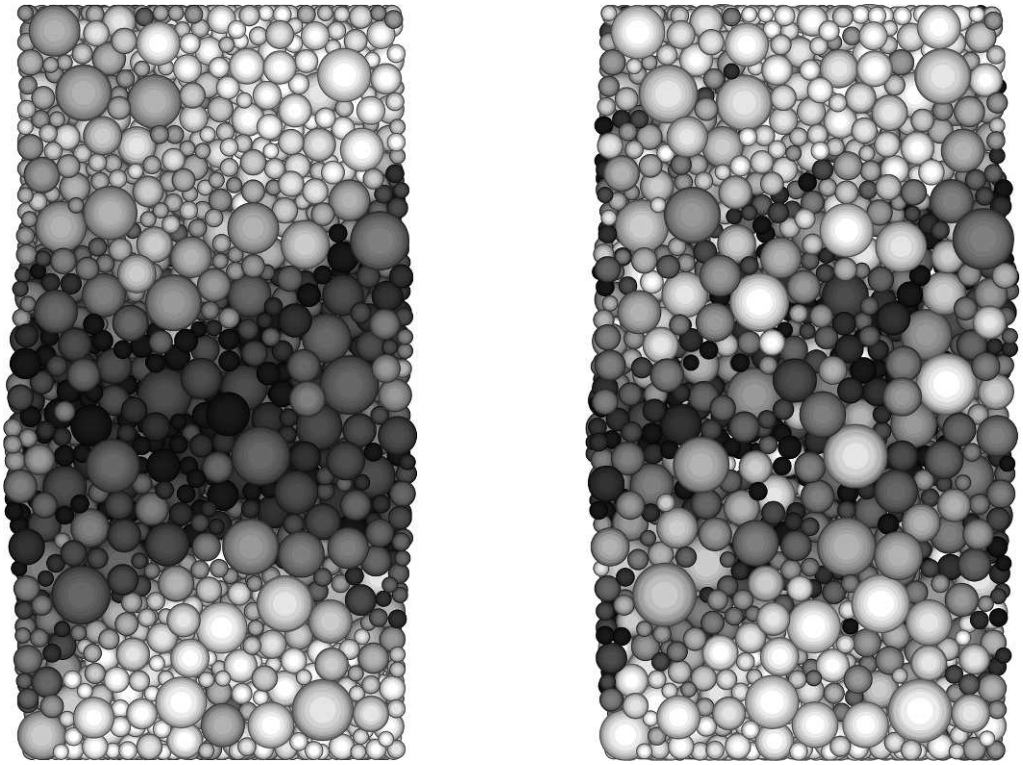

(a) (b)

Figure 3.12 Images displaying particle rotation at maximum rate of dilation: 1 MPa confining pressure (a), and 12 MPa confining pressure (b). Dark greyscale indicates particles which have undergone the most rotation; white denotes the least.

These simulations highlight the ability of the developed triaxial model to accommodate various failure modes. The membrane is capable of applying a high, constant confining pressure while exhibiting a non-uniform shape as the sample distorts. The flexible boundary also allows the vertical component of confining pressure to be applied to the specimen.

3.3 TRIAXIAL SHEARING OF CEMENTED SAND

3.3.1 Sand

Most of the current literature modelling cemented sand using DEM has been limited to two dimensions, for example Jiang et al. (2005, 2006) Wang and Leung (2008), Utili and Nova (2008), Camusso and Barla (2009), with very limited material in three dimensions.

The sand used as the basis of the following simulations is Portaway sand (full details of which can be found in Wang, 2005), the sand used in experiments by Marri (2010) using the high-pressure triaxial system at the University of Nottingham. The sand particles are modelled as described in the previous section (details provided in Table 3.1), with parameters chosen to reflect those of the real sand. The notable difference is the particle size—the numerical sample having a median grain size, d_{50} of 4.0 mm, as opposed to a size of 0.4 mm for Portaway sand. This artificially large value gives a total number of particles in the specimen of 6759, which although is not realistic, is larger than the number of particles used in most of the aforementioned literature on DEM (typically less than 2500). However, having a smaller size and greater quantity of particles results in an impractical simulation length, and considering the size and number of particles required for the membrane, 6759 was deemed acceptable. As before, platen friction was set to zero, and after confinement was applied, the top platen was accelerated gradually to 0.05 m/s. The numerical and experimental particle size distributions are visible in Figure 3.13.

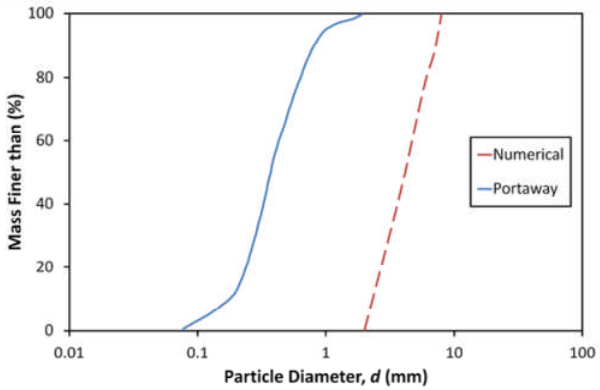

Figure 3.13 Particle size distributions for both Portaway sand and the numerical sand specimen

3.3.2 Inter-Particle Bonding

The high-pressure triaxial tests performed by Marri (2010), which will be used as the benchmark for modelling cemented sand in DEM, used Portland cement as the bonding agent. Following on from section 3.2, cement bonds are modelling using the parallel bond feature of the software (section 2.6.2;

Itasca, 2005). To recap, these are defined by normal and shear stiffness (in terms of stress/displacement), normal and shear strength (in terms of stress) and size.

With regard to the literature, it is somewhat unclear how to simulate the size of cement bonds. One might consider them as small relative to the particles, occurring just at the contacts and independent of particle size, or alternatively to consider them as proportional to the particles, filling much of the void space. Both of these approaches seem justifiable depending on interpretation of the nature of cementation and analysis of images. Initially, in order to isolate and investigate bond strength distributions, all bonds are created with equal size; the bond diameter, d_{bond} is set equal to the smallest specimen particle, i.e. $d_{bond} = d_{min}$ (unless stated otherwise). This gives all bonds the same moment resistance. To clarify, parallel bond stiffnesses have been defined to give values equal to the particle stiffnesses (in terms of force/displacement), except where mentioned—this is to reduce the number of variables, and because the current simulations are not exclusively concerned with calibration against physical tests. The influence of parallel bond size is explored later in section 3.3.4, which investigates modelling an increasing degree of cementation.

Bonds are installed at existing inter-particle contacts. For the dense arrangement of particles with the parameters described above, and shown in Figure 3.2, this method installs approximately 5 bonds per particle, and leaves a small number (4%) of free particles with no bonds. This is a result of the simulations having no gravity; if gravity was applied, there would be less 'floating' particles, although no significant effects on the results. A series of simulations have been conducted to investigate solely the bond strength distributions, using a triaxial sample with approximately 17000 parallel bonds—meaning each particle has an average of 5 neighbouring particles bonded to it.

The principal effects of the parallel bonds are evident in Figure 3.14 where the deviatoric stress, volumetric strain, and remaining bonds versus axial strain responses are shown from simulations of the cemented material showing the effects of varying strength, along with the behaviour of the uncemented sample all sheared under a confining pressure of 1 MPa. The bonded samples have completely uniform bonds, i.e. there is no strength distribution. All bonds are equal in size, stiffness and strength in each test, with only the bond strength varied across the three simulations. The three different parallel bond strengths have been defined as 7.96, 15.92 and 31.83 N/mm^2, to give strengths of 25, 50 and 100 N respectively in pure shear and tension.

It is immediately evident that the introduction of cement bonds with strengths 50 and 100 N cause a large peak deviatoric stress to appear and increases the maximum stress compared to the unbonded sample. The simulation with bonds of strength 25 N has a smaller peak stress, with almost all the bonds breaking soon upon commencement of shearing, after which behaviour similar to the uncemented sample is observed. The peak stress witnessed in the cemented simulations is caused by the presence of bonds, with the peak appearing to coincide with the onset of major bond breakage. All bonded samples exhibit a stiffer initial response compared to the unbonded equivalent. The cemented samples approach the stress state of the uncemented simulation as the bonds eventually become broken down, and the material becomes destructured. Inspecting the graphs of volumetric strain versus axial strain shows that the most strongly bonded sample undergoes slightly more dilation than the other simulations.

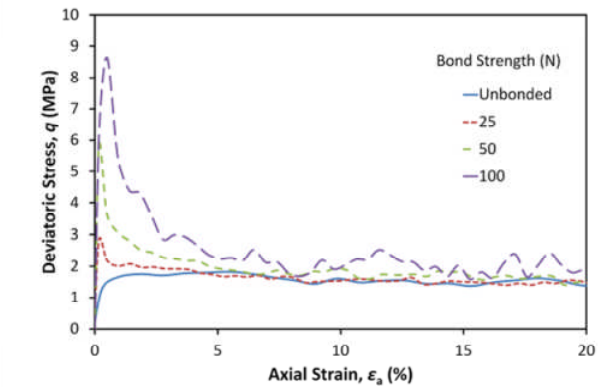

(a)

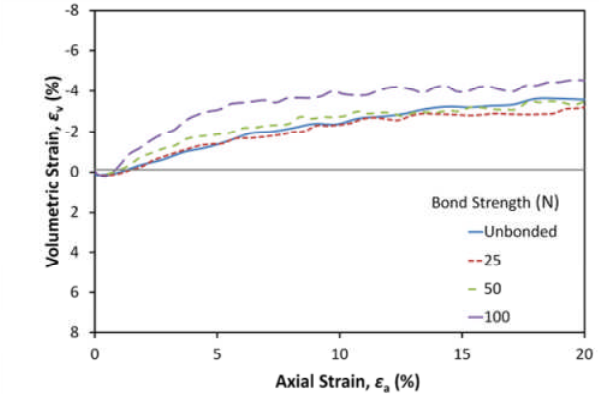

(b)

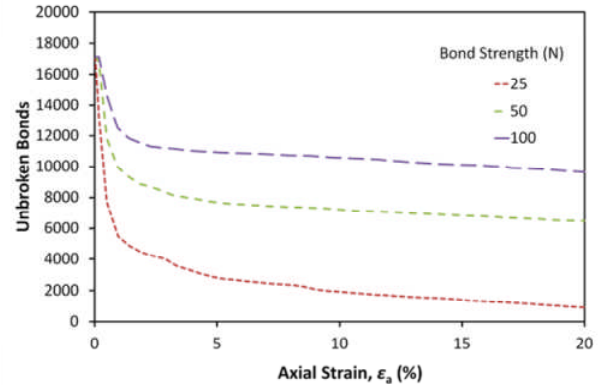

(c)

Figure 3.14 Stress-strain behaviour of simulations with various bond strengths: deviatoric stress (a), volumetric strain (b) and unbroken bonds (c) versus axial strain

Figure 3.15 shows the deviatoric stress, volumetric strain, and remaining bonds versus axial strain responses from simulations of the cemented material with varying bond stiffness, alongside the unbonded sample (sheared under a confining pressure of 1 MPa). The bond stiffnesses are varied by the same magnitudes as the strengths above: normal and shear stiffnesses of 5, 10, and 20 x 10^6 N/m are used. The differences resulting from varying bond stiffnesses are less pronounced, with very similar peak values of

stress and dilation. The simulation with the stiffest bonds has the slightly lower peak strength, and the fewest bonds remaining after shearing. The increased stiffness causes the bonds to break earlier, and therefore fewer remain to resist deformation.

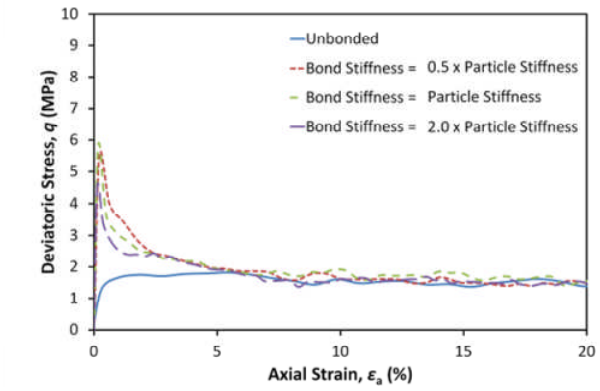

(a)

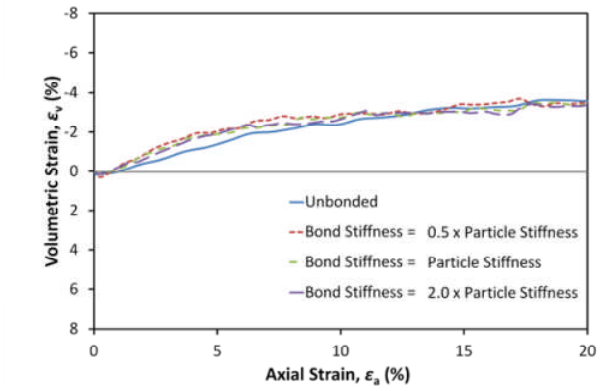

(b)

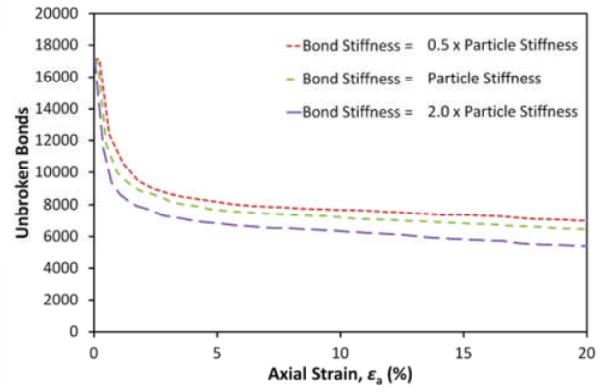

(c)

Figure 3.15 Stress-strain behaviour of simulations with different bond stiffnesses: deviatoric stress (a), volumetric strain (b) and unbroken bonds (c) versus axial strain

3.3.3 Bond Strength Distributions

From considering the figures in the last section, in particular Figure 3.14, the bond uniformity is reflected in the graphs; the very sharp peak indicates extremely brittle failure and rapid onset of bond breakage. It is apparent from the graph that there is initially a linear relationship between deviatoric stress and axial strain, during which no bonds have broken, particularly for the 100 N bond strength. This seems somewhat unrealistic, especially at these stress levels. It is evident from the literature (e.g. Airey, 1993; Asghari et al., 2003; Lo et al., 2003) that one might expect such a sharp peak with an initially linear response at very low pressures (typically under 100 kPa), however as is visible in the work of Asghari et al. (2003) or Marri (2010), in Figures 2.14, 2.17 and 2.18 respectively, no sharp peaks or such brittle behaviour is witnessed at higher pressures, with only the highest cement content producing a rounded peak. In other words, the yielding of bonds occurs before failure, and a curve characteristic of type 2 in the schematic given in Figure 2.11 is expected. One might therefore assume that a distribution of bond strengths would yield more realistic results, i.e. a more rounded peak stress with gradual bond failure. This echoes the sentiment of Camusso and Barla (2009), who declared that a combination of weak and strong bonds are required for realistic behaviour. Figure 3.17 compares the results of cemented simulations with the same initial setup as the previous, but with parallel bond strengths satisfying three different probability distributions: uniform, normal and Weibull—the probability density functions are given in Figure 3.16.

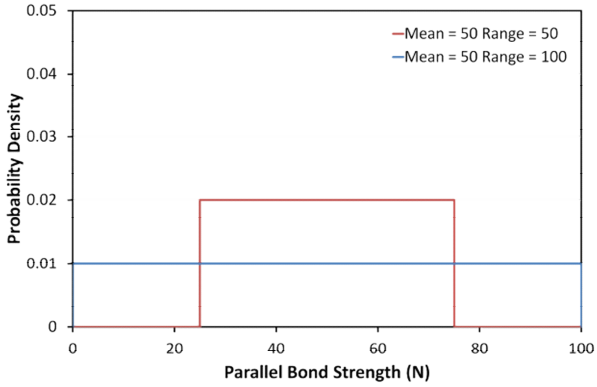

(a)

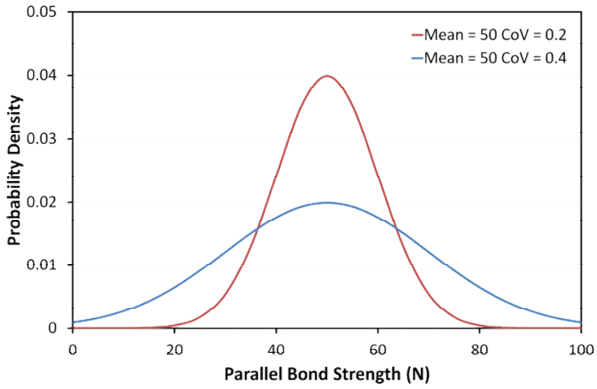

(b)

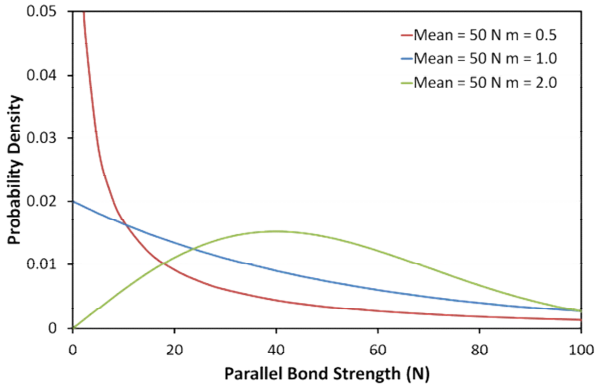

(c)

Figure 3.16 Probability density functions of the various uniform (a), normal (b) and Weibull (c) distributions used for parallel bond strengths

Figures 3.17(a) and 3.17(b) show the deviatoric stress response of samples with bond strengths satisfying two alternative uniform distributions and two normal distributions, all with the same mean strength of 50 N. The bonds with uniformly distributed strengths have ranges of 50 and 100 N, and the normally distributed bonds have coefficient of variations of 0.2 and 0.4. Also included is the response of the simulation with completely uniform bonds with unique strength of 50 N, as well as the unbonded simulation.

It can be seen that the samples with uniformly distributed bond strengths show lower maximum stresses, with the peaks more rounded. The sample with bond strengths ranging from 0–100 N experiences bond breakage immediately, and as such has the lowest and most rounded peak deviatoric stress. The simulation with the narrower range, i.e. bond strengths ranging from 25–75 N has a finite minimum bond strength, so there will be an initial linear region during which no bond breakage is witnessed.

The samples with normal bond strength distributions give similar stress-strain results, despite exhibiting slightly different bond breakage. The simulation with the smaller coefficient of variation behaves very similarly to the sample with no strength distribution, while the sample with the larger coefficient displays an earlier, less sudden onset of breakage. However, both the simulations with uniform and normal bond strength distributions still display sharp distinct peak stresses, indicating sudden failure due to most bond strengths lying close to the mean value. All of these simulations display approximately the same volumetric strain during shearing.

Figure 3.17(c) shows the results from 3 simulations with bond strengths from Weibull distributions, all with the same mean value but with differing distribution parameters. A Weibull distribution (as described in section 2.5.2) is defined by two variables: the modulus, *m*; and a characteristic value of the variable that determines the scale of the distribution, denoted at this juncture as F_0 (which is the value of bond strength such that 37% of bonds are stronger). The modulus determines the shape of the distribution; the parameter F_0 determines the size/range. The mean of a Weibull distribution is given by:

$$F_{\mathrm{m}} = F_0 \Gamma\left(1 + {}^{1}/_{m}\right) \qquad [3.10]$$

and so is affected by both parameters; Γ is the gamma function. Changing the modulus (shape) of a Weibull distribution slightly alters the mean, so the scale of the distribution needs to be adjusted to maintain the same mean. For a

given scale, F_0, increasing the modulus results in a narrower distribution (shown earlier in Figure 2.38). Weibull probability is used widely in materials science, especially in failure probability of brittle materials, so it seems reasonable that such a distribution of strengths may be applicable to cementation. It has also been used in the field of geomechanics, in particular particle breakage, for example McDowell & Amon (2000) and McDowell (2001).

Examining the results of the various Weibull distributions of bond strengths reveals that the lower the modulus, the more rounded the peak stress. A higher value of m—i.e. the simulation with $m = 2$—renders the distribution and behaviour of the bonded sample similar to that with a normal distribution of strengths. A lower value of m—i.e. less than or equal to 1—produces a positively skewed, very wide distribution of strengths. It can be seen that the sample with a modulus $m = 0.5$ produces a rounded peak stress, which appears the most similar to the experimental stress-strain curves at high pressures shown in Figure 2.17 or Figure 2.18 from Marri (2010). The simulation exhibits a yield point prior to peak failure, much like work reported in the literature (e.g. Lagioia and Nova, 1995; Asghari et al., 2003). This indicates a much less sudden onset of bond breakage, which is also apparent from the graph displaying the number of intact bonds versus axial strain. Although a significant number of bonds are broken during consolidation, the maximum rate of breakage during shearing is slightly lower.

The full triaxial results for the Weibull simulations are shown in Figure 3.18, which also shows the volumetric strain versus axial strain, and the number of intact bonds versus strain. The simulation with the lowest m value demonstrates the most dilation and also the fewest remaining bonds for a given axial strain, a different trend to that in Figure 3.14(a), where the greatest dilation is associated with the *largest* number of intact bonds after shearing. This suggests that for the simulation with a Weibull modulus of 0.5, although fewest bonds remain, the bonds that do remain heavily influence the behaviour. For the simulation with $m = 0.5$, after shearing (20% axial

strain) the remaining bonds (approximately 2000) have a mean strength of 256 N covering a range of 2992 N. In contrast, the simulation with m = 2.0 has approximately 4200 bonds remaining with a mean strength of 63 N covering a range of 158 N.

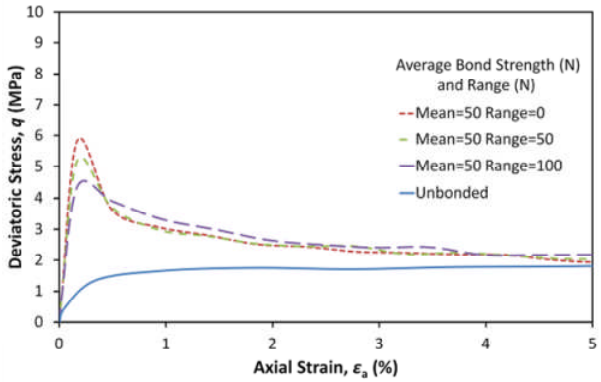

(a)

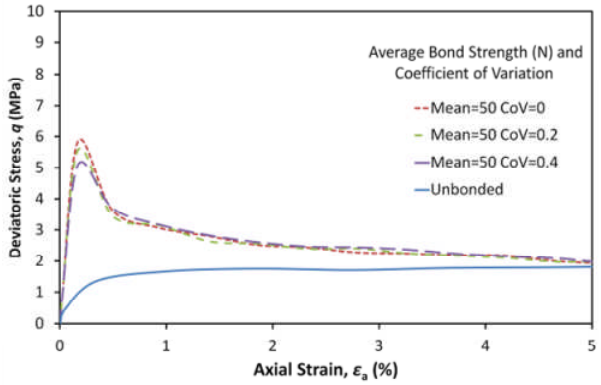

(b)

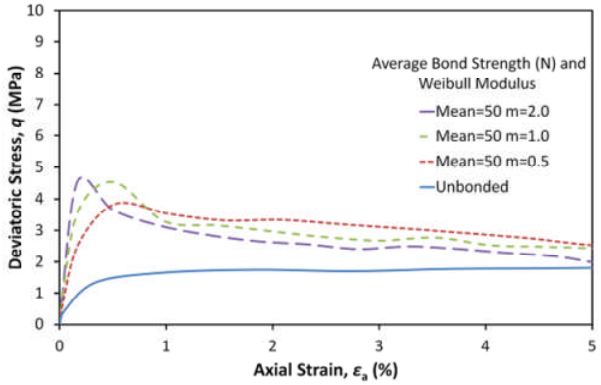

(c)

Figure 3.17 Deviatoric stress versus axial strain for simulations with various uniform (a), normal (b) and Weibull (c) bond strength distributions, with mean strength of 50 N

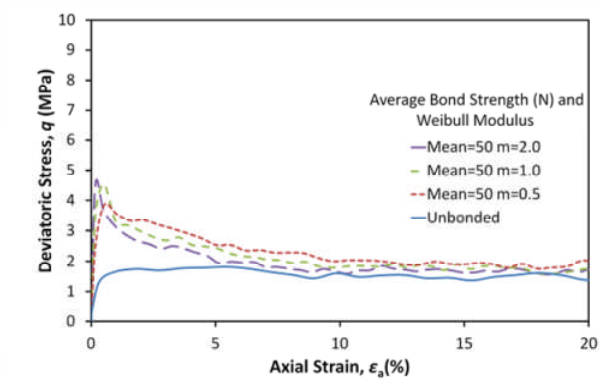

(a)

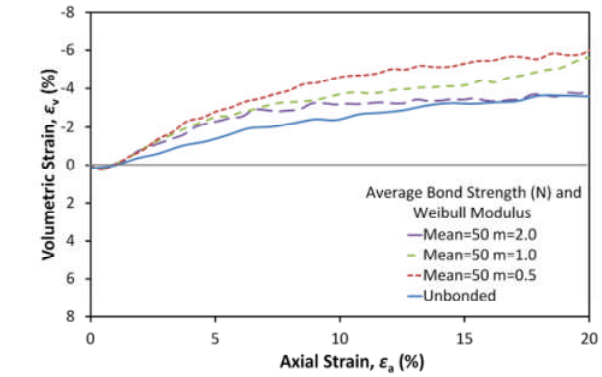

(b)

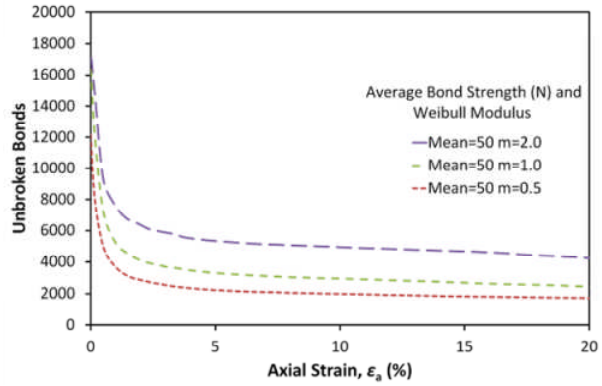

(c)

Figure 3.18 Triaxial behaviour of simulations with Weibull bond strength distributions with various m values: deviatoric stress (a), volumetric strain (b) and remaining unbroken bonds (c), versus axial strain

Figure 3.19 shows histograms for the bond strength distributions for the three simulations with Weibull moduli 0.5, 1.0 and 2.0, before and after shearing. Figure 3.19(a) shows the three histograms before consolidation, before any bonds have broken. Most bonds in the simulation with m = 0.5 have strengths between 0 and 40 N, whereas in the simulation with m = 2.0, most bond strengths lie around the mean value of 50 N. Although some bonds

break during consolidation, most breakage occurs at the start of shearing, as demonstrated by the plots in Figure 3.18(c). Figure 3.19 shows histograms plotting the residual bond strengths after shearing to approximately 20% axial strain, in which the difference in the quantity of remaining bonds can also be observed. While the simulation with m = 2.0 (narrower distribution of strengths) has a *greater* number of unbroken bonds remaining, the remaining bonds in the simulation with m = 0.5 are significantly *stronger*—there are a large portion of bonds remaining with strengths over 500 N, and almost all of the weaker bonds have yielded. This suggests that it is the strength of the *strongest* bonds that most influence the behaviour.

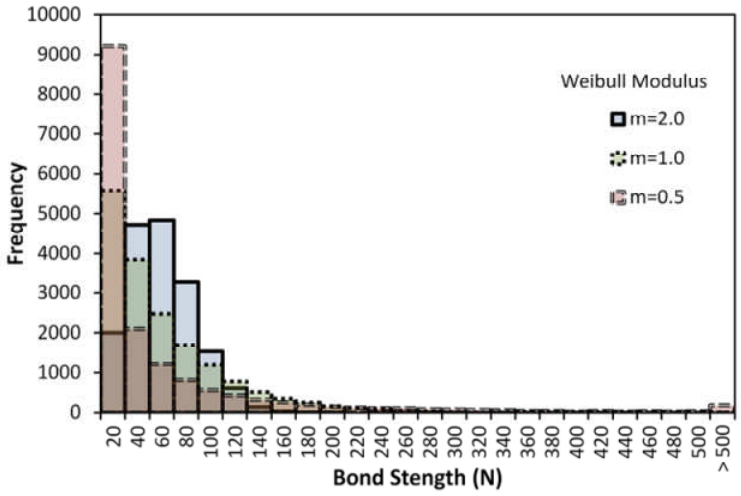

(a)

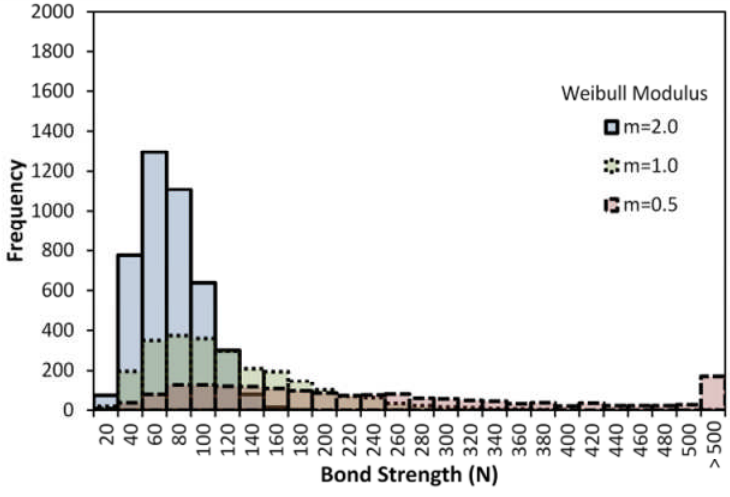

(b)

Figure 3.19 Histograms showing the character of bond strength distributions before (a) and after (b) triaxial shearing

Inspecting the sheared samples reveals contrasting patterns of breakage; the simulation with the wider range of bond strengths (m = 0.5) shows intact bonds distributed throughout the height of the sample, while the opposing specimen with m = 2.0 displays localised bond breakage, with most of the remaining intact bonds located close to the platens (Figure 3.20). During shearing, it tends to be the particles in the middle of a given specimen that will undergo the most displacement, and the images suggest that for the sample with a narrow range of bond strengths (m = 2.0), the bonds offer little resistance to this deformation, with almost no bonds remaining around the middle. For the sample with the much wider distribution (m = 0.5), fewer total bonds remain unbroken however there are still bonds distributed throughout the height of the sample, which offer most resistance to shear deformation, hence the higher dilation. This reveals that it is the strongest bonds which control the dilatation of the material. Groups of particles bonded together in 'clusters' exist, which behave as larger, irregular shaped particles, effectively changing the grading—similar to laboratory observations mentioned previously.

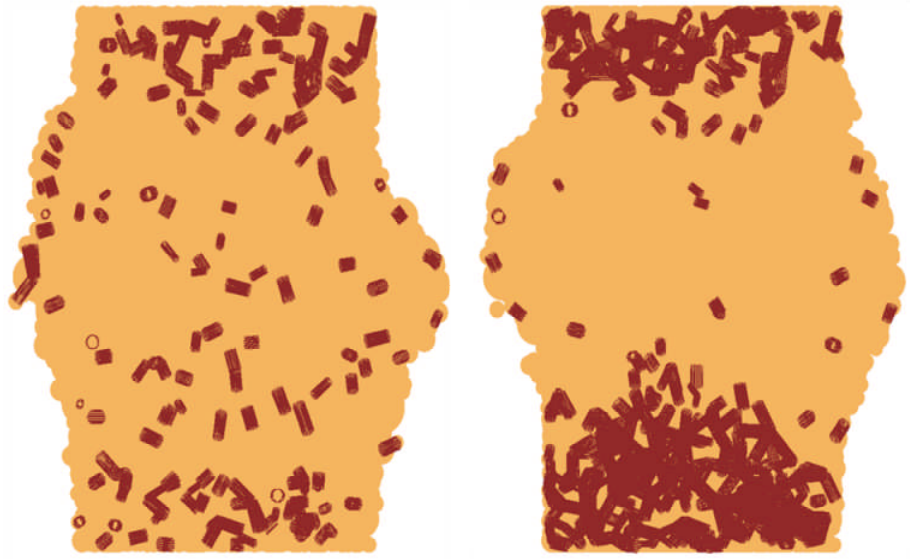

(a) (b)

Figure 3.20 Diagrams showing remaining unbroken bonds on a cross-sectional plane through the sample after 20% axial strain: sample with Weibull bond distribution with (a) m = 0.5 and (b) m = 2.0

3.3.4 Cement Content

There are potentially numerous ways in which one may consider simulating an increasing degree of cementation. Analysis of experimental data could suggest altering the variation or magnitude of bond strengths and stiffness, or various combinations thereof, while physical analysis may suggest altering the quantity of bonds and/or bond size.

The effects of increasing the magnitude of bond strength have been shown previously in Figure 3.14. While there is an increase in peak strength, there is little effect on the volumetric behaviour, and increasing the bond strength increases the strain at which the peak occurs, contrary to real behaviour. If the bond stiffness alone is increased (Figure 3.15), this causes a slight decrease in the axial strain to the peak strength, however the peak stress is decreased, and there is little effect on the amount of dilation. Figure 3.21 highlights the effects of increasing the size of the parallel bonds. It shows the simulation from earlier where the parallel bonds have a strength of 50 N and are equal in diameter to the smallest sample particle, d_{min}, and a simulation using parallel bonds with a strength of 50 N and diameter equal to 2 x d_{min}. If larger bonds are installed, the correct increase in dilation is observed, however there is very little change in the peak strength, and no effect on the specimen's initial stiffness. The increase in dilation is likely due to the increased moment resistance offered by the bonds, which hinders particles rolling over one another.

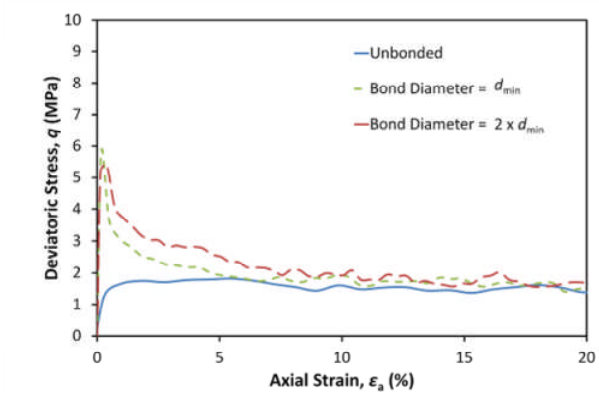

(a)

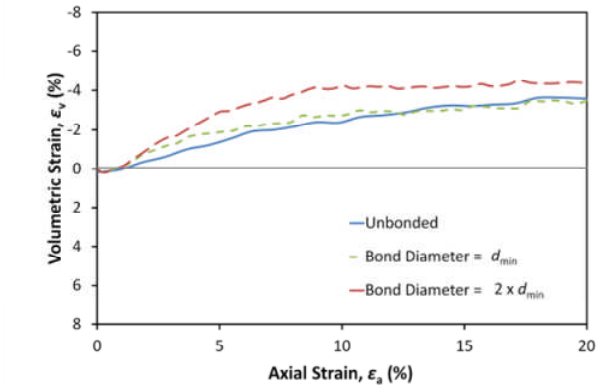

(b)

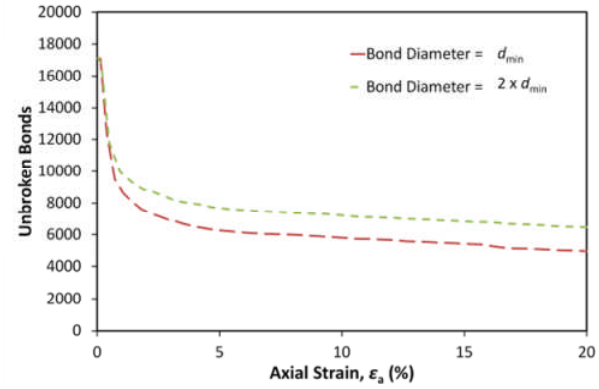

(c)

Figure 3.21 Triaxial behaviour of a simulation with standard bond size (equal to the diameter of the smallest particle, d_{min}), and a simulation with larger bond size (equal to double the diameter of the smallest particle)

If one considers the quantity of bonds, it appears common practise when modelling bonded granular materials to install bonds at existing inter-particle contacts (e.g. Potyondy and Cundall, 2004; Wang and Leung, 2008). For the dense sample described above, this method installs approximately 5 bonds per particle and leaves a small number of free unbonded particles. Considering that the numerical sample has an approximately equal coefficient

of uniformity and a density approximately equal to those values of the material from the results by Marri, shown in Figure 2.17, this configuration of bonds can be considered analogous to a given material, i.e. Portaway sand with 5% cement content.

Visually inspecting SEM images of the cemented sand shown in Figure 3.22 evidently suggests that a greater number of bonds are required to accurately represent varying levels of cementation. The cement can be seen to fill voids and connect particles which otherwise would not be in contact. Inspecting the figure which shows a specimen with 5% cement content, a typical sand particle visibly has 5 or 6 surrounding particles bonded to it, whereas a sand particle in the specimen with 15% cement content appears to have typically more—as many as 9 bonded to it which are visible. Bearing in the mind the planar nature of the images, one could expect a particle not on the surface of a cemented specimen to have an even greater number of surrounding particles bonded to it.

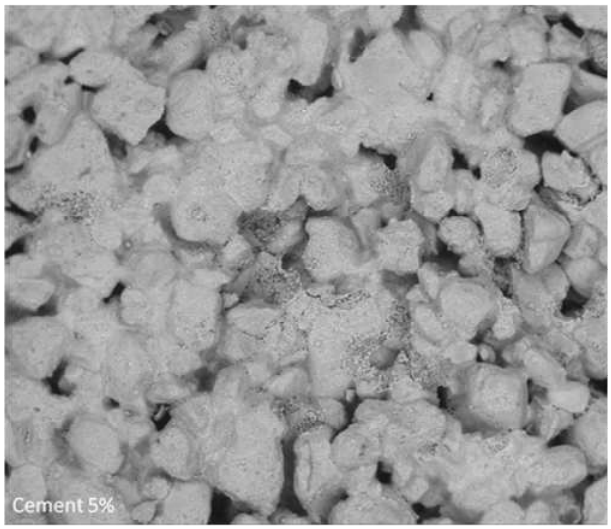

(a)

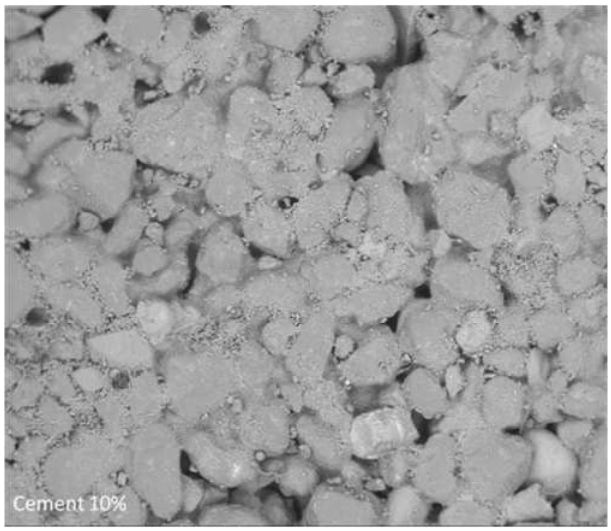

(b)

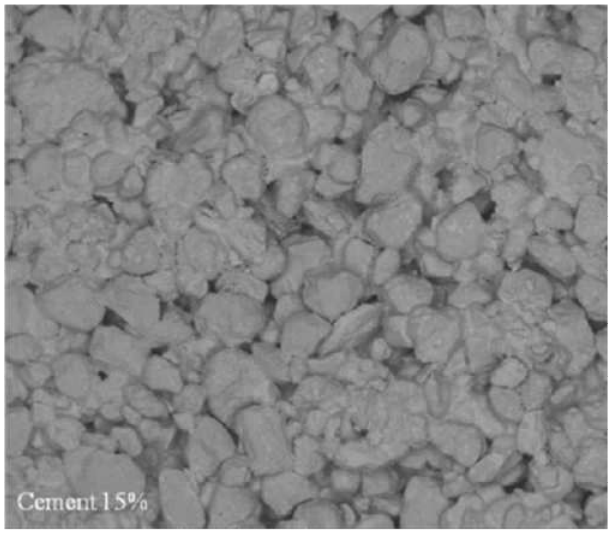

(c)

Figure 3.22 Images of cemented sand prepared with various cement contents: 5% (a); 10% (b); 15% (c) (Marri, 2010)

Using the bond parameters which give the most realistic stress behaviour (i.e. Weibull strength distribution with m = 0.5 and mean strength 50 N), a series of triaxial simulations have been performed with an increasing number of bonds. Considering the quantity of bonds (in this work measured by the average number of bonds per sand particle) as a gauge of cement content, results are presented for simulations with an average of 5, 10 and 20 parallel bonds per sand particle (considered lightly, moderately and highly cemented respectively), alongside an unbonded simulation. All simulations are sheared under a confining pressure of 1 MPa. The increased number of bonds is achieved by bonding particles which aren't necessarily touching, but which lie within a specified proximity of one another. Adjusting this proximity results in a larger or smaller number of bonds among the sand particles.

From Figure 3.23, it can be seen that the correct qualitative behaviour with regard to modelling increased cement content is reproduced by increasing the number of bonds. There is an increase in the peak and maximum deviatoric stress, a higher initial stiffness, and there is a more dilative response. The peak stress appears at approximately the same axial strain regardless of the number of bonds. The stress-strain responses appear to converge at large strains. Considering the increasing number of bonds to be representative of 5, 10 and 15% cement contents respectively, the results demonstrate good qualitative agreement with the results in Figure 2.17 from Marri (2010).

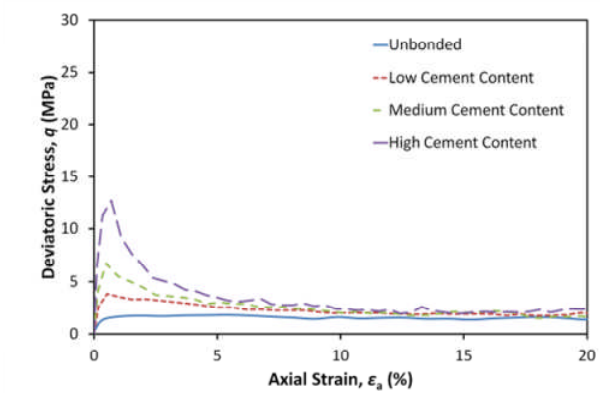

(a)

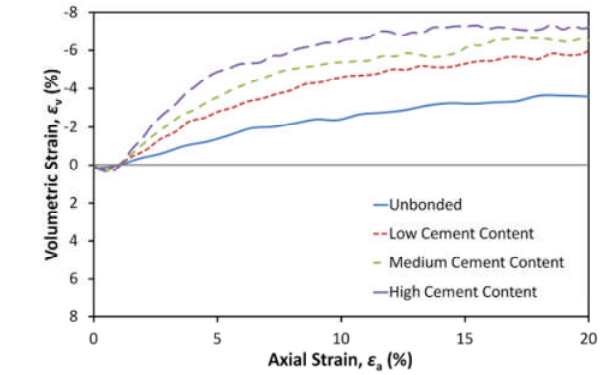

(b)

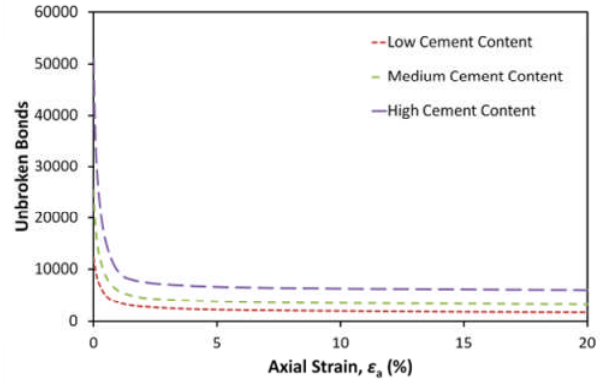

(c)

Figure 3.23 Triaxial results for simulations with various numbers of bonds representing increasing cement content: deviatoric stress (a), volumetric strain (b) and remaining unbroken bonds (c) versus axial strain

It has been shown experimentally in the literature (e.g. Coop and Cuccovillo, 1999, Yu at al., 2007) that the presence of cohesion inhibits dilatancy, and the same observation can be made in Figure 3.24(a), which shows the stress-dilatancy curves for the simulations with a range of cement contents. It can be seen that prior to the peak stress ratios, the most highly cemented sample (with 20 parallel bonds per particle) exhibits less dilatancy than the samples

with lesser degrees of cementation, suggesting that the cohesion arising from the parallel bonds inhibits dilatancy. This is in agreement with Cuccovillo and Coop (1999), who theorised that if work is spent on degrading the bonding, which is evident from Figure 3.23(c), the rate of dilation has to decrease, with the bonds preventing the intact material from dilating. Prior to the peak stress ratio, Yu et al. (2007) also proposed that cohesion shifts the dilatancy curve to the left when plotted on η-D space. As in experimental findings, this 'delay' in dilatancy is compensated for by a rapid increase culminating in the peak dilatancy, which was largest for the most highly cemented simulation. Marri (2010) showed that for a given confining pressure, increasing the degree of cementation shifts the dilatancy curve upwards, resulting in larger stress ratios at the peak and ultimate states. Experimental results are repeated in Figure 3.24(b) for comparison. The same pattern can be observed from the simulations, although there is not a considerable difference between the ultimate states.

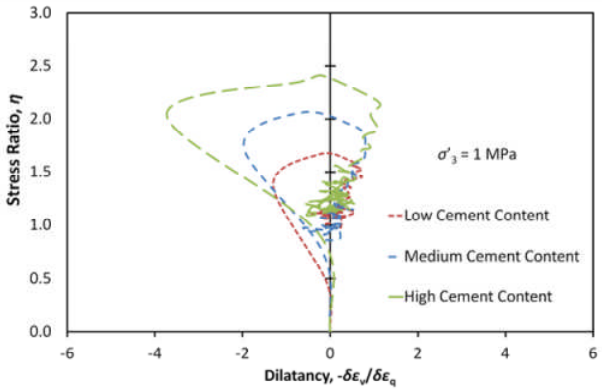

(a)

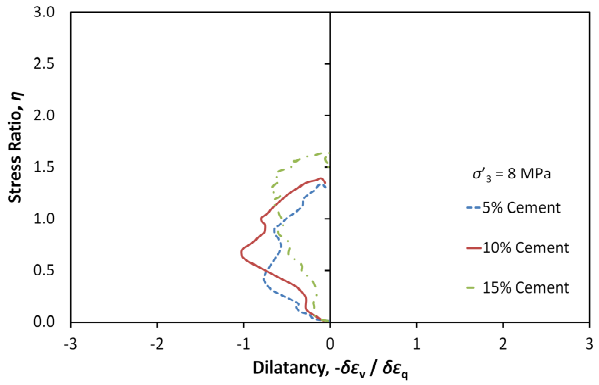

(b)

Figure 3.24 Stress–dilatancy curves from simulations (a) showing the effect of increasing the degree of cementation, compared with experimental results (b) from Marri (2010)

3.3.5 Confining Pressures

Using the bond parameters which give the most realistic stress-strain behaviour (i.e. Weibull distribution with m = 0.5 and mean strength 50 N) triaxial simulations have been performed over a range of high confining pressures (1–12 MPa) and various cement contents. Assuming that the average number of bonds per particle is representative of a given cement content, Figure 3.25 shows the effects increasing the confining pressure has on the behaviour of cemented sand. The behaviour of samples with an average of 0, 5, 10 and 20 bonds per particle (considered uncemented, and lightly, moderately, and highly cemented respectively) are plotted for confining pressures of 1, 4, 8 and 12 MPa.

From the graphs in Figure 3.25, it is clear that increasing the confining pressure leads to a higher maximum deviatoric stress. The strain associated with the maximum deviatoric stress increases with confining pressure. The

simulation with the medium cement content in Figure 3.25(c) is comparable with the experimental results shown earlier in Figure 2.18—the strain associated with the maximum deviatoric stress increases with confining pressure, and the peak is much more prominent at lower pressures, becoming less distinguished at 12 MPa. As with experimental results, there is a transition from brittle to ductile behaviour, with the effects of cementation/bonds being suppressed by increasing confinement.

Confining pressure also greatly reduces the volumetric dilation, with the samples becoming more contractive with increased confining pressure. It can be seen that the axial strain associated with the maximum rate of dilation increases with increasing confining pressure, in the same manner as the experimental results shown in Figure 2.18. However, the correct magnitude of contraction is impossible to attain in the simulations without taking particle crushing into consideration. This also is the reason why there exists a peak in the deviatoric stress graphs, even at pressures as high as 12 MPa.

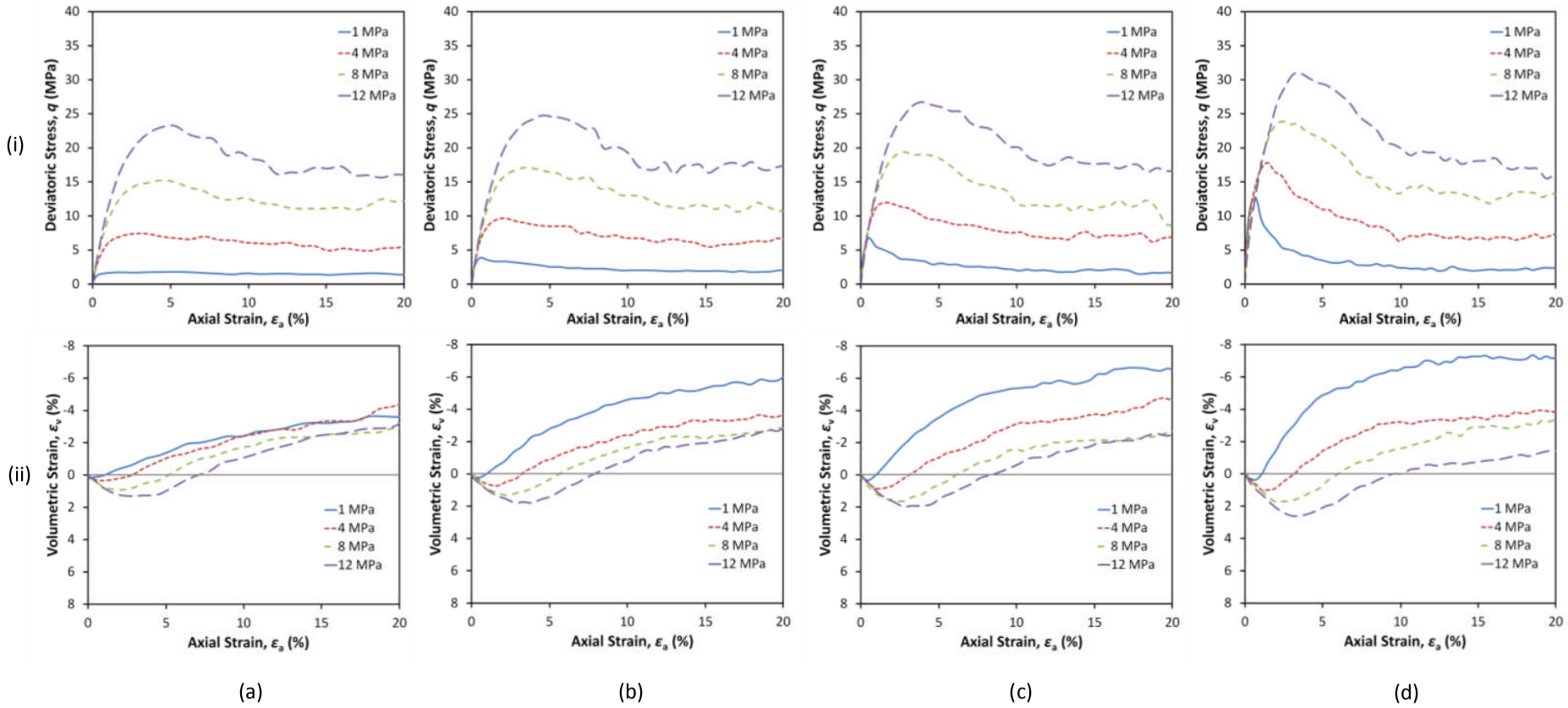

Figure 3.25 Triaxial Behaviour of unbonded sample (a), sample with low cement content (b), medium cement content (c) and high cement content (d), sheared across a range of high confining pressures (1–12 MPa): deviatoric stress (i) and volumetric strain (ii) versus axial strain

The dilatancy plots for the moderately cemented simulations with confining pressures 1–12 MPa are given in Figure 3.26(a). Increasing confining pressure reduces the peak dilatancy, as well as reducing peak stress ratio. Increasing the confining pressure generally shifts the dilatancy curve downwards in *η-D* space, which offers good agreement with the experimental work by Yu et al. (2007) and Marri (2010) shown in the literature review (section 2.3.4), the latter of which is repeated below in Figure 3.26(b).

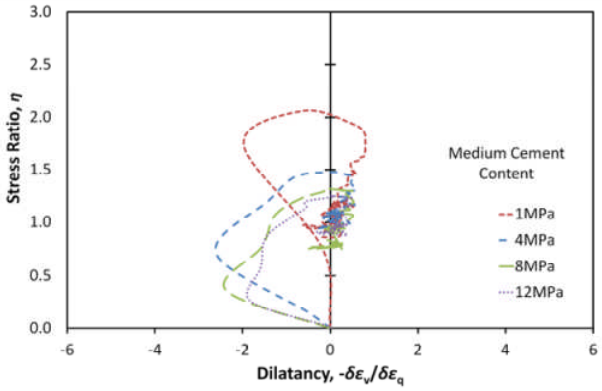

(a)

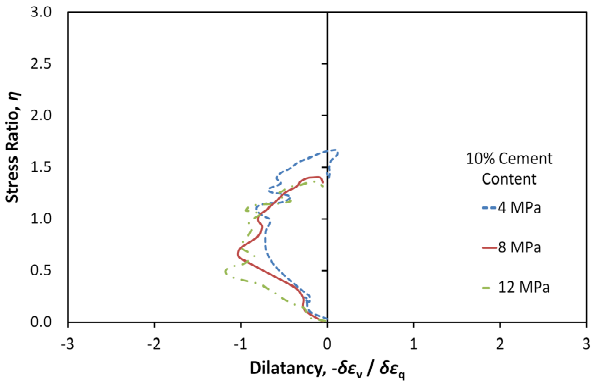

(b)

Figure 3.26 Stress–dilatancy curves from simulations (a) showing the effect of increasing the confining pressure, compared with experimental results (b) from Marri (2010)

3.3.6 Failure and Characteristics and Critical State

The peak failure data from the triaxial simulations for all cement contents are plotted in Figure 3.27. The envelopes are obtained by fitting linear trend-lines to the failure points from simulations across the full range of confining pressures. While it is not accurately possible to observe if the failure envelopes are curved as seen in some experimental studies (e.g. Asghari et al., 2003), it can be seen that increasing the cement content moves the failure

envelopes upwards to higher stress levels in *q*-*p*' space, as one would expect. The failure envelopes also show that the failure stress increases with confining pressure. The inclination of the envelopes appears to decrease slightly with increasing cement content, suggesting convergence towards very high pressures, as alluded to by Cuccovillo and Coop (1999), Lo et al. (2003) and Figure 2.19 from Marri (2010). As discussed in the literature, this observation indicates that the strength from cementation reduces when under high mean effective stresses, as bonds are broken during consolidation. Therefore the influence of cement is greatest at lower pressures, as shown by authors such as Asghari et al. (2003). The envelopes are extrapolated, which give increasing failure stresses at zero confinement with increasing cement content, supporting the idea that increasing the cement content (i.e. the number of inter-particle bonds) increases the cohesion.

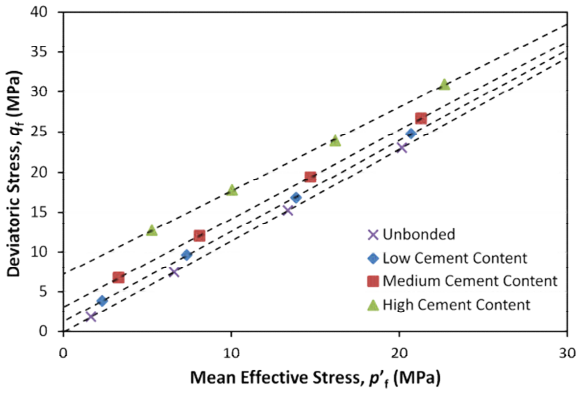

Figure 3.27 Failure envelopes of simulations with various cement contents

Increasing the number of bonds for a given confining pressure produces the correct transition from ductile to brittle failure. The difference in failure modes is most visible in Figure 3.28 which displays the particle rotations at approximately the point of maximum rate of dilation (2-3% axial strain) for simulations with various cement contents sheared at 1 MPa. The unbonded and lightly cemented samples display no clear patterns, and exhibit classic barrelling failure, while the moderately cemented sample (10 bonds per particle) displays a pair of shear bands, and the most heavily cemented sample displays a prominent steep shear plane, typical of a highly cemented, brittle material. The transition is in agreement with the literature (e.g.

Schnaid et al., 2001; Asghari et al., 2003). Also visible from (c) and (d) is the indication that increasing cementation increases the inclination of the shear band, as suggested by Haeri et al. (2005a).

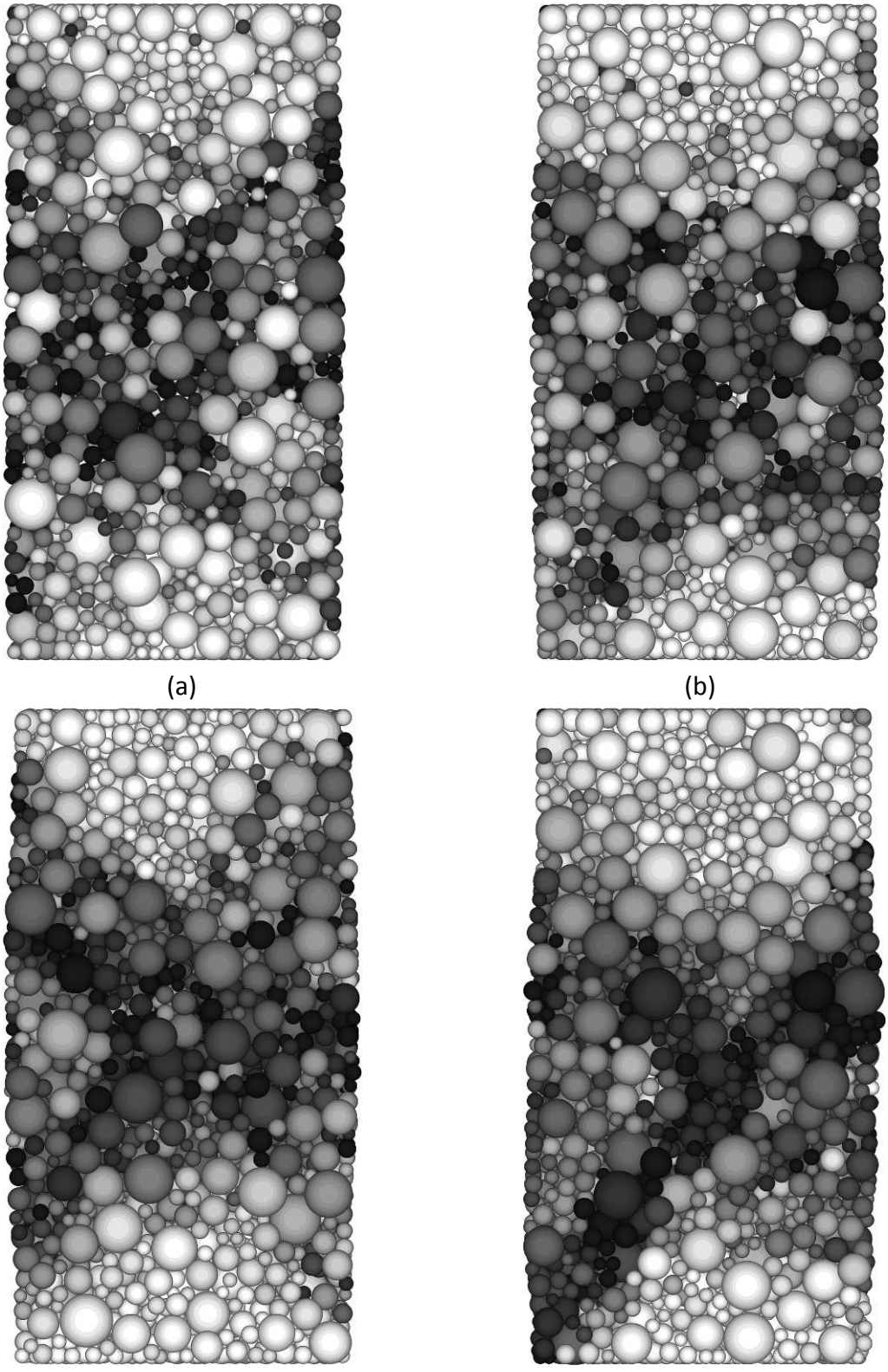

Figure 3.28 Images displaying particle rotation for samples sheared under 1 MPa confining pressure at maximum rate of dilation: unbonded sample (a), lightly cemented (b), moderately cemented (c) and heavily cemented sample (b). Dark greyscale indicates particles which have undergone the most rotation; white denotes the least.

The change in failure behaviour resulting from increasing the confining pressure (from brittle to ductile) is also visible in the sheared samples: Figure 3.29 plots the particle rotations at approximately the maximum rate of dilation (approximately 2–6% axial strain) for the moderately cemented simulations sheared under 1, 4, 8 and 12 MPa confining pressures. Conjugate shear bands are visible in the simulation at 1 MPa confining pressure, with shear zones barely visible in the 4 MPa simulation, and no distinct patterns visible at 8 or 12 MPa. Figure 3.30 shows the final numerical specimens (again with moderate cement content) from the 1 MPa and 12 MPa simulations after 20% axial strain, alongside the equivalent laboratory samples from Marri (2010). From the images of the laboratory specimens after shearing, conjugate shear planes can be observed through the membrane for the sample with 10% cement content sheared at 1 MPa. Similar failure can be seen in the corresponding image of the numerical sample, which has fairly distinctive non-uniform deformations. The same material shearing under a confining pressure of 12 MPa displays barrelling failure, i.e. expansion which is uniform in the radial direction, and concentrated around the mid height of the specimen.

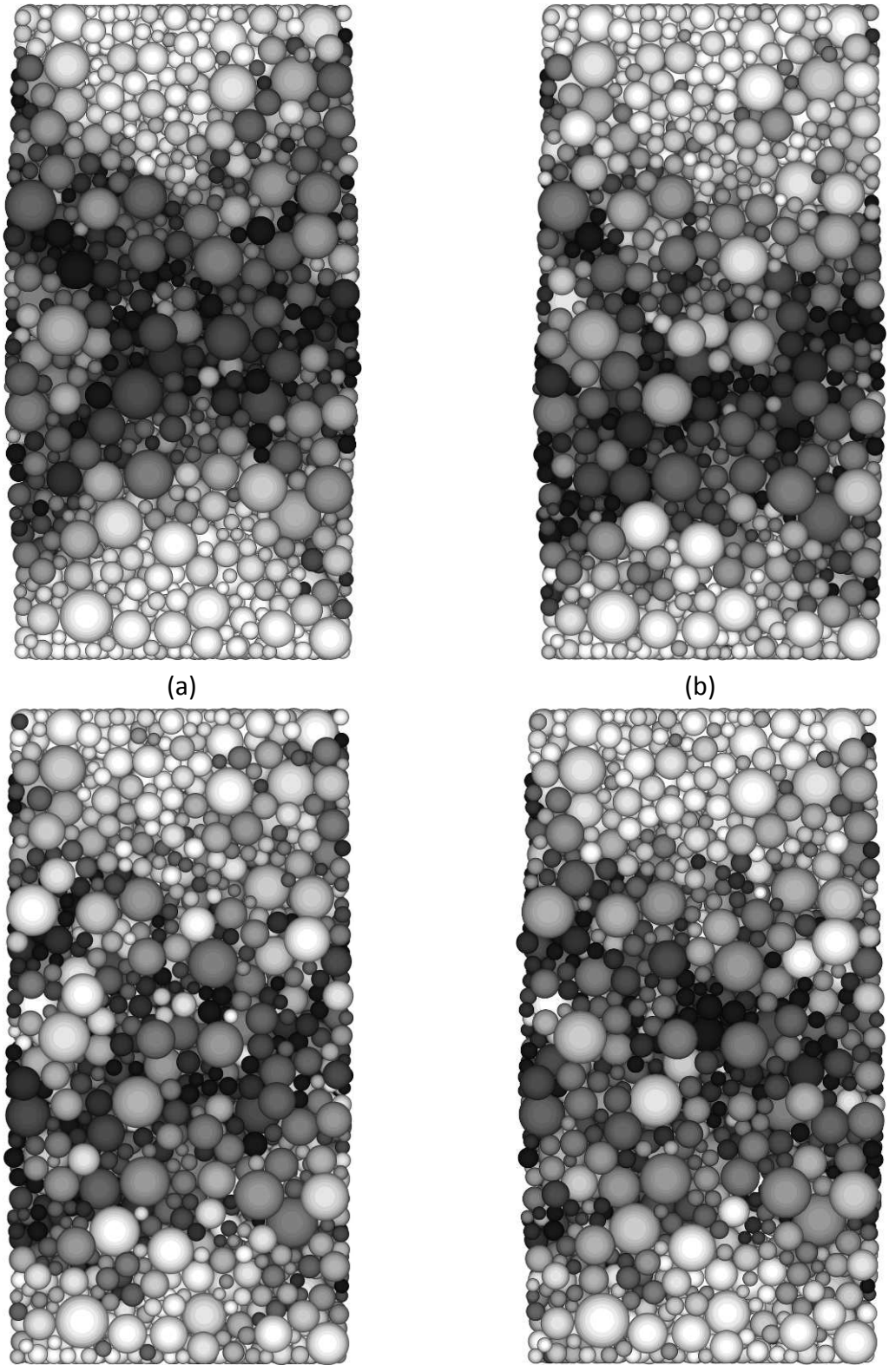

Figure 3.29 Images displaying particle rotation for moderately cemented samples at maximum rate of dilation (2–6% axial strain): 1 MPa (a), 4 MPa (b), 8 MPa (c) and 12 MPa confining pressure (d). Dark greyscale indicates particles which have undergone the most rotation; white denotes the least.

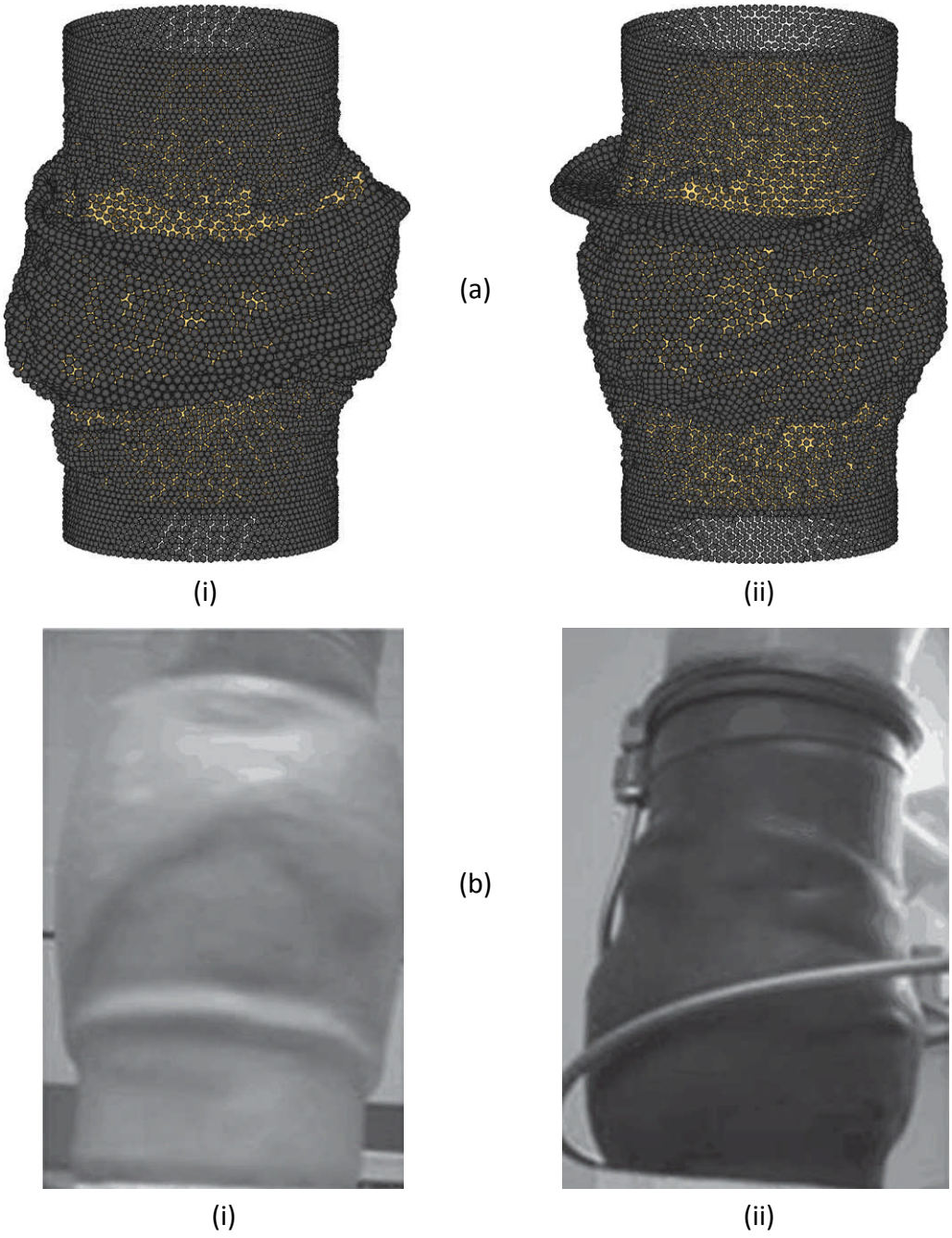

Figure 3.30 Cemented numerical sample (a) and laboratory sample (b; Marri, 2010) after shearing to 20% axial strain under 1 MPa (i) and 12 MPa (ii) confining pressures

The ultimate/critical state lines from the experimental triaxial tests by Marri (2010) for the cemented sand are given in Figure 3.31, alongside the equivalent plots obtained from the simulations in Figure 3.32. In deviatoric stress–mean effective stress space, the data from Marri (2010) all followed a slightly curved line. It was not possible to determine if the critical state lines were coincident, as suggested by authors such as Cuccovillo and Coop (1999) or, if as indicated from Figure 3.31, increasing the cement content shifts the

CSL line upwards in *q*-*p*' space. As such, Marri suggested a critical state zone may be more appropriate. In specific volume–mean effective stress space, the data displayed significantly more scatter, with all the points from the cemented materials located to the right of the uncemented material. The CSLs obtained from this plot were almost parallel, with slightly steeper lines revealed by the cemented material. This shift in volume-stress space was attributed to the change in grading caused by the addition of cement fines, which change the critical state voids ratio, e_{cr}.

The critical states from the simulations however, can both be seen to approximately lie on single critical state lines in Figure 3.32. In *q*-*p*' space, the simulations offer good agreement with experimental data, and the plot is in harmony with the hypothesis that that a material has a single CSL (in *q*-*p*' space) regardless of cement content (e.g. Airey, 1993; Coop and Atkinson, 1993; Cuccovillo and Coop, 1999). In *v*-*p*' space, there is some scatter, with increasing cement content possibly shifting the critical states to the right. However, there is no clear trend, and the points may be considered to lie about the same line. Although this is dissimilar to experimental results, it is explicable by the fact that increasing the degree of cementation in the simulations doesn't change the grading as such, and once the materials have become completely destructured they have identical particle size distributions. Parallel bonds fail to capture the change in grading associated in reality with the addition of cement fines. Any difference in critical/ultimate voids ratio can therefore be attributed to the continuing presence of bonds maintaining a higher voids ratio.

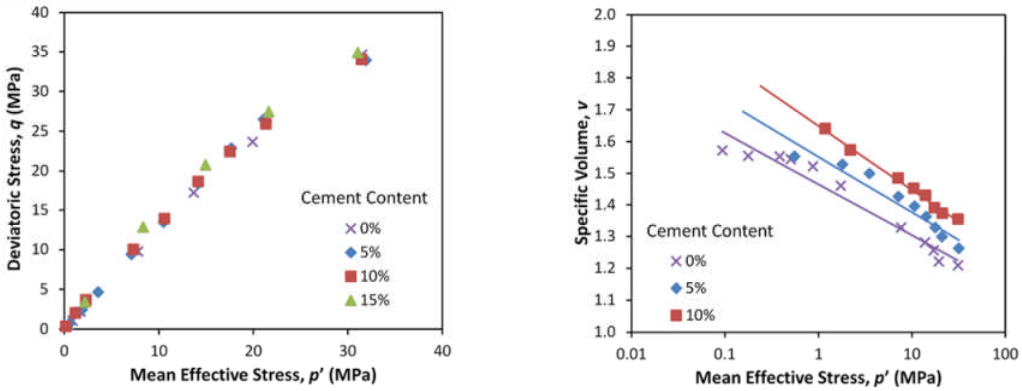

(a) (b)

Figure 3.31 Critical states lines for experimental testing on Portaway sand with various Portland cement contents (Marri, 2010), plotted in *q*-*p*' space (a) and *v*-*p*' space (b)

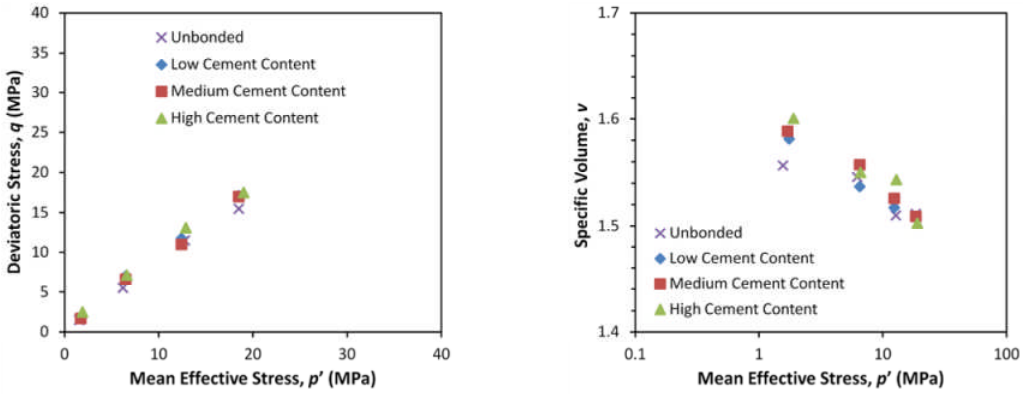

(a) (b)

Figure 3.32 Critical states for simulations ranging from unbonded to highly cemented, plotted in *q*-*p*' space (a) and *v*-*p*' space (b)

3.4 CONCLUSIONS

Using the discrete element method, simulations of high-pressure triaxial tests on cemented and uncemented sand have been presented. The triaxial model developed has a flexible membrane allowing the correct failure modes to develop, without inhibiting deformation as rigid boundaries have been shown to. The model uses a simple and effective method to apply the correct confining pressure after the sample becomes distorted and exhibits a non-uniform shape. The flexible boundaries also allow the vertical component of confining pressure to be applied to the specimen.

In the series of simulations of cemented sand, the cementation has been modelled with parallel bonds, and the influence of bond size, stiffness and

strength has been investigated, as well as a variety of bond strength distributions. For a given mean bond strength, a Weibull distribution with a low modulus, such as 0.5 appears to give the most realistic results; with some bonds failing during consolidation and immediately after commencement of shearing, while the strongest remain intact throughout the tests. Such a distribution produces a sharp peak strength at lower confining pressures, and a more rounded peak at the highest pressures. The presence of bonds, which represent cementation, also cause additional dilation when compared to the uncemented simulations. For a sample with a given number of bonds and initial density, the results indicate that it is the strength of the strongest bonds which govern any additional dilation caused by cementation.

Increasing the quantity of bonds in a given sample appears to be the most effective way of modelling increased cement content. For a distribution of bond strengths, increasing the quantity, by bonding particles to neighbouring ones which aren't in contact but lie within a specified proximity, results in the correct qualitative change in behaviour that an increase in cement content causes in laboratory triaxial tests. It causes a more clearly defined peak strength, an increase in strength (maximum deviatoric stress), increases the dilation, and renders the behaviour more brittle.

The flexible membrane used has allowed the correct failure modes to develop, allowing contrasting brittle and ductile failure modes caused by varying the cement content. By plotting the individual particle rotations, it has been shown that for a given confining pressure such as 1 MPa, increasing the number of bonds (i.e. the degree of cementation) increases the strength and brittleness of the material, with shear planes produced in the most highly cemented simulations. For a given cement content, increasing the confining pressure to 12 MPa suppresses the behaviour of the cementation, with no shear planes visible for even the most highly cemented samples. In between these pressures there is 'transitional' behaviour where the material behaves neither completely brittle nor ductile. DEM has therefore been shown to be

able to capture the behaviour of cemented sand under a range of confining pressures and cement contents.

However, particle crushing needs to be incorporated into the model to enable realistic magnitude of volumetric contraction to be observed, which will have an effect on the stress response, especially if a distribution of particle strengths are used.

CHAPTER 4
MODELLING PARTICLE BREAKAGE—ONE-DIMENSIONAL COMPRESSION

4.1 INTRODUCTION

The role of particle crushing and its significance with regard to the behaviour of soil has been summarised in section 2.5. To recap, there are several factors which control the degree of crushing (particle size distribution, particle shape, mineralogy and strength of the grains, density, water conditions of the soil, the stress path and the effective stress state), with the influence of crushing greatest at high pressures. Particle crushing causes a great reduction in the volumetric dilation observed during triaxial shearing at high confining pressures, which is evident from the previous chapter (section 3.3) where no overall contraction was observed during simulations with unbreakable particles at high pressures. It therefore seems essential to incorporate particle crushing into the simulations to enable the samples to exhibit realistic volumetric strains.

As such, a simple breakage mechanism has been developed, which is presented in this chapter. A review of the literature on modelling particle breakage was given in section 2.6.5, which described two main schemes: modelling particles as agglomerates, consisting of groups of smaller, bonded particles; or replacing 'breaking' grains with new, smaller fragments.

Using agglomerates, McDowell and Harireche (2002b) used DEM to show that for normal compression, yielding was the onset of bond breakage for an aggregate of agglomerates and that normal compression lines resulted from the one-dimensional compression of an aggregate of agglomerates. However, their aggregates only contained a small number of agglomerates. The bonds within the agglomerates were such as to give a Weibull distribution of particle strengths when crushed between flat platens. They did not consider the evolution of a particle size distribution during normal

compression due to the insufficient number of agglomerates in the model. Similar work was published by Cheng et al. (2003) and Bolton et al. (2008), who investigated various stress paths in addition to isotropic compression, although again a limited number of agglomerates were used.

Using the latter method, i.e. replacing breaking grains by new fragments, Åström and Herrmann (1998) showed it was possible to model the fragmentation of grains in two dimensions using DEM. This work was supplemented by Tsoungui et al. (1999), while Lobo-Guerrero and Vallejo (2005) developed a similar 2D model of granular crushing but in that model mass was not conserved. Ben-Nun and Einav (2010) and Ben-Nun et al. (2010) used their own 2D model of grain fracture to explore the particle and force-chain topology, and the evolution of fractal distributions, and also used a distribution of particle strengths. A similar approached is adopted in this work, where the crushing model is calibrated by modelling one-dimensional normal compression of sand using a simple oedometer.

To recap from the literature review, McDowell and Bolton (1998) related the normal compression of granular materials to the evolution of a fractal distribution of particle sizes using a work equation and the assumption of a Weibull distribution of particle strengths giving a particle size effect on strength. They did not consider the stresses induced within a particle by multiple contacts and simply considered the strength of a particle as measured by crushing between flat platens. Their work proposed that normal compression lines should be linear on a plot of voids ratio e against the logarithm of applied stress log σ. There has been much theoretical work since: for example Russell et al. (2009), who *did* consider the internal stress field within particles with regard to crushing; and Russell (2011), who also linked the compression line to the evolving fractal particle size distribution.

McDowell (2005) showed analytically that based on the kinematics of particle fracture and the void collapse caused by the fracture of a particle, that normal compression lines according to this argument should be linear in log e–log σ

space. No consideration was given to the complex distribution of loads on each particle at its multiple contacts.

By modelling one-dimensional normal compression, this chapter not only shows a calibration of the crushing model, but aims to make the next step in understanding the mechanics of normal compression, by allowing particles to fracture without the use of agglomerates and by considering the stresses induced in a particle due to the multiple contacts. The normal compression is linked using the DEM software to the evolution of a fractal distribution of particles and the influence of the mechanics of fracture on the slope of the normal compression line are properly investigated.

4.2 NORMAL COMPRESSION

4.2.1 Oedometer

The sample consists of 620 spheres of diameter 2 mm, in a dense random packing, in a scaled-down oedometer with rigid boundaries, a diameter of 30 mm and a height of 7 mm, displayed in Figure 4.1. These dimensions mean initially only relatively short particle force chains can form between the top and bottom platens, however, it was decided to have such a geometry as is used in real oedometer (one-dimensional) experiments (in this case the aspect ratio is chosen to reduce wall friction). It was also deemed important to have a large enough diameter to permit a sufficient *number* of force chains to develop. Although a larger initial sample and/or more initial particles would be ideal, exploratory simulations using larger samples appeared to result in the same compression behaviour, but were unable to reach high pressures due to the large number of particles covering a very wide range of scales rendering the timestep too small. This relatively small number (620) of initial particles means that the behaviour is initially sensitive to particle breakage, however this diminishes once a large number of particles have been produced. Different strength characteristics, hardening laws and mechanisms of fracture are examined to investigate the influence on the

resulting particle size distribution and the slope of the normal compression line for the simulations.

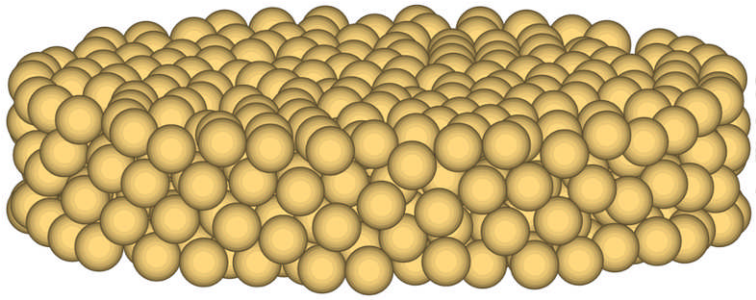

Figure 4.1 Oedometer sample, consisting of 620 particles

The initial monodisperse sample was created using the radii expansion technique (Itasca, 2005) resulting in a relatively dense random packing without any locked in forces or overlap. The voids ratio calculated for the compression plots was calculated using the total solid volume for convenience while the simulation was running. Retrospective calculations, using the same method outlined in section 3.2.3 which accounts for overlaps between particles demonstrated no significant difference (less than 0.5% difference in volume of solids).

For these simulations, the density of the particles is set as 2650 kg/m^3, reflecting that of silica sand as mentioned before, and a particle friction coefficient of 0.5 is again attributed. In contrast to the earlier simulations, the Hertz-Mindlin contact model is now used, as a very wide range of particle sizes are generated during the simulations. As outlined in section 2.6.2, the linear springs model is a simplification, primarily used to improve calculation time. The Hertzian model is more computationally demanding, but is more realistic as it captures the nonlinear stiffness of spheres in contact—hence is more suitable for these simulations, in which the stress induced in the particles is of such importance. As a very wide range of particle sizes are generated during the simulations, another advantage is that the Hertzian model automatically accounts for the different stiffness of particles of different sizes, by utilizing the shear modulus. The input value of shear modulus for the particles was arrived at assuming sand grains have an elastic

modulus of 70 GPa, a typical value for quartz, and an approximate value of 0.25 was given as the Poisson's ratio. The particle input parameters are listed in Table 4.1.

The sample is loaded one-dimensionally, i.e. the top platen is moved downwards to impose a vertical stress on the particles. The vertical stress is applied in increments of 1 MPa, by gradually accelerating the top platen, which is decelerated as the target stress is approached. The vertical stress (which is always effective) is measured from the top and bottom platens:

$$\sigma = \frac{\sigma_{\text{top}} + \sigma_{\text{bottom}}}{2} \qquad [4.1]$$

although the platen velocity is capped at 0.1 m/s to eliminate any loading rate effects.

Table 4.1 Summary of DEM parameters for the oedometer sample

Oedometer Sample Properties	
Size: height x diameter (mm)	7 x 30
No. of particles	620
Particle friction coefficient	0.5
Contact model	Hertz-Mindlin
Shear modulus, G (GPa)	28
Poisson's ratio, v	0.25
Density (kg/m^3)	2650
Particle diameter, d_0 (mm)	2.00
Voids ratio, e_0	0.90
37% Strength, q_0 (MPa)	37.5 (for $d = d_0$)
Weibull Modulus, m	3.3
Wall Friction Coefficient	0

4.2.2 Particle Strengths

McDowell and Bolton (1998) assumed that for a particle of diameter d compressed diametrically between flat platens by a force F, the characteristic stress, σ induced within the particle was:

$$\sigma = \frac{F}{d^2} \qquad [4.2]$$

after Jaeger (1967) and that the values of this stress at failure followed a Weibull distribution (Weibull, 1951). The 2D models mentioned earlier (such as Tsoungui et al., 1999; Ben-Nun and Einav, 2010 etc.) generally used fracture criteria based on shear stress derived from the principal stresses - which took into account the various possible combinations of loads on a particle. In the work on particle strength using agglomerates by McDowell—e.g. Lim and McDowell (2004), although agglomerates could break under complex distributions of loads, no consideration was given to the stress induced by multiple contacts other than for simple diametral loading.

In deciding whether a particle in an aggregate under multiple contacts should fracture or not, it is possible to make use of the stress tensor function within PFC3D, which will return the stress tensor for a sphere—similar to methods employed by Tsoungui et al. (1999) and Ben-Nun and Einav (2010) using discs. For a particle under multiple contacts, it would not be feasible to use the mean stress to establish whether a particle should break or not, because the particle, if under a high hydrostatic stress but low deviatoric stress, would be unlikely to break due to being loaded uniformly over its surface.

A decision was therefore taken to use the octahedral shear stress induced within each sphere, to determine whether fracture should occur or not. The octahedral stress in a particle is derived from the principal stresses, and is given by:

$$q = \frac{1}{3}[(\sigma_1 - \sigma_2)^2 + (\sigma_2 - \sigma_3)^2 + (\sigma_1 - \sigma_3)^2]^{1/2} \qquad [4.3]$$

where σ_1, σ_2 and σ_3 are the major, intermediate and minor principal stresses, respectively. While the use of this equation to determine whether fracture should occur or not is a simplification, it provides a simple criterion to facilitate breakage taking into account multiple contacts on a particle surface while avoiding the use of agglomerates. The decision was taken that if a particle is, for example, under diametral point loads, equal in three mutually orthogonal directions, then the particle would not break under this

hydrostatic stress (q = 0). In PFC3D (Itasca, 2005), the average stress tensor in a particle is:

$$\boldsymbol{\sigma}_{ij} = \frac{1}{V}\sum_{N_c} \left| x_i^{(c)} - x_i^{(p)} \right| n_i^{(c,p)} F_j^{(c)} \qquad [4.4]$$

where V is the volume of the particle, N_c is the number of contacts, $x_i^{(c)}$ and $x_i^{(p)}$ are the locations of the contact and particle respectively, $n_i^{(c,p)}$ is the unit-normal vector directed from the particle centroid to the contact location and $F_j^{(c)}$ is the force at the contact (Itasca (2005). For the case of a particle compressed diametrically between platens, the major principal stress is:

$$\sigma_{11} = \frac{1}{\frac{\pi}{6}d^3} F \times \frac{d}{2} \times 2 = \frac{6}{\pi}\frac{F}{d^2} \qquad [4.5]$$

From equation [4.3], it can be seen that the value of octahedral shear stress q for a sphere compressed diametrically between two walls is then given by:

$$q = \frac{\sqrt{2}}{3}\left(\frac{6}{\pi}\frac{F}{d^2}\right) = 0.9\frac{F}{d^2} \qquad [4.6]$$

which is the value of q returned by PFC3D for a sphere compressed between two walls; hence the average octahedral shear stress in a particle is proportion to the characteristic stress from equation [4.2]. Therefore the assumption was made that for particles loaded under multiple contacts, the particle would break if the octahedral shear stress was greater than or equal to its 'strength', where the strengths of the particles satisfy a Weibull distribution of q-values.

The Weibull distribution, which was described in more detail in section 2.5.2, and used for modelling cement bonds in the previous chapter, is one of the most commonly used tools for analysing the fracture of disordered material, and has a wide range of applications. The Weibull distribution of strengths used here was taken from McDowell (2002) for silica sand, and is described in

this chapter by the Weibull Modulus, m, and the 37% strength, q_0. The quantity q_0 is the value of octahedral shear stress for a particular particle size such that 37% of particles are stronger, and is related to the characteristic induced tensile stress. Size effects on the tensile strength of materials are usually described in the form of equation [2.17]: $\sigma \propto d^b$, where σ is the strength, d the size and b is a material constant. Using the working shown in section 2.5.2, but considering the octahedral shear strength q_0, instead of the tensile strength σ_0, it is possible to derive the following relation from Weibull's survival probability for a block of material:

$$q_0 \propto d^{-3/m} \qquad [4.7]$$

assuming bulk fracture dominates and Weibull gives a volume 'effect' on particle strength (McDowell and Bolton, 1998). Values of q_0 derived from McDowell (2002) are plotted in Figure 4.2 along with the values of q_0 used in the following simulation according to the above law in equation [4.7]. As mentioned in section 2.5.2, if surface flaws dominate, a different relation is appropriate, which is investigated later.

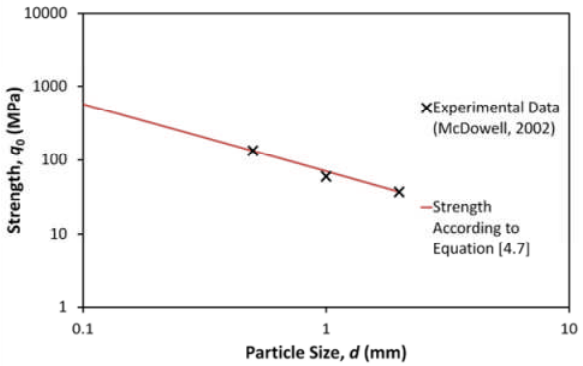

Figure 4.2 Strength as a function of particle size for silica sand

4.2.3 Simple Diametral Splitting

In a similar approach to the previous work with discs (e.g. Åström and Herrmann, 1998; Tsoungui et al., 1999; Lobo-Guerrero and Vallejo, 2005; Ben-Nun and Einav, 2010), in the interest of computational efficiency, allowing a large number of particles to be generated and fragments to be self-similar in

shape, each sphere was allowed to split into two equal spheres, without loss of mass, when the value of q was greater than or equal to its Weibull strength. Although the fragments of broken spheres are not spheres, realistic particle shape has not been employed in this work. However, using fragments that are similar in shape to the original particle does not seem too improbable; for example Bowman et al. (2001) analysed the change in particle shape resulting from crushing silica sand using Fourier descriptor analysis. For a processed, laboratory-grade silica sand, crushing resulted in only slight, statistically-insignificant changes in elongation and shape, although these were with initially *angular* particles, not spheres. One would expect implementing particle shape into the simulations to affect both the packing and coefficient of lateral earth pressure, in a similar way to adjusting the particle friction.

It has been acknowledged in the sphere of DEM that it is impossible to simulate a realistic fracture mechanism using discs, as typified by the various solutions adopted by others modelling two-dimensional problems such as Åström and Hermannn (1998), Lobo-Guerrero and Vallejo (2005) and Ben-Nun and Einav (2010)—shown in the literature in section 2.6.5. The same applies to three dimensions, where a solution needs to be as physically realistic as possible, while using only spheres and allowing a large number of breakages.

In the presented work, new sphere fragments overlap enough to be contained within the bounding parent sphere with the axis joining their centres aligned along the direction of the minor principal stress, as shown in Figure 4.3. This produces undesirable local pressure spikes during a breakage, however this overlap causes the particle fragments to move along the direction of the minor principal stress for the original parent particle, just as might occur for a single particle crushed between flat platens.

To ensure sample stability and to accommodate the artificial pressure increase due to the imposed elastic energy before particle release, particle

breakages are updated at once (for the whole sample) after a number of computational cycles equivalent to 0.003 seconds (the actual number of cycles during this time interval is inversely proportional to the 'timestep'). This period was deemed sufficient to allow the artificially induced energy to dissipate: increasing it has no effect on overall breakage. After each stress increment (1 MPa), the sample is cycled continuously until no further breakage occurs.

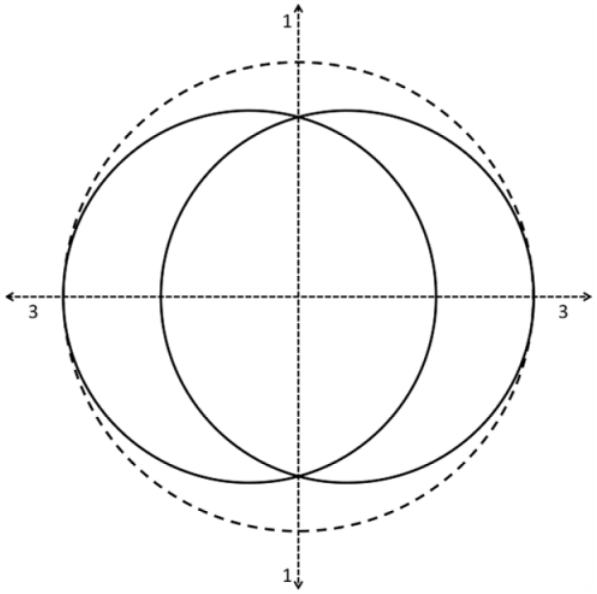

Figure 4.3 Equal diametral splitting mechanism

As mentioned, the particles are given a shear modulus of 28 GPa, assuming an elastic modulus of 70 GPa. It was found that the particle stiffness only affected the elastic component of the compression line. That is to say, before yield, the stiffness would affect the slope of the compression line. The value chosen was deemed to be realistic, and as a result the slope was shown to be small on unloading. In reality, the elastic modulus is related to the critical fracture stress according to Griffith (1921), and would influence the opening of cracks. More recently, Einav (2007) applied and extended this theory to granular material. Particle friction has also been investigated and has no effect on the plastic compressibility; it only affects the lateral earth pressure coefficient.

McDowell's compression plots and evolving particle distributions for the silica sand are reproduced in Figures 4.4 and 4.5 respectively. The resulting normal compression line and particle size distributions from the simulations as a function of applied stress level are shown in Figures 4.6 and 4.7. Figure 4.6 also shows the unloading curve, from which it is evident that the elastic component of deformation during normal compression is negligible. An images of the numerical sample after compression is presented in Figure 4.8 (Figure 4.1 shows the sample before).

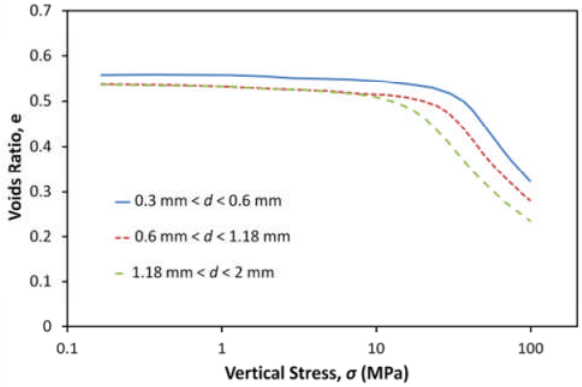

Figure 4.4 Normal compression lines for silica sand (McDowell, 2002)

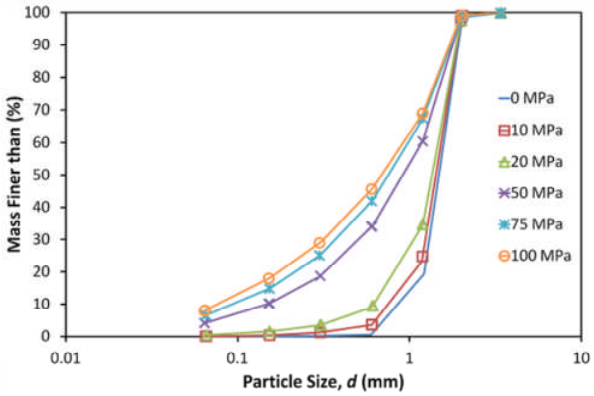

Figure 4.5 Evolving particle size distributions for silica sand (McDowell, 2002)

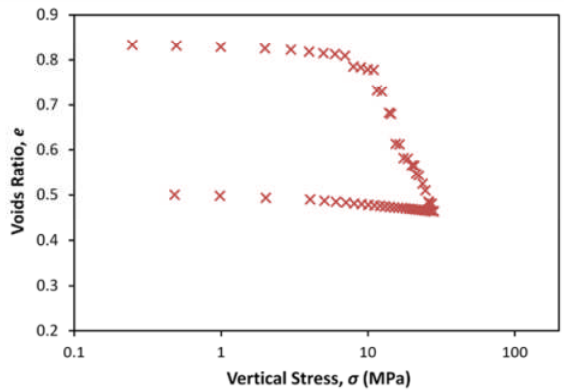

Figure 4.6 One-dimensional compression plot for simulation of silica sand

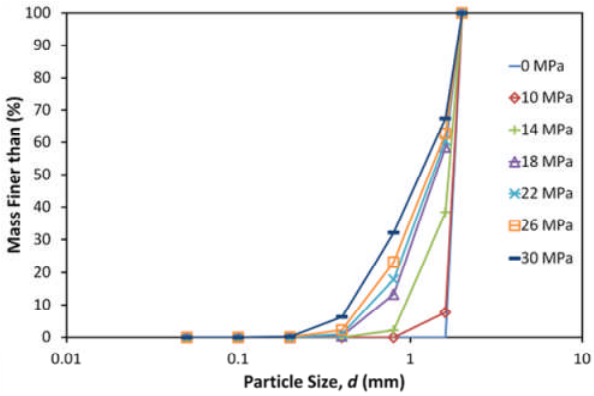

Figure 4.7 Evolving particle size distribution for simulation of silica sand

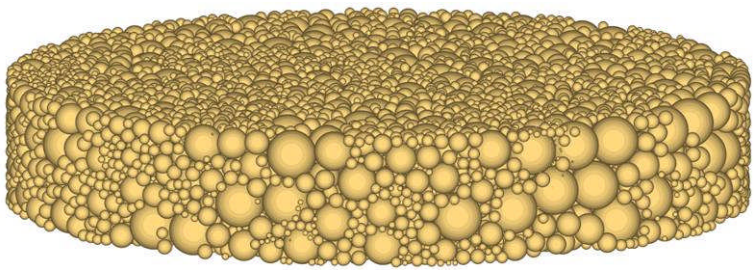
Figure 4.8 Oedometer sample after compression to 30 MPa

Following yield, a linear normal compression line emerges in e–log σ space (using common logarithms), with a plastic compression index C_c of approximately 0.5. Data points are plotted at frequent intervals (approximately 1 MPa) to show the compression line has a consistent slope. This is in line with published experimental findings, for example Figure 2.44 from Nakata et al. (2001a), which showed the compressibility value stabilising and reaching a steady value after yield. Minor fluctuations are visible due to the relatively small number of particles in the simulation, especially at lower pressures, similar to observations made by McDowell and Humphreys (2002)

when subjecting pasta shells to normal compression (refer to Figure 2.45). When the sample reaches a voids ratio much less than 0.5, the timestep becomes unsustainable due to the very wide range of particle sizes (d_{max} / d_{min} > 1000) and the simulation is halted. Significant crushing is still occurring at high stresses, however it is the smaller particles with low mass that are breaking, which is why the rate of change of the mass grading curve reduces at high pressures. The general trend in Figure 4.7 is the same as Figure 4.5, although the numerical sample is initially monodisperse; while the silica sand sample is reasonably uniformly graded. As stress increases, the overall number of contacts increase, particularly for the larger particles which become protected by the smaller fragments; the smaller particles continue to break, becoming statistically stronger.

In Figure 4.9 the lateral earth pressure coefficient, K_0 (= σ_v / σ_h) is plotted as a function of stress. K_0 increases until around 10–15 MPa, following the point at which yield is observed on the normal compression plot. After this it remains at a fairly constant value of 0.75. This is in line with the long-standing theory of lateral earth pressure at rest, given in equation [2.9]—that K_0 for *normally* consolidated soils is a function of the angle of shearing resistance, and therefore is a material constant. The value of 0.75 is conspicuously large for a real sand, and is attributable to the spherical nature of the numerical particles.

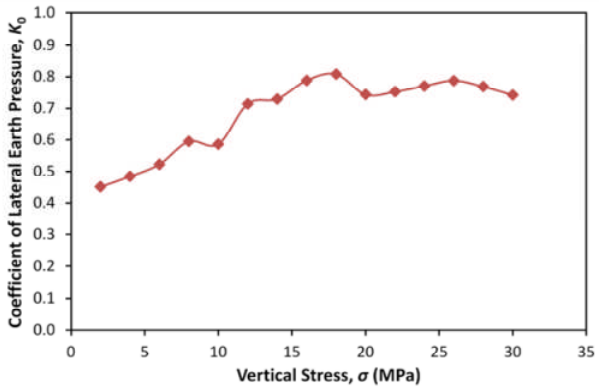

Figure 4.9 Lateral earth pressure coefficient as a function of vertical applied stress for simulation of one-dimensional compression of silica sand

Figure 4.10 shows the effects of increasing the initial strength q_0. The normal compression lines for all values of q_0 appear to have the same gradients, with the yield point for the material with q_0 = 80 MPa occurring at the highest stress. It is clear that the yield stress in one-dimensional compression, for a given initial voids ratio and grading, is proportional to the strength of individual grains, which agrees with the proposition first made by McDowell & Bolton (1998). Just how influential the individual grain strengths are is further demonstrated in the graph showing the normalised stress values (σ / q_0), in which the compression lines coincide. As one would expect, the weaker assemblies exhibit more breakage for the same magnitude of stress (30 MPa): a more well-graded aggregate has evolved in Figure 4.11.

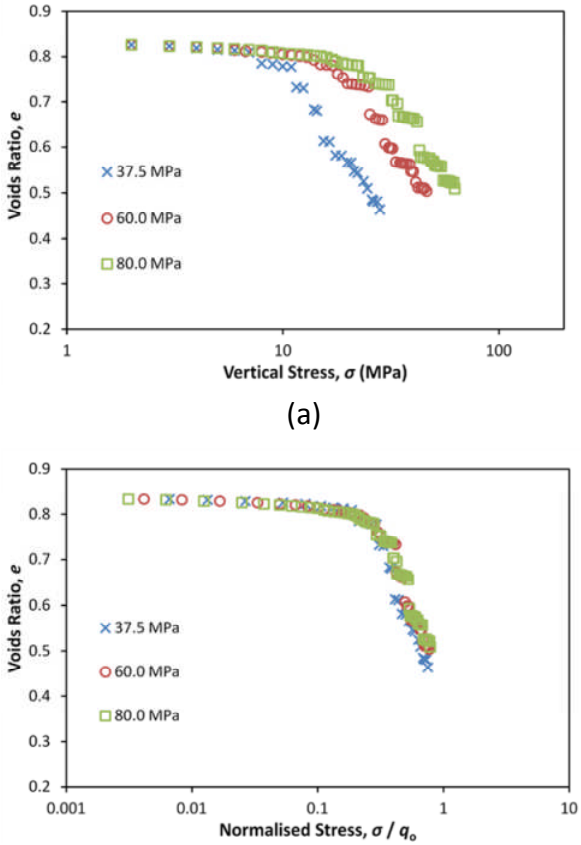

Figure 4.10 One-dimensional compression plot for various particle strengths q_0 (a) and plot showing vertical stress σ normalised by particle strength q_0 (b)

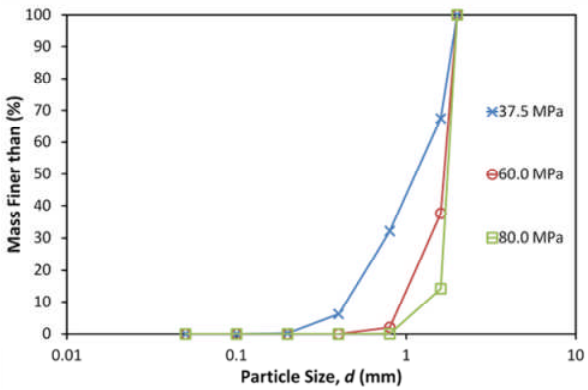

Figure 4.11 Particle size distributions at a vertical stress of 30 MPa for various initial particle strengths

For real soils subjected to one-dimensional clastic compression, the compression line is commonly observed to experience a change in curvature at very high stresses (e.g. McDowell, 2002). This is usually attributed to the largest particles being well protected by many neighbours meaning low tensile stresses are induced, and the smallest particles reaching the comminution limit, meaning fracture is no longer possible. Repeating the initial simulation (using parameters for the silica sand) but limiting the smallest permitted particle size reveals similar results. Capping the smallest particle size d_s at 0.5 mm (25% of d_0)—i.e. particles of size d_s have infinite strength—results in the compression line and grading curve shown in Figure 4.12 (compared with those from the initial simulation). The comminution limit clearly causes a change in curvature of the compression line at high stresses. The grading curve reveals the slightly different nature of the evolving material. As one would expect, the grading curve for the material with a finite minimum size curtails to 0% passing at a larger diameter than the uncapped material. The increasing quantity of unbreakable small particles necessitates the larger particles to break, which is also evident in the grading curve. For a vertical applied stress of approximately 30 MPa, the uncapped material has a larger percentage of particles larger than 0.8 mm and 1.6 mm compared with the material with a comminution limit.

As mentioned earlier, the above simulation became unsupportable when low voids ratios were reached, which was the case for the following simulations

where it was not possible to achieve as high macroscopic stresses as in the experimental work (e.g. 100 MPa).

Due to the monodispersity and lack of particle shape, it is difficult to conduct oedometer tests at different voids ratios. However, Figure 4.13 compares the initially monodisperse simulation with another featuring a broader, graded particle size distribution. The two simulations have the same strength parameters (q_0 = 37.5 MPa, m = 3.3) and use the same assumed hardening law defined in equation [4.7]. Both simulations have the same median grain size (d_{50} = 2 mm), however the graded sample has a coefficient of uniformity, C_u, of 1.5 giving minimum and maximum initial grain sizes of 1.3 mm and 3.0 mm respectively, starting with 820 initial particles. The sample is again generated in a random relatively dense state resulting in an initial voids ratio lower than the monodisperse sample. The compression lines have similar yield points but more significantly they appear to have the same slope, which agrees with experimental observations (e.g. Nakata et al., 2001a; McDowell, 2002) where, for a given sand, the plastic compression index is a constant independent of initial grading.

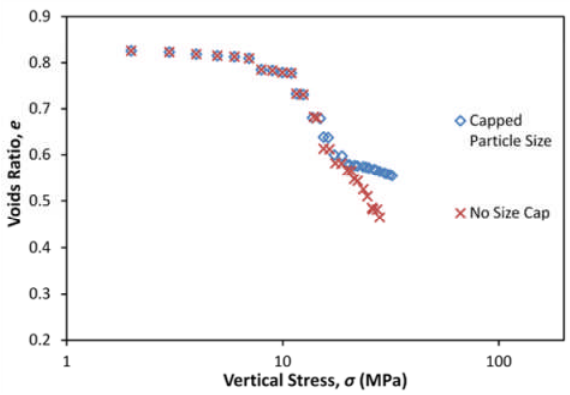

(a)

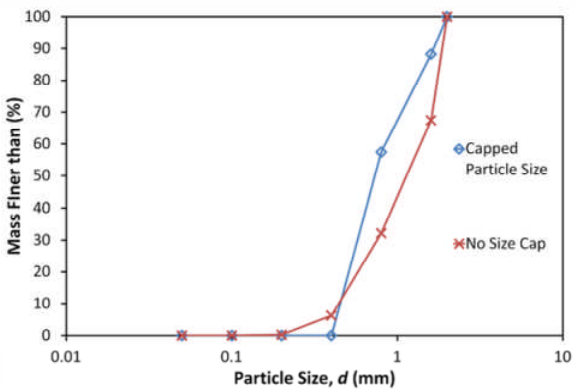

(b)

Figure 4.12 Effects of a comminution limit on the normal compression plot (a) and the particle size distribution (b) after compression to 30 MPa

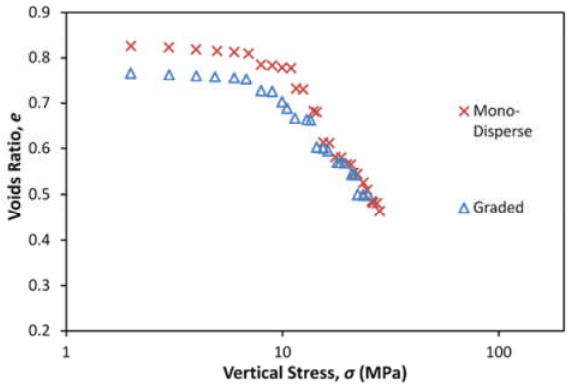

Figure 4.13 Effects of different grading on the normal compression plot

Simulations have been performed on monodisperse assemblies with the same initial size d_0 and strength q_0, but with various Weibull Moduli. Decreasing the modulus increases the variability in strength and also governs the assumed size-hardening law according to equation [4.7]. With d_0 = 2 mm and q_0 = 37.5 MPa, q_0 as a function of particle size is plotted for various values of Weibull Modulus which are related to the slope of the lines in Figure 4.14,

according to equation [4.7]. The resulting normal compression lines and the ensuing particle size distributions as a function of applied stress for assemblies with varying Weibull moduli are shown in Figure 4.15.

It is apparent from the normal compression curves that for a given initial value of q_0, the Weibull modulus dictates the rate of onset of yielding (the maximum curvature of the plot). Furthermore, because it has been assumed to control the hardening law as defined in equation [4.7], it also affects the gradient of the normal compression line following yield. As the modulus decreases, there is more variation in particle strengths for any given particle size. This means a portion of weaker particles hence the earlier onset of yielding and a less well-defined yield point.

The modulus of 4.0 means a fairly narrow distribution of strengths, which explains why this simulation demonstrated the latest and most sudden yielding. It also reduces the hardening effect (i.e. d reduces more rapidly with increasing stress), so has the steepest normal compression line and most overall breakage. The final number of particles is greater than all lower values of m. The lowest modulus, m = 1.0 shows some very early breakage, but a more gradual, early yield point followed by a shallower normal compression line. The grading curves reveal that the lowest modulus exhibits fewest breakages and the least developed grading; the highest modulus displays the most breakage and evolved grading curve. Because the hardening law in equation [4.7] has been assumed, m governs both the rate of onset of yield and the plastic compressibility index, which will be separated later in the chapter.

A lower modulus implies material 'disorder'. Considering critical flaw size with regard to Griffith's Law (Griffith, 1921), high Weibull moduli would imply that as grain size decreases, the size of the critical flaw becomes a higher proportion of the particle, meaning a narrower overall distribution of critical flaws (and critical stress) and less variability, regardless of particle size. A low modulus however implies that as particle size increases, the critical flaw size

increases at a greater rate (suggesting an upper limit of particle size), and resulting in much more variation in critical flaw size and fracture stress.

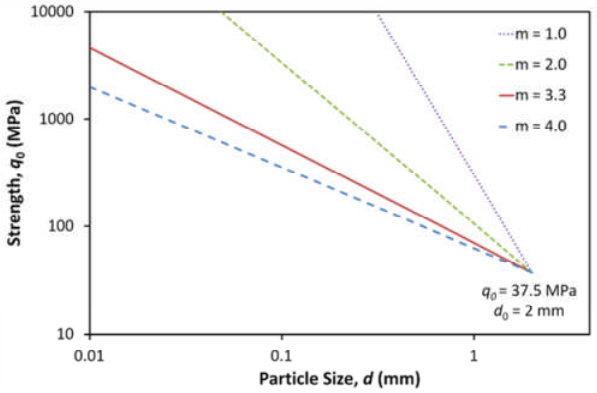

Figure 4.14 Strength as a function of size for various Weibull moduli with initial strength 37.5 MPa, using the hardening law in equation [4.7]

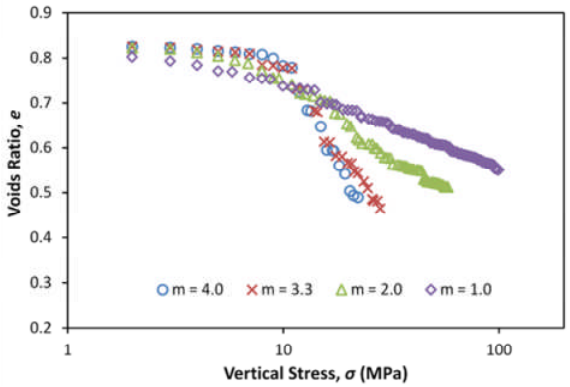

(a)

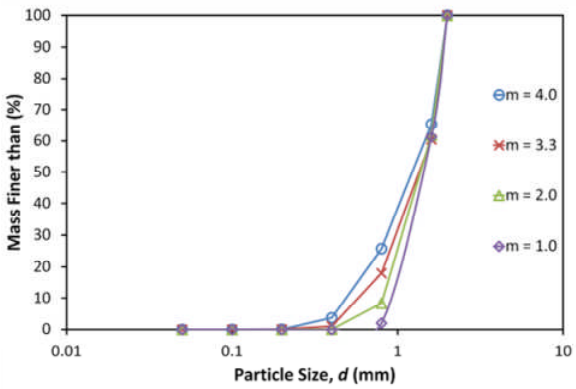

(b)

Figure 4.15 One-dimensional normal compression plots (a) and the particle size distributions (b) for various Weibull moduli

4.2.4 Alternative Breakage Mechanisms

Two alternative breakage mechanisms have also been explored: splitting into 3 and 4 equal fragments. For these mechanisms, the new particles created

overlap and are completely within the boundary of the original particle. This is similar to some of the investigative work performed by Ben-Nun and Einav (2010), except in 3D and with different breakage criteria and mechanisms. Ben-Nun and Einav explored three breakage configurations: splitting in to 3, 5 and 6 particles, each case randomly orientated. However, the kinematic constraints of this process are very different in three dimensions.

When splitting into three fragments—trilateral breakage—the emergent particles are placed at equal distance from one another and from the centre of mass of the original particle, illustrated in Figure 4.16(a). One emergent particle is placed in the direction of the major principal stress, while the axis connecting the centres of the two other emergent particles lies in the direction of the minor principal stress. The three fragments move outwards, along the lines connecting their centres of mass to that of the original parent particle.

For the case of splitting into four equal fragments—quadrilateral breakage—the emergent particles are placed in an equal quadrilateral arrangement, aligned with the major and minor principal stress axes. The overlap causes the particles to move outwards radially from the central point, in equal directions in the minor-major stress plane, shown in Figure 4.16(b). The same initial sample was used, with d_0 = 2 mm and m = 3.3, and an initial strength of q_0 = 37.5 MPa.

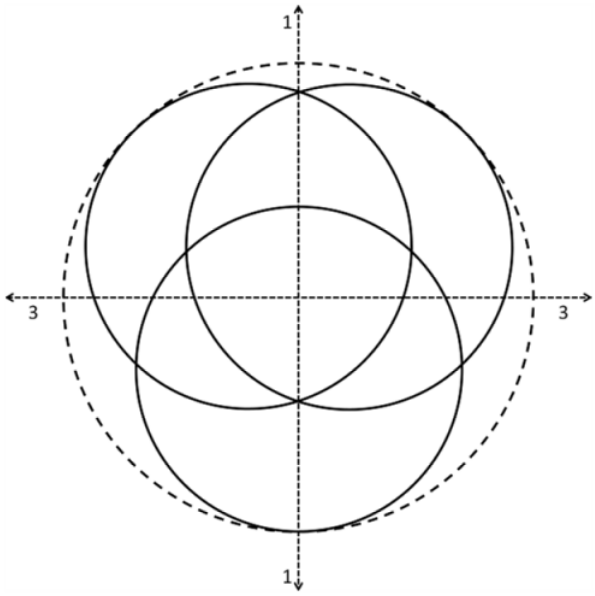

(a)

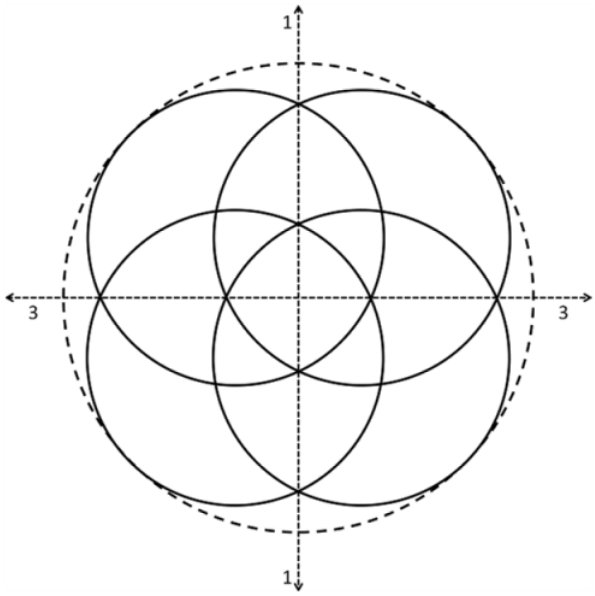

(b)

Figure 4.16 Alternative splitting mechanisms: trilateral splitting into 3 equal particles (a), and quadrilateral splitting into 4 equal particles (b)

As can be witnessed in Figure 4.17, there is not much difference in the normal compression lines; the curves appear to have very similar yield points and the same gradient. This suggests that the manner of breakage does not alter the normal compression line, which only depends on the particle strength as a function of size, which is a material constant. This seems logical when it is well known that various densities of the same material converge upon the same normal compression line (e.g. McDowell 2002). The fact that the

breakage mechanisms have little or no effect on the compression lines would imply that they also have little effect on the grading curves at a given stress. As can be viewed in Figure 4.17(b), this seems consistent—there is not much effect on the particle size distributions, however they are not fully evolved so it is difficult to confirm categorically that this is the case. Ben-Nun and Einav (2010) reported that changing the breakage configuration *did* change the final grain size distributions with regard to the fractal dimension, although this was in 2D, where the kinematic constraints are very different.

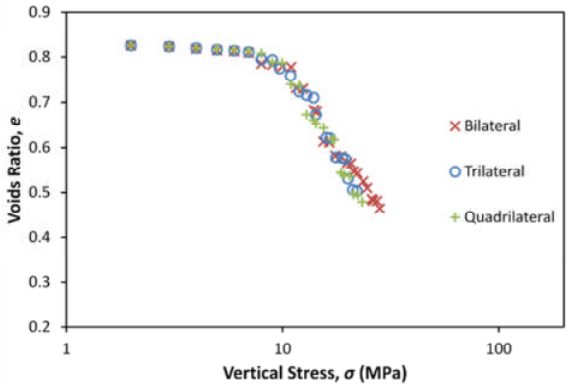

(a)

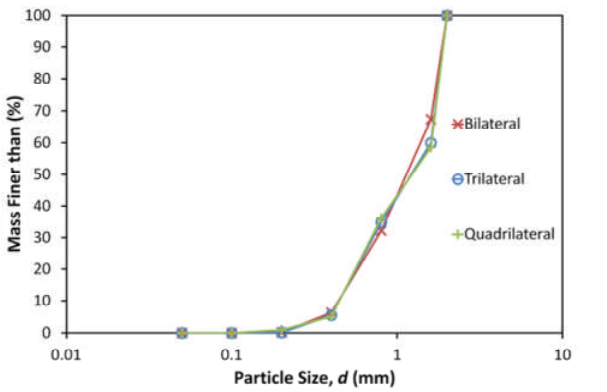

(b)

Figure 4.17 One-dimensional compression plots for various breakage mechanisms (a) and the associated final particle size distributions (b)

4.2.5 Alternative Hardening Laws

It seems rational to investigate size hardening laws which are independent of the Weibull modulus, isolating the size effect from the distribution of strengths. As such, two additional alternative laws have been employed. Each hardening law has its own degree of justification, however, the purpose

here is to determine the sole effects the size hardening law has on normal compression, rather than which provides the most realistic results.

The first alternative assumes that surface-initiated flaws dominate fracture. This would mean the surface area of a particle is the influential factor instead of volume. Using Weibull statistics as before, and as shown in section 2.5.2, one can arrive at the following relationship:

$$q_0 \propto d^{-2/m} \quad [4.8]$$

A second alternative, based on Griffith's Law of fracture mechanics (Griffith, 1921), assumes that the size of the critical flaw, *a,* in a particle is proportional to its size, i.e. $a \propto d$. Griffith (1921) states that the fracture stress is proportional to the square root of the flaw size, so one can say:

$$q_0 \propto d^{-1/2} \quad [4.9]$$

Using strength and size parameters as before (q_0 = 37.5 MPa, d_0 = 2 mm, and m = 3.3) it is possible to compare the various size hardening laws for a given initial distribution of strengths. Figure 4.18 shows the corresponding normal compression lines and final grading curves for the three laws described above. For the alternative hardening rules, i.e. equations [4.8] and [4.9], the plastic compressibility changes for a given Weibull modulus. This results in such a degree of particle breakage and reduction in voids ratio that it was not always possible to reach high stresses. This is evident in the normal compression graph: if the compression lines remained linear they would approach very low void ratios before reaching a stress such as 100 MPa. In reality the compression line would undergo a change in curvature due to the comminution limit as discussed earlier. All three compression lines have the same yield point and rate of onset of yield because the Weibull modulus is the same. This confirms that the initial distribution of strengths determine the nature of yielding. It is evident that Griffith's hardening law, which gives the smallest size-effect on particle strength, gives the steepest compression

line. When a particle breaks in the simulation with the original hardening law, given in equation [4.7], the new fragments have higher strengths than in the other two simulations, giving the compression line a shallower gradient as larger stresses are required to break particles and reduce the void ratio. This shows that it is the hardening law exclusively that determines the slope of the compression line. This is consistent with what was observed in Figure 4.15 when changing the modulus, but this time without altering the strength distribution. If one considers the extreme case where particles of all sizes have equal strengths, this would lead to a catastrophic collapse in void volume after yield.

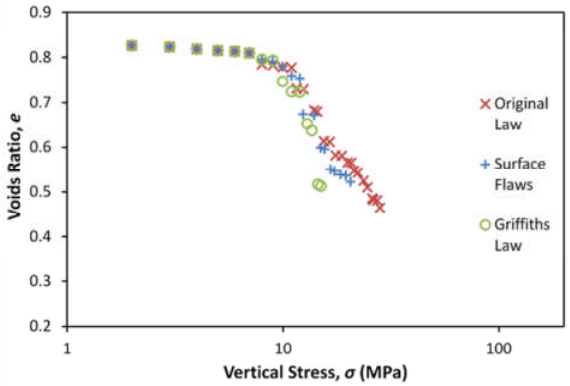

(a)

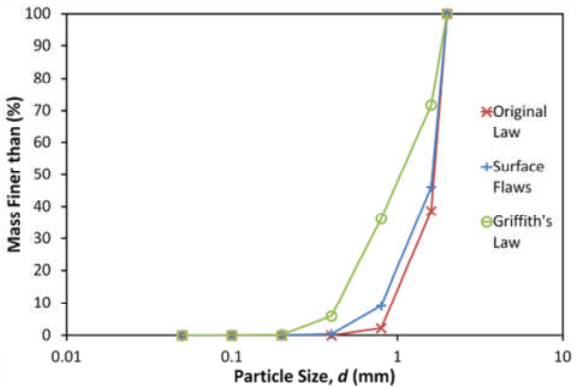

(b)

Figure 4.18 Effects of alternative hardening rules on the one-dimensional normal compression lines (a) and the particle size distributions (b) for a given stress

4.2.6 Alternative Strength Distributions

Continuing to separate the dual effects of the hardening law and strength distribution, it is possible to vary the distribution of strengths for a given size

of particle while keeping the size effect on strength constant. Using the assumed law from equation [4.7], with a Weibull modulus of 3.3, simulations were conducted using alternative distributions of particle strengths, so that Weibull cannot be deemed to be essential for normal compression. The variance of the distribution of initial strengths determines the rate of onset of yield, and to establish if non-Weibullian distributions have the same effect, different distributions have been employed. Two dissimilar uniform distributions of strengths were used, as well as a simulation using a single particle strength. All distributions (including single strength) had the same initial mean strength and size hardening law. The mean value of strength, q_{m} for Weibull distribution is given by:

$$q_{\mathrm{m}} = q_0 \cdot \Gamma\left(\frac{1}{m} + 1\right) \qquad [4.10]$$

where Γ is the gamma function. Values of m = 3.3 and q_0 = 37.5 MPa give a mean strength of 33.6 MPa, so the non-Weibullian distributions are given this average initial strength to enable comparison. Because $q_{\mathrm{m}} \propto q_0$, average strength has the same hardening law. That is to say, for each strength distribution, including a single strength as a function of size, it was assumed that:

$$q_{\mathrm{m}} \propto d^{-3/3.3} \qquad [4.11]$$

For the first alternative, the particle strengths for a single particle size satisfy a uniform distribution with a fixed range of 60 MPa, i.e. for particles of size d, crushing strengths lie within the range $q_{\mathrm{m},d} \pm 30$ MPa. The second alternative simulation also makes use of uniform distributions but with a constant coefficient of variation so that the standard deviation in particle strength for a given size is proportional to its mean with a minimum strength of 0 MPa.

The normal compression lines for these three simulations, along with the simulation using a Weibull distribution of strengths are given in Figure 4.19.

As expected, all simulations display the same slope at high stresses (about 0.5). The lines appear to converge, although there is a slight deviation exhibited by the simulation with varying range (constant coefficient of variation). It is clear that the distribution of strengths governs the rate of onset of yield, but it is the average strength as a function of particle size which governs the slope of the normal compression line. All plots have approximately equal slopes at approximately 30 MPa. The simulation with single particle strengths for a given size shows the latest, most sudden onset of yield before a sharp reduction in voids ratio. This is consistent with experiments on glass beads which tend to have a low variability in strength ($m \approx 6$) and uniform grading (Nakata et al, 2001a). The two simulations with uniformly distributed strengths undergo a more gradual onset of yielding, as does the simulation with strengths satisfying a Weibull distribution.

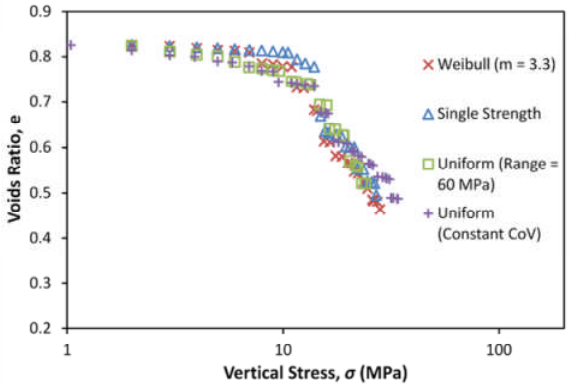

Figure 4.19 Plastic compression responses for simulations with the same mean particle strength (33.6 MPa) but varying particle strength distributions

4.2.7 Fractal Distributions

Inspecting the respective particle size distribution suggests that a fractal distribution has emerged. To recall equation [2.34] from section 2.5.6, a fractal distribution is one such that:

$$N\,(\,L > d\,)\;\propto\; d^{-D_{\mathrm{fr}}} \qquad [4.12]$$

Where N is the number of particles of size L, greater than size d, and D_{fr} is the fractal dimension (Turcotte, 1986). The nature of this equation means that a fractal distribution would appear linear on a distribution plot with two

logarithmic axes, with the fractal dimension emerging as the slope. It was shown in the literature review that most granular materials (not only soils but materials such as coal, fault gouge, and ice) under pure crushing evolve towards a distribution with a fractal dimension between 2.0 and 3.0, remarkably usually about 2.5 (Turcotte, 1986; Sammis et al., 1987; Palmer and Sanderson, 1991; Steacy and Sammis, 1991; McDowell and Daniell, 2001), with two-dimensional materials developing a dimension between 1.0 and 2.0. The simulations of Ben-Nun and Einav (2010) resulted in fractal dimensions of around 1.1–1.4 for discs.

Considering only the initial sample with silica sand parameters (d_0 = 2 mm, q_0 = 37.5 MPa, m = 3.3), as this simulation has the most fully evolved grading, it certainly appears a fractal distribution has emerged. The number of particles by percentage with a larger diameter is plotted against diameter on a logarithmic scale in Figure 4.20. The curves appear exponential. This data is plotted again with the percentage by number of particles also on a logarithmic axis in Figure 4.21, and the linearity implies fractal geometry. The slope becomes steeper (i.e. the fractal dimension increases) with increasing stress, with the slope appearing to become constant, indicating a steady value has been reached. As the stress increases, the linear portion of the curve from which the fractal dimension can be obtained increases in length, suggesting a more reliable value. The final slope (30 MPa) gives a value of D_{fr} = 2.5, which is encouraging considering what is observed for natural granular materials. Plotting the absolute number of particles (also on a logarithmic axis) against diameter, in Figure 4.22, shows that it is almost solely the smallest particles which are fracturing as the stress is increased. Despite encompassing approximately 20000 particles, the final distribution only covers approximately 1 log cycle of sizes—which should be considered a narrow range. In Ben-Nun and Einav's (2010) 2D analysis, their final distributions spanned almost 2 log cycles.

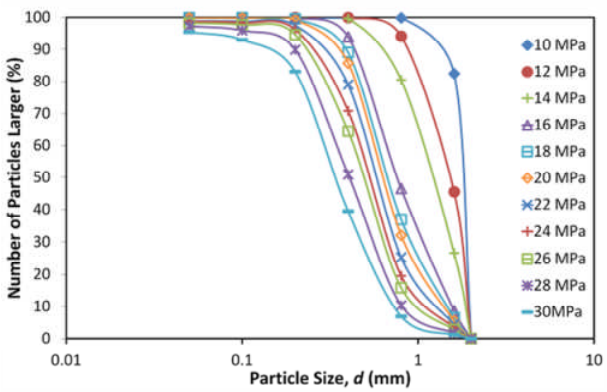

Figure 4.20 Evolving particle size distribution form the simulation of silica sand

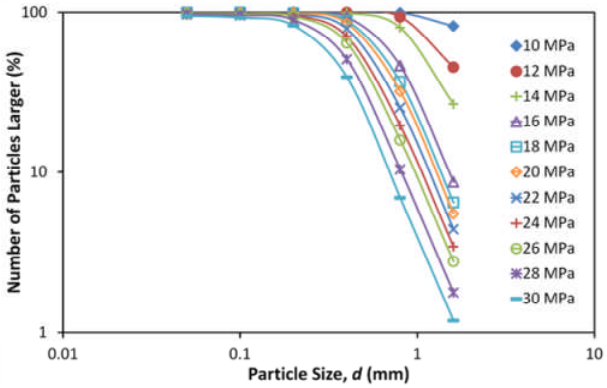

Figure 4.21 Evolving particle size distribution form the simulation of silica sand plotted on double logarithmic axes

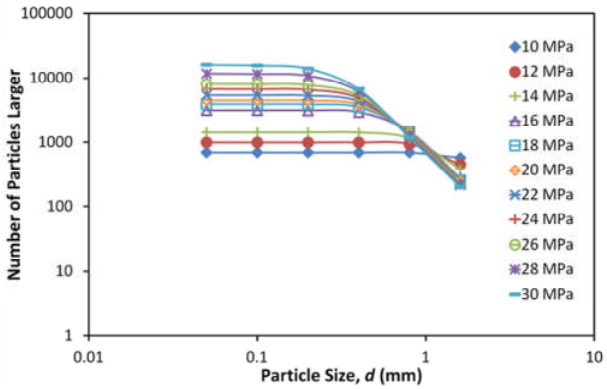

Figure 4.22 Evolving particle size distribution form the simulation of silica sand plotted using the absolute number of particles on double logarithmic axes

As discussed earlier, McDowell and Daniell (2001) investigated why a value of about 2.5 consistently emerges for soils and other granular materials. From analysis of simulations of uniform blocks by Steacy and Sammis (1991), they remarked a fractal dimensions of 2.5 emerged if blocks of the same size with finite contact area could not exist, and if a 'stress bias' influenced the probability of fracture. Hence it would seem worthwhile to examine

neighbouring particles in the simulations of silica sand after undergoing one-dimension compression. Defining neighbouring particles simply as two particles which are in direct contact (i.e. there exists an overlap and force acting between them), it is possible to observe how many same-sized particles are neighbours. The number of neighbouring particles of equal size, in terms of percentage of total particles in contact, is plotted against macroscopic vertical stress in Figure 4.23 for the original simulation based on data for silica sand. For the initially uniform sample, all contacts are between equal-sized particles; after loading to 30 MPa approximately 15% of all contacts are between particles of the same size. This value appears to exhibit little change after about 15 MPa, suggesting a steady condition. This is not quite the 0% speculated by Steacy & Sammis (1991), but it seems very reasonable when recognising that particles are considered most vulnerable when loaded by neighbouring particles of the same size, as this allows the particle to be loaded at opposite poles, inducing the maximum tensile stress. If you compare Figure 4.23 with Figure 4.24, which shows the fractal dimensions derived from the progressive grading curves for the same simulation, it shows a similar development under increasing stress: that is to say the fractal dimension reaches 2.5 when the number of same-sized neighbours reaches a minimum.

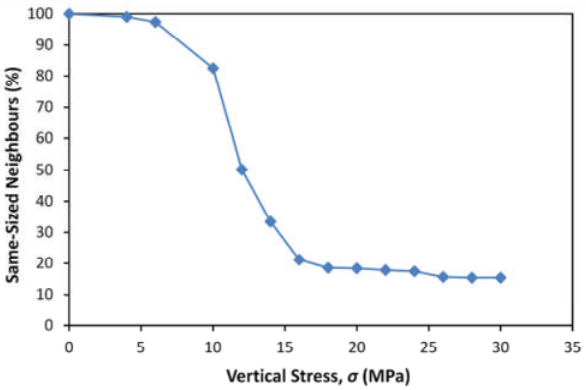

Figure 4.23 Percentage of equally sized neighbouring particles as a function of applied stress

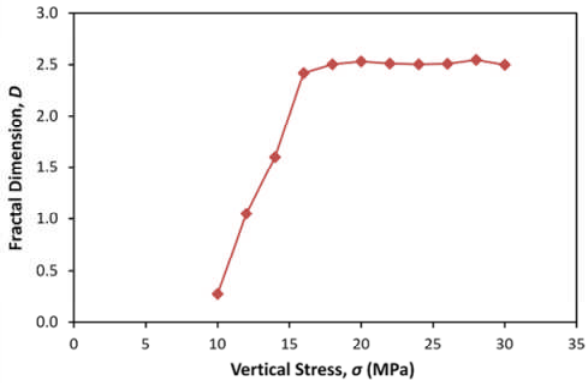

Figure 4.24 Fractal dimension as a function of applied stress

However, more is revealed by examining the contacts within the final crushed sample with regard to individual particle sizes. The particles can be described in terms of their hierarchical 'rank', or size—with the largest (initial) particle size d_0, with fragmentation producing subsequent particle sizes d_1, d_2,...,d_s, where d_s is the smallest. After compression, there are approximately 202 largest particles, size d_0, which have an average of 22.2 contacts each. For these 202 particles, the number of particles having 1 or more same-sized neighbours is 163, giving an average number of contacts with same-sized neighbours of 1.4. The remaining contacts are with smaller grains, as no larger particles exist. Considering the next sizes of particles (d_1, d_2, ...,d_8) each rank increases in quantity as the particle size decreases, with approximately 3,000 particles of size d_8 (0.32 mm). As one would expect, the average total number of contacts per ball reduces with decreasing particle size. However, interestingly, what remains constant is the number of contacts with particles of equal or larger size. Particles of all these sizes have an average of approximately 2 contacts with particles of equal or larger diameter. This number remains constant across the range of sizes, while the average number of contacts with smaller particles (and hence the average total number of contacts) per ball decreases steadily with reducing particle size. This apparent self-similarity is also visible in Figure 4.25, where similar random packing is visible across the scales. These observations imply the particle size distribution is indeed fractal in character, at least across the intermediate range of the discrete distribution. The subsequent ranks of particles, i.e. d_9,

d_{10},... up to d_{32} , decrease in number and have not fully evolved, with just 4 particles of size d_{32} = 0.0012 mm.

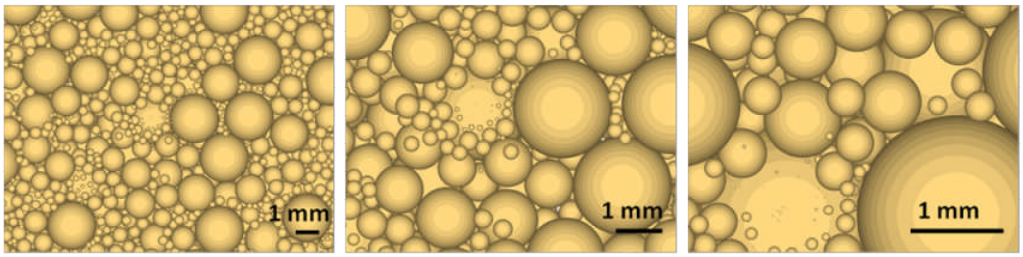

Figure 4.25 View of a virtual cutting plane through the numerical sample across several scales

It appears that it is breakage of particles which are primarily loaded by same-sized or larger particles that leads to a stable, fractally-distributed material. In this model, almost all particles regardless of rank have an average of 2 contacts with equally-sized or larger particles, however, the smallest particles have far fewer total contacts, and are therefore much more likely to have a high induced octahedral shear stress, and therefore continue to fracture as stress increases, leading to a fractal distribution of particle sizes, apparently tending towards an ultimate fractal dimension of 2.5.

With regard to the effect of a 'stress bias', there is almost certainly an influence when a single particle breakage is considered. The vertical load which was carried through the original particle will be apportioned to the surrounding particles, causing an increased stress concentration in the surrounding area. The simulations performed by Steacy & Sammis (1991) did not involve loading the array of blocks, which is why they deemed it necessary to implement an artificial influence. It seems sensible to assume there is such an influence in a loaded, stress-controlled simulation. For a single incidence of breakage, scanning the new fragments reveals that usually between 20–30% of them are within 2 radii distance of a particle which broke on the previous occasion, which supports this idea.

4.2.8 New Compression Law: Log e–Log σ

A double logarithmic plot was suggested by Pestana & Whittle (1995), who described typical values for the compression slope for sand lying between 0.4

and 0.5, usually towards the upper limit of 0.5. The compression line for silica sand from McDowell (2002) has a slope of 0.46 (≈ 0.5) when plotted on double logarithmic axes. The simulation in this chapter using the data of McDowell's silica sand has a corresponding slope of 0.5, which shows impressive agreement, and both are within the correct range. The slopes are displayed in Figure 4.26.

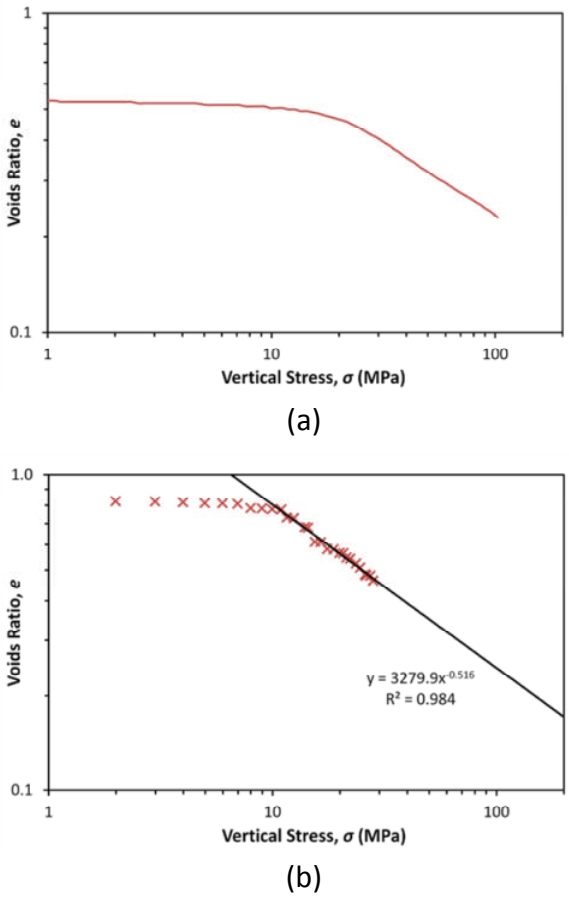

Figure 4.26 One-dimensional compression plots for silica sand from McDowell (a) and from the numerical simulation (b), plotted on log *e*–log *σ* axes

McDowell (2005) justified the use of a double logarithmic plot, and went on to validate the slope of the compression line physically using fractal crushing theory, which was outlined briefly in section 2.5.6. McDowell used an assumed fractal dimension of 2.5, which is what many granular materials evolve to under pure crushing (Turcotte, 1986; McDowell and Daniell, 2001). The plots in Figures 4.21 and 4.22 show fractal dimensions in good agreement with this, and from Figure 4.24 one might assume that the value of 2.5

remains consistent at higher stress levels with further crushing. Assuming a value of 2.5, McDowell (2005) showed that for a granular material with strengths forming a Weibull distribution with a modulus of approximately 3, the slope of the normal compression line should be about 0.5 on a log *e*–log *σ* plot.

Assuming the same fractal dimension (i.e. 2.5), just as McDowell (2005) did, from equation [4.12] it is possible to say that the number of particles *N* greater than or equal to a size d_i is given by:

$$N(L \geq d_i) \propto d_i^{-2.5} \quad [4.13]$$

Considering again a hierarchical splitting model, with largest (initial) particle size d_0, and subsequent broken particle sizes d_1, d_2,...,d_s. The distribution of discrete sizes can be approximated to be fractal if it covers a wide range of scales (Turcotte, 1986; Palmer and Sanderson, 1991). Using equation [4.13] and considering the next smaller size of particle d_{i+1}, we can write:

$$N(L \geq d_{i+1}) \propto d_{i+1}^{-2.5} \quad [4.14]$$

Subtracting gives the number of particles with size equal to d_{i+1}:

$$N(L = d_{i+1}) = N(L \geq d_{i+1}) - N(L \geq d_i) \quad [4.15]$$

This can be written:

$$N(L = d_{i+1}) = N(L \geq d_{i+1}) \left[1 - \left(\frac{d_i}{d_{i+1}}\right)\right] \propto d_{i+1}^{-2.5}\left[1 - n^{1/3}\right] \quad [4.16]$$

where *n* is the number of fragments produced by each fracture and is constant. Equation [4.16] implies a constant probability of fracture between each size (see Turcotte, 1986; Palmer and Sanderson, 1991). This is sensible because the normal compression lines have been shown to be independent of the distribution of strengths for a given particle size, and therefore the

probability of fracture must be dominated by the loading geometry, as discussed earlier. It can be inferred that for the smallest size, (i.e. particles of size d_s) some of which will break when stress is increased (a proportion of each particle size in the hierarchical splitting model remains as stress increases, this is what gives the fractal distribution):

$$N(L = d_s) \propto d_s^{-2.5} \quad [4.17]$$

which, considering volume leads to:

$$V(L = d_s) = N(L = d_s) \cdot d_s^3 \propto d_s^{0.5} \quad [4.18]$$

The size of the smallest particle is a function of stress level according to the assumed hardening law for the soil. Recalling the original hardening law in [4.7], re-written for the smallest particles as:

$$q_m \propto d_s^{-3/m} \quad [4.19]$$

and given that the current macroscopic stress, σ is proportional to the average strength of the smallest grains, rearranging and substituting equation [4.19] into [4.18], gives:

$$V(L = d_s) \propto \sigma^{-m/6} \quad [4.20]$$

McDowell (2005) proposed that the void space is dominated by the smallest particles—it is well known, for example, that soil permeability is governed by the smallest particle sizes (Hazen, 1911). McDowell (2005) then proposed, and justified in terms of the implied particle kinematics, that the void space is proportional to the total volume of the smallest particles once a fractal distribution has emerged. In this case, [4.20] implies:

$$e \propto \sigma^{-m/6} \quad [4.21]$$

A power law in this form makes sense when one considers that the void space is dependent on the smallest particle size. The smallest particle must in turn be related to the stress level according to the size effect on strength—which is a power law, and is assumed in this case to be governed by the Weibull modulus. The void space should therefore be a power function of stress, giving a linear normal compression line on double logarithmic axes.

The value of 3.3 used in the simulations, for all intents and purposes, can be considered equivalent to the value of 3 for which McDowell (2005) attained a slope of 0.5. Using the same approach for the assumed hardening law in equation [4.7], materials with Weibull moduli of about 4, 3, 2, and 1 should have slopes equal to approximately 0.7, 0.5, 0.3 and 0.2 respectively, according to equation [4.21]. The normal compression lines are plotted in Figure 4.27 for the range of m values used in the above simulations. For moduli of approximately 4, 3, 2, and 1, the slopes are 0.7, 0.5, 0.3 and 0.2 respectively. These values agree with the values predicted using McDowell's physical justification. All the lines appear linear, confirming a power law.

Pestana & Whittle (1995) supposed that sands should have a slope in the region of 0.3–0.5 which, assuming the original hardening law in equation [4.7] is applicable, would correspond to a material with crushing strengths obeying Weibull statistics with a modulus in the range of 1.8–3.0. This fits data from the literature: typical values of m for various sands are in the region 1.5 to 3.3 (e.g. McDowell, 2001, Nakata et al. 1999).

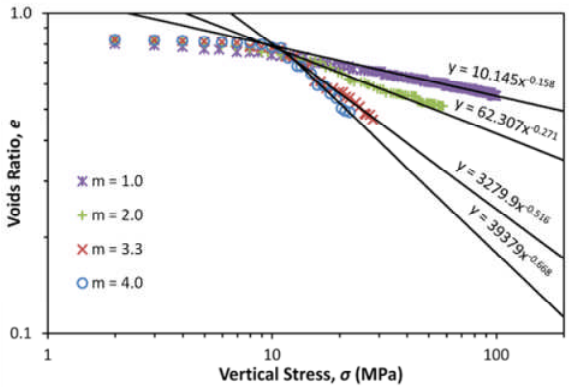

Figure 4.27 Normal compression lines on a double logarithmic plot for q_0 = 37.5 MPa with various Weibull moduli, assuming hardening law given in Equation [4.7]

Considering the alternative hardening laws, if surface flaws are alleged to dominate fracture and equation [4.8] is assumed, then the following relationship can be arrived at in a similar fashion to above:

$$e \propto \sigma^{-m/4} \qquad [4.22]$$

Whereas if the other alternative hardening relationship assuming Griffith's Law, in equation [4.9] is used, the following relationship is obtained:

$$e \propto \sigma^{-1} \qquad [4.23]$$

These would predict slopes of about 0.8 and 1.0 for former and latter hardening laws respectively, and Figure 4.28 appears encouraging, and indicates similar values for the slopes, although the compression lines aren't considered long enough to confirm this is the case.

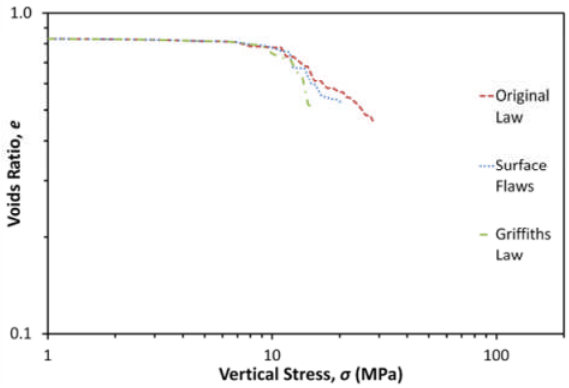

Figure 4.28 Normal compression plots far various hardening laws using double logarithmic axes

It has therefore been shown that the plastic compressibility of granular materials is solely a function of the size effect on particle strength. This has implications for the prediction of the compressibility of aggregates comprising very large particles. For example, if one is interested in the compressibility of a rockfill dam, then by crushing individual rocks and obtaining the size effect on strength, one would be able to predict the compressibility.

If particle strengths are related to size by a law in the form:

$$q_0 \propto d^{-b} \quad [4.24]$$

and one-dimensional compression can be described by the following equation:

$$\log e = \log e_0 - C_c \log \sigma \quad [4.25]$$

it is shown that the compression index, C_c, is a function of the parameter b: $C_c = f(b)$. Specifically, the following relationship can be inferred from the physical justification by McDowell (2005) and results of simulations with various assumed hardening laws:

$$C_c = {}^{1}/_{2b} \quad [4.26]$$

Hence, the end result is that for the first time, there is the following equation for the normal compression line:

$$\log e = \log e_0 - \frac{1}{2b} \log \sigma \quad [4.27]$$

where b controls the particle size effect on strength. Strictly speaking, to be dimensionally consistent, equation [4.27] should be rewritten as the following:

$$\log e = \log e_y - \frac{1}{2b} \log \frac{\sigma}{\sigma_y} \quad [4.28]$$

where e_y is the value on the linear log-log plot at a stress corresponding to the yield stress σ_y, and σ_y is proportional to the average particle strength.

In addition, for the first time, simulations in 3D have used a reasonable number of particles which holds much promise for use in boundary value problems.

4.3 CONCLUSIONS

In this chapter, DEM has been used to simulate one-dimensional compression to investigate particle crushing, the associated phenomenon of fractal particle size distributions. Particle fracture has been simulated using a range of very simple mechanisms, replacing the breaking particle with new smaller particles while maintaining constant mass. Previously only agglomerates have been used to simulate particle crushing in 3D during compression, these demand a very large number of initial particles and bonds. Particle fracture was governed by the octahedral stress within a particle, which takes into account multiple contacts, and has been related to data measured from single particle crushing tests.

Normal compression lines are clearly observed, and the observed slope is consistent with the theoretical prediction. For an initially uniform particle size, the rate of onset of yield is a function of the distribution of particle strengths. For an initial voids ratio and given Weibull modulus (coefficient of variation), the yield stress is proportional to the average particle octahedral shear strength. The slope of the normal compression line and the particle size distribution appear to be independent of the breakage mechanism or the distribution of strengths, and solely dependent on the size effect on average particle strength. This appears to clearly show, for the first time, that the plastic compressibility index is simply the hardening law due to the smallest particles breaking and becoming statistically stronger. This has implications for the prediction of the compressibility of aggregates comprising large particles.

The evolution of a fractal particle size distribution appears to be triggered by the tendency of similar sized neighbouring particles to fracture. The results show clearly that a fractal distribution of particle sizes emerges, with a fractal number of 2.5. The simulations also show the correct behaviour if a comminution limit is included, such that the compressibility index reduces at high stresses.

The compression lines have also been plotted in log e–log σ space and the prediction for silica sand shows agreeable similarity to the experimental results, and the slope is in agreement with McDowell's (2005) theoretical prediction.

The overall results show encouraging similarity with widely reported physical behaviour. Given that the simplest assumptions have been made—particles split according to octahedral shear stress and the fragments move in the direction of the minor principal stress—the resulting simulations have shown an insight into one-dimensional compression and replicated this process correctly in 3D for the first time. It would appear that the micro mechanics of normal compression have finally been exposed.

The model holds much promise in the application to solving boundary value problems, now that agglomerates are not required to simulate the crushing process.

CHAPTER 5

APPLICATIONS OF PARTICLE CRUSHING MODEL

5.1 CREEP

5.1.1 Introduction

In Chapter 4, a new equation for the one-dimensional normal compression line was proposed, which contained a parameter controlling the size effect on average strength. It was shown that this new equation held for a wide range of DEM simulations of crushable aggregates. This section incorporates the time dependence of particle strength, and a new equation is proposed and examined using simulations of one-dimensional creep.

Creep strain is traditionally reported as being linearly proportional to the logarithm of time, e.g. Figure 2.46 (Leung et al., 1996). However, although typical creep behaviour may seem linear on a plot of voids ratio against the logarithm of time, this section aims to show that the new proposed law, which is linear when voids ratio is *also* plotted on a logarithmic scale, is more appropriate. The simulations in this section examine the effect of the size-hardening law, the strength-time dependency and stress level and it is shown that the new equation holds for each case.

5.1.2 New Creep Law

McDowell (2003) proposed a theoretical explanation for observed creep behaviour, which will be briefly described again here. Granular materials creep under constant effective stress (Murayama et al., 1984; Leung et al., 1996; Lade and Liu, 1998), such that creep strain is usually reported to be proportional to log time:

$$\varepsilon = C \log(t/t_0) \qquad [5.1]$$

where t_0 is the time from which creep strains are measured. Recalling from the literature review, it has been shown that the creep of granular materials is

accompanied by particle crushing (e.g. Leung et al., 1996; Lade and Liu, 1998). McDowell (2003) proposed that a linear normal compression lines in voids ratio–log stress space (McDowell and Bolton, 1998):

$$e = e_{\mathrm{c}} - \lambda \ln\left({}^{\sigma}/_{\sigma_{\mathrm{c}}}\right) \qquad [5.2]$$

was consistent with equation [5.1]. The assumptions were that the current macroscopic stress should be proportional to the average strength of the smallest particles in the aggregate: these particles continue to crush under increasing stress levels, becoming statistically stronger and filling voids. According to equation [5.2], an aggregate should be in equilibrium with a voids ratio e_{c} under an applied stress σ_{c}, where σ_{c} is proportional to the average strength of the current smallest particles σ_{s}, so that:

$$\sigma_{\mathrm{c}} = k\sigma_{\mathrm{s}} \qquad [5.3]$$

where *k* is independent of particle size due to self-similarity across different orders of particle size. Substituting equation [5.3] into equation [5.2] gave:

$$e = e_{\mathrm{c}} - \lambda \ln\left({}^{\sigma}/_{k\sigma_{\mathrm{s}}}\right) \qquad [5.4]$$

To recap, the law for the time-dependent strength of ceramics is that for a tensile test on a ceramic specimen: if the standard test used to measure the tensile strength σ_{TS}, takes a time *t*(test), then the stress σ_{t} which the sample will support safely for a time *t* is given by the equation:

$$\left(\frac{\sigma_{\mathrm{t}}}{\sigma_{\mathrm{TS}}}\right)^{n} = \frac{t(\mathrm{test})}{t} \qquad [5.5]$$

where *n* is the slow-crack growth exponent (Ashby and Jones, 1986; Davidge, 1979). Data for *n* is very limited, but *n* is 10–20 for oxides at room temperature. It is widely accepted that the failure of a spherical body under diametral compression is, in fact a tensile failure (e.g. Jaeger, 1967)—hence if

$\sigma_{s,0}$ is the average particle strength which could be measured at time $t = t_0$, then the average strength σ_s after a time t, according to equation [5.5] would be:

$$\sigma_s = \sigma_{s,0}\left(t_0/t\right)^{1/n} \qquad [5.6]$$

and substituting equation [5.6] into equation [5.4] then gives:

$$e = e_c - \lambda \ln\left(\sigma/k\sigma_s\right) - \frac{\lambda}{n}\ln\left(t/t_0\right) \qquad [5.7]$$

hence the reduction in voids ratio, Δe as a function of time after time t_0 is simply:

$$\Delta e = \frac{\lambda}{n}\ln\left(t/t_0\right) = \frac{2.3\lambda}{n}\log(t/t_0) \qquad [5.8]$$

so that the log time effect is observed. Taking an initial voids ratio $e_0 = 0.5$, for example, at the onset of creep, the creep coefficient in equation [5.1], given as:

$$C = \frac{2.3\lambda}{n}\cdot\frac{1}{1+e_0} \qquad [5.9]$$

ranges typically from about 0.0015 (taking $\lambda = 0.1$, $n = 100$) to 0.03 (taking $\lambda = 0.2$, $n = 10$). Most of the values of creep coefficients published by Leung et al. (1996) for one-dimensional compression of sand at high stress level fall within this range.

In the previous chapter focusing on particle crushing during the compression of sand, it was shown that the one-dimensional normal compression law is actually given by the equation:

$$\log e = \log e_{\mathrm{y}} - \frac{1}{2b}\log\frac{\sigma}{\sigma_{\mathrm{y}}} \qquad [5.10]$$

where b controls the particle size-effect on mean particle strength, σ_{m}:

$$\sigma_{\mathrm{m}} = d^{-b} \qquad [5.11]$$

and e_{y} is the value on the linear log-log plot at a stress corresponding to the yield stress σ_{y}, and σ_{y} is proportional to the average particle strength for an initially uniformly graded aggregate. In this case, if the analysis described above in section 5.1.2 is reapplied to the new compression line described by equation [5.10], the following can be directly obtained:

$$\log e = \log e_0 - \frac{1}{2bn}\log\frac{t}{t_0} \qquad [5.12]$$

which is the new creep law proposed in this chapter.

5.1.3 Oedometer Sample

As with the simulations in the preceding chapter, an oedometer with a diameter of 30 mm and a height of 7 mm is used. The details are given in Table 4.1. The initial dense random sample consists of 620 particles with uniform size d_0 = 2 mm. The same breakage model is used whereby the octahedral shear stress, given in equation [4.3] is used to determine whether particle fracture should occur or not. When the stress within a particle is found to exceed the individual strength, it is replaced with two new fragments, in the manner of Figure 4.3. The particles have strengths as those in Chapter 4 for the simulations modelling silica sand, i.e. the characteristic value of octahedral shear strength, q_0 is 37.5 MPa for the initial particles (d_0 = 2 mm), the Weibull modulus, m is 3.3, and the size-hardening law is governed by equation [4.7]. In the subsequent simulations, the sample is loaded to a given vertical stress as before, but the particles are also subjected to a time-strength dependency.

5.1.4 Creep of Crushable Agglomerates

In this section, simulations are performed to establish whether equation [5.12] applies to a simple sample of crushable particles subjected to normal compression, and subsequently creep using DEM. To simulate creep, a strength-time dependency is introduced to the model already used and described in detail in Chapter 4. The oedometer sample is compressed beyond yield until the applied axial stress was 10 MPa, for a sample of spheres having a Weibull modulus m of 3.3 and a 37% q_0 strength of 37.5 MPa, which were the parameters used previously to model experimental data by McDowell (2002). Then, using a value of $t_0 = 0.001$ s, *all* particle strengths are decreased according to the relation given in equation [5.6]. The simulation is then cycled while continuously monitoring the octahedral shear stresses within each particle. When the stress within a particle is found to exceed the individual strength, it is replaced with two new fragments. Immediately afterwards, a number of computational cycles are completed to dissipate the artificial pressure increase due to the overlap between new fragments, the same method as used before. During this period, time is *not* considered. The top platen is then gradually reloaded to maintain the constant axial stress of 10 MPa. The stresses are then checked again and if any particles are found to be in a state of breakage, the process is repeated—i.e. particles are replaced with new fragments, the energy is allowed to dissipate, then the platen reloaded to a stress of 10 MPa. Once no more particles are in a state of breakage under a constant axial stress of 10 MPa, the current voids ratio and elapsed time are recorded, after which consideration of time is resumed, and the strength-time dependency is reapplied.

Figure 5.1(a) shows the results for voids ratio as a function of the logarithm of time for three different time exponents n. Figure 5.1(b) shows the same data plotted on a log-log scale according to equation [5.12]. The slopes are shown, and the predicted values according to equation [5.12] are also shown. If a larger value of t_0 is used, any plots of voids ratio against log time would have

the same slope according to equation [5.12], with the curve simply shifted to the right due to the higher starting value. However, the larger increments of time would necessitate a higher number of computational timesteps to complete the simulations.

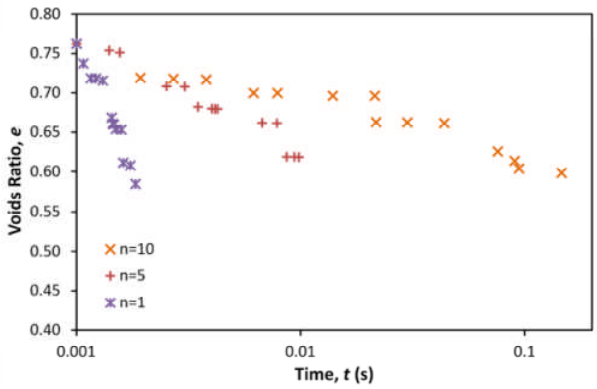

(a)

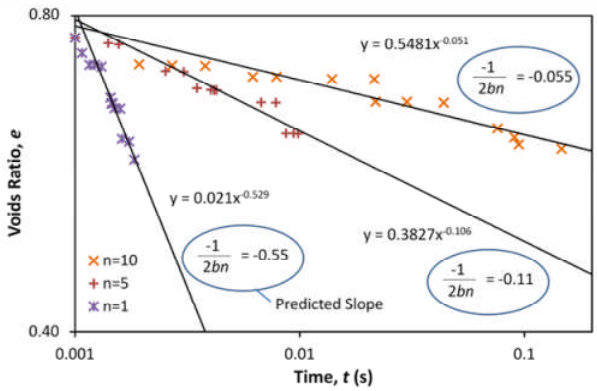

(b)

Figure 5.1 Voids ratio as a function of time for various time exponents *n*, plotted on conventional semi-logarithmic axes (a) and double logarithmic axes (b)

Figure 5.2 shows results for the same initial sample, with a time exponent $n = 1$, and three different Weibull moduli values of 1.0, 2.0 and 3.3 (all with $q_0 = 37.5$ MPa). Figure 5.2(a) shows the conventional plot of voids ratio against log time, and Figure 5.2(b) shows the results on the log-log plot, with the calculated slopes and the predicted values according to equation [5.12].

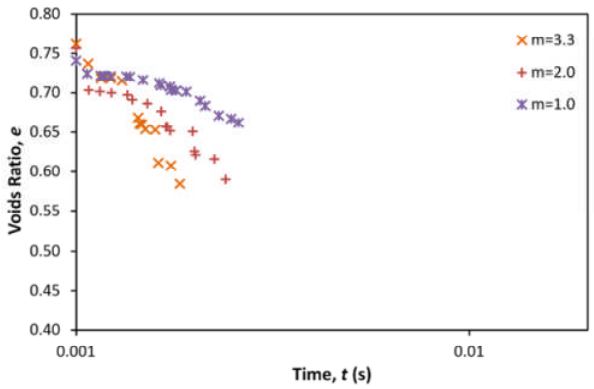

(a)

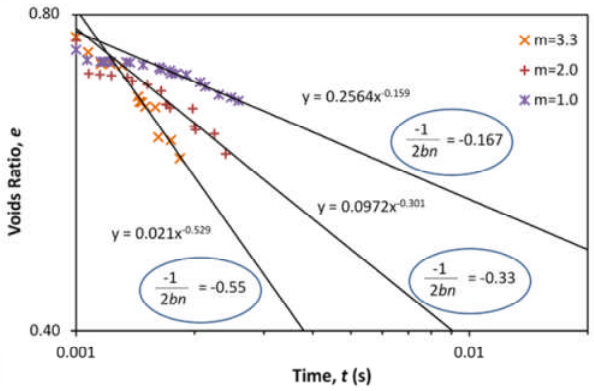

(b)

Figure 5.2 Voids ratio as a function of time for simulations with various Weibull moduli m, plotted on conventional semi-logarithmic axes (a) and double logarithmic axes (b)

Figure 5.3(a) shows the creep response for the sample with $q_0 = 37.5$ MPa, $m = 3.3$ and $n = 10$, one-dimensionally loaded to stresses of 10 MPa and 15 MPa. The same results are plotted in the log-log space in Figure 5.3(b). The simulation loaded to 15 MPa has undergone a higher degree of compression, so has a lower voids ratio at the start of creep. Although the initial voids ratios are different, the slopes are the same and agree with the predicted value according to equation [5.12]. The data points on the log e–log σ plots in all three figures do not fall on perfectly straight lines; this is simply because the initial sample contained only 620 balls. However the figures show clearly that the new equation [5.12] holds for each time exponent, size-effect on strength and stress level considered.

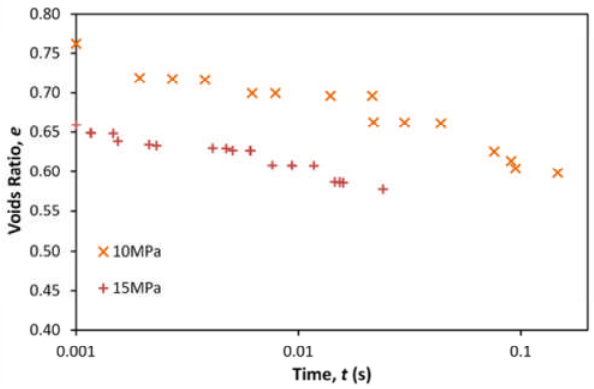

(a)

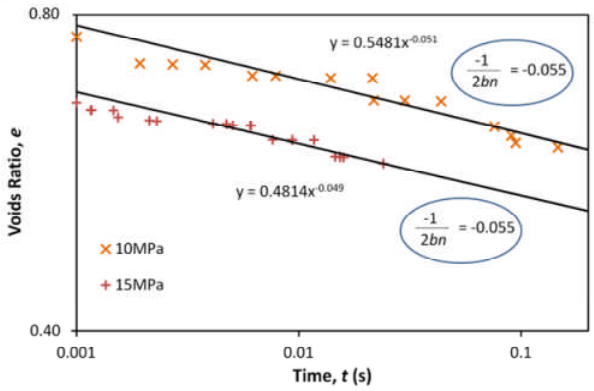

(b)

Figure 5.3 Voids ratio as a function of time for simulations with the same strength characteristics and time exponent under effective stresses of 10 MPa and 15 MPa, plotted on conventional semi-logarithmic axes (a) and double logarithmic axes (b)

5.1.5 Conclusions

The discrete element method has been used to show that the time-dependent law for the strength of ceramics gives rise to the correct creep behaviour under one-dimensional conditions. The simulation results presented agree with the hypothesis that the creep behaviour should be linear when the logarithm of voids ratio is plotted against the logarithm of time. The slope of the line has been shown to be given by a new equation [5.12], which also includes the size effect on average strength as well as the exponent for the time-dependent strength. Therefore, by performing standard tests to obtain the size effect on average tensile strength of grains of a material by crushing between flat platens, and if the exponent for time-dependent strength can be measured by allowing particles to be loaded

under constant stress and measuring the time to failure, then the creep behaviour of an aggregate of such grains can be predicted.

However, the assumption that *all* particle strengths degrade with time at the same rate may be somewhat unrealistic; as particles under no (or very low) stress are unlikely to experience the same decrease in strength, assuming that strength degradation is caused by stress-induced crack growth. A more fundamental analysis, relating strength, time *and* induced stress for each particle may be more appropriate.

5.2 ONE-DIMENSIONAL COMPRESSION OF CEMENTED SAND

5.2.1 Introduction

In this section, simulations are presented which simulate the one-dimensional normal compression of cemented sand. The behaviour of uncemented sand in compression has been investigated thoroughly in Chapter 4, and in the current section, the same model (using a scaled-down oedometer) is used but incorporating inter-particle bonding to simulate cementation.

In the previous chapter, it was shown that it is possible to accurately model the one-dimensional normal compression of uncemented sand. In the literature review it was shown that cemented and uncemented materials exhibit some similarities in compression, with both exhibiting stiff elastic behaviour before yield and particle crushing. However, the addition of cement is generally expected to increase the yield stress and enlarge the zone in voids ratio–log stress space that a material can exist in, with these effects increasing with the degree of cementation. Leroueil and Vaughan (1990) defined this as 'structure-permitted space', which is bounded by the compression line of the uncemented soil in its loosest state and that of the densest, most cemented soil.

The general consensus from the available literature is that after yielding, the normal compression lines of cemented and uncemented materials either run parallel (e.g. Huang and Airey, 1998; dos Santos, 2009; Bobet et al., 2011) or

converge at high pressures to a single 'intrinsic' line (e.g. Cuccovillo and Coop, 1999; Rotta et al., 2003), with the degree of cementation controlling the distance between them and/or the rate at which they converge (these schemes are compared in Figure 5.4).

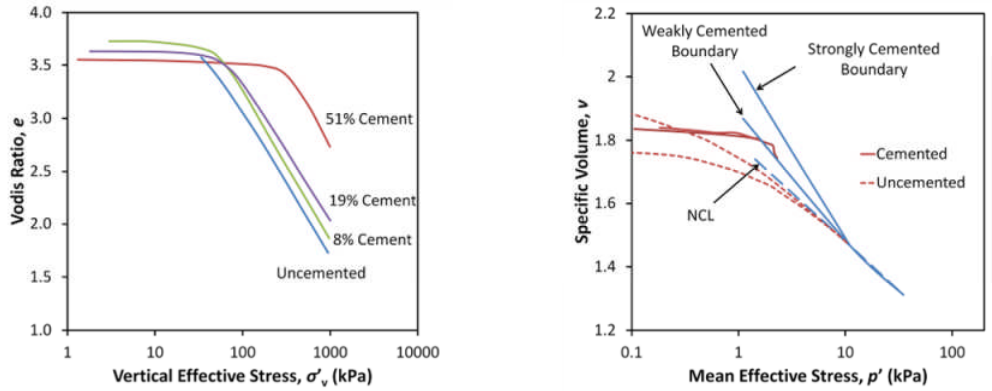

(a) (b)

Figure 5.4 Compression plots depicting the behaviour of cemented sands in compression, showing parallel NCLs (a) from Bobet et al. (2011), and converging NCLs (b), from Cuccovillo and Coop (1999)

Typical compression behaviour of a silica sand (which is the sand modelled in this work) bonded with Portland cement is shown in Figure 5.5 from Marri (2010). Silica sands are generally much stronger than naturally occurring carbonate sands and organic soils (such as those from Figure 5.4) and so exhibit larger yield stresses in compression. The effects of cementation are clearly visible in Figure 5.5, although the applied stress is not high enough to conclude if the NCLs are converging or independent of one another.

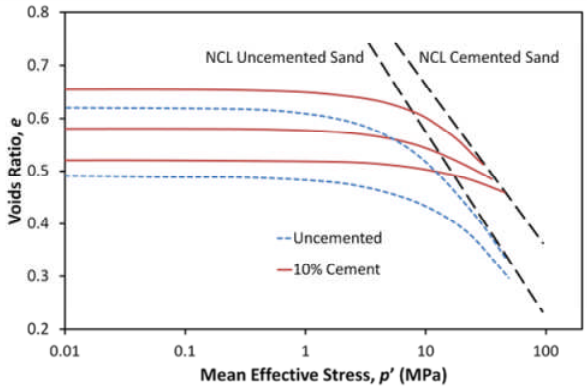

Figure 5.5 The effect of cementation on the behaviour of a silica sand in compression (Marri, 2010)

5.2.2 Oedometer Sample

The oedometer used in these simulations has the same dimensions as before: a diameter of 30 mm and a height of 7 mm. However, the initial sample is slightly denser, consisting of 640 particles of uniform size $d_0 = 2$ mm, with a voids ratio $e_0 = 0.84$. The sample was created at the *absolute* densest state possible to minimise the change in volume when a low stress is applied. As will be shown in the figures, the bonded samples (representing cemented sand) can sustain a higher voids ratio when the macroscopic stress is first applied, causing the compression curves to appear to start at different initial voids ratios. Other than a larger number of initial particles (and therefore lower initial voids ratio) the properties are the same as those given in Table 4.1. The particles have strengths as before for the simulations modelling silica sand; the characteristic value of octahedral shear strength, q_0 is 37.5 MPa for the initial particles (d_0 = 2 mm), the Weibull modulus, m is 3.3, and the size-hardening law is governed by equation [4.7].

The numerical sample is loaded in the same way as described previously, i.e. the stress is increased in increments, and the particles strengths are checked at once to allow for any breakages. When the octahedral shear stress according to equation [4.3] within a particle is found to exceed the individual strength, it is replaced with two new fragments, in the manner of Figure 4.3. However, a smaller stress increment of 0.25 MPa is used herein, as the sample is much stiffer due to the presence of bonds, although the data is still only plotted at approximately every 1 MPa for clarity.

5.2.3 Inter-Particle Bonding

Building on the simulations investigating cementation in triaxial tests in Chapter 3, cementation is once again modelled using the parallel bond feature of the software (Itasca, 2005)—details of which were given in section 2.6.2. In a similar fashion to before, parallel bonds are installed between contacting particles within the oedometer, with the noticeable difference between these simulations and those in Chapter 3 being the contact model used. In these simulations, the Hertz-Mindlin model is employed, as this was

deemed necessary when modelling particle breakage. Parallel bonds, which are defined by five parameters are set equal in size to the particles—i.e. $d_{bond} = d_0 = 2$ mm. The parallel bond normal and shear stiffnesses (which are defined in terms of stress per displacement) are set equal to one another to minimise input variables. The parallel bond normal stiffness in terms of stress per displacement should be equal to the elastic modulus divided by the length of the bond (assumed equal to 2 x r_{ball}). This gives a value of approximately 15×10^{12} Pa/m for bonds between balls of diameter 2 mm, assuming that cement has an elastic modulus of around 30 GPa (Ashby and Jones, 1986). The parallel bond strengths and strength distributions are investigated later, but at first are arbitrarily given uniform values of 37.5 MPa (in both pure shear and tension) for simplicity—equal to the strength (q_0) of the initial particles.

Bonds are installed via the same method described in Chapter 3 to create an average of 5 parallel bonds per sand particle. Another key difference between the previous simulations that utilized parallel bonds and the current set are that bonds are now only allowed to break at given intervals – in the same manner as the particles. To recap, after particles are allowed to break in the simulations, a number of computational timesteps are completed to allow the elastic energy from new overlaps to dissipate, and avoid triggering a chain reaction of breakage. So rather than allowing bonds to break in real time, the same approach to particle breakage is adopted: after the sample is loaded one-dimensionally, the parallel bonds are checked at once and if the normal or shear stress at any contact exceeds the strength of the bond (if one is present), then the bond is considered broken and removed. After the bonds have been checked and allowed to break, the octahedral shear stresses within the particles are then checked to allow for any particle breakages, after which a number of computational timesteps are completed to allow the artificially induced energy to dissipate. By comparison, if the bonds *were* allowed to break in real time, a large portion would fail immediately after particles have broken due to the artificial pressure spike caused by the

creation of new particles. After each stress increment (0.25 MPa), the sample is cycled continuously until no further breakage occurs.

In these initial simulations, if the octahedral shear stress q of any particle exceeds its strength, then the particle will break, regardless of whether it is bonded or not. If a breaking particle does happen to be bonded, when the broken particle is deleted and replaced by smaller fragments, the bonds associated with the original particle by default are also deleted (depicted in Figure 5.6).

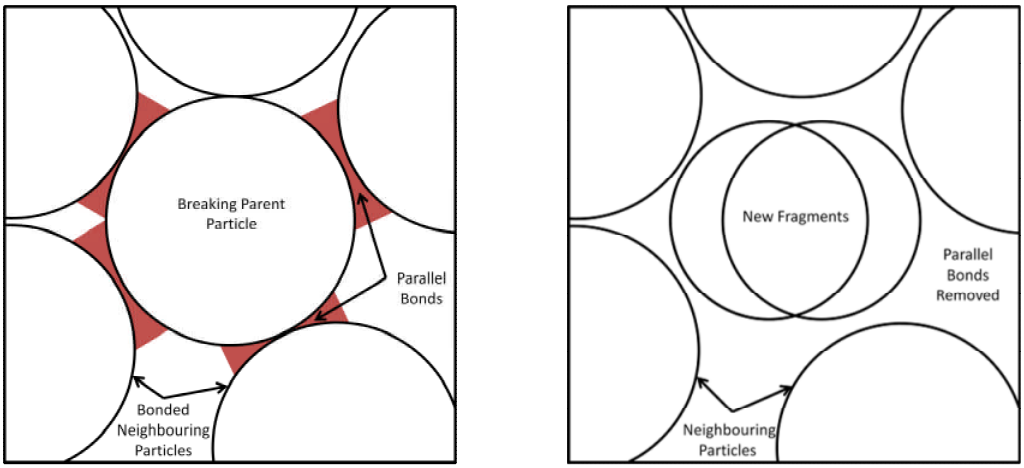

Figure 5.6 Schematic showing the results of particle fracture on the particle's parallel bonds (parallel bonds not to scale)

Figure 5.7 displays the normal compression line from the unbonded simulation, which has the same slope as the equivalent simulation of silica presented in Chapter 4, as well as the normal compression lines from two bonded simulations (the parallel bonds in the two bonded materials have uniform strengths of 37.5 MPa and 75.0 MPa) showing the effects of increasing bond strength.

Considering just the unbonded simulation and the simulation with bond strengths of 37.5 MPa – although the two simulations are initially created at the same voids ratio (0.84), the unbonded material readily compacts to a denser state when a low macroscopic stress is applied, which is evident from the plot in Figure 5.7 where the compression lines appear to start at different voids ratios. The parallel bonds resist compression when the vertical stress is

applied, and help to maintain a looser packing; when the bonds break at approximately 4 MPa, the bonded NCL almost converges to that of the unbonded simulation. The bond breakage is catastrophic, with only 8% remaining at 5 MPa, compared with over 99% at 4 MPa. It appears as though the catastrophic bond breakage is triggered, or at least coincides with particle breakage, as 51 particles also break at a vertical stress of approximately 4 MPa, which is the first significant fragmentation (only 5 particles had broken previously). The bonded NCL then continues apparently parallel to the unbonded NCL until about 8 MPa, at which point most of the remaining bonds break, and the compression line then converges with the unbonded equivalent (the intrinsic compression line). The unbonded simulation exhibits little particle breakage up until the yield point at around 9 MPa. It is evident that the bonds enable the material to exist at higher voids ratios at low macroscopic stresses, which is in accordance with the experimental literature discussed in Section 2.4.3; the bonded NCL displaying similar behaviour to that depicted in Figure 2.34(a) or Figure 5.4(b) from Cuccovillo and Coop (1999) for a weakly bonded cemented sand. However, the bonded NCL does not extend *beyond* the unbonded intrinsic compression line and exhibit a larger yield stress, as strongly cemented sands have been shown to (e.g. Figure 5.4).

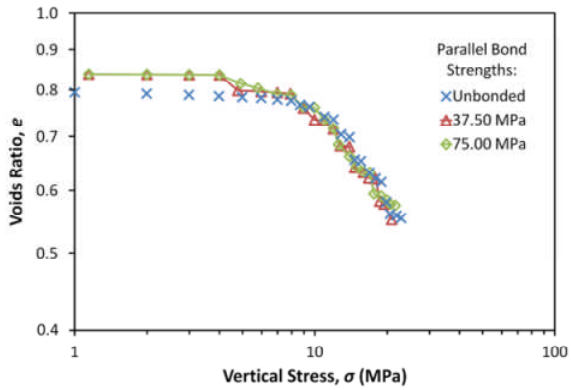

Figure 5.7 Normal compressions lines for bonded simulations, showing the effects of increasing the bond strength along with the unbonded material

Increasing the bond strength has little effect on this—the NCL of the same bonded material but with double the strength of the parallel bonds (75 MPa)

is also shown in Figure 5.7. The compression lines of both bonded materials are very similar, with both exhibiting a higher voids ratio than the unbonded material until bond breakage occurs at around 4 MPa. The sample with the stronger bonds does not converge quite as rapidly as the more weakly bonded sample to the unbonded material, but nonetheless by a vertical stress of 9 MPa, all three simulations have converged and are essentially at the same state, with a voids ratio of around 0.76 and approximately 800 particles each. At this stage, there are almost no parallel bonds remaining in either of the bonded simulations, and all three NCLs all then follow the same path and exhibit the same slope during compression, which has been shown to be controlled by the size-hardening law of the particles.

An alternative particle and bond breakage mechanism is now presented—which does not automatically remove bonds when a particle breaks. Instead, new parallel bonds are installed between the new fragments and the corresponding particles which were bonded to the original particle prior to breakage. This new configuration, with 'durable' bonds seems feasible if one considers that in reality when a sand particle breaks, any cementation will certainly not disappear, and may continue to provide cohesion between broken fragments and surrounding particles. This seems plausible from Figure 5.8, which displays a magnified close-up of cemented sand particles after being compressed to a mean effective stress of approximately 50 MPa. The figure shows a particle which has suffered significant fracturing while still appearing to have cement bonded to it, although it is unclear from the image if the cementitious bonds to neighbouring particles are intact.

The new parallel bonds are given the exact same properties as the bonds which exist before the broken particle is deleted (i.e. the same size, strength and stiffness), and this configuration is shown in Figure 5.9. Bonds still break in the same manner—that is they are checked and allowed to break at once.

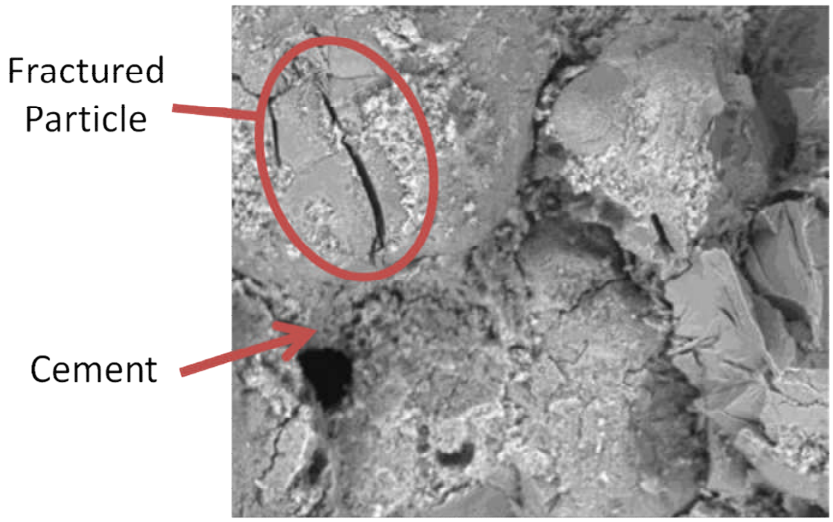

Figure 5.8 SEM image showing close up of a fractured particle from a sample of sand bonded Portland cement, after compression to 50 MPa (Marri, 2010)

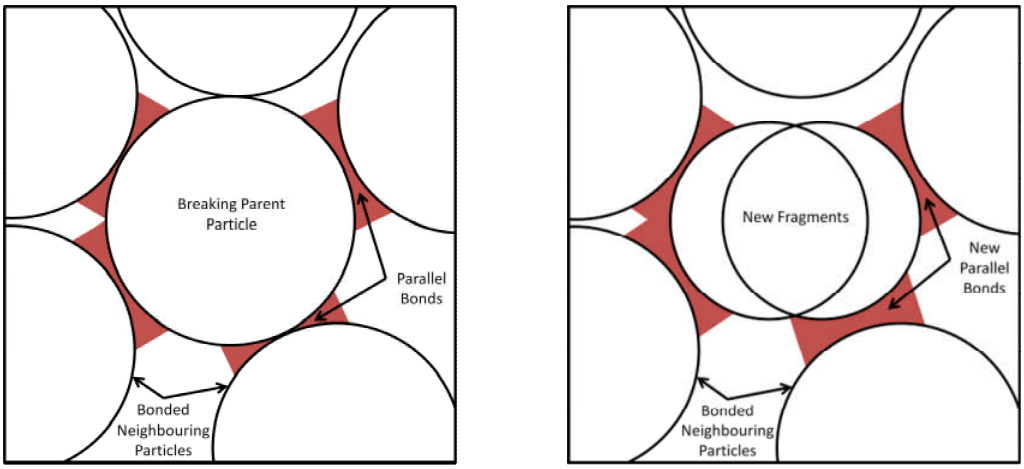

Figure 5.9 Schematic showing the installation of new replacement parallel bonds after a particle has fractured (parallel bonds not to scale)

The compression lines of two simulations using this configuration are shown in Figure 5.10, again with bond strengths of 37.5 and 75 MPa to show the effects of increasing the strengths of the parallel bonds, as well the results from the unbonded simulation. In Figure 5.10, the two bonded compression lines appear very similar to the previous set of simulations; both bonded materials initially exhibit a higher voids ratio at low stresses, before undergoing major bond breakage and the NCLs converge with the unbonded material. The material with 'durable' parallel bond strengths of 37.5 MPa displays a slightly lower bond yield stress than the equivalent previous simulation, with major bond breakage occurring after approximately 3 MPa. Although one may expect that they would exhibit bond breakage at the same

stress as in the previous simulations, those with durable bonds (i.e. using the bond mechanism depicted in Figure 5.9) experience some bond breakage at very low stresses. At a vertical stress of 3 MPa, shortly before catastrophic bond breakage occurs, only 75% of the bonds remain unbroken. The previous simulation (without durable bonds) with the same bond strengths still had over 99% of the parallel bonds intact. This increased quantity of broken parallel bonds is most likely due to the new fragments being bonded as soon as they are created, while still overlapping by a large degree. The new fragments (as discussed in Chapter 4), will move quite rapidly outwards in the direction of the minor principal axis, due to the artificial overlap—if parallel bonds exist between these new fragments and surrounding particles, this sudden excessive force will be transferred to the parallel bonds potentially causing additional bond breakage.

Again, the NCLs of the bonded simulations do not extend beyond the intrinsic NCL of the uncemented simulation and do not display a larger yield stress. Increasing the bond strength also has very little effect, with catastrophic bond breakage occurring at a slightly higher macroscopic stress. Both bonded compression curves swiftly converge with the unbonded curve, and after an applied stress of approximately 6 MPa, all three simulations display approximately equal voids ratio and total number of particles, and the compression lines appear coincident.

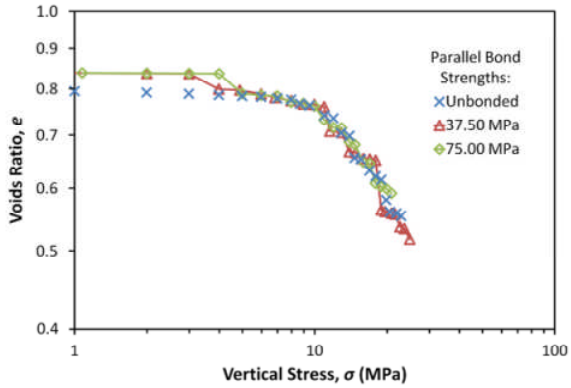

Figure 5.10 Normal compression lines for simulations bonded with 'durable' parallel bonds, showing the effects of increasing bond strength

Figure 5.11 shows the particle size distributions at a stress of 20 MPa from the unbonded simulation and two bonded simulations with the alternative bond breakage configurations (see Figures 5.6 and 5.9). Both the simulation with 'standard' bonds and that with 'durable' bonds have almost identical particle size distributions to the unbonded material at the given stress, further indicating the parallel bonds have no significant effect on the simulations of the compression of sand. Other than maintaining a looser packing in the early stages of compression, the bonds have little or no effect on the overall one-dimensional behaviour of the sand. It is possible that increasing the parallel bond strengths further could result in more realistic cemented normal compression lines—i.e. bonding sufficiently strong enough compared to the sand particle strengths to allow the sample to reach states outside of the uncemented NCL. However, it seems somewhat unrealistic having parallel bond strengths with magnitudes higher than the particle strengths, as cement by its nature is weaker than sand, and is known to have a very low fracture toughness (Ashby and Jones, 1986).

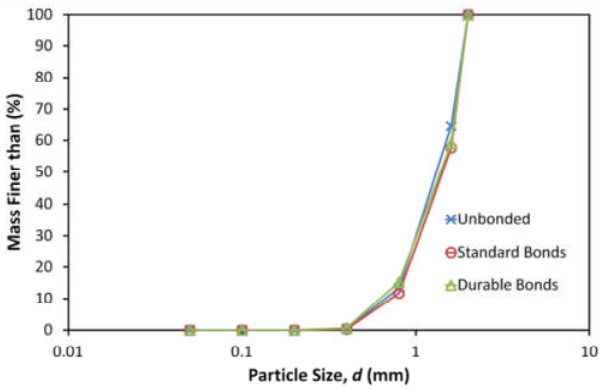

Figure 5.11 Final particle size distributions for the unbonded material, and simulations with 'standard' and 'durable' parallel bonds with uniform strengths of 75 MPa

Coop and Atkinson (1993) suggested that bond breakage precedes or coincides with particle breakage—however, as mentioned, in the above simulations particles could break regardless of whether they were bonded or not (and in the first case, any parallel bonds associated with breaking particles were deleted by default). There is no conclusive evidence in the literature with regard to how cementation affects particle crushing, although authors

such as Marri et al. (2012) proposed that during compression, cementation reduces particle crushing. This was based on the observation that increasing the cement content of the sand reduces the compressibility—i.e. the reduction in volume for a given vertical stress. This proposition seems feasible if one envisages a sand particle bonded by cement to other particles—the cement will increase the contact area, which would reduce the induced tensile stress (Jaeger, 1967). With this in mind, a final alternative configuration is presented with the aim of reproducing the behaviour of cemented sand in compression, in which bond breakage *must* precede any particle breakage. This is achieved by simply not allowing any particle to break if there exists one or more parallel bonds attached to it—shown in Figure 5.12. This approach is reasonable if one considers a particle coated in cement, or heavily bonded (such as those previously shown in Figure 3.22)—for the particle to be loaded diametrically (which has been shown to give the highest octahedral shear stress) then the cementation will have to be broken first.

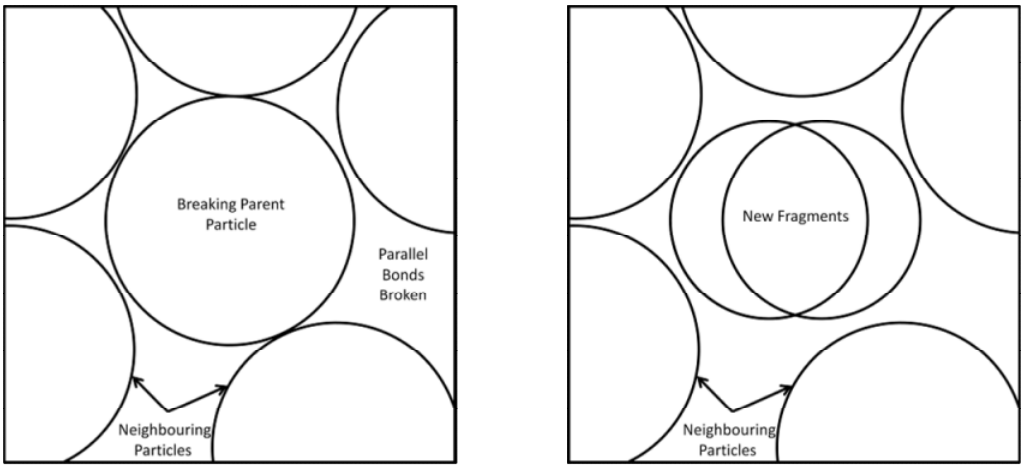

Figure 5.12 Schematic showing how particles can only break once all contacting parallel bonds have also broken (not to scale)

The compression results of these simulations are presented in Figure 5.13, which displays the compression curves of three bonded simulations, along with that of the uncemented simulation. It includes the compression curves of a simulation with uniform parallel bond strengths of 37.5 MPa as well as one with double (75.0 MPa) and half (18.75 MPa) the magnitude. All three

bonded simulations display higher voids ratios in the early stages of compression, and this time they display a clearly defined yield point, at higher stresses than the unbonded simulation. The yield stress appears directly proportional to the parallel bond strengths, with the most strongly bonded sample not yet yielded at a macroscopic applied stress of 50 MPa. The other two bonded simulations, i.e. those with parallel bond strengths of 18.75 and 37.5 MPa, display catastrophic bond breakage followed by rapid convergence to the intrinsic compression line of the unbonded material. For both of these simulations, immediately prior to the catastrophic bond breakage (at stresses of 12 and 26 MPa, respectively) almost all the parallel bonds remain intact, and furthermore, no particles have broken. After this, nearly all bonds have broken, which is accompanied by significant particle breakage. Once the bonded compression lines converge with the unbonded compression line, all simulations follow the same slope, and contain a similar number of particles at a particular voids ratio. This is representative of the behaviour of a very brittle cemented sand, and is similar in essence to that of the calcarenite in isotropic normal compression from Lagioia and Nova (1995), shown in Figure 5.14, although calcarenites in general are much weaker, hence the lower yield stress.

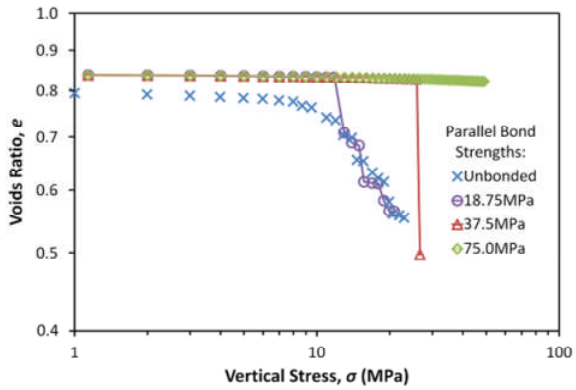

Figure 5.13 Normal compression lines for simulations with parallel bonds that prevent particle fracture, showing the effects of increasing bond strength

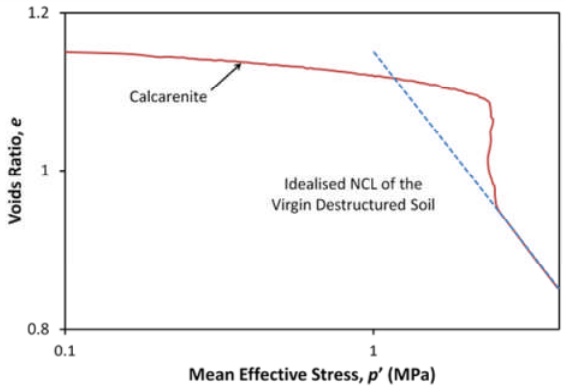

Figure 5.14 Normal compression line for a calcarenite, demonstrating brittle yielding followed by convergence to unbonded/destructured NCL (Logioia and Nova, 1995)

Figure 5.15 shows the particle size distributions from these simulations at a stress of 20 MPa, which confirms the convergent behaviour. The unbonded simulation and that with bond strengths of 18.75 MPa have almost identical grading curves, showing that after the bonds have broken, the latter material demonstrates the same behaviour as the unbonded material. The two simulations with higher bond strengths (37.5 and 75.0 MPa), which have not yet yielded at this stress, display no particle breakage and hence have the same grading curve as at the start of the simulations.

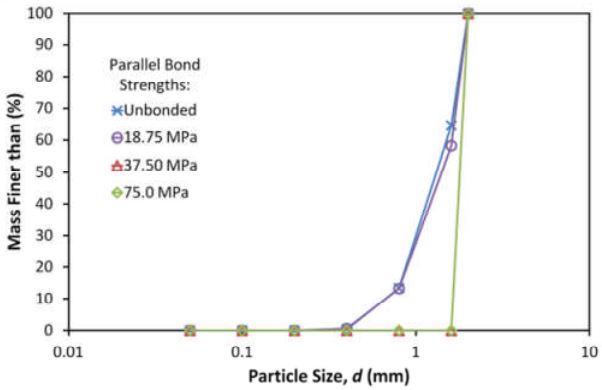

Figure 5.15 Particle size distributions at a stress of 20 MPa, for simulations with parallel bonds that prevent particle fracture

Although using this approach (not allowing bonded particles to fracture) results in the correct form of NCL—i.e. the bonded NCLs exhibit a higher yield stress, and exist in structure-permitted space (Leroueil and Vaughan, 1990)—the NCLs jump at once to the unbonded compression line, and do not reproduce the gradual yielding and convergence, or parallel nature that is observed in the literature (e.g. Leroueil and Vaughan, 1990; Cuccovillo and

Coop, 1999; Bobet et al., 2011; Dos Santos, 2009; Marri, 2010). The post-yield compression lines for the bonded simulations are very steep, due to the catastrophic bond breakage whereby nearly all break at once.

5.2.4 Bond Strength Distributions

Using the same logic when investigating and modelling cemented sand in triaxial shearing (Chapter 3), one-dimensional compression tests have been performed utilizing various distributions of bond strengths. Using the criteria which displayed the correct qualitative compression curve (whereby bonded particles aren't allowed to fracture), simulations with four different Weibull distributions of parallel bond strength are now presented, with the compression curves shown in Figure 5.16.

All four bonded simulations (representing cemented sand) have mean parallel bond strengths of 37.5 MPa, but with Weibull moduli *m* of 0.5, 1.0, 2.0 and 3.0. The Weibull distribution (see Figure 2.38) has been used to model cementation previously in Chapter 3. To recap, a low Weibull modulus signifies high variability. The simulation with a parallel bond strength distribution with a Weibull modulus of 0.5 has the widest distribution of strengths, and from Figure 5.16 it can be seen that this compression line displays the earliest onset of yield, and has the most gradual convergence to the intrinsic compression line. Following this yield, there appears a post-yield compression line and behaviour which fits the schematics depicted previously in Figures 2.34–2.36 and 5.4(b). The simulation with the bond strength distribution with the highest Weibull modulus (m = 3.0) displays the latest and most catastrophic bond yielding, similar to both a brittle cemented sand (e.g. Lagioia and Nova, 1995) and the previous simulation showed in which there is a uniform bond strength of 37.5 MPa (Figure 5.13).

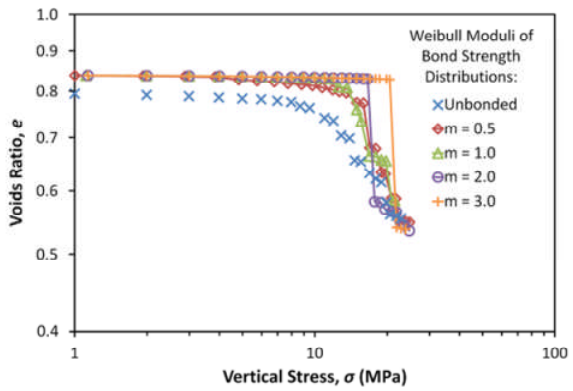

Figure 5.16 Normal compression lines for simulations with parallel bond strengths with various Weibull moduli

Liu and Carter (1999, 2000) developed a framework to describe the idealised behaviour of structured soils in compression. They proposed that the post-yield behaviour in one-dimensional compression could be described by:

$$e = e_0 + \Delta e - \lambda \ln \sigma \qquad [5.13]$$

where Δe is the additional part of the voids ratio sustained by the soil structure, in this case cementation, although to be consistent with equation [4.28], this can be written:

$$\log e = \log(e_y + \Delta e) - \frac{1}{2b} \log \frac{\sigma}{\sigma_y} \qquad [5.14]$$

A value of $\Delta e = 0$ represents unstructured soil, in this case the uncemented silica sand. The additional component of voids ratio sustained by the structure is expressed as:

$$\Delta e = S \left(\frac{\sigma_{s,y}}{\sigma} \right)^{\beta} \log \sigma_{s,y} \qquad [5.15]$$

where S is a soil parameter called the structure index, $\sigma_{s,y}$ is the vertical stress at which yield of the structured soil occurs, β is the destructuring index, and σ is the current vertical stress (Liu and Carter, 2000). The value of S can be calculated if the yield stress of the structured soil and the voids ratios of both the structured and unstructured soils at the yield stress are known.

Using this framework, the simulation with a bond strength distribution with a Weibull modulus of 0.5 has a destructuring index, β of approximately 5, shown in Figure 5.17(a). The simulation with the narrowest distribution of bond strengths (m = 3) has a destructuring index of around 50, shown in Figure 5.17(b). Experimental data for values of β for cemented sands is quite limited: Liu and Carter (2000) found a value of 3 for artificially cemented silica sand (after Maccarini, 1987), and a value of 35 for a calcarenite (from Lagioia and Nova, 1995); shown in Figure 5.18.

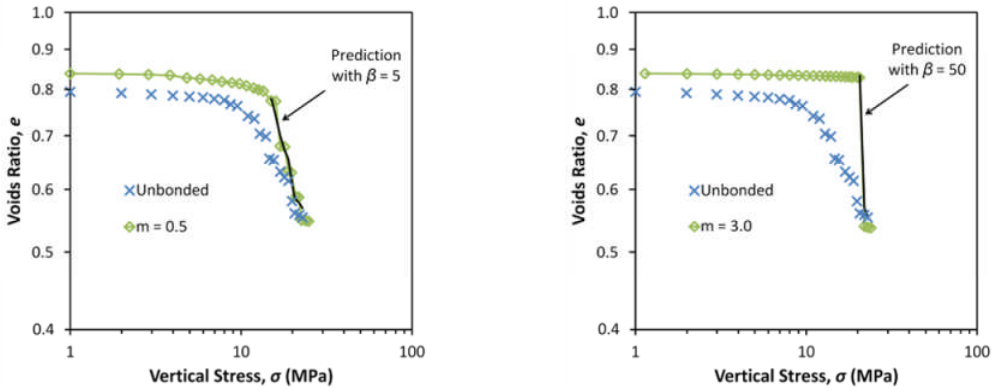

(a) (b)

Figure 5.17 Compression behaviour from the simulations of sand with a parallel bond strength distribution with Weibull moduli of 0.5 (a), and 3.0 (b), with the destructuring indices β and predictions using equation [5.15] shown

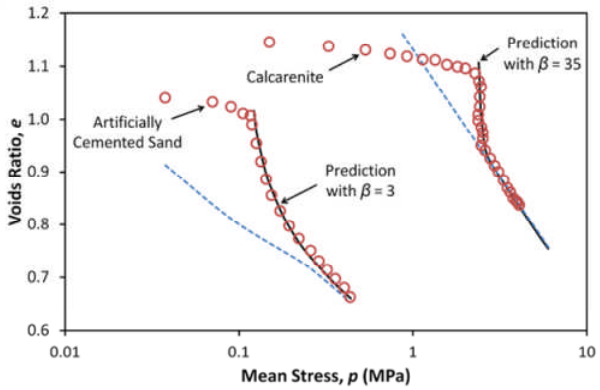

Figure 5.18 Compression behaviour with predictions using Equation [5.15] for an artificially cemented sand and a calcarenite (Liu and Carter, 1999)

It is clear that the parameter β, i.e. the rate at which destructuring occurs, is representative of the brittleness of the structured material. Higher values indicate very brittle cementation, while lower values are typical of more ductile cementation. For the simulations, it is the distribution of bond

strengths that control the destructuring index, leading to the conclusion that brittle cemented sands such as naturally occurring cemented carbonate sands have a narrow distribution of bond strengths. On the other hand, ductile cemented sands, for instance those bonded with materials such as Portland cement would appear to have a much wider distribution of bond strengths. This fits with observations from Haeri et al. (2006) who concluded that of Gypsum, lime and Portland cement; the latter was the most ductile cementing agent.

In these simulations, the parallel bonds by their nature have a significant influence on particle crushing, and as a result noticeably affect the compression of the material. While intact, the parallel bonds prevent bonded particles from breaking, thereby resisting significant reductions in volume. The simulation which displays the most gradual convergence to the intrinsic compression line, i.e. the simulation which requires the largest increase in stress from yielding to convergence, is the simulation with the widest distribution of bond strengths. This simulation, with a parallel bond distribution Weibull modulus of 0.5 has some parallel bonds with significantly higher strengths than the other simulations (although the mean strength is the same). This means there are still intact parallel bonds reducing particle crushing at high macroscopic stresses, which sustain an additional voids ratio. Figure 5.19 shows the percentage of parallel bonds remaining unbroken versus applied stress, which confirms the influence bonds have on the compression behaviour. The simulation with m = 0.5 exhibits a steady decline in the number of intact bonds from first loading, with 6% of the parallel bonds remaining unbroken at termination. The corresponding simulation, with m = 3.0 displays very sudden, catastrophic bond breakage after which no bonds remain intact, which corresponds to the sudden yielding and convergence with the intrinsic compression line shown in Figures 5.16 and 5.17(b). These observations certainly suggest that cementation (or at least the parallel bonds in the simulations) reduces particle crushing, which in turn reduces the compressibility, in line with the speculation by Marri et al. (2012).

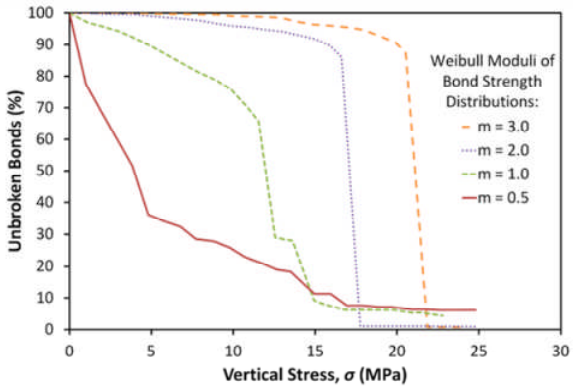

Figure 5.19 Percentage of intact parallel bonds remaining as a function of vertical applied stress

The final particle size distributions are given in Figure 5.20 for the simulations with various Weibull distributions of bond strengths. These are obtained at a vertical stress of 23 MPa (the highest stress all simulations reached), at which point the compression curves have essentially converged. Although the particle size distributions appear similar, the two simulations with a portion of bonds remaining unbroken ($m = 0.5$ and 1) have experienced less crushing and demonstrate less-developed grading curves.

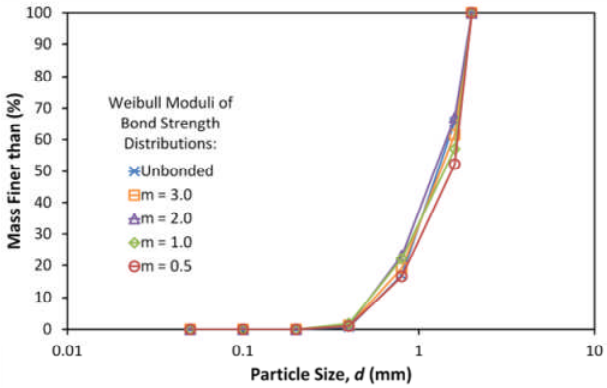

Figure 5.20 Final grading curves for the simulations with bond strengths with Weibull distributions with various moduli

5.2.5 Cement Content

The literature showing the effects of increasing cement content on the behaviour of cemented sand in compression is relatively limited, especially with regard to artificially cemented silica sand. For example, in Figure 5.4: Bobet et al. (2011) performed one-dimensional compression tests

investigating the effects of increasing quantities of Portland cement using an organic soil (with a loss on ignition of approximately 50%); Cuccovillo and Coop (1999) meanwhile compared the behaviour of weak and strong naturally cemented carbonate soils.

The effects of increasing the quantity of Portland cement for a cemented silica sand are shown in Figure 5.21 from Marri et al. (2012). As with Figure 5.5, Figure 5.21 shows that the addition of cement appears to cause the compression curve to extend beyond the intrinsic curve of the uncemented material, increasing the yield stress. The graph shows that increasing the content of cement reduces the compressibility, i.e. the reduction in volume for a given applied stress, however the applied stresses are not large enough to determine the true nature of the cemented NCLs. As mentioned, there is some discrepancy between the observed effects during compression of increasing the degree of cementation: some authors speculating parallel normal compression lines, and others suggesting NCLs unique for each cement content, converging to the intrinsic compression line. It is generally accepted however that the degree of cementation, or at least the strength of the cementation, increases the yield stress and the extent at which the cemented compression curves extends in to 'structure-permitted space'.

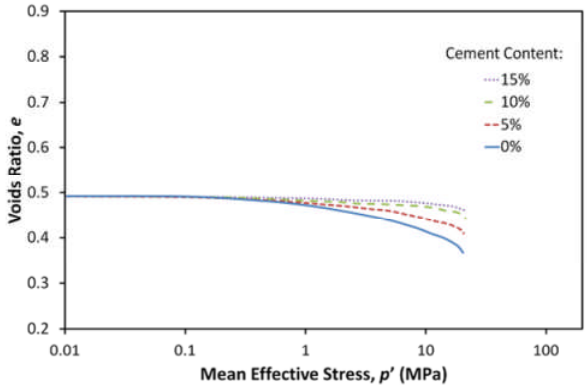

Figure 5.21 Effect of Portland cement content on the isotropic compression of silica sand (Marri et al., 2012)

There are several ways in which one may approach modelling an increasing degree of cementation using DEM, which were discussed in Chapter 3 (such as altering the variation/magnitude of bond strengths and stiffness, or various

combinations thereof; or altering the quantity of bonds and/or bond size). The effects of increasing the bond strength have already been shown; increasing the stiffness simply results in earlier bond breakage; increasing the bond size has little effect on compression. From the triaxial simulations presented earlier, it was shown that the most effective method, i.e. that which produced the correct qualitative change in behaviour, was increasing the *quantity* of parallel bonds within the sample.

In the current section thus far, neighbouring particles and those within very close proximity are bonded to one another – the proximity defined so as to result in an average of 5 parallel bonds per sand particle. Additional one-dimensional compression simulations have been completed for samples with an average of 10, 15 and 20 parallel bonds per particle, by increasing the bonding proximity to achieve the desired quantity/degree of bonding: the compression lines shown in Figure 5.22.

It is visible from Figure 5.22 that increasing the quantity of bonds, measured in these simulations by the average number of parallel bonds per particle, magnifies the effects of cementation—resulting in an increase in yield stress with increasing number of bonds. The simulations representing cemented sand converge towards the intrinsic NCL, with increasing the quantity of bonds causing the post-yield compression line (which begins at the yield point) to become steeper. This agrees with the framework described by Cuccovillo and Coop (1999) and shown in Figure 5.4(b). The compression curves also appear to be in harmony with those from Marri (2010) shown in Figure 5.21, although the curves of the cemented material in the latter figure haven't fully yielded, and don't reach stresses high enough to determine whether they converge or run parallel. Considering just the pre-yield compression curves of the simulations in Figure 5.22 (i.e. up to a stress of approximately 12 MPa), equating the number of bonds to cement content reveals the same pattern of behaviour as the experimental results in Figure 5.21.

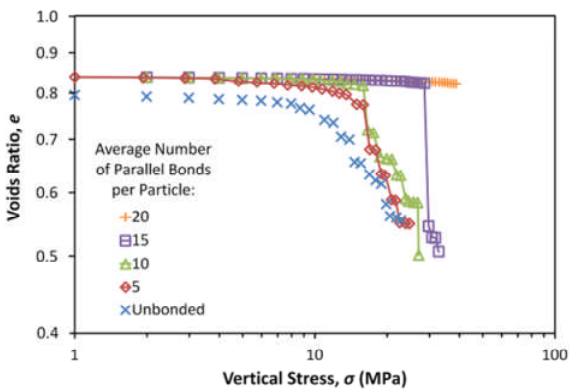

Figure 5.22 Compression curves for simulations with increasing number of parallel bonds

Marri et al. (2012) also suggested that particle crushing reduces with increasing degree of cementation, due to the associated reduction in compressibility. This makes sense when one considers that the reduction in volume experienced in compression is facilitated by the crushing of particles. This is confirmed in the simulations by comparing the particle size distributions at a given stress—Figure 5.23 compares the grading curves for the simulations with various degrees of bonding at an applied stress of 20 MPa. As can be seen, the two most heavily cemented simulations (those with an average of 15 and 20 parallel bonds per particle) have the least developed grading curve, and so have experienced the least amount of crushing. These two simulations also display the largest current volume. The unbonded simulation displays the greatest degree of crushing in Figure 5.23, followed by the simulations with an average of 5 and 10 parallel bonds per particle. These simulations underwent the largest decrease in volume.

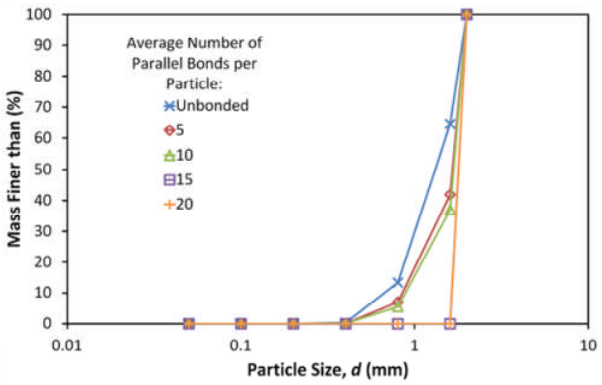

Figure 5.23 Particle size distributions for simulations with increasing number of parallel bonds, at an applied stress of 20 MPa

5.2.6 Conclusions

Simulations have been presented showing that the behaviour of cemented sand in one-dimensional compression can be replicated using DEM. The cementation has been modelled with parallel bonds, and it has been shown that if the bonds are configured so to prevent particle breakage, the correct transition is witnessed in the compression curves—the cemented simulations extending into structure-permitted space and displaying stronger yield stresses. Although the influence of certain bond parameters such as size and stiffness have not been investigated in this section (see Chapter 3), the distribution of bond strengths has been shown to control the post-yield compression line.

A narrow bond strength distribution results in a sudden and catastrophic failure of bonds, i.e. brittle yielding whereby the post-yield compression line converges immediately to the intrinsic NCL. A much wider bond strength distribution produces a less rapid onset of yield, and more gradual convergence to the intrinsic compression line. A distribution with a low modulus such as 0.5 gave the most realistic behaviour with regard to modelling a strongly cemented sand, and analysing the simulations using Liu and Carter's (1999, 2000) framework for the compression of structured soils, the value of the destructuring index, β appeared to be in the correct range. The destructuring indices obtained from the simulations appeared to be a function of the bond strength distribution.

The simulation with the widest distribution of parallel bond strengths still had some of the strongest bonds remaining at high pressures (> 20 MPa). The presence of bonding within the material was shown to reduce the compressibility and also the degree of particle crushing for a given applied stress, which confirms speculation from Marri et al. (2012). The Weibull modulus for the distribution of parallel bond strengths has been shown to control the post-yield compression line and appears to have a direct influence on the destructuring index.

It was shown previously in triaxial simulations that increasing the quantity of bonds appears to be the most effective way of modelling increasing cement content, the same appears to be the case in one-dimensional normal compression. Increasing the quantity of bonds magnifies the effects of cementation, i.e. it increases the yield stress, renders the sample more brittle and reduces the degree of particle crushing for a given applied macroscopic stress. Therefore it appears that increasing the degree of cementation suppresses particle crushing.

This section has therefore shown that it is possible to capture—using DEM—the essential features of the mechanical behaviour of cemented sand under one-dimensional normal compression.

5.3 HIGH-PRESSURE TRIAXIAL TESTS

5.3.1 Introduction

It has been shown in the literature (e.g. Bolton et al., 2008), that particle crushing is necessary for achieving realistic levels of volumetric contraction in triaxial simulations of granular soils. This observation was also evident in Chapter 3, in which triaxial simulations of uncemented sand, even with confining pressures as high as 12 MPa, all exhibited dilation. This section aims to show that it is possible to simulate the phenomenon of particle crushing in high-pressure triaxial tests on cemented and uncemented sand, using the discrete element method. Using the triaxial model presented in Chapter 3 (which features a flexible membrane allowing accurate deformation), and incorporating the simple breakage mechanism from Chapter 4 the following work aims to show that particle crushing is essential to replicate realistic behaviour of uncemented sand in high-pressure simulations. The general effects of particle crushing during shear are explored, as well as the influence of particle strength, packing and confining pressure on the degree of crushing.

Finally, using the criteria developed earlier in this chapter (section 5.2) for the combined breakage of parallel bonds and particles—i.e. breakage of cementation must precede particle fragmentation—the behaviour of cemented sand under high-pressure triaxial shearing is modelled. While some authors speculate that cementation suppresses particle crushing during shear (e.g. Marri, 2010), using the intrusive capabilities of DEM, an insight on the effects cementation has on the degree of crushing is hereby presented.

5.3.2 Triaxial Model

The triaxial model used in this section is an adaptation of that described in detail in Chapter 3. The triaxial specimen has the same dimensions as used in that section, i.e. a cylinder with a height of 100 mm and a diameter of 50 mm; although it should be noted that a different grading is used in the following simulations. How the triaxial model is generated, and the general procedure is the same as given previously, and won't be repeated. The only notable differences to the model mechanism, which *will* be described here are that the Hertz-Mindlin contact model is used, and that strain is applied in increments, rather than a constant strain rate; both due to the implementation of the particle crushing mechanism.

The use of the Hertz-Mindlin contact model means that particle stiffnesses are defined by the Poisson's ratio v and shear modulus, G. The sand particles are given the same values used in the crushing simulations, i.e. $v = 0.25$ and $G = 28$ GPa. The membrane particles are ascribed a Poisson's ratio of 0.5 (a typical value for rubber), and for the same reasons outlined in section 3.2.4, are given an arbitrarily high shear modulus. An empirical value of $G = 1$ GPa (for a confining pressure of 1 MPa) was found sufficient to prevent the penetration previously shown in Figure 3.8. Membrane particles are now bonded with parallel bonds, as the contact bonds used previously are incompatible with the Hertz-Mindlin contact model. The membrane parallel bonds are defined as having radii equal to 1×10^{-10} times that of the membrane particles, (mimicking the contact bonds used previously, which act on an infinitely small point). The normal and shear strengths are set

arbitrarily high again to prevent the membrane from splitting (equivalent to a force of approximately 5×10^{12} N in pure shear or tension). The membrane parallel bond stiffnesses (defined in terms of stress per displacement) are given values of 1×10^{30} Pa/m (equivalent to about 60 kN/m) for a confining pressure of 1 MPa. This value was found to prevent the problem of membrane particles not staying aligned, shown in Figure 3.9.

The second major difference here is that strain is applied in increments, rather than simply applying a constant velocity to the top platen, as done previously—this is due to the particles not being allowed to break in real time. In these simulations, axial strain increments of 0.0001 are used, i.e. the top platen is accelerated and moved downwards, then decelerated and stopped after an increase in axial strain of 0.01%. After each increment, the particles are checked and allowed to break (any broken particles are replaced with new fragments), until no further breakages occur and then the next strain increment is applied. Particle breakage is determined by the same criteria as throughout Chapters 4 and 5, using the octahedral shear stress according to equation [4.3]. Breaking particles are replaced by new fragments in the manner depicted in Figure 4.3. The particles have strengths as before for the simulations modelling silica sand, although the initial particles are *larger*: the characteristic value of octahedral shear strength, q_0, is 20.0 MPa for the initial particles (d_0 = 4 mm); the Weibull modulus, m, is equal to 3.3; and the size-hardening law is governed by equation [4.7].

The details of the specimen and membrane used in the following simulations are given in Table 5.1, unless otherwise stated. As these simulations are solely intended to investigate particle crushing during shear, and not calibration against experimental results, the simulations all start with an initially mono-disperse sample. Hence the coefficient of uniformity, C_u, of the initial specimen is equal to 1 (except for the simulation which investigates the effect of grading on the degree of particle crushing). In general, all specimens have an initial voids ratio of 0.75; this was chosen as a somewhat arbitrary value. The densest initial state that could be achieved without any locked-in

forces was a voids ratio of 0.66, so the simulations with $e = 0.75$ could be considered *relatively* loose; however without irregular particle shape, the soil samples invariably compact to a denser state during isotropic consolidation, and are unable to maintain large voids. Nonetheless, the effects of varying initial density are investigated later.

Table 5.1 Summary of DEM parameters for triaxial model

Triaxial Sample Properties	
Size: height x diameter (mm)	100 x 50
No. of particles	3350
Particle friction coefficient	0.5
Contact model	Hertz-Mindlin
Shear modulus, G (GPa)	28
Poisson's ratio, v	0.25
Density (kg/m^3)	2650
Coefficient of uniformity, C_u	1.0
Particle diameter, d_0 (mm)	4.00
Voids ratio, e_0	0.75
37% Strength, q_0 (MPa)	20.0 (for $d = d_0$)
Weibull Modulus, m	3.3
Wall Friction Coefficient	0
Triaxial Membrane Properties	
No. of particles	3224
Friction coefficient	0
Contact model	Hertz-Mindlin
Shear modulus, G (GPa)	28
Poisson's ratio, v	0.25
Density (kg/m^3)	1000
Particle diameter, d_0 (mm)	1.33
Parallel bond diameter (mm)	1.33 x 10^{-10}
Parallel bond stiffness (Pa/m)	1 x 10^{40}
Parallel bond strength (Pa)	1 x 10^{30}

5.3.3 General Factors Influencing Particle Crushing

In this section, the general effects of particle crushing during triaxial simulations will be demonstrated, as well as the influence that factors such as the particle strength, initial density and initial grading have on the degree of crushing. As such, the simulations are all sheared under a confining pressure of 1 MPa, and have the properties and initial grading given in Table 5.1, apart from where stated.

Firstly, to demonstrate the effects of particle crushing, simulations *with* and *without* the possibility of crushing are presented. Figure 5.24 presents the triaxial results of simulations of three mono-disperse samples (d_0 = 4 mm), with initial voids ratios of 0.75, subjected to shearing under 1 MPa confining pressure. The results comprise one simulation with unbreakable particles, and two with particles that can break—demonstrating the influence of particle strength on crushing. Of the breakable simulations, one has particle strengths of silica sand (as given in Table 5.1), i.e. q_0 = 20 MPa for the initial particles, the other has strengths half the magnitude, i.e. q_0 = 10 MPa. The sand particle strengths in both of these crushable simulations have a Weibull modulus, *m* of 3.3, and follow the same hardening law expressed in [4.7].

There is not much difference visible between the unbreakable simulation and the material with the strength of silica sand (q_0 = 20 MPa) in the stress-strain responses. They demonstrate almost identical deviatoric stress curves, and there is almost no difference in the volumetric strain curves either, although it is possible to see that the material with no particle breakage is exhibiting slightly higher dilatancy at the end of the test. For the weaker crushable material, the very initial part of the deviatoric stress response (usually considered elastic), is the same until an axial strain of approximately 1%, after which the stress curve of this weaker material becomes less inclined. However, this curve appears to lead to a value of ultimate (and critical) strength similar to the stronger material. This would suggest that the two breakable soils (and indeed the unbreakable material) have the same critical state parameter *M*, meaning the frictional resistance is the same; the same deviatoric stress is required to keep the soil flowing continuously at a critical state. This is to be expected, as the two soils—although consisting of different quantities and sizes of particles after crushing—have the same particle friction coefficient and particle shape. The simulations with breakable particles produce a more fluctuating deviatoric stress curve, which is a result of the particles fracturing. Immediately after particles have broken and been replaced with new fragments, the stress on the platens decreases—

and due to the relatively *small* overall number of particles, this has a noticeable effect on the stress response.

Figure 5.24(b) shows that the breakable material with weaker particles undergoes much less volumetric dilation compared to the unbreakable simulation, this is not surprising and is the same observation as that made by Bolton et al. (2008), who subjected breakable and unbreakable agglomerates to shearing using a rigid cubical cell (Figure 2.72). The weaker crushable material also shows markedly less dilation than the stronger crushable material; the weaker sample only *just* displaying an overall dilation. This makes sense, as when the weaker sample is sheared, to accommodate the macroscopic strain, particles in contact are more likely to break. In the stronger sample (or the unbreakable one), by comparison, the particles are less likely to, or will not fracture and will need to rearrange by sliding and rolling over one another, requiring dilation. The two breakable materials therefore have different final voids ratios: 0.63 and 0.66 for the weaker and stronger materials respectively. If these are considered to be the critical voids ratios (or approaching such states), then one may conclude that the critical state lines in specific volume–mean stress space are different, and that the position of the CSL is dependent on the characteristic strength of the particles. This is in accord with the findings in Chapter 4, where it was shown that the position of the normal compression line is related to the average particle strength (Figure 4.10)—as the critical state line (in volume-stress space) is assumed to be parallel with the normal compression line (e.g. Bolton, 1979; Coop, 1990; Craig, 2004), as shown in Figure 2.27 (with the separation a property of the soil). So one may assume that decreasing the particle strengths shifts both the CSL and NCL to the left in volume–stress space.

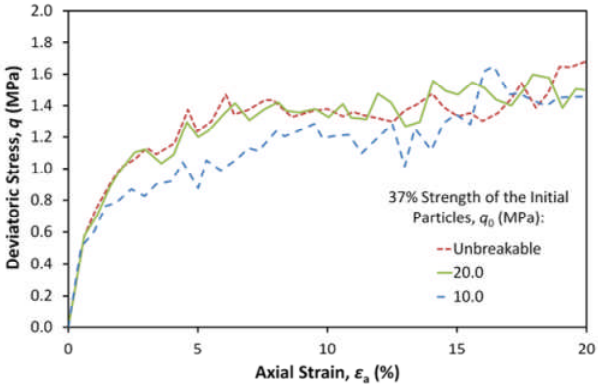

(a)

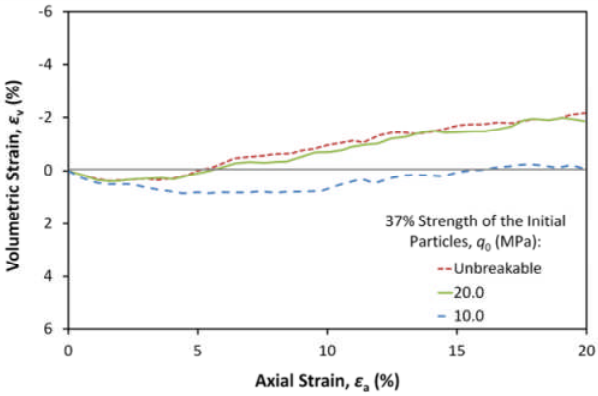

(b)

Figure 5.24 Triaxial results of an unbreakable sample, and two breakable materials with different particle strengths: deviatoric stress response (a) and volumetric behaviour (b)

The stronger crushable material experiences 40 breakages by an axial strain of 20%, with a fairly constant rate of breakage throughout the test. Out of the original 3350 specimen particles, 3312 remain at this stage, i.e. 38 have been crushed. The weaker material by comparison has experienced 463 breakages by the same axial strain, significantly more than the stronger sample. A total of 316 of the original particles have fractured, i.e. 9.43% by mass, compared to just 38—1.13% by mass—in the stronger simulation. Despite such a large number of particles undergoing fracture, only 7 particles break during isotropic confinement to 1 MPa; essentially all breakage occurs during shearing. The three final specimens—with the broken fragments highlighted—are shown in Figure 5.25. The material with unbreakable particles is displayed in Figure 5.25(a), and as can be seen from Figure 5.25(b) which shows the stronger crushable sand, the relatively small number (40) of breakages that occur are uniformly distributed throughout the height of the

specimen. The weaker material is shown in Figure 5.25(c), and also in Figure 5.25(d), which gives an internal view of the same sample revealing all broken fragments throughout the depth of the material. From these two images of the weaker sample, it appears that there is a concentration of breakage close to the platens and reduced breakage close to the membrane. These two observations are attributable to the fact that if a particle is loaded equally in all directions—e.g. has contacts uniformly spread over its surface—then the particle will have a high mean stress but a low octahedral shear stress; particles that are primarily loaded in one direction—e.g. diametral loading—will have a high induced shear stress. It is clear that the particles in contact with either of the platens are unlikely to be surrounded by particles, especially when the neighbouring particles are of the same size. Particles in contact with the membrane on the other hand are more likely to be loaded uniformly, due to the membrane being flexible and consisting of smaller particles, spreading the load.

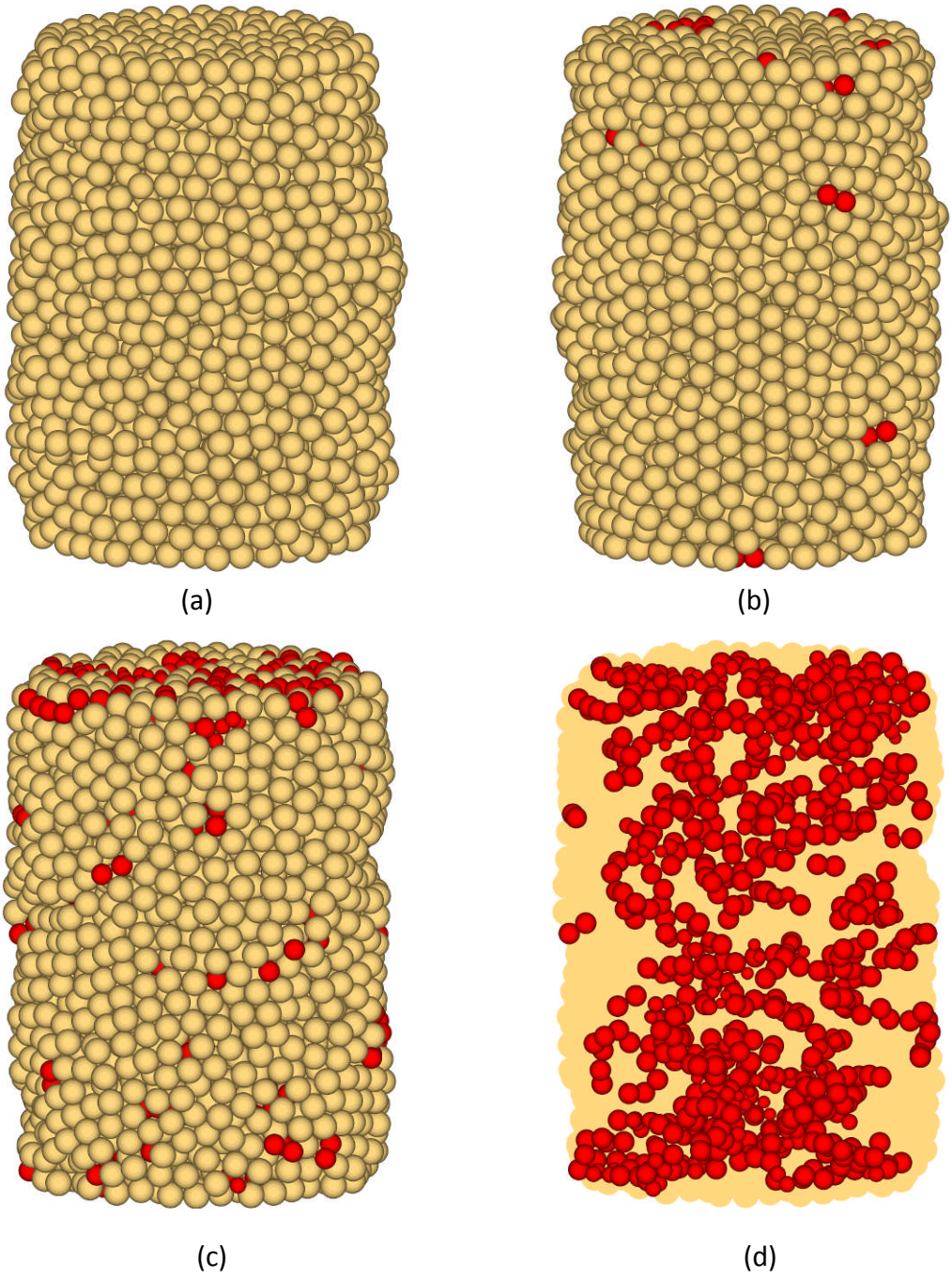

Figure 5.25 Images of the final specimens after shearing under 1 MPa of confining pressure to 20% axial strain: unbreakable simulation (a), crushable simulation with q_0 = 20 MPa (b), crushable simulation with q_0 = 10 MPa (c), and internal view of the same crushable simulation with q_0 = 10 MPa (d)

A series of simulations using the same crushable sand as in the above simulation are now presented, which demonstrate the effects of initial density and grading on the degree of particle crushing during triaxial shearing.

The effects of varying initial density are shown in Figure 5.26. The figure shows the triaxial results of the simulation above, with initial voids ratio of 0.75 alongside *looser* and *denser* simulations with initial voids ratios of 0.85 and 0.66 respectively (before the confining pressure of 1 MPa is applied). All simulations use particle strengths obtained from silica sand (q_0 = 20.0 MPa for d_0 = 4 mm). The voids ratio of 0.66 was found to be the densest stress-free initial state achievable, and so can be considered relatively very dense; while the voids ratios of 0.75 and 0.85 can both be considered relatively loose and very loose correspondingly.

The stress-strain response of the densest material (which originally consisted of 3530 particles) is initially noticeably steeper, almost displaying a peak stress. The loosest material (initially comprising 3165 particles) has the least steep deviatoric stress curve at the start of shearing. All three simulations appear to have essentially the same value of ultimate deviatoric stress, as well as the same final voids ratio. The three simulations—with increasing initial densities—begin shearing at voids ratios of approximately 0.64, 0.64 and 0.58 accordingly—all have a final value of e = 0.66 at 20% axial strain. Hence the densest sample displays a greater amount of dilation, as one would expect. Although the differences in behaviour between the simulations are not *as* pronounced, the stress-strain results show classic behaviour of loose-versus-dense sand in triaxial shearing, with the results comparable to those shown in Figure 2.1.

The densest material exhibits a slightly larger quantity of breakages, with 46 breakages occurring by an axial strain of 20%, compared to 38 for the loosest initial material. Further inspection reveals that of these 46 breakages in the dense simulation, 42 of them were related to the original particles—that is to say 42 of the 3530 initial particles have broken, constituting 1.19% of the mass of the sample. In the intermediate simulation, 1.13% of the original material has been crushed by this stage, while in the loosest simulation, 1.17% of the material has been crushed. Although the densest material displays a marginally higher amount of crushing, there is no clear correlation;

in all simulations between 1.1–1.2% of the material has undergone fragmentation. The simulations suggest that while a denser material will undergo a higher number of particle breakages, the increased number of broken particles is most likely a result of having a larger number of particles to begin with, and that the degree of crushing (if measured by mass of the sample that has broken) is fairly consistent across the various initial densities.

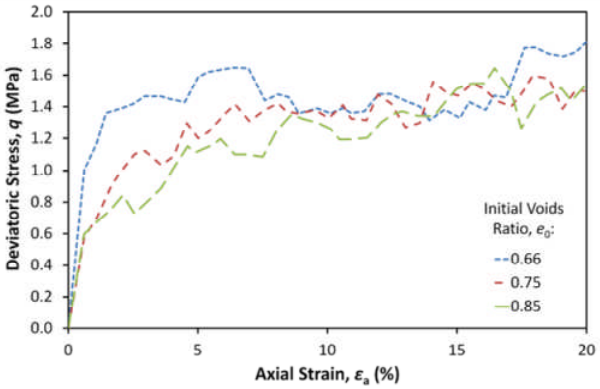

(a)

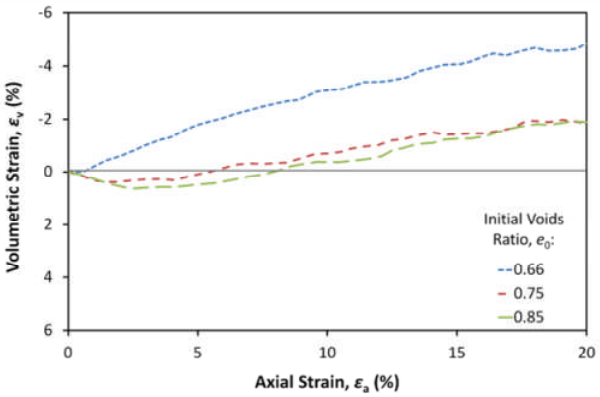

(b)

Figure 5.26 Triaxial results from three breakable samples with various initial voids ratios: deviatoric stress response (a) and volumetric behaviour (b)

The following graphs compare the triaxial response of the same mono-disperse sample with an initial voids ratio of 0.75, with that of a material with the same initial voids ratio but with a *graded* particle size distribution. The graded specimen has a coefficient of uniformity, C_u of 2: giving a total of 5986 initial particles, with minimum and maximum particle sizes of 2 and 8 mm respectively, and 12584 membrane particles. The two initial particle size distributions are given in Figure 5.27, and Figure 5.28 shows the triaxial results of the two materials sheared under 1 MPa of confining pressure.

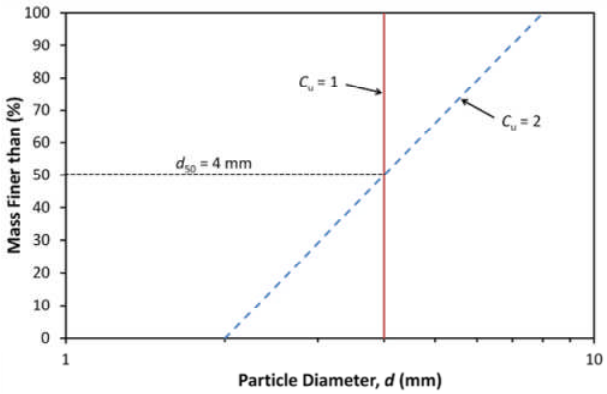

Figure 5.27 Particle size distributions for the mono-disperse (C_u = 1) and graded (C_u = 2) samples of sand

The graded sample appears to have a lower ultimate deviatoric stress, although one may expect them to display the same values due to the reasons mentioned above discussing the simulations with varying particle strengths. Although the difference in ultimate strength is conspicuous (approximately 0.25 MPa), they can be considered similar in view of the fact that the samples have such different fabrics (even at the end of the simulations, the initially graded material has in excess of 2700 more particles than the initially mono-disperse simulation). The simulation which displays the higher deviatoric stress also exhibits the largest dilation; one may assume that after much larger strains, the materials would approach the same ultimate stress.

Figure 5.28(b) shows that the graded specimen also undergoes significantly less volumetric dilation, which can largely be attributed to this material being relatively looser, despite having the same initial value of e_0—the final voids ratio of the graded simulation is 0.54 (much lower than 0.66). This difference would also suggest that the CSL in volume-stress space is lower for the graded (C_u = 2) material. Authors such as Muir Wood and Maeda (2008) and Yan and Dong (2011) conducted 2D and 3D simulations, shearing various gradings of a given material, and both presented critical state lines *unique* to each initial grading. They suggested the more well-graded a material is, the smaller the gradient and lower the position of the CSL in *v*-*p* space. However, they did *not* consider particle breakage, although Muir Wood and Maeda (2008) suggested the crushing limits the extent of the CSL, and causes it to move

downwards as the grading evolves. If indeed the critical state line is parallel with the normal compression line, one would expect the CSLs of different gradings of a given material to converge and have the same slope at high stresses. If, for example, the two simulations in Figure 5.28 were repeated but at a much higher confining pressure, one would expect significantly more crushing, and if they reach the same normal compression line, one would expect the two final samples also to approach the same critical state line.

With regard to particle crushing, the initially graded sample has experienced 89 breakages at an axial strain of 20% (compared with 40 for the initially mono-disperse simulation). Of these 89 particles that have broken, 77 were original sample particles, constituting 1.06% of the original specimen by mass (compared with 1.13% for the mono-disperse simulation). Further analysis reveals that of these 77 sample particles that have broken to form new fragments, 47 of them had diameters in the region d_{min}–d_{20}, and 21 were of the region d_{20}–d_{40}. So clearly it is the smallest particles that account for most of the breakages. This agrees with the findings expressed in Chapter 4 in which it was shown that it is the smallest particles that are most susceptible to fracture due to the increased possibility of being loaded diametrically (and therefore having the largest induced shear stress). It is interesting to note that while a larger *quantity* of original particles have fractured in the graded sample, the broken fragments constituted a smaller proportion *by mass* of the original specimen when compared to the mono-disperse simulation. It is known that the continued breaking of the smallest fragments is what leads to fractal particle size distributions; this appears to be the case in triaxial shearing.

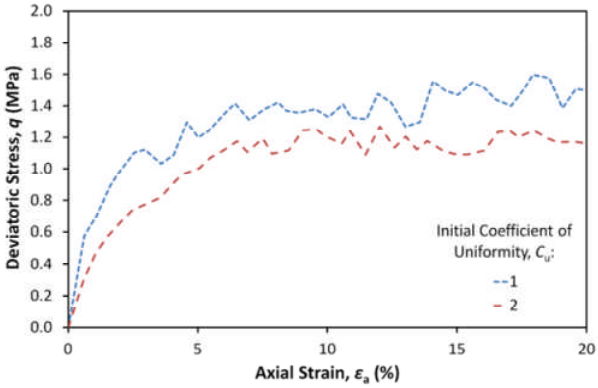

(a)

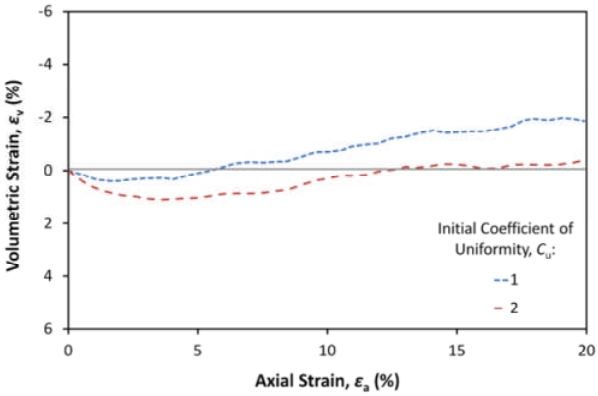

(b)

Figure 5.28 Triaxial results from two breakable simulations, one with a mono-disperse sample with coefficient of uniformity, C_u = 1, the other a graded sample with C_u = 2: deviatoric stress response (a) and volumetric behaviour (b)

5.3.4 Confining Pressure

Simulations of crushable sand subjected to triaxial tests with confining pressures up to 4 MPa are now presented. All simulations start with identical specimens, the same as outlined above: the initial voids ratio is 0.75, the mono-disperse sample consists of spheres of diameter 4 mm, and the initial characteristic particle strength q_0 is 20.0 MPa.

The stress-strain results of four simulations, with confining pressures of 1, 2, 3 and 4 MPa are displayed in Figure 5.29, in which the simulations reproduce the well-known behaviour of sand in triaxial shearing when subjected to an increase of confining pressure. There is an increase in maximum deviatoric stress (and a slight increase in the axial strain to this stress) and dilation is greatly suppressed causing an overall contraction to be observed. For comparison, an equivalent set of simulations using *unbreakable* particles are

presented in Figure 5.30. The same pattern of behaviour is observable in the graph giving the deviatoric stress response; although the ultimate values of shear strength are higher. The most visible difference however is in the volumetric responses; the non-crushable simulations in Figure 5.30(b) reveal very little difference between the simulations, with shearing at *all* levels of confining pressure resulting in dilation. Both of these differences are due to the inability of the particles to break, and the fact that the samples all assume very similar dense packing upon application of the confining pressure (in turn due to the lack of irregular particle shape). The graphs in Figures 5.29 and 5.30 show the same behaviour as presented by Bolton et al. (2008), whose triaxial simulations on unbreakable agglomerates displayed higher ultimate deviatoric stress, and dilation even under confining pressures as high as 40 MPa.

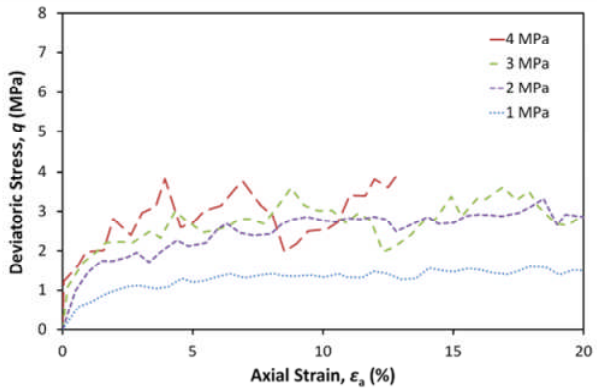

(a)

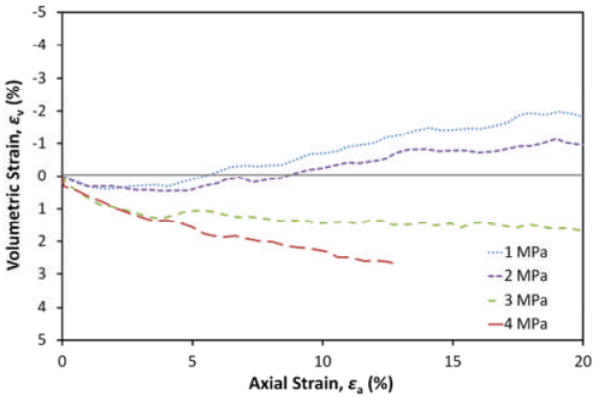

(b)

Figure 5.29 Triaxial results from simulations on crushable sand at various high confining pressures: deviatoric stress response (a) and volumetric response (b)

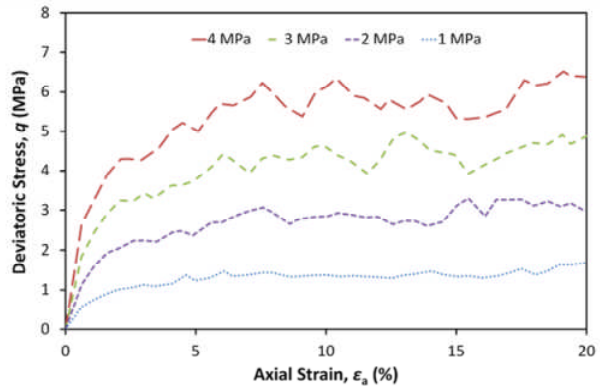

(a)

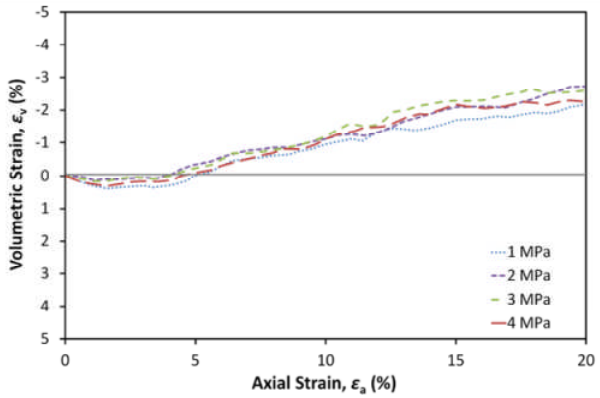

(b)

Figure 5.30 Triaxial results from simulations on sand with unbreakable particles, at various high confining pressures: deviatoric stress response (a) and volumetric response (b)

In the simulations using breakable particles, due to the nature of the particle breakage mechanism—as mentioned earlier—there are major fluctuations visible in Figure 5.29(a), particularly in the simulations with confining pressures of 3 and 4 MPa. Due to such a large proportion of particles breaking and being replaced with smaller fragments at any particular occasion, there are noticeable drops in the stress exerted on the platens (and hence the deviatoric stress), which are only recovered after a moderate amount of further axial strain. The simulation with a confining pressure of 4 MPa was terminated at approximately 13% axial strain; the amount of crushing causing it to become onerous (very small timestep and a large number of different-sized particles).

In the simulations with larger confining pressures (3 and 4 MPa), it may be reasonable to consider the average peak values of deviatoric stress as the ultimate values. Aside from the fact that the ultimate values of shear

strength would otherwise be too close to the simulation at 2 MPa, the peaks observed in the simulations at 3 and 4 MPa confining pressure are recovered and appear to be a result of the particle breakage mechanism (as opposed to a *single* peak resulting from the soil fabric/structure, followed only by strain softening). The breakage mechanism used (Figure 4.3) causes a complete loss of contact in the major principal stress direction (due to the placement of the new fragments), which would naturally cause an imminent drop in the global major principal stress. In reality, in a dense sample of sand, any particle breakage would not necessarily cause a complete loss of contact, and in any case due to the *larger* total number of particles and the fact that breakage can occur at any moment in time, the effects on the deviatoric stress would not be as visible. With this in mind, the ultimate stresses increase with increasing confining pressure, with the simulations that were taken to 20% axial strain displaying fairly constant values. The simulations with σ_3 = 1 and 2 MPa appear to have reached (or be approaching) a state of constant volume, indicative of a critical state; the simulation with σ_3 = 3 MPa appears as though it *could* be still contracting slightly; while the simulation with 4 MPa of confining pressure, which was terminated early, clearly still appears to be contracting.

The ability of the sand particles to crush enables the simulations at higher confining pressures to exhibit significant contraction, which was not observed in the simulations using unbreakable particles. This more realistic volumetric strain can also be observed in the stress-dilatancy plots, which are presented in Figure 5.31, and show that the simulations under the highest confining pressure display very little positive dilatancy and have lower peak values of dilatancy and stress ratio.

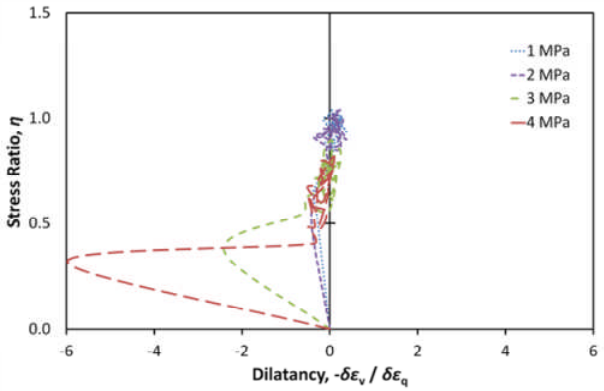

Figure 5.31 Stress-dilatancy plots for uncemented simulations across a range of confining pressures

The stress ratio versus axial strain for the four crushable simulations is shown in Figure 5.32. The sand displays a similar ultimate stress ratio at the lower levels of confinement, which could suggest a steady critical state parameter *M*. However, at a confining pressure of 3 MPa, the ultimate value of stress ratio appears slightly lower, whereas the simulation with 4 MPa of confining pressure did not reach comparable strains. It is possible that continuing the simulations to higher axial strains would result in convergence in the ultimate values of stress ratio, especially when one considers the graphs from Marri (2010) or for example Figure 2.40 from Yamamuro and Lade (1996), in which steady/critical states were only reached at or above 30% axial strain. In Figure 5.32, increasing the confining pressure appears to reduce the initial steepness/inclination of the normalised stress curve, and hence increases the axial strain at which the steady, ultimate stress is reached. If one overlooks the fluctuations in the deviatoric stress responses for the simulations at 3 and 4 MPa, this graph shows good agreement with that shown in Figure 2.40(a) from Yamamuro and Lade (1996), albeit not to the same level of axial strain.

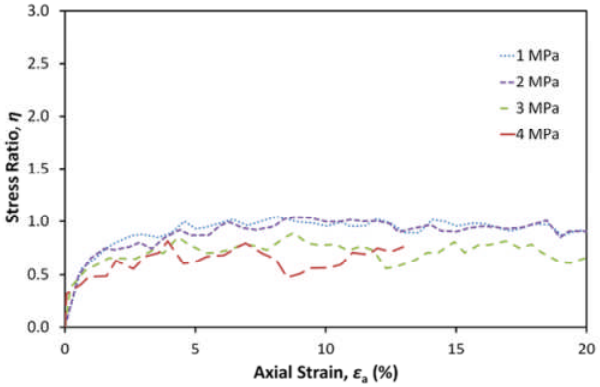

Figure 5.32 Graph showing the stress ratio versus axial strain for the four simulations across various high confining pressures

The end point for most of the simulations was 20% axial strain, however the simulation at the highest confining pressure (4 MPa) was terminated prior to this, due to a large number of particles covering a wide range of sizes rendering the calculation time impractical (at the point of termination, the simulation with 4 MPa of confining pressure had undergone over 3300 breakages). Nonetheless, comparing the state of the simulations at an axial strain of 10%, for example reveals an increasing degree of particle crushing with increasing confining pressure. At this strain, the simulations with σ_3 = 1, 2, 3 and 4 MPa had experienced 16, 195, 677 and 1949 breakages respectively. Of the original specimens, 15, 159, 394, and 703 particles had broken, which represent 0.45, 5.82, 11.76 and 20.99% by mass of the original specimens, respectively. There is a clear correlation between level of confining pressure and the degree of crushing exhibited during shear.

Figure 5.33 plots the overall number of breakages (at 10% axial strain) as a function of confining pressure, as well as the number of original particles broken. The upper curve shows that the overall number of breakages increases rapidly, and non-linearly with confining pressure. The lower curve however, suggests that the actual number of original particles that break during shearing increases more steadily (although not linearly) with confining pressure. These two curves together show that at higher pressures, most of the particles that are breaking are themselves fragments of larger broken particles.

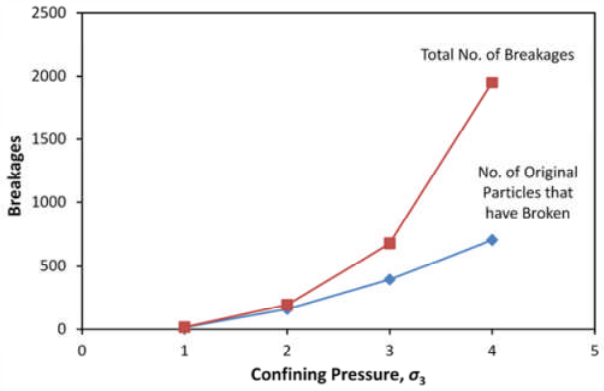

Figure 5.33 Graph showing the overall number of breakages, and the number of original particles that have fragmented by an axial strain of 10%, as a function of confining pressure

Figure 5.34 shows the total number of particles as a function of axial strain, for the four simulations at different confining pressures. The graph confirms the observation from the previous figure that confining pressure greatly increases the degree of crushing. The trends of the curves in Figure 5.34, particularly for the simulations at 3 and 4 MPa confining pressures, demonstrate that breakage increases rapidly with shearing, and that breakage shows no indication of reducing as steady states are approached. However, it appears that most of breakages that continue to occur are the fragments, which comprise the smallest particles; this would suggest that the particle size distributions are still evolving, potentially tending to fractal distributions.

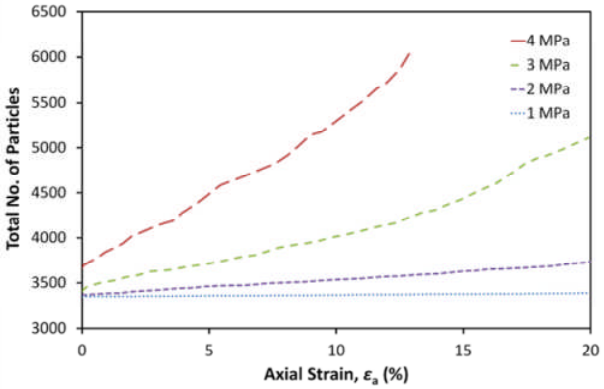

Figure 5.34 Graph showing the total number of particles, as a function of axial strain for the four simulations at various confining pressures

Figure 5.35 displays the total surface area of the particles as a function of axial strain. The curves in this figure appear to increase more linearly than those in Figure 5.34, although they also show no indication of reaching ultimate values. This suggests that there is still significant crushing occurring

when the simulations were terminated, which one may not expect at critical states, when the volume is constant. However, Miura and Yamamoto (1976) and Miura and O-hara (1979)—who quantified breakage during triaxial shearing by measuring the change in surface area—showed that the particle surface area was still increasing at axial strains as high as 50%; when the deviatoric stress and volumetric strain appeared to be reaching stable values. Coop et al. (2004) also conducted a series of ring shear tests, and showed that not only particle crushing, but also volumetric strains continue to occur at very high strains. Although the rate of change of volume was small, Coop et al. (2004) showed that in most cases the volumetric strain only completely stabilised at shear strains of around 2000%. Hence this would suggest that crushing continues to very high strains during shear, and that the volume also may continue to change, although by a very small amount. Although crushing is still clearly occurring in the simulations, it is largely the smaller particles that are continuing to fragment; in reality, the smallest particles would eventually stop breaking due to the comminution limit, leading to an ultimate particle size distribution, which was also suggested by Coop et al. (2004).

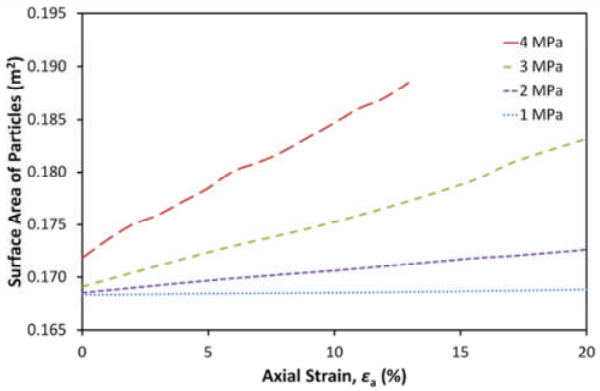

Figure 5.35 Graph showing the total surface area of the particles as a function of axial strain for the four simulations at various confining pressures

Inner views of the samples showing the broken fragments are given in Figure 5.36, which reveal the increasing degree of crushing experienced by the four simulations. The images are taken at 10% axial strain, and *all* the crushed fragments are highlighted, throughout the depth of the sample.

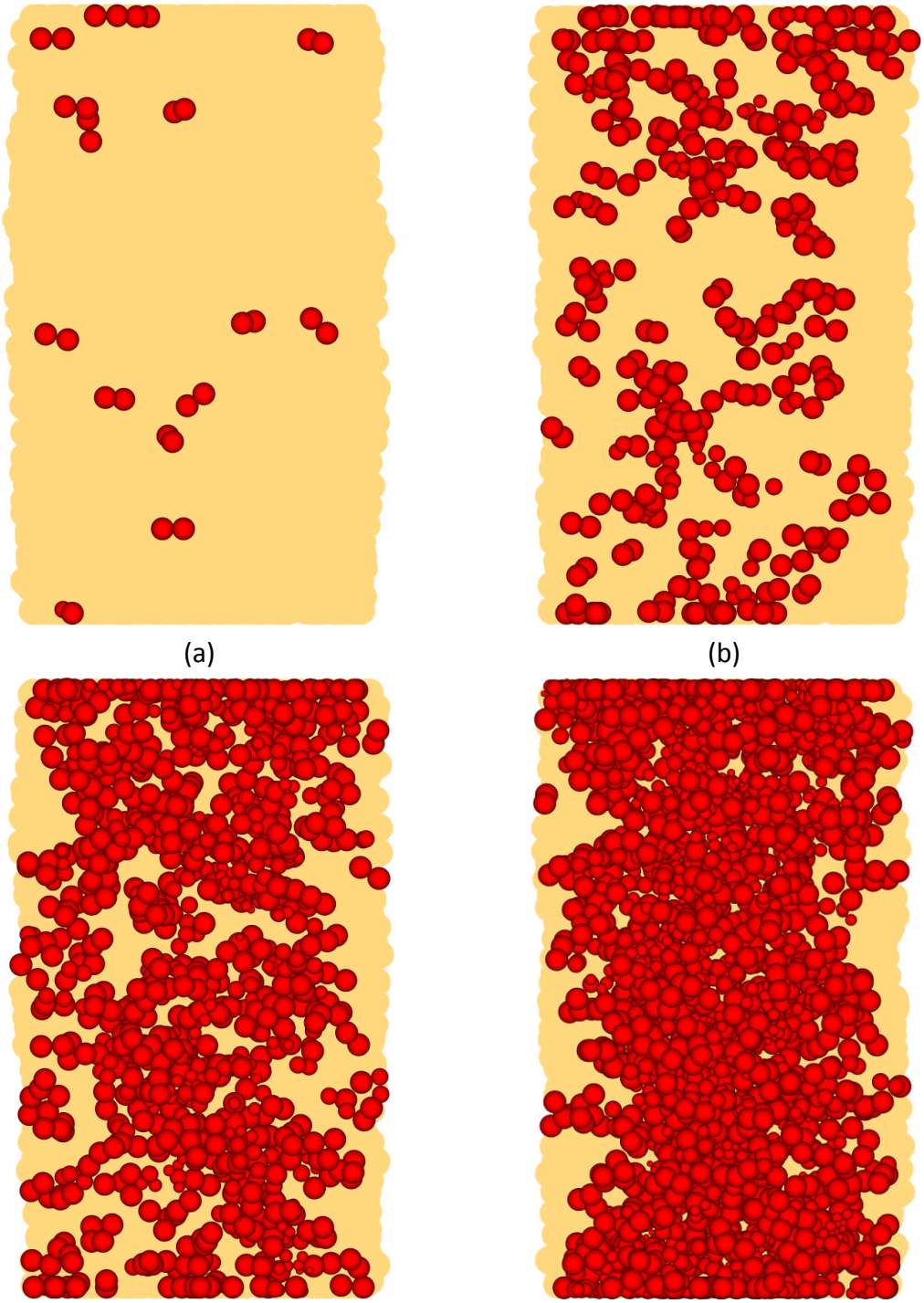

Figure 5.36 Inner views of specimens after shearing to 10% axial strain, showing highlighted broken fragments from simulations across a range of confining pressures: 1 MPa (a), 2 MPa (b), 3 MPa (c) and 4 MPa (d)

For the simulations at 1 and 2 MPa of confining pressure, the peak (failure) stress coincides with the ultimate deviatoric stress. For the two simulations with higher confining pressures, it is the average peak values in Figure 5.29 which are considered the ultimate deviatoric stress in the following analysis

(this is because the stress troughs are caused by particle breakage, and are recovered; as opposed to a single peak resulting from the soil packing, as mentioned earlier). Although Figure 5.29 suggests that the soils haven't yet *all* reached critical states, the ultimate states are plotted in deviatoric stress–mean effective stress space in Figure 5.37, alongside the equivalent simulations using *unbreakable* particles from Figure 5.30.

The disparity between the crushable and non-crushable simulations at σ_3 = 3 and 4 MPa would suggest different critical state lines, and hence different values of *M* for the two materials; with the non-crushable material having a slightly higher value (approximately equal to 1). The points from the crushable simulations give lower ultimate values of deviatoric stress, *q*, and indicate a curved line—the angle of friction appearing to decrease with confining pressure. This is similar to the observations by Cheng et al. (2004), who conducted constant *p*' shear tests using agglomerates in a cubical cell. They showed that the maximum angle of internal friction continued to decrease with the logarithm of mean stress, apparently approaching the angle of inter-particle friction, even after deviatoric strains of 40%. With regard to experimental data—for example Figure 3.31(a) from Marri (2010)—the critical state line for Portaway sand also appeared curved in *q*-*p*' space, similar to the numerical results for the crushable sand.

It is worth noting that all points from the simulations appear typically low; if realistic particle shape was incorporated, any critical state lines would appear much steeper and give more realistic *M* values.

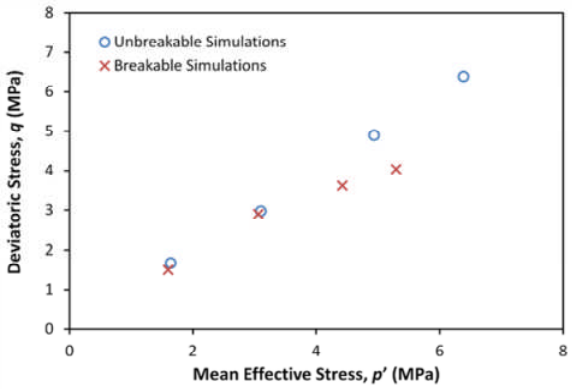

Figure 5.37 Critical/ultimate states of simulations on crushable and non-crushable sand under a range of confining pressures, plotted in *q*-*p*' space

The ultimate states for both the crushable and non-crushable sands are plotted on the conventional specific volume–mean stress space in Figure 5.38. The two sets of points are distinct from one another, although neither suggest completely linear critical state lines. However, if comparison is drawn between the crushable and non-crushable simulations, one can see that the points for the crushable simulation indicate a critical state line that has a noticeably larger negative gradient—i.e. steeper or more declined. Fitting a trendline to the points of the crushable simulation gives a gradient of approximately 0.08, which is reassuring, as typical values range from around 0.01–0.05 at low pressures, and larger at higher pressures (e.g. Wang, 2005; Wanatowski and Chu, 2007; Marri, 2010). There crushable material therefore again appears to offer much more realistic behaviour compared to the non-crushable simulations. It is important to note however that the crushable simulation at the highest confining pressure (4 MPa) was terminated prematurely at an axial strain of about 13%, well before appearing to approach a state of constant volume. Although one may assume the values of ultimate stress for this simulation may not change *significantly*, it is evident from the graph of volumetric strain in Figure 5.29(b) that one would expect the sample to continue contracting.

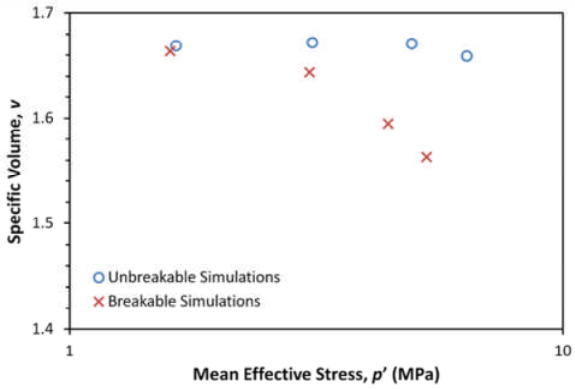

Figure 5.38 Critical/ultimate states of simulations on unbonded, crushable sand under a range of confining pressures, plotted in *v*-*p*' space

These states for the crushable sand are plotted in voids ratio–mean effective stress space in Figure 5.39, with double-logarithmic axes. If the critical state line is indeed parallel with the normal compression line, then as proposed in Chapter 4 it will also be linear when plotted in this space, and can be described by:

$$\log e = \log e_0 - C_c \log \frac{p'}{p'_0} \qquad [5.16]$$

where e is the voids ratio, e_0 and p'_0 define a reference point on the critical state line, and C_c is the rate at which the volume of voids decreases as the logarithm of mean effective stress increases—and is the slope of the normal compression line (compressibility index), governed by the size-hardening law of the particles according to equation [4.26].

The slope of the one-dimensional NCL for the material used in these triaxial simulations has a negative slope of approximately 0.5 as according to equation [4.26]—a critical state line with this ideal slope (0.5) is also shown in Figure 5.39. At *low* mean effective stresses, critical state points in *e*-*p*' or *v*-*p*' space often do not conform to the CSL at high stresses; if the linear CSL at high stresses is extrapolated, at low stresses critical state points usually lie *below* this line (e.g. Wood, 1990; Russell and Khalili, 2004). Considering that the rightmost point is still contracting and moving downwards towards the idealised CSL (as indicated by an arrow), the points appear to be approaching

a critical state line that is parallel with the normal compression line, and linear in log *e*–log *p*' space, although further points at higher pressures are desired.

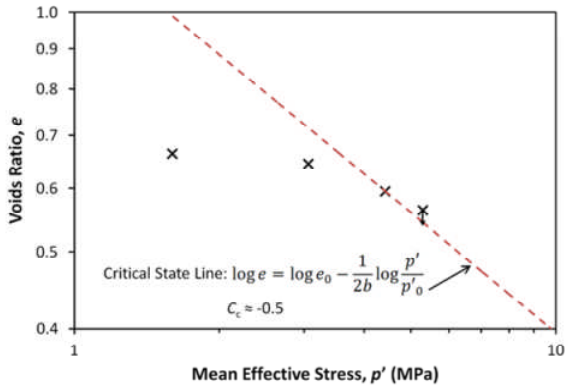

Figure 5.39 Critical/ultimate states from simulations of unbonded, crushable sand and idealised critical state line plotted in *e*-*p*' space

5.3.5 Cemented Sand

Simulations are now presented of triaxial tests on cemented sand with crushable particles. Using the same initial triaxial sample as above, and the same technique for modelling cementation (parallel bonds), simulations ranging from unbonded to highly cemented have been performed.

Experimental data for triaxial tests on sand bonded with various quantities of Portland cement are shown in Figure 5.40 from Marri (2010). The graphs show the deviatoric stress, stress ratio and volumetric strain responses from tests conducted under 1 MPa confining pressure. The effects of cementation are easily observed, with the graphs demonstrating an increase in strength, stiffness and dilation caused by the addition of cement.

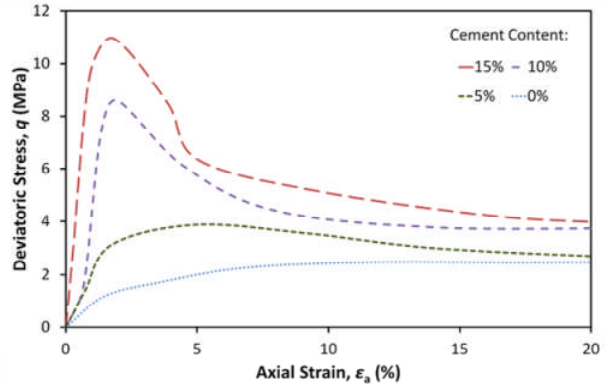

(a)

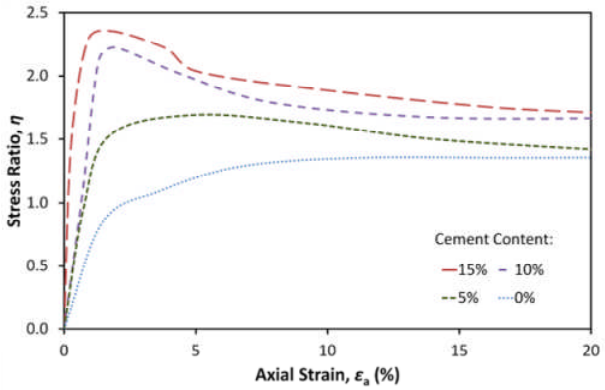

(b)

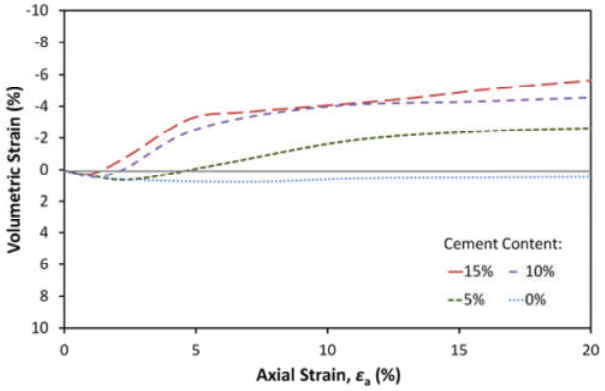

(c)

Figure 5.40 Experimental triaxial results for sand with a range of Portland cement contents: deviatoric stress (a), stress ratio (b) and volumetric response (c), versus stain (Marri, 2010)

The numerical sample used in the following simulations, is the same as that used throughout this section and described in Table 5.1. The parallel bonds are installed in the same manner as throughout the work on cemented sand, and have the properties described in section 5.2.3. Summarily, the initial sample is mono-disperse, comprising particles with diameter 4 mm, with an initial voids ratio of 0.75 (relatively loose). The particles are given a shear

modulus of 28 GPa and a Poisson's ratio of 0.25. The parallel bonds are equal in diameter to the particles (d_{bond} = 4 mm), are assumed to have an elastic modulus of 30 MPa (Ashby and Jones, 1986), and an arbitrary characteristic strength of approximately 10 MPa (in both pure shear and tension). The effects of varying the bond strength in triaxial simulations is not investigated here (see Chapter 3). The parallel bond strengths fit a Weibull distribution with a modulus, *m* of 0.5 (this was shown in Chapters 3 and 5 to result in the most qualitatively correct behaviour with regard to Portland cement). Increasing the degree of cementation is again implemented by increasing the quantity of inter-particle bonds, achieved by increasing the proximity in which non-touching particles are bonded. All simulations are subjected to 1 MPa of confining pressure. As detailed in section 5.2.3, parallel bonds, while intact, prevent particle breakage and hence bond breakage must precede particle crushing.

The triaxial results of four simulations ranging from uncemented to heavily cemented sand are shown in Figure 5.41. The increasing number of average parallel bonds per particle reflects increasing degree of cementation, i.e. cement content. The simulations with an average of 5, 10 and 15 bonds per particle can be considered lightly, medium and heavily cemented sand respectively. The results show the correct trend that one would expect from an increase in cement content: there is an increase in the peak and maximum deviatoric stress, a higher initial stiffness and there is a more dilative response; in general the material displays more brittle stress-strain behaviour. The peak deviatoric stress appears to occur at slightly earlier axial strains with an increasing degree of cementation, in agreement with typical experimental results such as those shown in Figure 5.40. Interestingly, the deviatoric stress responses do not appear to completely converge at large strains (as opposed to earlier simulations in Chapter 3). However, the graphs display good agreement with the experimental results shown in Figure 5.40, which also do not converge, even at strains as high as 30%. Both numerical and experimental stress ratio graphs display the same pattern of behaviour,

and reveal slightly different final values of η for the various materials. The most heavily cemented samples display the highest final stress ratios, suggesting that there is still active cementation at high strains under such a confining pressure. This is confirmed by the quantity of intact parallel bonds: at the end point of the simulations (i.e. ε_a = 20%), the lightly, medium, and heavily cemented simulations had 1029, 1262 and 1738 parallel bonds remaining respectively. Repeating the tests with a higher confining pressure would be expected to reduce the difference in the final values of stress ratio.

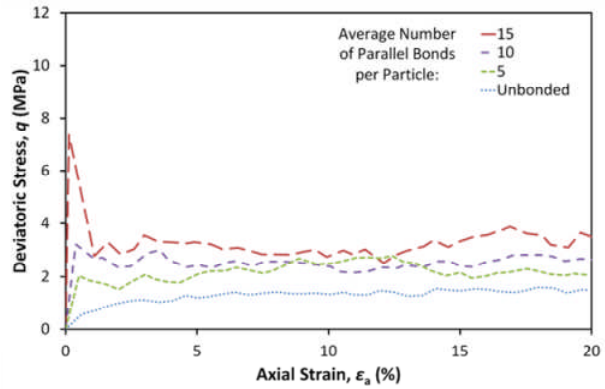

(a)

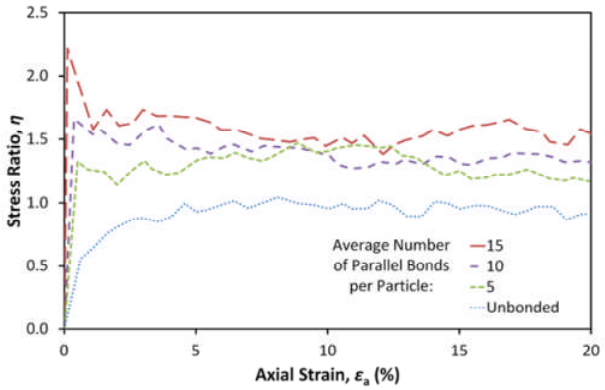

(b)

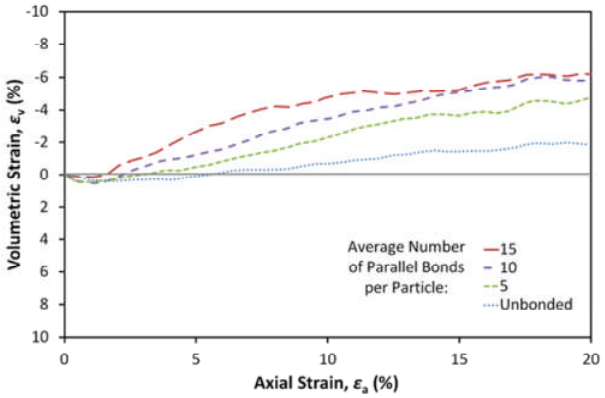

(c)

Figure 5.41 Triaxial results for simulations of crushable sand with an increasing degree of cementation: deviatoric stress (a), stress ratio (b) and volumetric response (c) versus strain

Figure 5.42 shows the corresponding results for simulations using unbreakable particles. The stress-strain behaviour is largely the same as above, with the introduction of cement producing the same results: an increase in peak/maximum deviatoric stress, higher initial stiffness and increased dilation; with these effects increasing with cement content. The unbreakable simulations however appear to display very slightly higher values of peak stress and dilation. This is for the same reasons as outlined earlier for

uncemented simulations; as particles are unable to break in these simulations, they will need to rearrange to accommodate the macroscopic strain by sliding and rolling over one another (as opposed to breaking), requiring additional dilation.

At the end of these simulations (20% axial strain), the quantities of intact bonds are 1048, 1352, and 1682, respectively for the lightly, medium and heavily cemented non-crushable materials; similar to the crushable cemented sand simulations above.

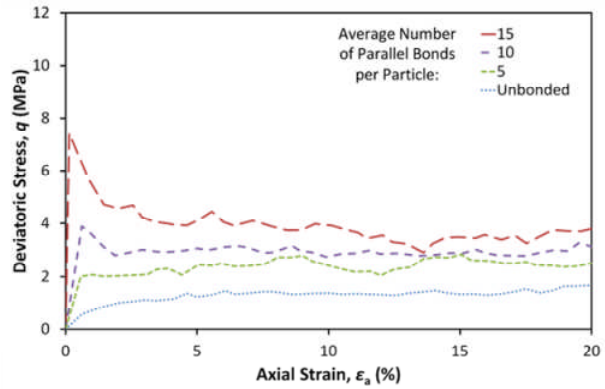

(a)

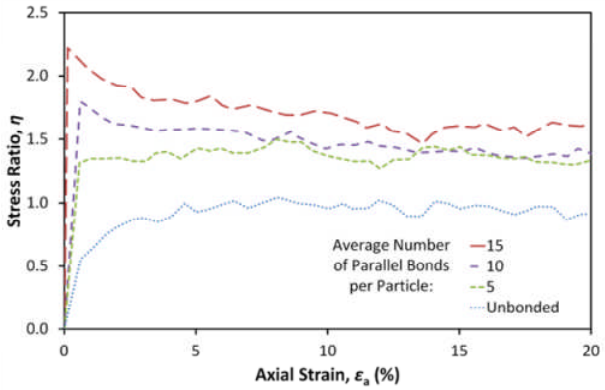

(b)

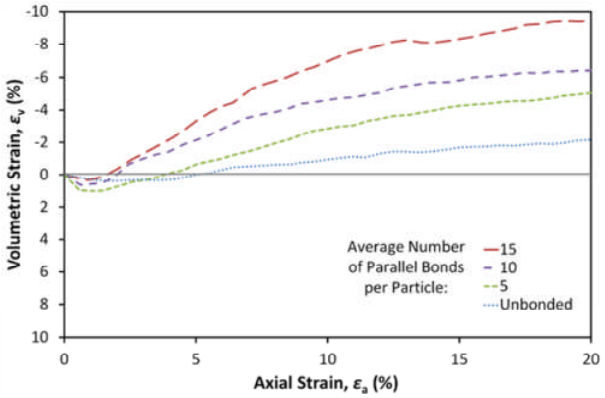

(c)

Figure 5.42 Triaxial results for simulations of non-crushable sand with an increasing degree of cementation: deviatoric stress (a), stress ratio (b) and volumetric response (c) versus strain

The stress-dilatancy response for the crushable simulations is presented in Figure 5.43, in which the stress ratio, η is plotted against dilatancy, D (in terms of $\delta\varepsilon_v$ / $\delta\varepsilon_q$). As shown in the literature review, Yu et al. (2007) proposed that increasing the cohesion shifts the dilatancy curve leftwards in η-D space and hence reduces dilatancy—but this is followed by a rapid increase which culminates in the peak value. This 'delay' in dilatancy is attributed to the cementation which prevents the intact material from dilating. This was in

accordance with authors such as Cuccovillo and Coop (1999), who theorised that if work is spent on degrading the bonding, the rate of dilation has to decrease. Marri (2010) and Marri et al. (2012) meanwhile proposed that at *high* confining pressures, increasing the cement content rather shifted the dilatancy curve upwards at a given confining pressure, as shown earlier in Figure 2.24(a).

It can be seen from Figure 5.43 that increasing the degree of cementation in the simulations initially inhibits dilatancy, with all the cemented samples extending further to the left than the uncemented equivalent. The cemented samples all display a rapid increase in dilatancy, culminating in peak values greater than that of the uncemented simulation. The most heavily cemented sample—with an average of 15 bonds per particle—demonstrates the highest peak dilatancy, as well as the highest values of peak and ultimate stress ratio η. Although Marri (2010) didn't provide the stress-dilatancy behaviour for sand with various cement contents at this confining pressure (1 MPa), the numerical results shown in Figure 5.43 in general agree with his experimental results, for example those shown Figure 2.24(a). Increasing the degree of cementation shifts the dilatancy response upwards in η-D space, and results in larger peak and ultimate stress ratios.

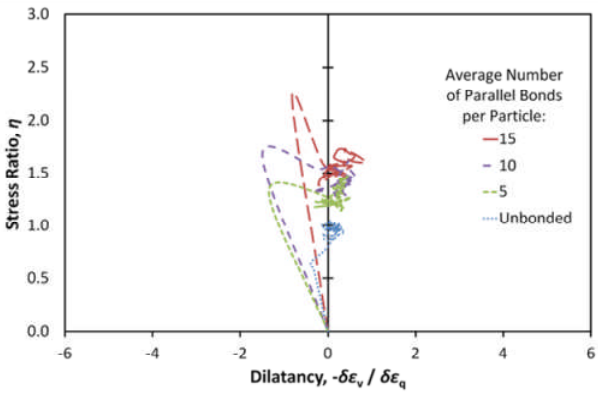

Figure 5.43 Stress-dilatancy plots for the crushable simulations at 1 MPa confining pressure with various cement contents

Increasing the cement content (by increasing the quantity of parallel bonds) causes the material to become more brittle; this is also evident in the deformation. Figure 5.44 displays the particle rotations on a vertical cutting

plane at approximately 4% axial strain (roughly the point of maximum dilation). The rotations are given for the unbonded and most heavily bonded simulations, for both crushable *and* non-crushable simulations. Both unbonded simulations in Figure 5.44(a) display no clear pattern, while the heavily cemented simulations in Figure 5.44(b) display localised failure with mild shear planes. This indicates that the ability for particles to crush has little effect on the failure mode and the overall deformation of cemented sand.

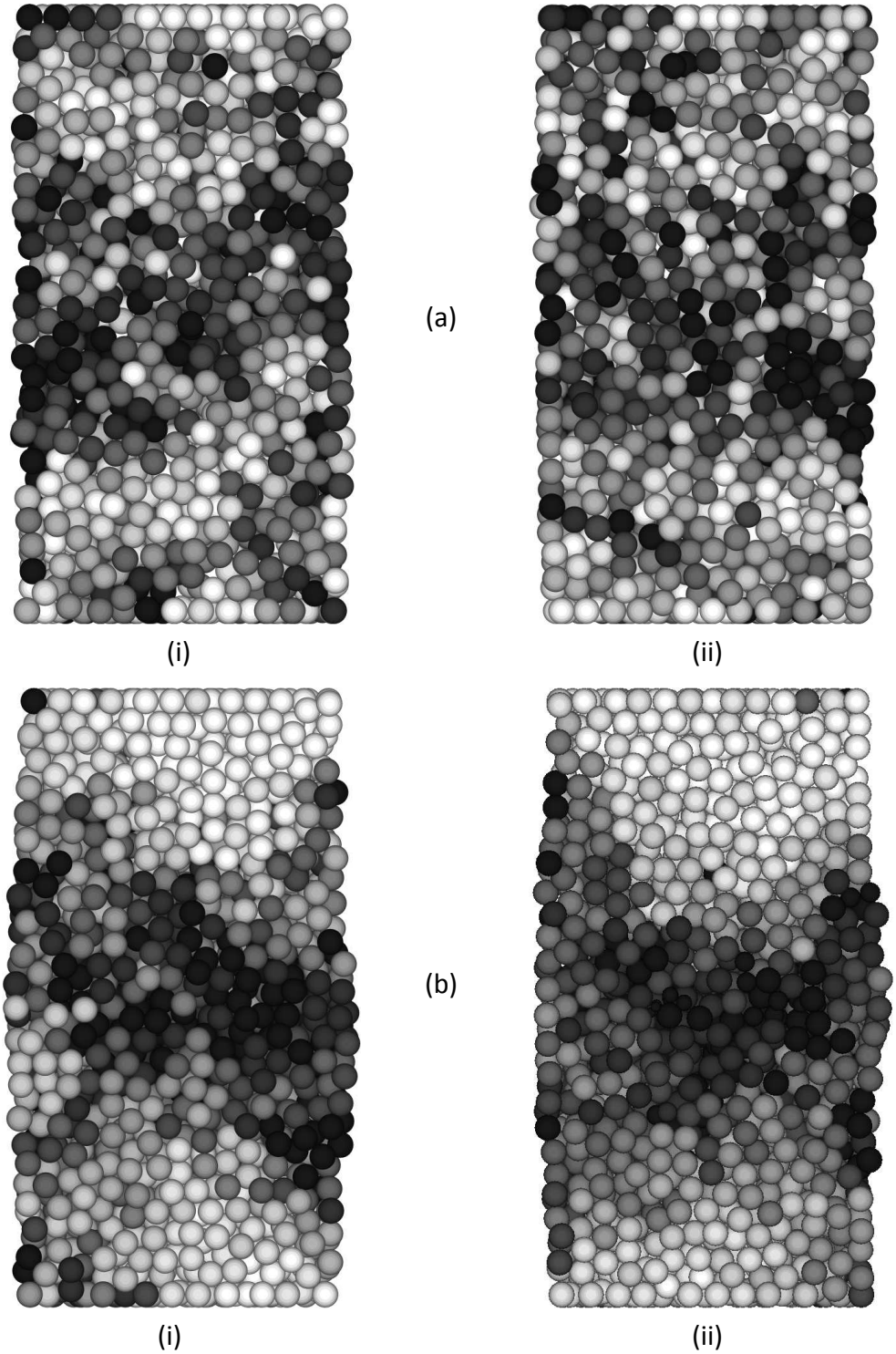

Figure 5.44 Particle rotations on a vertical cutting plane through the samples, at 4% axial strain: unbonded simulations (a) and heavily cemented simulations (b), with unbreakable particles (i) and breakable particles (ii). Dark indicates the most rotation

From experimental work, comprising series of triaxial tests covering a range of confining pressures and cement contents, Marri (2010) presented photographic images of samples after being subjected to shearing to 30% axial strain (given in Figure 2.42). From Figures 2.42(a) and 2.42(b), Marri

(2010) suggested that the inclusion of cement appeared to *reduce* the amount of particle crushing at a given confining pressure (in that case, 20 MPa). The SEM photographs were of the 'bulging' section of the uncemented sand, and of the external part of the shear zone in the heavily cemented sand. Despite Marri's (2010) suggestion, there is still crushing and surface fracture of the particles visible in the image of heavily cemented sand in Figure 2.42(b). However, it should be noted that the cementation in Figure 2.42(b) somewhat obscures the particles, and furthermore that SEM photographs by their nature are non-intrusive and do not reveal the interior micro-scale behaviour.

With regard to the *crushable* simulations, the unbonded and most heavily cemented samples (with an average of 0 and 15 bonds per particle respectively) sheared under 1 MPa confining pressure are shown in Figure 5.45(a), after shearing to 20% axial strain. Although the broken fragments are highlighted, no major differences with regard to the amount of crushing are *externally* visible. However, the cemented material has experienced a total of 244 breakages. Overall, 140 original particles have undergone fragmentation, meaning 4.18% by mass has crushed. This is markedly more crushing than the unbonded specimen, in which only 1.13% of the sample has broken at the same stage. These numbers can be confirmed visually in Figure 5.45(b), which presents similar images of the samples, but reveal the inner breakages.

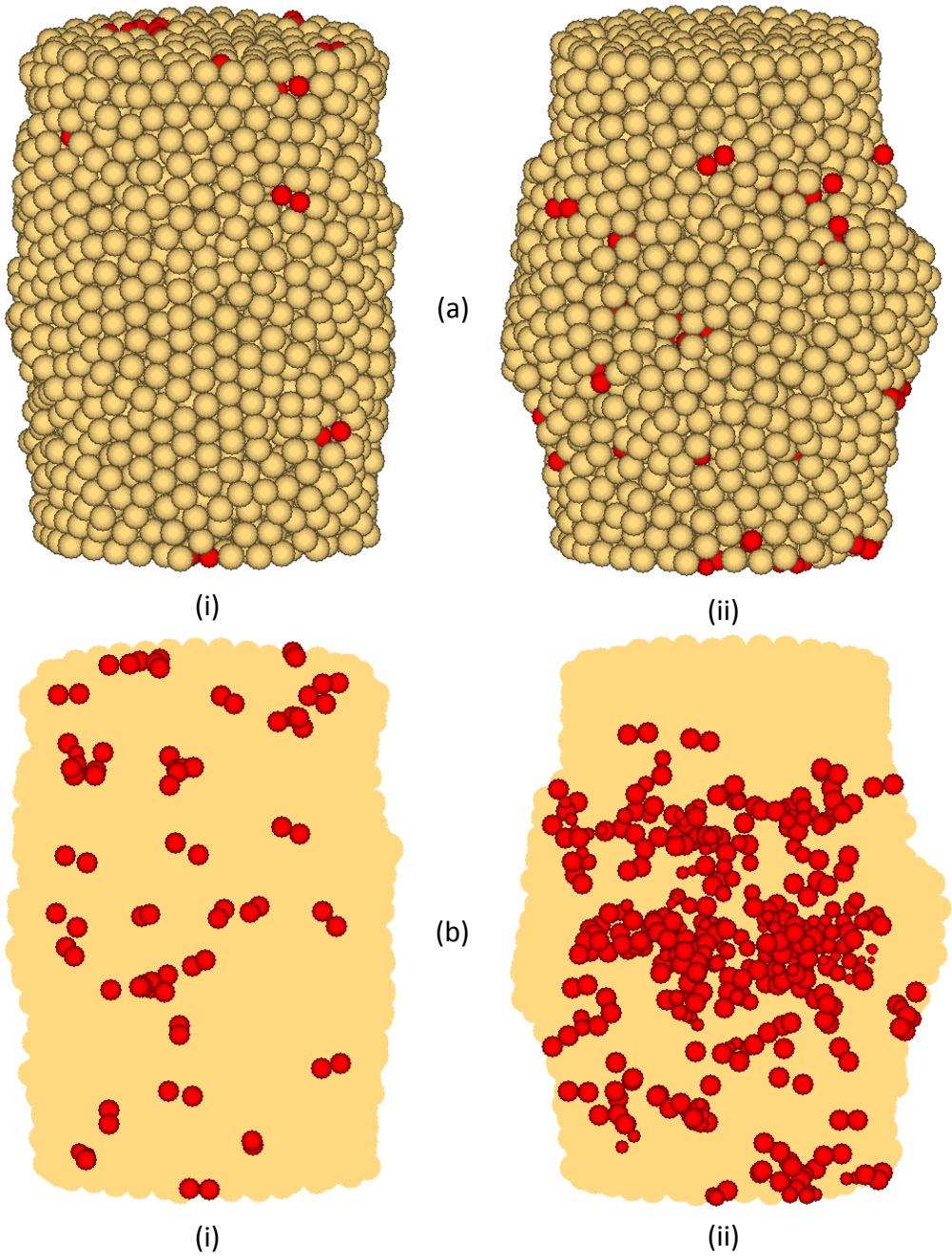

Figure 5.45 External views of the samples (a), with the broken fragments highlighted, and inner views showing all broken fragments (b); for the unbonded simulation (i) and heavily cemented (ii)

Considering just the heavily cemented sample, the broken fragments are shown again in Figure 5.46, in which a horizontal view at 4% axial strain is presented (all fragments are displayed, throughout the sample), taken from the same point of view as Figure 5.44(b)(ii). The crushing does not appear to occur uniformly throughout the sample, rather it appears very localised. The fragments indicate a shear plane, in harmony with the Figure 5.44(b)(ii), which displays the particle rotations from an identical point of view. From

this same point of view, Figure 5.47(a) shows the remaining unbroken parallel bonds at the same axial strain (for clarity, only bonds on a vertical cutting plane through the centre of the sample are displayed). Most bond breakages have occurred in the same area as crushing (Figure 5.46), which is unsurprising considering bond breakage must *precede* particle fragmentation. Particle crushing, bond breakage and the particle rotations all conform to the same shear plane, showing that the deformation and failure is brittle, and highly localised. At the same strain, the uncemented simulation has experienced only 8 breakages.

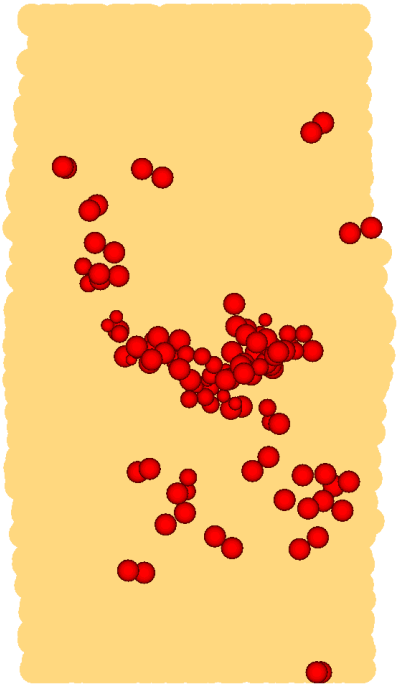

Figure 5.46 Inner view of heavily cemented specimen after 4% axial strain, with all broken fragments highlighted

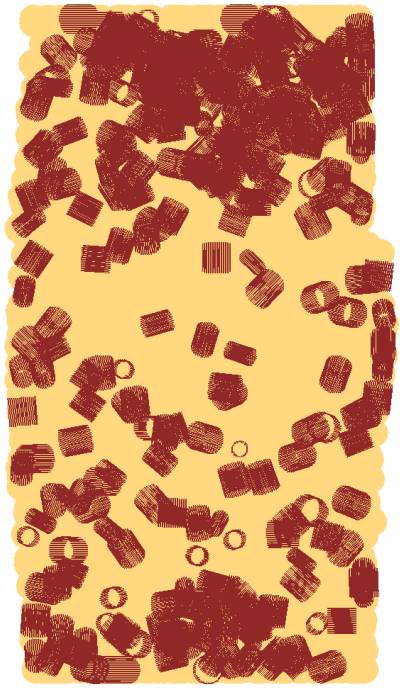

Figure 5.47 Remaining intact parallel bonds in the heavily cemented, crushable simulation on a vertical cutting plane through the sample, after 4% axial strain

Therefore the simulations suggest that the presence of cement—contrary to what Marri (2010) proposed—actually increases the degree of crushing, although the crushing is localised and concentrated around the shear plane. Increasing the degree of cementation/cement content in the simulations (by increasing the quantity of parallel bonds) increases not only the number of overall breakages but also the percentage of mass of the original material that undergoes breakage; with 1.13%, 2.36%, 2.96% and 4.18% by mass of the original samples undergoing crushing in the simulations with averages of 0, 5, 10 and 15 bonds per particle respectively. However, the introduction of crushing does not largely affect the overall stress-strain behaviour of the cemented sand, at least at a confining pressure of 1 MPa.

The observation that increasing the degree of cementation *increases* the amount of crushing during shear is intriguing, and may seem somewhat contrary to the conclusions from section 5.2—in which cementation was shown to *decrease* the amount of crushing for a given applied stress during one-dimensional compression. There are a number of differences which could explain these phenomena, such as that the one-dimensional compression simulations were stress-controlled tests and the triaxial

simulations were strain-controlled tests. The principal difference, however is that during the one-dimensional compression simulations, the cemented sand specimens could exhibit deformation in only one direction (the z-axis); during the triaxial simulations the specimens could deform freely in all three directions. In the triaxial shear test simulations, increasing the quantity of bonds rendered the material more brittle, and *changed* the method of deformation/failure mode. A high level of cementation resulted in localized failure in the form of a shear plane (regardless of whether the particles could break or not); across which parallel bonds broke as the macroscopic strain was applied. According to classical soil mechanics, a shear plane separates two intact 'blocks' of soil, and after rupture, the soil *only* shears on this plane, which becomes much weaker than the rest of the sample and continues to distort. As shearing only takes place between these two intact blocks, the particles on this plane are subjected to much larger shear stresses than elsewhere in the sample. This explains the concentration of breakages on the shear plane witnessed in the simulation of heavily cemented sand—and can also explain the increased overall amount of crushing. If one considers the uncemented crushable simulation, as axial strain is applied to the specimen, there is fairly uniform deformation, resulting in barrelling failure, as indicated by Figure 5.45(a)(i). To accommodate the macroscopic strain, *all* particles are free to move relative to each other; by sliding, rotating and rolling over one another. This means that local shearing takes place throughout the whole sample (on a particle-to-particle scale), and therefore almost all particles are subjected to local shear stresses—however, the individual particle stresses will be relatively uniform, and not as high as those on the shear plane in the heavily cemented, brittle material.

In the simulations of one-dimensional normal compression by comparison, all samples regardless of cement content exhibited the same mode of failure and deformation, during which, as the applied stress increased, so did *all* the local particle stresses. This is in contrast to the triaxial simulations, in which the

bonded particles within the intact 'blocks' were largely not subjected to increasing shear stresses as the test progressed.

5.3.6 Conclusions

The series of simulations presented in this section has demonstrated that it is possible to simulate high-pressure triaxial tests on a crushable soil, using a flexible membrane that allows free deformation. Sand was modelled using an aggregate of crushable particles, in which the octahedral shear stress was used as the fracture criterion. Significantly, it was shown that allowing particles to break enables realistic volumetric strain to be observed, with the crushable materials able to exhibit overall contraction instead of dilation. The particle strength had a major influence on the degree of crushing, which in turn influenced the amount of contraction. The initial density and grading were also investigated, as well as the confining pressure, which was shown to increase the quantity of breakage exponentially (Figure 5.33). The distribution of broken fragments after shearing was also explored, and it was found that breakage is slightly concentrated around the platens. In the simulations at higher confining pressures, it was shown that it was the breaking of the fragments themselves that accounted for the majority of overall breakages; showing that particle size distributions evolve to span wider ranges of scales as shearing progresses. The simulations were still exhibiting breakage at axial strains of 20%, which could indicate the eventual emergence of fractal particle size distributions.

From the results of simulations under a range of confining pressures, using the strength characteristics of a silica sand, the critical states were investigated. Critical states were plotted in deviatoric–mean stress space and voids ratio–mean stress space (as well as the conventional specific volume–mean stress space). According to the hypothesis put forward in Chapter 4—which stated that the slope of the normal compression line is a function of the size-hardening law—an idealised CSL with this theoretical slope was also plotted in voids ratio–mean stress space, under the assumption that the CSL and NCL are parallel at *high* stresses—once a significant number of particles

have resulted from crushing. The results were encouraging, and points from the simulations with the highest confining pressures appeared to be approaching this theoretical CSL; however, further tests at much higher confining pressures are needed to fully define the critical state line in three-dimensional volume-stress space.

Cemented sand was modelled by incorporating cementation using parallel bonds, in the same manner as in section 5.2. The existence of a parallel bond on a sand particle prevented the particle from breaking, and the presence of parallel bonds in general was shown to cause the correct qualitative change in behaviour that an increase in cement content causes in laboratory tests: a clearly defined peak strength, an increase in maximum strength, an increase in dilation, and more brittle deformation. Increasing the degree of cementation—by increasing the quantity of bonds—in concurrence with the simulations in Chapter 3, magnified these effects. The most heavily cemented material resulted in the most brittle failure, with a clear shear plane visible, which was manifested in the location of broken fragments, broken parallel bonds, and the particle rotations. In the cemented material, an *increase* in the degree of crushing was observed with increasing cement content, with this observation attributed to the change in deformation and failure from ductile to brittle; particle breakage appeared localised and concentrated on the failure plane.

CHAPTER 6

CONCLUSIONS AND RECOMMENDATIONS

6.1 CONCLUSIONS

The discrete element method (DEM) has been used, via the software PFC3D (Itasca, 2005) to perform extensive simulations on uncemented and cemented sand under high pressures.

A high-pressure triaxial model has been developed, which has a flexible membrane that allows the correct failure mode to develop, without inhibiting deformation, as rigid boundaries have been shown to. The model allows the triaxial specimen to become distorted and exhibit non-uniform shape, while maintaining the correct confining pressure. In the series of simulations in Chapter 3, cemented sand was modelled using an aggregate of spherical particles bonded with parallel bonds, and the influences of bond size, stiffness, strength, and strength distribution were explored. It was shown that for a given mean bond strength, a Weibull distribution with a modulus of 0.5 gave the most realistic results, with some bonds failing during consolidation and immediately after commencement of shearing, while the strongest remain intact throughout the tests. Such a distribution produced a sharp peak strength at lower confining pressures, and a more rounded peak at the highest pressures. The presence of bonds—representing cementation—also caused additional dilation when compared to the uncemented simulations. For a sample with a given number of bonds and initial density, the results indicated that it is the strength of the strongest bonds which govern any additional dilation caused by cementation. Increasing the quantity of bonds in the material appeared to be the most effective way of modelling an increased cement content. For a distribution of bond strengths, increasing the quantity (by bonding particles to neighbouring ones which aren't necessarily in contact, but lie within a specified proximity), resulted in the correct qualitative change in behaviour that an increase in

cement content causes in laboratory triaxial tests (a more clearly defined peak strength, an increase in strength, increased dilation, and more brittle behaviour). The flexible membrane permitted the correct failure modes to develop, allowing contrasting brittle and ductile failure modes caused by varying the cement content. By plotting the individual particle rotations, it was shown that increasing the number of bonds (i.e. the degree of cementation) increased the strength and brittleness of the material at a given confining pressure, with shear planes visible in the highly cemented simulations.

DEM was then used in Chapter 4 to simulate the one-dimensional compression of sand to investigate particle crushing, which is an essential feature of the behaviour of granular soils under high pressures, as well as the associated phenomenon of fractal particle size distributions. Particle fracture was simulated using a range of breakage mechanisms, replacing breaking particles with new smaller fragments while maintaining constant mass and avoiding the use of agglomerates. The octahedral shear stress was used as the fracture criterion, based on the assumption that particles are unlikely to break under just hydrostatic stresses. Normal compression lines were clearly observed, and the slope was consistent with theoretical predictions. For an initial voids ratio and given Weibull modulus (coefficient of variation) for the distribution of particle strengths, the yield stress was shown to be proportional to the average particle octahedral shear strength. For an initially uniform particle size, the rate of onset of yield was then shown to be a function of the distribution of particle strengths. The slope of the normal compression line and the particle size distribution appeared to be independent of both the breakage mechanism and the distribution of strengths, and solely dependent on the size effect on average particle strength. This appeared to clearly demonstrate that the plastic compressibility index is simply the hardening law due to the smallest particles breaking and becoming statistically stronger, which led to a new equation for the one-dimensional normal compression of sand. The evolution of fractal

particle size distributions was triggered by the tendency of similar sized neighbouring particles to fracture. The results showed evidently that a fractal distribution of particle sizes emerges, with a fractal dimension of 2.5. The simulations also showed the correct behaviour when a comminution limit was included, such that the compressibility index reduced at high stresses. The compression lines were also plotted in double logarithmic space (log e–log σ) and the NCL for the simulation of silica sand showed good agreement to both the experimental results and McDowell's (2005) theoretical prediction.

In Chapter 5 the discrete element method was used to show that the time-dependent law for the strength of ceramics gives rise to the correct creep behaviour under one-dimensional conditions. The simulation results agreed with the hypothesis that creep behaviour should be linear when the logarithm of voids ratio is plotted against the logarithm of time. The slope of the line was shown to be given by a new equation, which included the size effect on average strength as well as the exponent for the time-dependent strength. Therefore, by performing standard tests to obtain the size effect on average tensile strength of grains of a material by crushing between flat platens, and if the exponent for time-dependent strength can be measured by allowing particles to be loaded under constant stress and measuring the time to failure, then the creep behaviour of an aggregate of such grains can be predicted.

The behaviour of cemented sand in one-dimensional compression was also replicated using DEM. The cementation was modelled with parallel bonds, and it was shown that if the bonds were configured so to prevent particle breakage, the correct transition is witnessed in the compression curves—the cemented simulations extended into the structure-permitted space, and displayed stronger yield stresses. The distribution of bond strengths was shown to control the post-yield compression line: a narrow bond strength distribution resulted in a sudden and catastrophic failure of bonds (i.e. brittle yielding whereby the post-yield compression line converges immediately to the intrinsic NCL); a much wider bond strength distribution produced a less

rapid onset of yield, and a more gradual convergence to the intrinsic compression line. A distribution with a low modulus such as 0.5 gave the most realistic behaviour with regard to modelling a strongly cemented sand, and analysing the simulations using Liu and Carter's (1999, 2000) framework for the compression of structured soils, the value of the destructuring index, β appeared to be in the correct range. The destructuring indices obtained from the simulations appeared to be a function of the bond strength distribution. The presence of bonding within the material was shown to reduce the compressibility and also the degree of particle crushing for a given applied stress, which confirms speculation from Marri et al. (2012). The Weibull modulus for the distribution of parallel bond strengths also appeared to have a direct influence on the destructuring index. Increasing the quantity of parallel bonds again appeared to be the most effective way of modelling increasing cement content—increasing the quantity of bonds magnified the effects of cementation (i.e. it increased the yield stress, rendered the sample more brittle and reduced the degree of particle crushing for a given applied macroscopic stress).

The final series of simulations presented demonstrated that it is possible to simulate high-pressure triaxial tests on a crushable soil, using a flexible membrane that allows free deformation. Sand was modelled using an aggregate of crushable particles, in which the octahedral shear stress was used as the fracture criterion. Allowing particles to break enabled realistic volumetric strain to be observed, with the crushable materials able to exhibit overall contraction instead of dilation. The particle strengths had a major influence on the degree of crushing, which in turn influenced the amount of contraction. The initial density and grading were also investigated, as well as the confining pressure, which was shown to drastically increase the quantity of breakage. Critical states were also investigated, and plotted in deviatoric–mean stress space as well as in specific volume–mean stress space. It appeared as though the position of the CSL in volume-stress space was influenced by the characteristic particle strengths, similar to the NCL.

According to the proposition from Chapter 4—that the slope of the normal compression line is a function of the size-hardening law—an idealised CSL was also plotted in voids ratio–mean stress space, under the assumption that the CSL and NCL are parallel at *high* stresses. The results were encouraging, with the points from the simulations with the highest confining pressures appearing to approach this theoretical CSL; although tests at higher confining pressures are required to fully define the critical state line in *e*-*p* space.

Cemented sand was then modelled by incorporating cementation using parallel bonds in the familiar manner (the existence of a parallel bond on a sand particle prevented the particle from breaking). The presence of parallel bonds in general was shown to cause the correct qualitative change in behaviour that an increase in cement content causes in laboratory tests: a clearly defined peak strength, an increase in maximum strength, an increase in dilation, and more brittle deformation. Increasing the degree of cementation—by increasing the quantity of bonds—magnified these effects. The most heavily cemented material resulted in the most brittle failure, with a clear shear plane visible, which was manifested in the location of broken fragments, broken parallel bonds, and the particle rotations. In the cemented material, an increase in the degree of crushing was observed with increasing cement content; particle breakage appeared localised and concentrated on the failure plane. This observation was attributed to the change in deformation and failure—from ductile to brittle—caused by increasing the degree of cementation.

6.2 RECOMMENDATIONS

The current research has provided a useful insight into the fundamental behaviour of sand under high pressures, in particular during one-dimensional compression, and has highlighted the importance of particle crushing. The behaviour of both uncemented and cemented sand during shear and compression has been investigated, however there remain many areas in which future research is desirable.

The simple breakage model presented in Chapter 3 has been shown to be an effective way of capturing particle crushing, and has many potential applications, in addition to those pursued in Chapter 5.

With regard to the compression of sand—as with any numerical modelling—there is a desire to improve the efficiency and realism of the simulations presented in this thesis. In general, the simulations became unsustainable upon reaching applied stresses of approximately 30 MPa, and contained around 20000 particles. The limiting factor was the range of particle sizes, rather than sheer quantity, which greatly reduced the numerical timestep. Ideally, with future advances in computing and DEM software, it would be highly desirable to conduct simulations that comprise significantly higher numbers of particles, compressed to higher pressures. This would enable wider, more continuous fractal particle size distributions to be observed, and longer compression lines that display fewer fluctuations to be plotted. Alternatively, as the breakage mechanism was shown to not affect the overall compressibility of resultant particle grading, different mechanisms could be explored, (e.g. Ben-Nun and Einav, 2010)—which could reduce the number of computational steps required to dissipate the artificial elastic energy induced following breakage.

Further work fully exploring not only the one-dimensional compression but also the isotropic normal compression of sand is an immediate objective. A full investigation of isotropic compression would shed light on how the macroscopic loading conditions influence the induced shear stresses and evolution of fractal particle size distributions. The separation of the one-dimensional and isotropic compression lines could be investigated, including simulations of soils with various coefficients of lateral earth pressure (K_0). To fully and realistically model the behaviour of sand in one-dimensional or isotropic compression, the incorporation of particle shape is a necessity. All of the principal work presented in Chapter 3 could be repeated with irregular shaped particles, using the clump feature of PFC3D, however the breakage

mechanism would need attention with regard to replacing particles with fragments self-similar in shape.

There are also plenty of opportunities for further work progressing from the triaxial model; primarily involving the modelling of crushable soils. Clearly, the simulations presented could be repeated to further axial strains to ensure critical states are reached. Additionally, further simulations at higher confining pressures are desired to predict accurate critical state lines in both deviatoric–mean stress space and voids ratio–mean stress space. However, as shown at the end of Chapter 5, the triaxial simulations also became unsustainable with a confining pressure of 4 MPa, which was not only due to the timestep and the range of particle sizes, but also the use of the flexible membrane. An obvious way of improving the efficiency of such simulations is to eliminate the use of a particle-based membrane—this comprised a high proportion of the total particles, which were inherently required to be smaller than the specimen particles. Avoiding the use of such a membrane, for example by using a rigid cylindrical boundary—while not providing realistic laboratory triaxial conditions (as outlined in Chapter 3)—would render the simulations significantly more economical and could enable a fuller analysis of the critical state line. However, this would not allow the natural deformation to occur; hence an alternative model, which *does* provide a flexible boundary but that is computationally less demanding than the particle-based membrane would be the ideal solution.

By analysing the critical state line to high pressures, it would be possible to shed light on the micro mechanics of critical state soil mechanics, and determine how the slope and position of the CSL in volume-stress space is related to both the micro properties of the soil and the evolving particle size distribution. It would also be possible to explain the true nature of the CSL in volume-stress space—for example: to determine if it is indeed parallel with the NCL line (and at what pressures is this the case); and, if it is parallel with the NCL in log voids ratio–log mean stress space, then the conventional use of specific volume could be questioned. This work should also involve the use of

realistic particle shape, not only to gauge its effects, but to ensure the simulations replicate soil as realistically as possible.

REFERENCES

Abdulla, A. A., & Kiousis, P. D. (1997). Behavior of cemented sands-I. Testing. *International Journal for Numerical and Analytical Methods in Geomechanics , 21* (8), 533-547.

Airey, D. (1993). Triaxial Testing of Naturally Cemented Carbonate Soil. *Journal of Geotechnical Engineering , 119* (9), 1379-1398.

Asghari, E., Toll, D., & Haeri, S. (2003). Triaxial behaviour of a cemented gravelly sand, Tehran alluvium. *Geotechnical and Geological Engineering , 21* (1), 1-28.

Ashby, M. F., & Jones, D. R. (1986). *Engineering Materials 2: An Introduction to Microstructures, Processing and Design.* New York: Pergamon Press.

Åström, J. A., & Herrmann, H. J. (1998). Fragmentation of grains in a two-dimensional packing. *The European Physical Journal B-Condensed Matter and Complex Systems , 5* (3), 551-554.

Banton, J., Villard, P., Jongmans, D., & Scavia, C. (2009). Two-dimensional discrete element models of debris avalanches: Parameterization and the reproducibility of experimental results. *114* (F4).

Belheine, N., Plassiard, J. P., Donze, F. V., Darve, F., & Seridi, A. (2009). Numerical simulation of drained triaxial test using 3D discrete element modeling. *Computers and Geotechnics , 36* (1), 320-331.

Ben-Nun, O., & Einav, I. (2010). The role of self-organization during confined comminution of granular materials. *Phil. Trans. Roy. Soc. A: Mathematical, Physical and Engineering Sciences , 368* (1910), 231-247.

Ben-Nun, O., Einav, I., & Tordesillas, A. (2010). Force attractor in confined comminution of granular materials. *Physical Review Letters , 104* (10).

Billam, J. (1972). Some aspects of the behaviour of granular materials at high pressures. In R. H. Parry (Ed.), *Proceedings of the Roscoe Memorial Symposium*, (pp. 69-80).

Bobet, A., Hwang, J., Johnston, C. T., & Santagata, M. (2011). One-dimensional consolidation behavior of cement-treated organic soil. *Canadian Geotechnical Journal , 48* (7), 1100-1115.

Bolton, M. (1979). *A guide to soil mechanics.* Macmillan Press Ltd., London, England.

Bolton, M. D., Nakata, Y., & Cheng, Y. P. (2008). Micro-and macro-mechanical behaviour of DEM crushable materials. *Geotechnique , 58* (6), 471-480.

Bowman, E. T., & Soga, K. (2003). Creep, ageing and microstructural change in dense granular materials. *Soils and Foundations , 43* (4), 107-117.

Bowman, E. T., Soga, K., & Drummond, W. (2001). Particle shape characterisation using Fourier descriptor analysis. *Geotechnique , 51* (6), 545-554.

Budhu, M., Ramakrishnan, S., & Frantziskonis, G. Modeling of granular materials: A numerical model using lattices. In C. S. Chang, A. Misra, R. Y. Liang, & M. Babic (Ed.), *Mechanics of deformation and flow of particulate materials.* Northwestern University, Evanston, Ill.: ASCE.

Camusso, M., & Barla, M. (2009). Microparameters calibration for loose and cemented soil when using particle methods. *International Journal of Geomechanics , 9* (5), 217-229.

Cheng, Y. P., Bolton, M. D., & Nakata, Y. (2004). Crushing and plastic deformation of soils simulated using DEM. *Geotechnique , 54* (2), 131-141.

Cheng, Y. P., Nakata, Y., & Bolton, M. D. (2003). Discrete element simulation of crushable soil. *Geotechnique , 53* (7), 633-641.

Cheng, Y. P., White, D. J., Bowman, E. T., Bolton, M. D., & Soga, K. (2001). The observation of soil microstructure under load. *Proc. Powders and Grains, Sendai* , 69-72.

Cheung, G., & O'Sullivan, C. (2008). Effective simulation of flexible lateral boundaries in two-and three-dimensional DEM simulations. *Particuology , 6* (6), 483-500.

Clough, G., Sitar, N., Bachus, R., & Rad, N. (1981). Cemented Sands under Static Loading. *Journal of Geotechnical Engineering , 107*, 799-818.

Consoli, N. C., Foppa, D., Festugato, L., & Heineck, K. S. (2007). Key parameters for strength control of artificially cemented soils. *Journal of Geotechnical and Geoenvironmental Engineering , 133* (2), 197-205.

Coop, M. R. (1990). The mechanics of uncemented carbonate sands. *Geotechnique , 40* (4), 607-626.

Coop, M. R., & Atkinson, J. H. (1993). The Mechanics of Cemented Carbonate Sands. *Geotechnique , 43* (1), 53-68.

Coop, M. R., Sorensen, K. K., Bodas Freitas, T., & Georgoutsos, G. (2004). Particle breakage during shearing of a carbonate sand. *Geotechnique , 54* (3), 157-163.

Craig, R. F. (2004). *Soil Mechanics.* Taylor and Francis.

Cuccovillo, T., & Coop, M. R. (1999). On the mechanics of structured sands. *Geotechnique , 49* (6), 741-760.

Cuccovillo, T., & Coop, M. R. (1997). Yielding and pre-failure deformation of structured sands. *Geotechnique , 47* (3), 491-508.

Cundall, P., & Strack, O. (1979). A discrete numerical model for granular assemblies. *Geotechnique* (29), 47-65.

Davidge, R. W. (1987). *Mechanical behaviour of ceramics.* Cambridge: Cambridge University Press.

dos Santos, A. P., Consoli, N. C., Heineck, K. S., & Coop, M. R. (2009). High-pressure isotropic compression tests on fiber-reinforced cemented sand. *Journal of Geotechnical and Geoenvironmental Engineering , 136* (6), 885-890.

Einav, I. (2007). Fracture propagation in brittle granular matter. *Proc. Roy. Soc. A. Mathematical, Physical and Engineering Science , 463* (2087), 3021-3035.

Ergenzinger, C., Seifried, R., & Eberhard, P. (2011). A discrete element model to describe failure of strong rock in uniaxial compression. *Granular Matter , 13* (4), 341-364.

Fu, X., Dutt, M., Bentham, A., Hancock, B., Cameron, R. E., & Elliott, J. A. (2006). Investigation of particle packing in model pharmaceutical powders using X-ray microtomography and discrete element method. *Powder Technology , 167* (3), 134-140.

Griffith, A. A. (1921). The phenomena of rupture and flow in solids. *Phil. Trans. Roy. Soc. Lond. , 221*, 163-198.

Haeri, S. M., Hamidi, A., & Tabatabaee, N. (2005b). The effect of gypsum cementation on the mechanical behavior of gravely sands. *Geotechnical Testing Journal , 28* (4), 380-390.

Haeri, S. M., Hamidi, A., Hosseini, S. M., Asghari, E., & Toll, D. G. (2006). Effect of cement type on the mechanical behavior of a gravely sand. *Geotechnical and Geological Engineering , 24* (2), 335-360.

Haeri, S. M., Hosseini, S. M., Toll, D. G., & Yasrebi, S. S. (2005a). The behaviour of an artificially cemented sandy gravel. *Geotechnical and Geological Engineering , 23* (5), 537-560.

Hagerty, M. M., Hite, D. R., Ullrich, C. R., & Hagerty, D. J. (1993). One-dimensional high-pressure compression of granular media. *Journal of Geotechnical Engineering , 119* (1), 1-18.

Hardin, B. O. (1985). Crushing of soil particles. *Journal of Geotechnical Engineering , 111* (10), 1177-1192.

Henkel, D. J., & Gilbert, G. D. (1952). The effect of the rubber membrane on the measured compression strength of clay samples. *Geotechnique , 3* (1), 20-29.

Huang, J. T., & Airey, D. W. (1998). Properties of artifically cemented carbonate sand. *Journal of Geotechnical and Geoenvironmental Engineering , 124* (6), 492-499.

Ismail, M. A., Joer, H. A., Randolph, M. F., & Merritt, A. (2002a). Cementation of porous materials using calcite. *Geotechnique , 52* (5), 313-324.

Ismail, M. A., Joer, H. A., Sim, W. H., & Randolph, M. F. (2002b). Effect of cement type on shear behavior of cemented calcareous soil. *Journal of Geotechnical and Geoenvironmental Engineering , 128* (6), 5220-529.

Itasca. (2005). *Particle Flow Code in Three Dimensions, Software Manual.* Minnesota, MN: Itasca Consulting Group Inc.

Iwashita, K., & Oda, M. (1998). Rolling resistance at contacts in simulation of shear band developments by DEM. *Journal of Engineering Mechanics , 124* (3), 285-292.

Jaeger, J. C. (1967). Failure of rocks under tensile conditions. *International Journal of Rock Mechanics and Mining Sciences , 4* (2), 219-227.

Jaky, J. (1948). Pressure in silos. *Proc. 2nd Int. Conf. on Soil Mechanics and Foundation Engineering*, *1*, pp. 103-107.

Jewell, R. J., & Andrews, D. C. (1988). *Proc. Int. Conf. Calcareous Sediments* (Vol. 1). (R. J. Jewell, & D. C. Andrews, Eds.) Perth: Balkema, Rotterdam, The Netherlands.

Jewell, R. J., & Khorshid, M. S. (1988). *Proc. Int. Conf. Calcareous Sediments* (Vol. 2). (R. J. Jewell, & M. S. Khorshid, Eds.) Perth: Balkema, Rotterdam, The Netherlands.

Jiang, M. J., Yan, H. B., Zhu, H. H., & Utili, S. (2011). Modeling shear behavior and strain localization in cemented sands by two-dimensional distinct element method analyses. *Computers and Geotechnics , 38* (1), 14-29.

Jiang, M., Leroueil, S., & Konrad, J.-M. (2005). Yielding of microstructured geomaterial by DEM analysis. *Journal of Engineering Mechanics , 131* (11), 1209-1213.

Jiang, M., Yu, H.-S., & Leroueil, S. (2006). A simple and efficient approach to capturing bonding effect in. *International Journal for Numerical Methods in Engineering , 69* (6), 1158-1193.

King, R., & Lodge, M. (1988). North West Shelf development-the foundation engineering challenge. *Proc. Int. Conf. Calcareous Sediments , 2*, 333-342.

Lade, P. V., & Liu, C. T. (1998). Experimental study of drained creep behavior of sand. *Journal of Engineering Mechanics , 124* (8), 912-920.

Lade, P. V., Yamamuro, J. A., & Bopp, P. A. (1996). Significance of particle crushing in granular materials. *Journal of Geotechnical Engineering , 122* (4), 309-316.

Lagioia, R., & Nova, R. (1995). An experimental and theoretical study of the behaviour of a calcarenite in triaxial compression. *Geotechnique , 45* (4), 633-648.

Lee, D. M. (1992). *The angles of friction of granular fills.* University of Cambridge.

Leroueil, S., & Vaughan, P. R. (1990). The General and Congruent Effects of Structure in Natural Soils and Weak Rocks. *Geotechnique , 40* (3), 467-488.

Leung, C. F., Lee, F. H., & Yet, N. S. (1996). The role of particle breakage in pile creep in sand. *Canadian Geotechnical Journal , 33* (6), 888-898.

Lim, W. L., & McDowell, G. R. (2005). Discrete element modelling of railway ballast. *Granular Matter , 7* (1), 19-29.

Lim, W. L., McDowell, G. R., & Collop, A. C. (2004). The application of Weibull statistics to the strength of railway ballast. *Granular Matter , 6* (4), 229-237.

Liu, M. D., & Carter, J. P. (2000). Modelling the destructuring of soils during virgin compression. *Geotechnique , 50* (4), 479-483.

Liu, M. D., & Carter, J. P. Virgin compression of structured soils. *Geotechnique , 49* (1), 43-57.

Lo, S. C., Lade, P. V., & Wardani, S. P. (2003). An experimental study of the mechanics of two weakly cemented soils. *Geotechnical Testing Journal , 26* (3), 328-341.

Lobo-Guerrero, S., & Vallejo, L. E. (2005). Crushing a weak granular material: experimental numerical analyses. *Geotechnique , 55* (3), 245-249.

Maccarini, M. (1987). *Laboratory studies for a weakly bonded artificial soil.* PhD Thesis. Imperial College London (University of London).

Marri, A. (2010). *The Mechanical Behaviour of Cemented Granular Materials at High Pressures (PhD Thesis).* University of Nottingham.

Marri, A., Wanatowski, D., & Yu, H. S. (2012). Drained behaviour of cemented sand in high pressure triaxial compression test. *Geomechanics and Geoengineering , 7* (3), 159-174.

McDowell, G. R. (2005). A physical justification for log e-log σ based on fractal crushing and particle kinematics. *Geotechnique , 55* (9), 697-698.

McDowell, G. R. (2003). Micromechanics of creep of granular materials. *Geotechnique , 53* (10), 915-916.

McDowell, G. R. (2002). On the yielding and plastic compression of sand. *Soils and Foundations , 42* (1), 139-145.

McDowell, G. R. (2001). Statistics of soil particle strength. *Geotechnique , 51* (10), 897-900.

McDowell, G. R., & Amon, A. (2000). The application of Weibull Statistics to the fracture of soil particles. *Soils and Foundations , 40* (5), 133-141.

McDowell, G. R., & Daniell, C. M. (2001). Fractal compression of soil. *Geotechnique , 51* (2), 173-176.

McDowell, G. R., & Harireche, O. (2003). Discrete element modelling of cyclic loading of crushable aggregates. *Granular Matter , 5* (3), 147-151.

McDowell, G. R., & Harireche, O. (2002a). Discrete element modelling of soil particle fracture. *Geotechnique , 52* (2), 131-135.

McDowell, G. R., & Harireche, O. (2002b). Discrete element modelling of yielding and normal compression of sand. *52* (4), 299-304.

McDowell, G. R., & Humphreys, A. (2002). Yielding of granular materials. *Granular Matter , 4* (1), 1-8.

McDowell, G. R., & Khan, J. J. (2003). Creep of granular materials. *Granular Matter , 5* (3), 115-120.

McDowell, G. R., Bolton, M. D., & Robertson, D. (1996). The fractal crushing of granular materials. *Journal of the Mechanics and Physics of Solids , 44* (12), 2079-2102.

McDowell, G., & Bolton, M. D. (1998). On the micro mechanics of crushable aggregates. *Geotechnique , 48* (5), 667-679.

Mindlin, R. D., & Deresiewicz, H. (1953). Elastic spheres in contact under varying oblique forces. *Journal of Applied Mechanics , 20*, 327-344.

Miura, N., & O-hara, S. (1979). Particle-crushing of a decomposed granite soil under shear stresses. *Soils and Foundations , 19* (3), 1-14.

Miura, N., & Yamamoto, T. (1976). Particle-crushing properties of sands under high stresses. *Technical Reports of the Yamaguchi University , 1* (4), 439-447.

Muir Wood, D., & Maeda, K. (2008). Changing grading of soil: effect on critical states. *Acta Geotechnica , 3* (1), 3-14.

Murayama, S., Michihiro, K., & Sakagami, T. (1984). Creep characteristics of sand. *Soils and Foundations , 24* (5), 1-15.

Nakata, Y., Hyde, A. F., Hyodo, M., & Murata, H. (1999). A probabilistic approach to sand particle crushing in the triaxial test. *Geotechnique , 49* (5), 567-583.

Nakata, Y., Hyodo, M., Hyde, A. F., Kato, Y., & Murata, H. (2001b). Microscopic particle crushing of sand subjected to high pressure one-dimensional compression. *Soils and Foundations , 41* (1), 69-82.

Nakata, Y., Kato, Y., Hyodo, M., Hyde, A. F., & Murata, H. (2001a). One-dimensional compression behaviour of uniformly graded sand related to single particle crushing strength. *Soils and Foundations , 41* (2), 39-51.

Ng, T. T. (2004). Triaxial test simulations with discrete element method and hydrostatic boundaries. *Journal of Engineering Mechanics , 130* (10), 1188-1194.

O'Sullivan, C. (2002). *The application of discrete element modelling to finite deformation problems in geomechanics.* Phd Thesis, University of California, Berkeley.

O'Sullivan, C., & Cui, L. (2009). Micromechanics of granular material response during load reversals: Combined DEM and experimental study. *Powder Technology , 193* (3), 289-302.

Palmer, A. C., & Sanderson, T. J. (1991). Fractal crushing of ice and brittle solids. *Proc. Roy. Soc. A. Mathematical and Physical Sciences , 433* (1889), 469-477.

Pestana, J. M., & Whittle, A. J. (1995). Compression model for cohesionless soils. *Geotechnique , 45* (4), 611-631.

Pestana, J. M., & Whittle, A. J. (1998). Time effects in the compression of sands. *Geotechnique , 48* (5), 695-701.

Potyondy, D. O., & Cundall, P. A. (2004). A bonded-particle model for rock. *International Journal of Rock Mechanics and Mining Sciences , 41* (8), 1329-1364.

Roscoe, K. H., Schofield, A. N., & Wroth, C. P. (1958). On the yielding of soils. *Geotechnique , 8* (1), 22-53.

Rotta, G. V., Consoli, N. C., Prietto, P. D., & Graham, J. (2003). Isotropic yielding in an artifically cemented soil cured under stress. *Geotechnique , 53* (5), 493-501.

Rowe, P. W. (1962). The stress-dilatancy relation for the static equilibrium of an assembly of particles in contact. *Proc. Roy. Soc. A. Mathematical and Physical Sciences , 269* (1339), 500-527.

Russell, A. R. (2011). A compression line for soils with evolving particle and pore size distributions due to particle crushing. *Geotechnique Letters , 1* (1), 5-9.

Russell, A. R., & Khalili, N. (2004). A bounding surface plasticity model for sands exhibiting particle crushing. *Canadian Geotechnical Journal , 41* (6), 1179-1192.

Russell, A. R., Muir Wood, D., & Kikumoto, M. (2009). Crushing of particles in idealised granular assemblies. *Journal of the Mechanics and Physics of Solids , 57* (8), 1293-1313.

Salot, C., Gotteland, P., & Villard, P. (2009). Influence of relative density on granular materials behaviour: DEM simulations of triaxial tests. *Granular Matter , 11* (4), 221-236.

Sammis, C., King, G., & Biegel, R. (1987). The kinematics of gouge deformation. *Pure and Applied Geophysics , 125* (5), 777-812.

Schnaid, F., Prietto, P., & Consoli, N. (2001). Characterization of Cemented Sand in Triaxial Compression. *Journal of Geotechnical and Geoenvironmental Engineering , 127* (10), 857-868.

Shi, G. (1988). *Discontinuous deformation analysis-a new numerical model for the statics and dynamics of block systems.* University of California, Berkely, USA.

Sitharam, T. G., Dinesh, S. V., & Shimizu, N. (2002). Micromechanical modelling of monotonic drained and undrained shear behaviour of granular media using three-dimensional DEM. *International Journal for Numerical and Analytical Methods in Geomechanics , 26* (12), 1167-1189.

Steacy, S. J., & Sammis, C. G. (1991). An automaton for fractal patterns of fragmentation. *Nature , 353* (6341), 250-252.

Tijskens, E., Ramon, H., & De Baerdemaeker, J. (2003). Discrete element modelling for process simulation in agriculture. *Journal of sound and vibration , 266* (3), 493-514.

Tsoungui, O., Vallet, D., & Charmet, J.-C. (1999). Numerical model of crushing of grains inside two-dimensional granular materials. *Powder Technology , 105* (1), 190-198.

Turcotte, D. L. (1986). Fractals and Fragmentation. *Journal of Geophysical Research , 91* (B2), 1921-1926.

Utili, S., & Nova, R. (2008). DEM analysis of bonded granular geomaterials. *International Journal for Numerical and Analytical Methods in Geomechanics , 32* (17), 1997-2031.

Wanatowski, D., & Chu, J. (2007). Drained behaviour of Changi sand in triaxial and plane-strain compression. *Geomechanics and Geoengineering: An International Journal , 2* (1), 29-39.

Wang, J. (2005). *The stress-strain and strength characteristics of Portaway sand.* PhD Thesis, University of Nottingham.

Wang, Y., & Leung, S. (2008). A particulate-scale investigation of cemented sand behavior. *Canadian Geotechnical Journal , 45* (1), 29-44.

Wang, Y., & Tonon, F. (2009). Modeling triaxial test on intact rock using DEM with membrane boundary. *Journal of Engineering Mechanics , 135* (9), 1029-1037.

Weibull, W. (1951). A statistical distribution function of wide applicability. *Journal of Applied Mechanics , 18* (3), 293-297.

Williams, J. R., & Mustoe, G. G. (1993). *Proc. 2nd Int. Conf. on Discrete Element Methods (DEM).* Massachussetts Institute of Technology: IESL Publications.

Wood, D. M. (1990). *Soil behaviour and critical state soil mechanics.* Cambridge University Press.

Wroth, C. P. (1984). The interpretation of in situ soil tests. *Geotechnique , 34* (4), 449-489.

Yamamuro, J., & Lade, P. (1996). Drained Sand Behaviour in Axisymmetric Tests at High Pressures. *Journal of Geotechnical Engineering , 122*, 109-119.

Yan, W. M., & Dong, J. (2011). Effect of particle grading on the response of an idealized granular assemblage. *International Journal of Geomechanics , 11* (4), 276-285.

Yu, H. S., Tan, S. M., & Schnaid, F. (2007). A critical state framework for modelling bonded geomaterials. *Geomechanics and Geoengineering , 2* (1), 61-74.